POWER SYSTEM OSCILLATION IDENTIFICATION, CLASSIFICATION AND CONTROL BASED ON SUBSPACE IDENTIFICATION

by

Fahim Al Hasnain

A dissertation submitted to the faculty of
The University of North Carolina at Charlotte
in partial fulfillment of the requirements
for the degree of Doctor of Pholosophy in
Electrical Engineering

Charlotte

Approved by:

_____
Dr. Sukumar Kamalasadan

_____
Dr. Badrul Chowdhury

_____
Dr. Abasifreke Ebong

_____
Dr. Brett Tempest

©
Fahim Al Hasnain
ALL RIGHTS RESERVED

ABSTRACT

FAHIM AL HASNAIN. Power system oscillation identification, classification and control based on subspace identification. (Under the direction of DR. SUKUMAR KAMALASADAN)

Accurate knowledge and estimation of the electro-mechanical modes in the power system are of great importance since a system-wide outage can be caused by one single unstable mode of oscillation. Most of these unstable mode of oscillations are inter-area oscillations which typically are in the range of 0.15Hz to 1Hz. Generally oscillation identification and damping are performed based on Model-based frequency studies. However, the stochastic nature of modern power grid with the advent of renewables and changing load dynamics, and nonlinear interactions makes the oscillation study with apriori models inaccurate and inefficient. Due to these factors, recently, measurement-based power grid mode estimation has attracted great attention.

In this research work, a series of measurement-based oscillation identification methods are proposed. First, a comparison of various measurement-based electro-mechanical oscillation mode detection methods is studied. Among the measurement-based techniques, Prony analysis, Eigenvalue Realization Algorithm (ERA), and Matrix Pencil (MP) methods are found to be very useful. These methods have successfully been used to determine low-frequency oscillatory modes from measurement data. Recently, Subspace Identification (SSI) methods have become popular as they are robust to variations, and can be represented in state-space form, thus making it easier for designing time-domain control approaches. Thus, second, an online wide-area direct coordinated control architecture for power grid transient stability enhancement based on subspace identification and Lyapunov energy functions has been designed and studied. Third, a novel hybrid deterministic-stochastic online measurement-based identification framework using subspace theory is introduced. The novelty of the design using a fully recursive algorithm and the effectiveness of combined treatment are further discussed. For controlling electro-mechanical oscillations of the power system effectively, identifying the

location of the oscillation source is very important. Thus, fourth, an approach for power system oscillatory mode estimation and classification and source location identification based on Lyapunov energy functions are proposed. This new method is then compared with the most commonly used method known as dissipated energy flow (DEF). Finally, this work explores grid following and grid forming control architecture of battery energy storage and the use of identification methods to observe low-frequency oscillation with Distributed Energy Resource (DER) connections.

TABLE OF CONTENTS

LIST OF TABLES

LIST OF FIGURES

CHAPTER 1: INTRODUCTION

1.1 General Background

Oscillation in power system network is a common phenomenon. Low frequency oscillations in power system also known as electro-mechanical oscillation (0Hz-2Hz) can increase risk factor regarding stability in power system and also can cause failure to transmit power reliably. Hence, detection and control of the low frequency oscillatory modes in power system in a fast and reliable method is of absolute importance. The power system grid is stochastic in nature and identifying different modes and controlling the modes to improve damping ratio is a major task. Moreover, with integration of different distributed energy resources and renewable energy sources such as solar panel, wind farms, battery energy storage systems, static var compensator etc. to existing power grid often creates reliability issues and make the oscillation identification method more challenging.

There are two major approaches to identify and analyze power system oscillations: model-based methods and measurement-based methods. Several approaches for modeling the power system has been studied extensively. From generator modeling to different kinds of loads modeling, generally modeling approaches have been performed using widely available simulation software. Different kinds of events are studied from the obtained results of these established models. For specific studies, specific modification and modeling is necessary in the available power system model. For example, for small signal stability studies, the synchronous generators and their field excitation systems are the two major components of a power system that require detailed dynamic modeling. Besides generators and exciters, other components such as the dynamic loads, controllable devices such as power system stabilizers, prime-movers etc. require dynamic modeling as well. Analyzing power system oscillation from model based methods require detailed dynamic modeling of different parts of power

system grid as well as eigenvalue analysis. But model based methods for analyzing power system oscillations are becoming more challenging now-a-days due to some factors such as:

- The power system dynamic model could not include all the details of the power system because of the hypotheses and simplifications
- The topology of the power system changes all the time
- The computational time should be sufficiently small to solve and develop a solution in real-time.

Applying synchrophasor measurement technology, Wide-Area Measurement System (WAMS) provide a powerful tool to monitor and analyze the dynamics of interconnected power grids. With the deployment of phasor measurement units (PMU), the global positioning system (GPS) synchronized phasor data have become an important resource for studying and monitoring power system oscillations [2–4]. Fig. 1.1 shows a map containing deployed PMU in North American Power Grid as of March 2012. According to the North American Synchro-Phasor Initiative (NASPI) reports, there were about 500 networked PMUs installed as of March 8, 2012. NASPI expected that approximately 1,000 PMUs would be in place and networked by the end of 2014, a timeline associated with the Department of Energy's Smart Grid Investment Grant (SGIG) program.

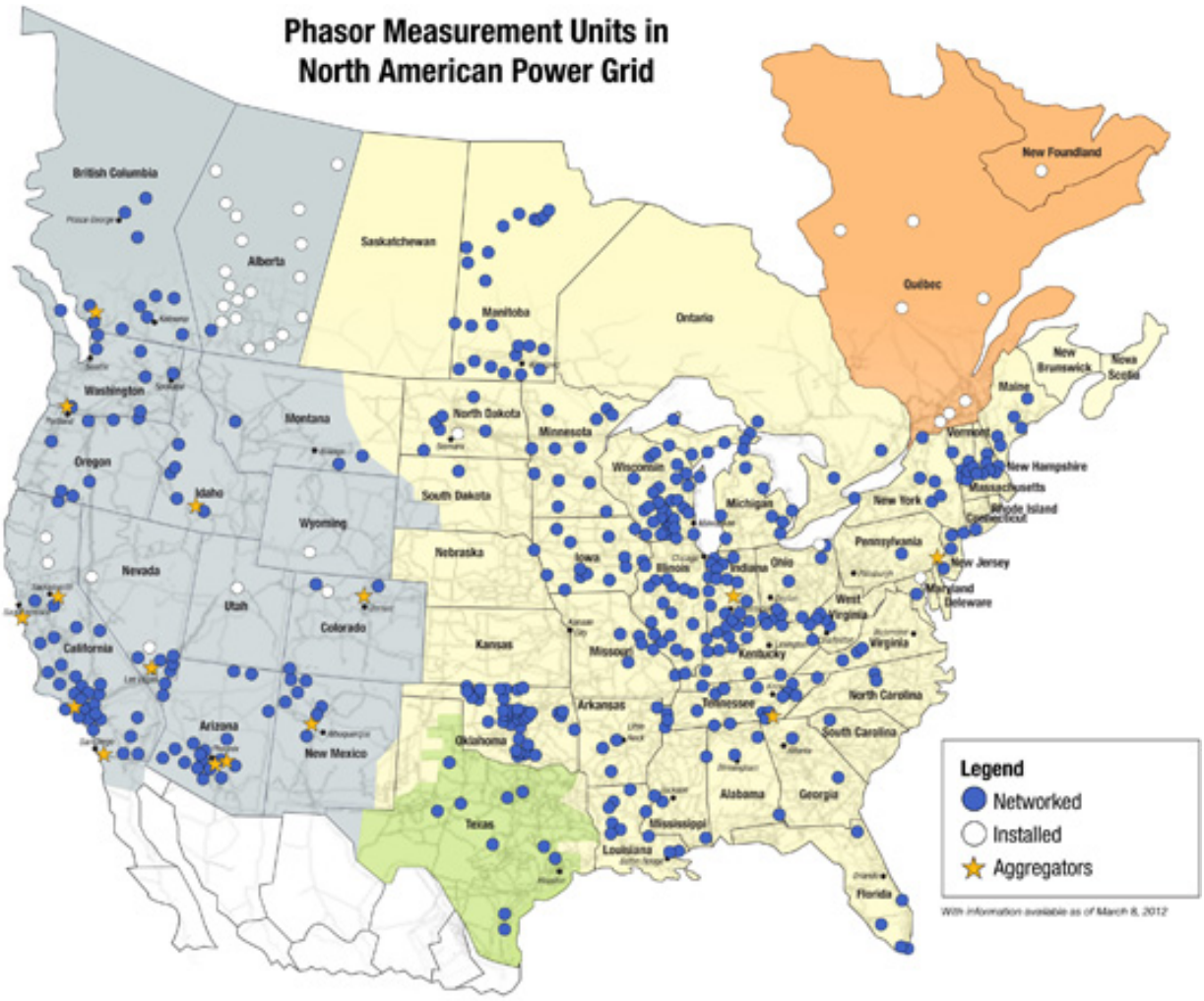

Fig. 1.1: PMU Map of North America as of March 8, 2012. (Source: NERC.)

The synchrophasor networks in North America includes phasor measurement units throughout the power system and a control center for gathering data from PMU through digital communication channels. The control center is built with Phasor Data Concentrators (PDC). The PDC's gather data from installed PMUs and from the real-time wide area PMU data. It is possible to extract dynamic information of the system such as the presence of oscillatory modal responses. There are two different data types for measurement data approach of mode estimation: ring-down data and ambient data [5]. A ring-down data is from system response to an event of large magnitude such as fault scenario or generator outage or any sudden disturbances in the system. An ambient data comes from smaller changes from

power system due to random load changes and white noises. Power system is assumed to be steady around a steady state point and any load change or small fluctuations in the system can excite small signal dynamic of power system. Hence, ambient data analysis provides the inherent system oscillatory modes of a power system. Since power system in stochastic in nature and ambient data is always available through measurement, the algorithms which can be applied on ambient data are quite useful in this context.

There are several techniques which can identify oscillatory modes from ring-down data or ambient data obtained from measurement. For ring-down data analysis, several methods such as Prony analysis [6–9], Eigenvalue Realization Algorithm (ERA) [10–18] and Matrix Pencil (MP) methods [19–21] are being used. While these methods are successfully used to determine low frequency oscillatory modes from ring-down data, they are not reliable for determining modes form ambient data. For both ambient data and ring-down data, Subspace Identification (SSI) methods [22–26, 26–29] have become popular because of their numerical simplicity, robustness of the techniques that are used in the algorithms and, their state-space form which is convenient for control purposes. This method is effective algorithms for modal estimation of a system from both ring-down data and ambient data. This method also has a relatively simple order selection approach and they are good choices for handling large data and system dynamic changes. Subspace identification method is also an effective method to estimate mode shapes. However, a non-recursive SSI is computationally expensive as it has to perform Singular Value Decomposition (SVD) to calculate the state-space matrices with every new data. A recursive method to apply the subspace identification method on the measurements can solve the drawbacks of a non-recursive subspace identification system of being computationally extensive. Studies about recursive methods of identification have been done recently [30,31]. This approach also provides robust performance as it can identify modal information for all types of signals such as ambient, ring-down, and cycling signals. In this approach, first, the power grid measurements are used as both input and output data set to develop measurement-based models of the grid. Then, an oblique projection is designed

recursively to find the system state-space considering grid oscillations. The approach also uses a system observability matrix recursively that avoids the need for SVD.

Control of relevant generators for managing grid stability during or after the abnormal conditions is a very important aspect [32–34]. Identifying the faults, selection of important generators for control, and providing an appropriate control action considering the whole system dynamics in mind is a very challenging and important task. Even though several wide-area control designs are proposed in the literature, almost all of them don't show methods that can control relevant generators or they cannot be implemented online. In this work, a unique method is proposed that can select and control a single or a group of generators to mitigate the power grid inter-area oscillations. The choice of generators is based on the identified mode and the generator's contribution to that mode. The online control architecture designed provides optimal control such that the grid stability is improved.

While identifying the oscillatory mode in the power system is important, it is also of great importance to locate the oscillation source through measurement data available. Various methods of finding oscillation source location have been conducted over the time. Among them travelling wave based methods, damping torque based methods, mode shape estimation based methods and energy based methods are noteworthy [35–50]. In this work, a measurement based identification method has been applied on PMU measurement data to identify poorly damped natural mode and forced mode. Then Lyapunov based energy functions are used to calculate energy functions of a power system and to identify oscillation source location based on the energy calculated. All these methods are combined in a way that they can be implemented online. The advantage of the proposed method is that it can identify modes and their damping ratio as well as provide reduced order system matrix which can help to perform a control scheme to improve damping scenario.

1.2 Motivation

An unstable oscillatory mode can cause a system wide outage and instability in the whole power system. There have been several incidences where system breakups and power out-

ages happened due to an undamped mode. As an example, on August 10, 1996, an inter-area electro-mechanical mode at western interconnection (WI) was unstable and it caused a widespread failure of the system throughout Westerm North America. Fig. 1.2 (Source: NERC) shows a widely published graph of the real power flowing on a major transmission line during the breakup. At start, the system is to be observed in ambient condition from the graph. A line trip event happened at 400 seconds and it caused a ring-down event or transient event. The low frequency oscillatory mode at that time was 0.26Hz. The system went back to steady state but at nearly 720 seconds, the next event occurred and made the 0.26Hz mode unstable which eventually caused the breakup of the system. [51]. From the graph, it can be seen that hundreds of MW peak to peak swing occurred in real power until the breakup.

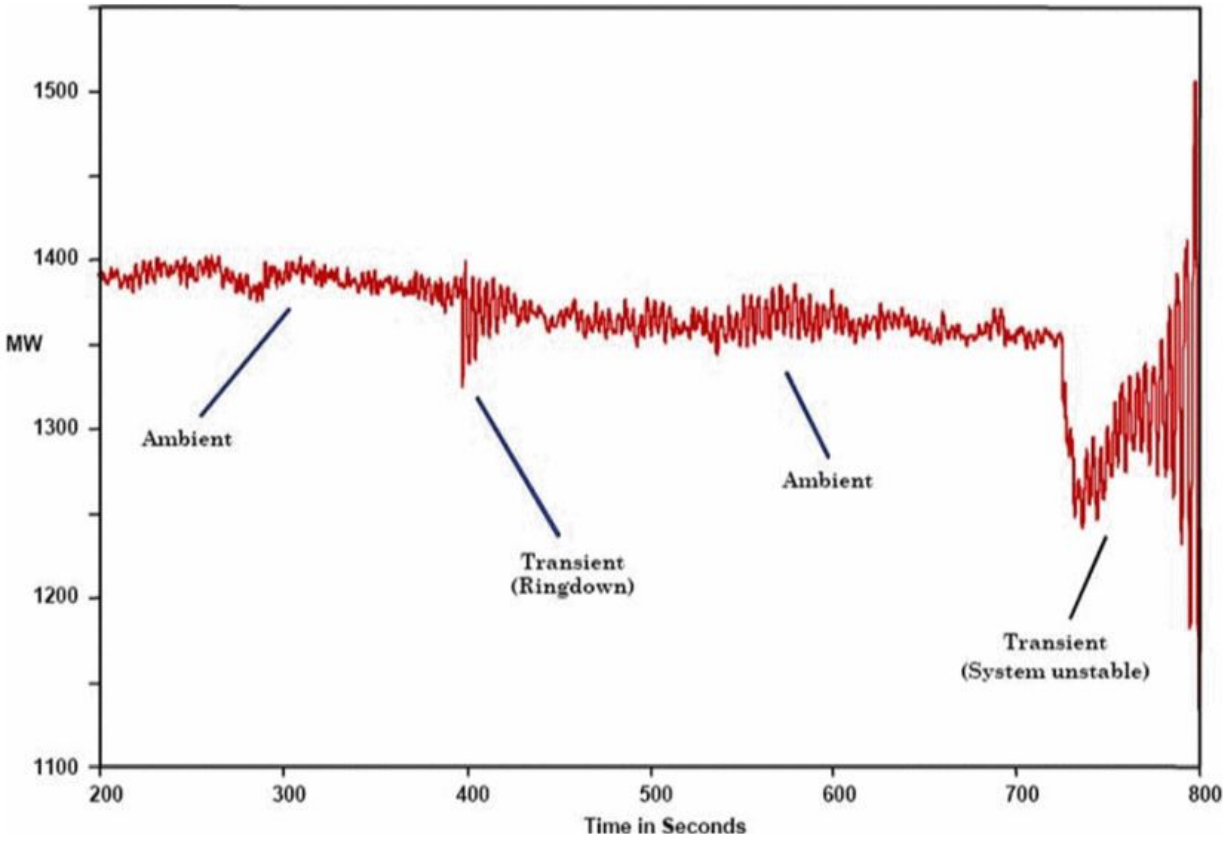

Fig. 1.2: Real power flowing on a major line during the WI breakup on August 10, 1996. [Source:NERC]

The time series data was analyzed and an inter-area mode was identified. The analysis of

the ambient data or first 400 seconds data showed a mode of 0.27Hz with a damping ratio of 7%. After the first transient event until the second transient event, the mode that was present in the timeseries data was found at 0.26Hz with a damping ratio of 3.5%. After the second transient event, the data was analysed and the mode was found to be 0.26Hz with a damping ratio of 1.2%. As we can see that the mode's damping ratio is getting worse after every event and it caused a system wide failure. It is also important to mention that model based methods predicted a stable operation of the power grid under those conditions. As a result model based methods prediction of the system behavior failed to predict the breakup. Measurement based methods have the capability to capture data in real time and can provide operators and engineers with useful information about system stability in real time.

On August 4, 2000, Alberta disconnected from the rest of the WSCC system, which later caused a marginally damped inter-area oscillation. In November of 2005, due to a failed control valve, a facility in Alberta caused a 20 MW peak to peak oscillation at 0.27 Hz. The WI system has a system mode about that has the same frequency of that oscillation. The forced oscillation due to the failure at that plant resulted in 200 MW peak to peak oscillations on the California-Oregon intertie. On July 17, 2016, similar kind of incident happened in the eastern interconnection (EI) due to a forced oscillation around 0.27 Hz. All of these events exhibited sustained low frequency inter-area oscillations which led to serious concern about stability of the whole system. In short, it is of much importance to analyze and control these types of oscillations in real-time.

1.3 Current Research Gaps and Main Contributions

1.3.1 Current Research Gaps

- With increasing number of PMU integration to modern power system, measurement based oscillation identification methods are becoming popular. But still SCADA is being used to capture real time data which is much slower than PMU data and can not capture detailed dynamic behavior of the system under normal and event condition. To

prevent any kind of unwanted breakout or failure of power system due to low frequency oscillation, a measurement based identification method which is both fast and accurate and can be implemented online is necessary.

- Some measurement based identification methods such as Prony analysis or Matrix Pencil method are faster but they do not provide better accuracy under noisy situation or different events. Some measurement based identification methods such as subspace identification methods are accurate and is robust but takes longer time to identify oscillatory modes. A recursive based subspace identification method can solve the problem.

- Currently the mostly used mode damping mechanism is power system stabilizers (PSS). Operating a PSS is not centralized and the damping does not depend on different kind of events. A centralized online control method which can provide damping to the oscillatory mode as soon as any event happens in power system can be very helpful.

- Identifying and differentiating between forced mode and natural mode of power system in an online environment.

- Online oscillation source location identification method is required to locate oscillation source to prevent any blackout or failure of equipment.

- Low frequency oscillation identification from measurement based method for inverter based resource integration in modern power grid.

1.3.2 Main Contribution

- Comparison between existing measurement based identification methods based on measurement data for both natural mode and forced mode under ring-down, ambient and forced condition.

- A unique approach for energy function based identification and control that can be applied to the multi-machine system, thus scalable.

- An unique wide-area optimal control designed for multiple generators that can prioritize generator contribution to improve stability.
- A unique method to identify and detect relevant generators for control just by using measurements from the grid and provide a control model.
- The proposed approach is computationally robust and adjusts the power grid model order dynamically.
- Provide oscillation monitoring of the power grid considering internal and external disturbance and classify natural and forced-modes of oscillations based on damping ratio threshold.
- The approach is implementable online and can estimate the oscillation modes and classify them dynamically changing with respect to grid changes.
- A unique approach to reduce computational burden of non-recursive SSI by implementing recursive SSI and also compare the performance of recursive SSI with other measurement based methods.
- The approach combines Sub-space Identification methods with Lyapunov energy function method to identify oscillation source location.
- Online low frequency oscillation identification for IBR integrated power grid.

1.4 Dissertation outline

The dissertation outline is as follows:

In Chapter 2 a comprehensive literature review of the state-of-the-art measurement based oscillation identification methods is done. This chapter explains the importance of measurement based methods over model based studies. A brief explanation about different measurement based methods such as Prony analysis, Eigenvalue Realization Algorithm, Matrix Pencil method and Subspace Identification and a comparative analysis between different

methods is also discussed. This chapter also sheds some light on the challenges of applying any measurement methods in real time environment.

Chapter 3 explores different measurement based methods to identify oscillatory modes in power system in details. This chapter also introduces an algorithm which uses recursive algorithm to improve the performance of non-recursive subspace identification. Kundur two area system and IEEE 68 bus systems are used as test systems. A comparative study is also provided in this chapter. All these measurement based methods are applied online and the implementation of this procedure is also explained.

In Chapter 4 an online Wide-Area Direct Coordinated Control Architecture For Power Grid Transient Stability Enhancement Based On Subspace Identification is explained. A dynamic control architecture is applied along with subspace identification to identify oscillatory mode in power system and to control the most affected generators to enhance the stability of the system. For this chapter, Kundur two area system and IEEE 68 bus system is taken as test systems.

In chapter 5 a hybrid deterministic-stochastic recursive subspace identification method for mode estimation, classification and control is proposed. The proposed method avoids numerically exhaustive steps like Singular Value Decomposition while identifying oscillatory modes. It can also identify both natural and forced modes based on damping ratio. A dynamic control architecture is also used to improve damping scenario. A comparison between proposed control architecture and tuned PSS is also explored.

In Chapter 6 an oscillation source location identification algorithm is proposed based on Lyapunov energy functions. The proposed method's performance is compared to existing state of art methods like dissipated energy flow (DEF) method.

In Chapter 7 inverter based resource integration to existing grid and low frequency oscillation identification for connection of IBRs into grid have been studied.

Chapter 8 concludes the paper and future works are discussed.

CHAPTER 2: Literature Review

2.1 Power system modes

It is well established that power system can be linearized about an operating point despite being higher order non-linear and time varying system [52]. The linearized power system can be represented in state space form as:

$$x_{k+1} = Ax_k + Bu_k + w_k \tag{2.1}$$

$$y_k = Cx_k + Du_k + v_k \tag{2.2}$$

where

x_k : The state vector

u_k : The input vector (measured and available)

y_k : The output vector (measured and available)

w_k,v_k : Unknown disturbances

The graphical representation with block diagrams of the state space representation is represented in Fig. 2.1.

Analyzing and estimating power system electro-mechanical modes and dynamics is of great importance in order to control and mitigate the low frequency oscillations of power system that can lead to breakdown of the whole system and blackouts. But at the same time, determining these dynamics are a challenging task due to the following issues:

- Power system is nonlinear in nature, time varying and it is a higher order system which leads to complexity in modeling. Fortunately, the system behaves as a relatively linear system when it is in steady state.

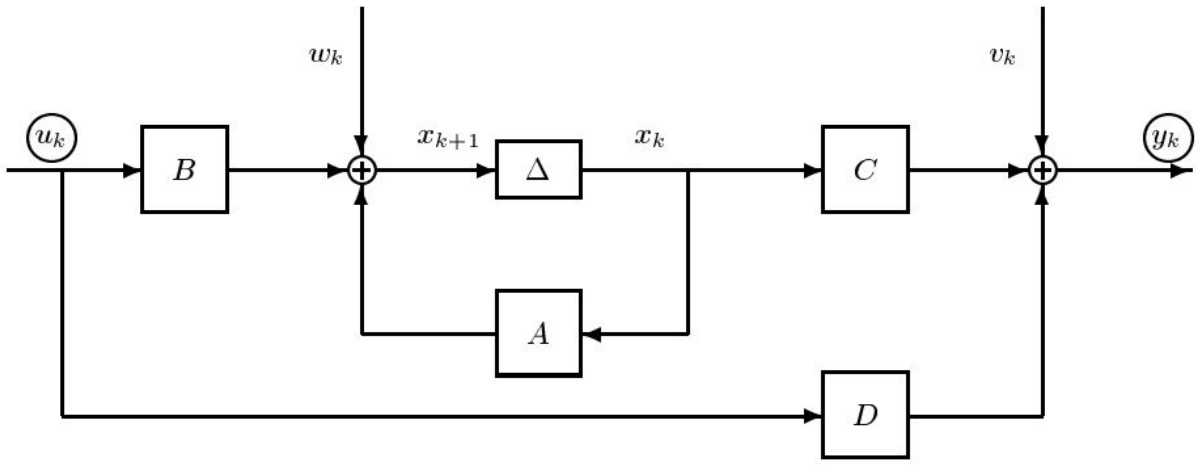

Fig. 2.1: Graphical representation of state space system.

- Power system is stochastic in nature which means that it is expected to be excited by random signals all the time; most of them come from random load changes and noises.
- Contains many electro-mechanical modes of oscillation which are close to natural oscillation modes.

The electro-mechanical modes are a subset of the eigenvalues of the system A matrix. Both a modeâs frequency and damping ratio can be found from the eigenvalues. Electro-mechanical modes are usually classified as local or inter-area modes [51,52]. Local modes tend to be in the frequency range from 1 to 2 Hz. Inter-area modes are usually in the frequency range of 0.15 to 1 Hz and involve multiple generators in a geographical area swinging against generators in another area usually over long distances. These modes are of particular interest and are usually of greater concern.

2.2 Model Based Power System Studies

The logical steps to study a physical system are to define the model which includes hypotheses and simplifications. Then comes formalizing the equations of the model. Finally, the equations have to be solved either in a closed form or numerically. The steps are illus-

trated in Fig. 2.2.

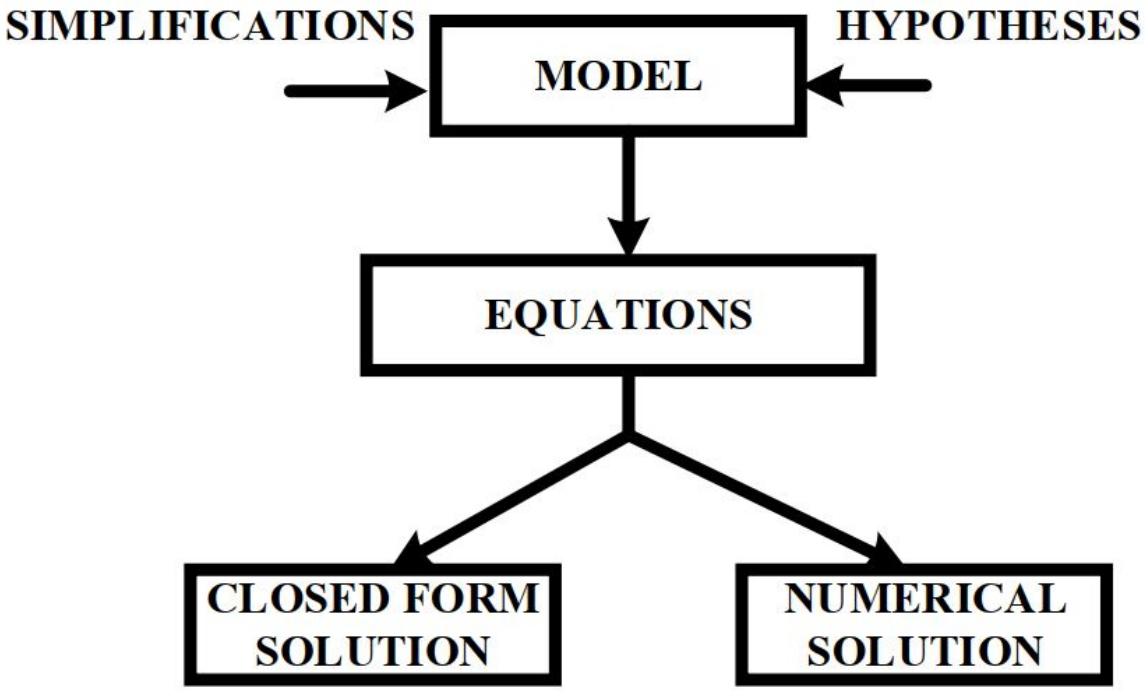

Fig. 2.2: General approach for studying a physical system

Several approaches for modeling the power system in this form has been studied extensively. From generator modeling to different kinds of loads modeling, generally modeling approaches have been performed using widely available simulation software's. Different kinds of events are studied from the obtained results of these established models.

A power system consists of three primary components: The generating system, the transmission line, and the load. For the purposes of fault transient analysis, the generator or the load needs to be changed in such a way that it can impose realistic boundary conditions on the differential equations. Also simulation of fault is required at a certain point or line of the network. The four possible types of faults are designated by:

- Three phase to ground fault
- Single line to ground fault
- Line to line fault

- Double line to ground fault

After creating the fault at different location in the model, time-domain simulation is performed. It has been widely recognized that time-domain simulation is the most accurate method to describe power system transient behaviour since it can represent controls, non-linearities, saturation, strong dissipative effects and the protection systems. From, time-domain analysis, the eigenvalues of the system which are the roots of the characteristic equations of the system and the related eigen-vectors can be calculated. As the power grid is becoming more and more interconnected with newer technologies, the identification and assessment of stability issues in the power system is also becoming more and more challenging. The power system stability refers to the ability of the power system to be operated around a stable point or steady state point even after any random ambient or transient event happens in the network. It depends on the nature of the disturbance or the event. If after any event, the power system is near its stability limit, actions must be taken by system operators to identify the critical states in the network. Although model based methods have detailed modelling of different parts of the network, the power system analysis is based on numerical solutions of system differential algebraic equations.

2.3 Measurement Based Power System Studies

With a large number of synchrophasors and PMU being deployed, it is entirely possible for mathematical based identification methods to model the power system based purely on measurement data. Several state of art measurement based identification methods used in this dissertation are: Prony analysis, Eigenvalue Realization Algorithm, Matrix Pencil method and Subspace Identification method.

2.3.1 Prony Analysis

The first published work in the power literature on transient analysis was by Hauer [7] using Prony analysis [6], which is a method designed to directly estimate the parameters for the exponential terms in Eqn. 2.3 by fitting a function to an observed record for y_t. The

Prony method is a polynomial method and it includes the process of finding the roots of a characteristic polynomial. In [8], a method has been established by extended Prony analysis to simultaneously fit multiple signals. In [9], determination of modal content from measured power system response by Prony method is discussed.

$$x_{\mathrm{i}}(t) = \sum_{i=1}^{n} (r_{\mathrm{i}} x_{\mathrm{i0}} e^{\lambda_{\mathrm{i}} t}) \tag{2.3}$$

where

r_{i} : Residue of the mode i

x_{i0} : Initial internal states

λ_{i} : Eigenvalues of A matrix

While this method is quite efficient and accurate for extracting poles and residues from given equally spaced transient data, Pronyâs method is notorious for its extreme sensitivity to noise. And also Prony's method does not have any order selection technique in the algorithm, so the operator or the researcher has to choose a random order for the reduced order operation and try to fit with already known values. More importantly, for ambient data condition, Prony's method is not well suited as it is much of a fitting algorithm and in ambient condition, the changes are totally random.

2.3.2 Eigenvalue Realization Algorithm (ERA)

The ERA is a system identification algorithm introduced by Jer-Nan Juang and Richard S. Pappa in 1985 [10]. While identifying the modes and eigenvalues of the system characteristic equation, this method also allows to identify the system matrices and it also allows model reduction of linear systems. The popularity of ERA can be attributed to its straightforward implementation, numerical robustness and sound mathematical foundation. Although ERA was introduced within the aerospace community where it has been used extensively; it is also used as a very helpful tool in power system [11–16]. In [53], a recursive method to

apply ERA is proposed to reduce the computational time. In [17], the effects of noise while identifying system dynamics by ERA is discussed. Another extension of ERA is established in [18] and the method is called general realization algorithm (GRA).

The ERA is based on the singular value decomposition (SVD) of the Hankel matrix associated with the ring-down event of the system. A Hankel matrix is a square matrix with constant skew-diagonals. The Hankel matrix is typically assembled using all of the available data such that the top left most element of the Hankel matrix is the first available measurement and the bottom right most element is the last available measurement. From the singular values, the model order is reduced by choosing most significant singular values and the system matrices are calculated based on this choice.

$$H(_{\mathrm{k|i,j}}) = \begin{vmatrix} H_{\mathrm{k}} & H_{\mathrm{k+1}} & . & . & . & H_{\mathrm{k+j}} \\ H_{\mathrm{k+1}} & H_{\mathrm{k+2}} & . & . & . & H_{\mathrm{k+j+1}} \\ . & . & . & . & . & . \\ . & . & . & . & . & . \\ H_{\mathrm{k+i}} & H_{\mathrm{k+i+1}} & . & . & . & H_{\mathrm{k+i+j}} \end{vmatrix} \tag{2.4}$$

where

H_{k} : Blocks of data formed from input and output measurements

i, j : Specified integers

For ERA algorithm, two shifted Hankel matrix are formed: $H(_{\mathrm{1|i,j}})$ and $H(_{\mathrm{2|i,j}})$. SVD of $H(_{\mathrm{1|i,j}})$ is performed and allows for finding the minimum order realization. So, this method has a clear advantage over Prony's method when it comes to select an appropriate reduced order of the model. The disadvantage of this method is that it is highly computationally complex and slow when compared to other methods as it runs SVD which takes more time especially when performed online. By running this method recursively, the computational performance can be upgraded. And this method same as Prony's method works only on transient or ring-down data, and can not perform in ambient condition.

2.3.3 Matrix Pencil Method

The Matrix Pencil method approach was introduced by Hua and Sarkar [19]. Initially it was intended to use for estimating poles from electromagnetic transient responses from antennas. This method uses almost the same algorithm as ERA as it also runs SVD on Hankel matrix. The Hankel matrix is formed in a different way than that of ERA. As this method has SVD built-in, choosing lower order model from the singular values is also possible in this algorithm. Also, this method is capable of handling noisy signals accurately, has less sensitivity to different sample sizes and easier and poles of the system can be directly found from the eigenvalues in a single step whereas normal polynomial methods require two steps to find the poles. The disadvantage of pencil matrix method is that due to SVD, this method is computationally extensive and this method can not handle ambient data as well.

2.3.4 Yule Walker (YW) Method

Yule Walker method is a correlation method which solves a non-linear equation by an iterative search technique. The method is based on a set of linear equations which can be solved fast and reliably. Correlation method works on the principle that for a good model, no information of the past data is required for future calculation as for a good model, prediction error at a certain time step is independent of past data. There are several techniques that can be utilized to solve the coefficients of the non-linear equations such as auto-regressive (AR) or auto-regressive moving average (ARMA).

$$A(q) = \sum_{i=0}^{p} (a_i q^{-i}); a_0 = 1 \tag{2.5}$$

A strictly AR process can be rewritten as

$$y(k) = -\sum_{i=1}^{p} (a_i y(k-1) + b_0 e(k)); \tag{2.6}$$

k=Integer time index

After modifying the (6.4), YW equation can be obtained

$$r_{\mathrm{yy}}(j) = \begin{cases} -\sum_{i=1}^{p} r_{\mathrm{yy}}(i-j) & forj \geq 1 \\ -\sum_{i=1}^{p} a_(i) r_{\mathrm{yy}}(-i) + b_0\sigma^2 & forj = 0 \end{cases} \tag{2.7}$$

By solving the following set of linear equations, the parameters of an AR can be determined.

$$\begin{vmatrix} r_{\mathrm{yy}}(0) & r_{\mathrm{yy}}(-1) & . & . & . & r_{\mathrm{yy}}(-(p-1)) \\ r_{\mathrm{yy}}(1) & r_{\mathrm{yy}}(0) & . & . & . & r_{\mathrm{yy}}(-(p-2)) \\ . & . & . & . & . & . \\ . & . & . & . & . & . \\ r_{\mathrm{yy}}(p-1) & r_{\mathrm{yy}}(p-2) & . & . & . & r_{\mathrm{yy}}(0) \end{vmatrix} \begin{vmatrix} a_1 \\ a_2 \\ . \\ . \\ a_{\mathrm{p}} \end{vmatrix} = \begin{vmatrix} r_{\mathrm{yy}}(1) \\ r_{\mathrm{yy}}(2) \\ . \\ . \\ r_{\mathrm{yy}}(p) \end{vmatrix} \tag{2.8}$$

A reasonable approximation can be obtained by calculating the elements of the correalation matrix from limited available data. In the Modified Yule Walker (MYW) method, a similar procedure like YW algorithm can be applied to an ARMA model which is as follows.

$$\begin{vmatrix} r_{\mathrm{yy}}(d) & r_{\mathrm{yy}}(d-1) & . & . & . & r_{\mathrm{yy}}(d-(p-1)) \\ r_{\mathrm{yy}}(d+1) & r_{\mathrm{yy}}(d) & . & . & . & r_{\mathrm{yy}}(d-(p-2)) \\ . & . & . & . & . & . \\ . & . & . & . & . & . \\ r_{\mathrm{yy}}(d+p-1) & r_{\mathrm{yy}}(d+p-2) & . & . & . & r_{\mathrm{yy}}(d) \end{vmatrix} \begin{vmatrix} a_1 \\ a_2 \\ . \\ . \\ a_{\mathrm{p}} \end{vmatrix} = \begin{vmatrix} r_{\mathrm{yy}}(d) \\ r_{\mathrm{yy}}(d+1) \\ . \\ . \\ r_{\mathrm{yy}}(d+p) \end{vmatrix} \tag{2.9}$$

where d= The order of the MA component.

In this method, the stability of the poles of AR is not guaranteed. another approach is the Least Square Modified Yule Walker approach. Here (6.10) can be rewritten as

$$r_{\mathrm{yy}}(k) = -\sum_{i=1}^{p} (a_{\mathrm{i}} r_{\mathrm{yy}}(k-i) \qquad fork \geq (q+1) \tag{2.10}$$

In this case, the correlation matrix is not a square matrix, hence least square has to be employed.

2.3.5 Regularized Robust Recursive Least Squares (R3LS) Method

R3LS is a method to estimate power system modes based on PMU data to continuously monitor power system modes. The R3LS method uses an auto-regressive moving average exogenous (ARMAX) model to account for typical measurement data, which includes ring-down, ambient and probing data. A regularized method is used to utilize past data information about the system and a recursive method is used for improving computational efficiency.

2.3.6 Subspace Identification

The overview of subspace identification and classical identification methods can be described by Fig. 2.3. System identification aims at constructing state space models from input-output data. The left hand side shows the subspace identification approach : first there is orthogonal or oblique projection, then the Kalman filter states are estimated directly from input-output data, then the system matrices can be obtained. The right hand side is the classical approach : first obtain the system matrices, then estimate the states.

Subspace identification process can be divided into two sub-categories: Deterministic subspace identification and Stochastic subspace identification. In deterministic subspace identification method, both input and output vectors are known and available and the noise vectors are zero. In stochastic subspace identification method, only output vectors are known from measurements and the system matrices are estimated from only output vectors.

The summary of these method's advantages and limitations are shown in table 2.1.

2.4 Controls for power system oscillation

Oscillation in the power system can be local to a single generating unit or a generator plant (local oscillation) or several number of generating units can participate in an oscillation (inter-area oscillations). Local oscillatory modes can occur due to a faster exciter usage on a generating unit and power system stabilizers are designed according to the plant parameters to add damping to those oscillations. Inter-area oscillation can appear due to any weak part

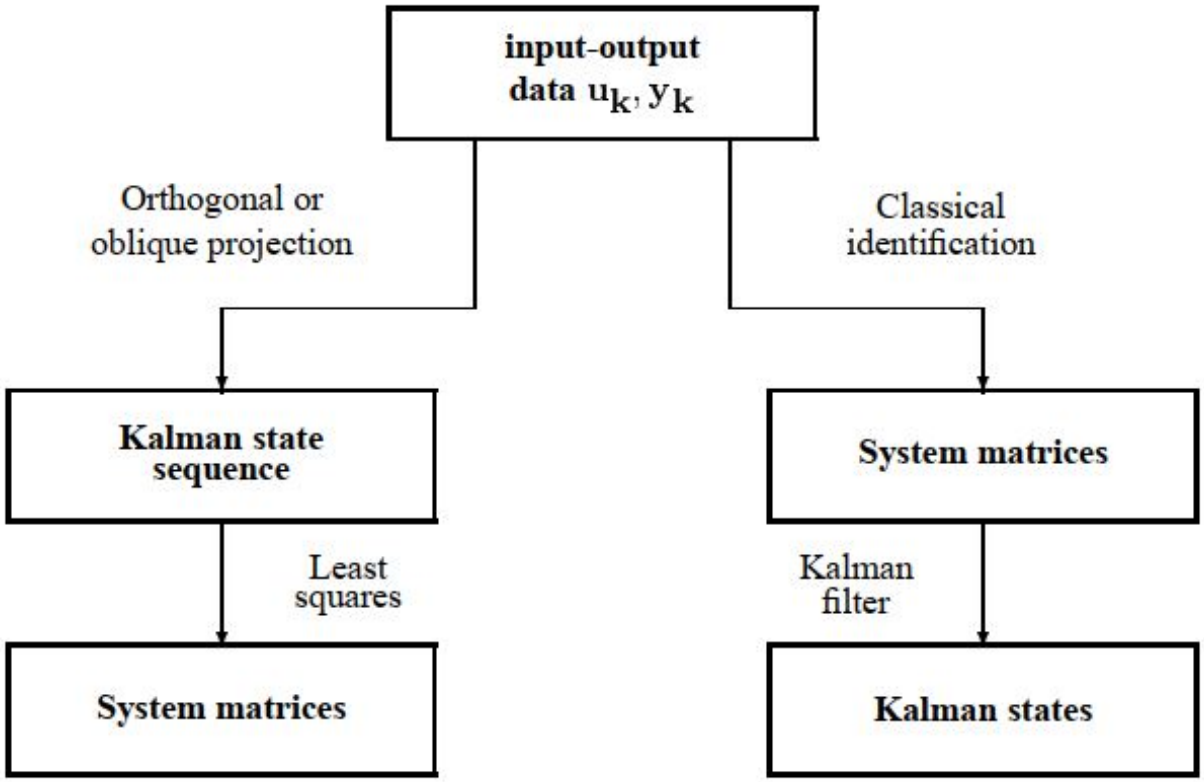

Fig. 2.3: Subspace identification Vs Classical identification.

of the grid or increase of loading scenario or any transient event. If not controlled, these oscillations can travel within the network and can cause a blackout of a very large scale.

2.4.1 Power system stabilizer (PSS)

A power system stabilizer (Fig. 2.4) is an additional block of a generator excitation control or AVR. It is used to provide additional damping to the overall system dynamic performance especially to the control of low frequency oscillatory modes. PSS controls the AVR output by controlling the input signal to AVR and thus effectively manages to improve damping ratio of various low frequency oscillatory modes. For each generating unit of a large power system, individual PSS is designed based on generating unit's parameters to control any unstable low frequency oscillatory mode. Thus, PSS is designed and tuned to some specific mode and to improve those modes' damping ratio.

Table 2.1: Comparison of different methods

Method	Application	Advantage	Limitations
Prony Analysis	Ring-down data analysis and mode estimation	Reliable and fast for ring-down analysis	No order selection technique, extremely sensitive to noise
ERA	Ring-down data analysis and mode estimation. Also calculates system matrices.	Order selection technique included by SVD algorithm.	Highly computationally intensive because of SVD operation and can not handle ambient data
Matrix Pencil	Ring-down data analysis and mode estimation. Also calculates system matrices.	Order selection technique included by SVD algorithm. Handles noisy data better than Prony and ERA	Computationally intensive and poor performance on ambient data
Yule Walker	Handles ring-down and ambient data to calculate modes.	Provide stable poles of the system.	No order selection techniques. High variance in outputs.
Modified YW	Handles ring-down and ambient data to calculate modes.	Better at estimating poles than YW.	Sometimes provide unstable poles and no order selection techniques
LSMYW	Handles ring-down and ambient data to calculate modes.	Performs better than MYW	No order selection technique and computationally intensive
R3LS	Handles ring-down and ambient data to calculate modes.	Regularized, recursive and robust. Can perform near real-time operation. Computationally effective.	No order selection technique. Less data increases variances of estimation
Subspace Identification	Handles ring-down and ambient data to calculate modes and mode shapes	In-built order selection process and noise handling process. Can handle large data, convergence, incorporation of probing data.	Computationally intensive, tuning problem.

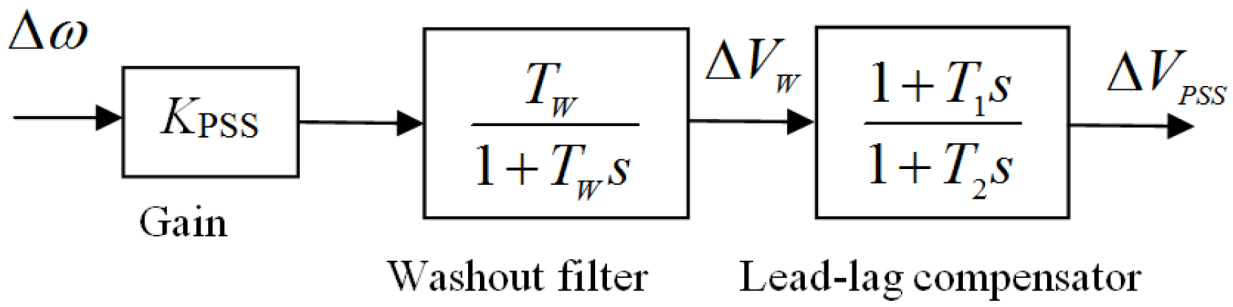

Fig. 2.4: PSS Architecture.

2.4.2 Static Var Compensator (SVC)

SVC (Fig. 2.5) is basically a shunt connected static var compensator to supply or absorb reactive power (Capacitive or Inductive) to improve dynamic voltage profile of that particular bus. SVC is widely used to control dynamic voltage control and increase system loadability. In any weaker part of the large power system network, SVC is installed to improve low voltage pprofile scenario. Additional stabilizing signal can be added to SVC to improve damping of oscillatory modes.

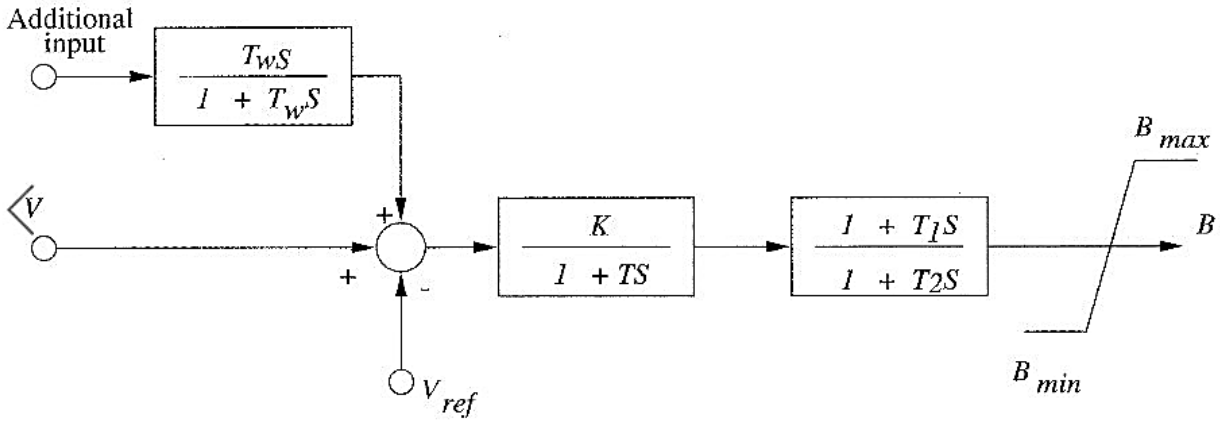

Fig. 2.5: SVC Functional Block.

2.4.3 Static synchronous compensator (STATCOM)

The STATCOM (Fig. 2.6) rworks as a synchronous compensator but it does not have inertia like synchronous generating units. As a result STATCOM can not provide any short circuit current contribution. It works as a voltage source converter. It can provide reactive

power support to the connected bus. STATCOM has a very fast response to any change in voltage. It can control and improve voltage by controlling phase angle control strategy. Additional control blocks can be implemented with STATCOM to improve oscillation in the system.

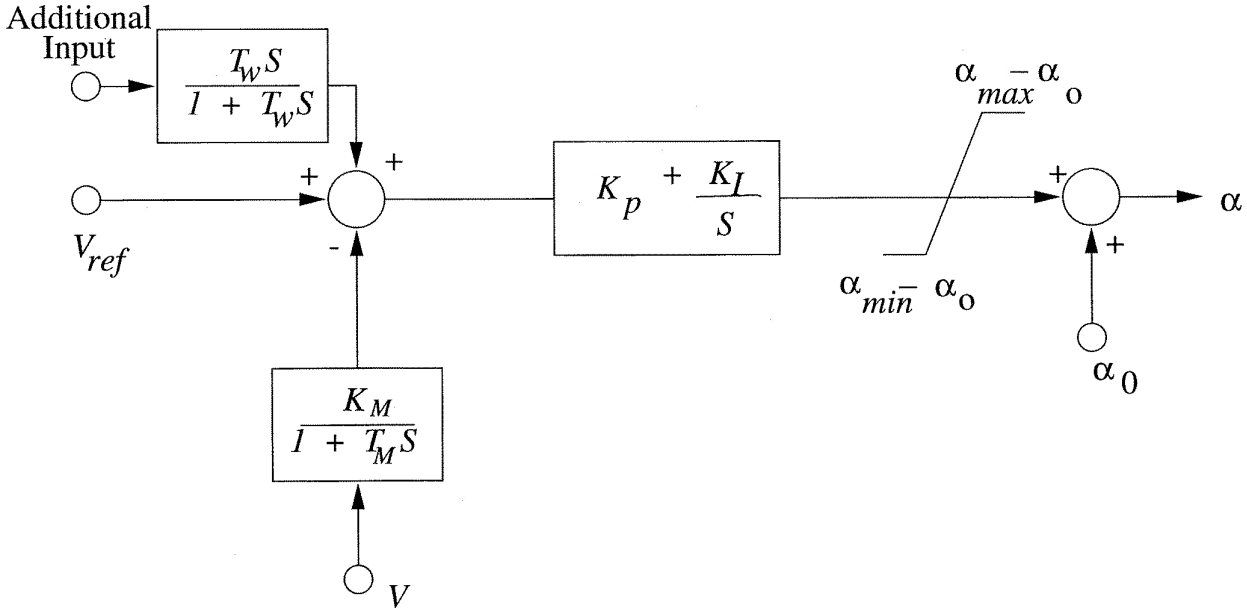

Fig. 2.6: STATCOM Functional Block.

2.4.4 LQR Controller

A Linear Quadratic Regulator (LQR) type controller is usd along with measurement based identification method to control and add damping to undamped oscillations and the methods are implemented near real time scenario.

The object of LQR controller is to determine the optimal control law u which can transfer the system from its initial state to it's final state such that a given performance index is minimized. The performance index is given in the quadratic form which can be defined as,

$$J(U) = \sum_{k=1}^{N-1} ({x_\mathrm{k}}^T Q x_\mathrm{k} + {u_\mathrm{k}}^T R u_\mathrm{k}) + ({x_\mathrm{N}}^T Q_\mathrm{f} x_\mathrm{N}) \tag{2.11}$$

where,

U : $(u_0, u_1, u_2, ..., u_{\mathrm{N}\text{-}1})$

Q and R are given state cost and input cost matrices. Q and R set relative weights of state deviation and input usage. To minimize J(U); $\left({u_0}^{LQR}, {u_1}^{LQR}, {u_2}^{LQR}, ..., {u_{\text{N-1}}}^{LQR}\right)$ need to be solved. To solve these, dynamic programming is used. Then, the feedback gain k can be computed and the closed loop system responses can be found by solving the following equation:

$$K_{\text{t}} = -(R + B^T P_{\text{t+1}} B)^{-1} B^T P_{\text{t+1}} A \tag{2.12}$$

This method has an advantage of allowing all control loops in a multi-loop system to be closed simultaneously, while guaranteeing closed loop stability. For $t = 0, 1, 2, ..., N-1$; optimal u is given by,

$${u_{\text{t}}}^{LQR} = -K_{\text{t}} x_{\text{t}} \tag{2.13}$$

Optimal 'u' is a linear function of the state (called linear state feedback). Recursion for minimum cost-to-go runs backward in time.

2.5 Challenges to implement real-time application

There are some challenges to implement measurement based identification along with controller in online environment.

- Finding the appropriate sampling time is very challenging. If very low sampling time is selected, the data becomes computationally complex to handle and if a high sampling time is selected as sampling time, the measured data can not capture low frequency oscillations.

- Finding appropriate data length for input and output data vectors as the identified matrix changes with the data length is very challenging. In real-time implementation, the subspace identification method needs a certain amount of data to calculate the system matrices. Identified system matrices varies with the length of the data window

and it is difficult to select the right amount of data.

- Finding the appropriate order from the identification methods so that the reduced model can represent nearly all characteristics of the original system, so that the modes can be observed as well as the computational complexity is reduced.

2.6 Summary of literature review

From the literature review of model based identification methods and measurement based identification methods, it is evident that measurement based methods have certain advantage over model based methods. Measurement based methods do not need to have any model parameters to identify oscillation in power system and with increasing number of installed PMUs throughout North American power system grid, it is easier than ever to identify and control low frequency oscillatory modes through measurement based identification methods. Among different state of the art measurement based methods used in recent years, subspace identification based methods are more promising as they can be implemented in real-time scenario to capture dynamic data from power system, can work for both ring-down or ambient situation, is robust when facing noisy data and can provide with state space matrix to help implementing control architecture. For classifying different modes, a threshold of 2Hz will be used throughout this research work as low frequency oscillatory modes are of more importance when it comes to overall stability of the power system. And finally, an LQR based control algorithm will be implemented to control and add damping to unstable mode as LQR control methods can be implemented in real-time environment, can be utilized as wide area control and can utilize identified state space matrix to act on specific identified mode of the power system.

CHAPTER 3: Investigation and Design of a Measurement Based Electro-Mechanical Oscillation Mode Identification and Detection in Power Grid

3.1 Introduction and main contributions

Modern power systems are really complex in nature. Accurate knowledge and estimation of the electro-mechanical modes in the power system are of great importance since a system-wide outage can be caused by one single unstable mode of oscillation. Hence, advanced mathematical tools and signal processing methods are necessary to estimate the electro-mechanical modes of the power system. There have been several incidences where system breakups and power outages happened due to an undamped mode and all of these events exhibited sustained low-frequency inter-area oscillations which typically are in the range of 0.15Hz to 1Hz. Model-based frequency studies have been established for a long time. However, model-based studies cannot anticipate every kind of event in real-time because the power system is nonlinear, time-varying and it is a higher-order system that leads to complexity in modeling. Besides, the power grid is stochastic with the advent of renewables and changing load dynamics, which means that it is expected to be excited by random signals all the time; most of them come from random load changes and noises. Recently, measurement-based power grid mode estimation has attracted great attention [54].

Several techniques can identify oscillatory modes from ring-down data or ambient data obtained from measurement. Generally, ring-down events occur during the sudden changes in grid operation due to faults, generator outages, or controller operations of the generator. Ambient data changes are rather slow varying close to the steady-state operation of the grid due to small changes in eh load or such events. Among the measurement-based techniques, Prony analysis [6–9], Eigenvalue Realization Algorithm (ERA) [10–13] and Matrix Pencil methods [19–21] are noteworthy. These methods have successfully been used to determine

low-frequency oscillatory modes from measurement data. Recently subspace identification methods (SSI) [22–25] have become popular as they are robust to variations, and can be represented in state-space form thus making it easier for designing time-domain control approaches. However, a non-recursive SSI is computationally expensive as it has to perform Singular Value Decomposition (SVD) to calculate the state-space matrices.

A recursive method to apply the subspace identification method on the measurements can solve the drawbacks of a non-recursive subspace identification system of being computationally extensive. Studies about recursive methods of identification have been done recently [30, 31]. Earlier in [30] we have introduced an approach for determining power system modes (forced and natural). This approach also provides robust performance as it can identify modal information for all types of signals such as ambient, ring-down, and cycling signals. In this approach, first, the power grid measurements are used as both input and output data set to develop measurement-based models of the grid. Then, an oblique projection is designed recursively to find the system state-space considering grid oscillations. The approach also uses a system observability matrix recursively that avoids the need for SVD. In this chapter, a comparison of various measurement based methods in estimating oscillation modes is presented including the recursive forced and natural mode identification method. The main contribution of this chapter is as follows:

- Explore different measurement based identification methods to identify low frequency oscillation.
- Compare various methods' performance and analyze how they perform on different ring-down and ambient data and in noisy environment.
- Classification between natural mode and forced mode.
- Implement measurement based identification methods in real-time environment.
- Compare different methods' computing time to find out most efficient method.

The chapter is organized as follows. In section 3.2, we present or refer all the methods include the recursive mode identification method. Section 3.3 discusses the experimental results and provides a comparison among different methods and section 3.4 concludes the chapter.

3.2 Measurement-Based Oscillation Detection Methods

In this study, we are comparing the following methods a) Prony method, b) ERA method, c) Matrix Pencil method d) Non-recursive sub-space identification method and e) the recursive sub-space identification method.

3.2.1 Prony Analysis

The first published work in the power literature on transient analysis was by Hauer [7] using Prony analysis [6], which is a method designed to directly estimate the parameters for the exponential terms in Eqn. 2.3 by fitting a function to an observed record for y_{t}. The Prony method is a polynomial method and it includes the process of finding the roots of a characteristic polynomial. In [8], a method has been established by extended Prony analysis to simultaneously fit multiple signals. In [9], determination of modal content from measured power system response by Prony method is discussed.

$$x_{\mathrm{i}}(t) = \sum_{i=1}^{n} (r_{\mathrm{i}} x_{\mathrm{i0}} e^{\lambda_{\mathrm{i}} t}) \tag{3.1}$$

where

r_{i} : Residue of the mode i

x_{i0} : Initial internal states

λ_{i} : Eigenvalues of A matrix

While this method is quite efficient and accurate for extracting poles and residues from given equally spaced transient data, Pronyâs method is notorious for its extreme sensitivity to noise. And also Prony's method does not have any order selection technique in the

algorithm, so the operator or the researcher has to choose a random order for the reduced order operation and try to fit with already known values. More importantly, for ambient data condition, Prony's method is not well suited as it is much of a fitting algorithm and in ambient condition, the changes are totally random.

3.2.2 Eigenvalue Realization Algorithm (ERA)

The ERA is a system identification algorithm introduced by Jer-Nan Juang and Richard S. Pappa in 1985 [10]. While identifying the modes and eigenvalues of the system characteristic equation, this method also allows to identify the system matrices and it also allows model reduction of linear systems. The popularity of ERA can be attributed to its straightforward implementation, numerical robustness and sound mathematical foundation. Although ERA was introduced within the aerospace community where it has been used extensively; it is also used as a very helpful tool in power system [11–16]. In [53], a recursive method to apply ERA is proposed to reduce the computational time. In [17], the effects of noise while identifying system dynamics by ERA is discussed. Another extension of ERA is established in [18] and the method is called general realization algorithm (GRA).

The ERA is based on the singular value decomposition (SVD) of the Hankel matrix associated with the ring-down event of the system. A Hankel matrix is a square matrix with constant skew-diagonals. The Hankel matrix is typically assembled using all of the available data such that the top left most element of the Hankel matrix is the first available measurement and the bottom right most element is the last available measurement. From the singular values, the model order is reduced by choosing most significant singular values and the system matrices are calculated based on this choice.

$$H_{(\mathrm{k|i,j})} = \begin{vmatrix} H_{\mathrm{k}} & H_{\mathrm{k+1}} & . & . & . & H_{\mathrm{k+j}} \\ H_{\mathrm{k+1}} & H_{\mathrm{k+2}} & . & . & . & H_{\mathrm{k+j+1}} \\ . & . & . & . & . & . \\ . & . & . & . & . & . \\ H_{\mathrm{k+i}} & H_{\mathrm{k+i+1}} & . & . & . & H_{\mathrm{k+i+j}} \end{vmatrix} \tag{3.2}$$

where

H_{k} : Blocks of data formed from input and output measurements

i, j : Specified integers

For ERA algorithm, two shifted Hankel matrix are formed: $H_{(\mathrm{1|i,j})}$ and $H_{(\mathrm{2|i,j})}$. SVD of $H_{(\mathrm{1|i,j})}$ is performed and allows for finding the minimum order realization. So, this method has a clear advantage over Prony's method when it comes to select an appropriate reduced order of the model. The disadvantage of this method is that it is highly computationally complex and slow when compared to other methods as it runs SVD which takes more time especially when performed online. By running this method recursively, the computational performance can be upgraded. And this method same as Prony's method works only on transient or ring-down data, and can not perform in ambient condition.

3.2.3 Matrix Pencil Method

The Matrix Pencil method approach was introduced by Hua and Sarkar [19]. Initially it was intended to use for estimating poles from electromagnetic transient responses from antennas. This method uses almost the same algorithm as ERA as it also runs SVD on Hankel matrix. The Hankel matrix is formed in a different way than that of ERA. As this method has SVD built-in, choosing lower order model from the singular values is also possible in this algorithm. Also, this method is capable of handling noisy signals accurately, has less sensitivity to different sample sizes and easier and poles of the system can be directly found from the eigenvalues in a single step whereas normal polynomial methods require two steps

to find the poles. The disadvantage of pencil matrix method is that due to SVD, this method is computationally extensive and this method can not handle ambient data as well.

3.2.4 Non-recursive Subspace Identification

Subspace identification process can be divided into two sub-categories: Deterministic subspace identification and Stochastic subspace identification. In deterministic subspace identification method, both input and output vectors are known and available and the noise vectors are zero. In stochastic subspace identification method, only output vectors are known from measurements and the system matrices are estimated from only output vectors.

3.2.4.1 Deterministic Subspace Identification

The algorithm of deterministic subspace identification method is discussed in algorithm 1.

3.2.4.2 Stochastic Subspace Identification

The algorithm of deterministic subspace identification method is discussed in algorithm 2.

3.2.5 Recursive Subspace Identification

The details of the recursive sub-space identification method is discussed next. The details of the other methods can be seen in [6] to [25]. In the recursive subspace identification, first, from the measurements, Hankel matrices are formed as shown in the following equations.

$$Y_{\mathrm{p}} = \begin{vmatrix} y_0 & y_1 & . & . & y_{\mathrm{j\text{-}1}} \\ . & . & . & . & . \\ . & . & . & . & . \\ . & . & . & . & . \\ y_{\mathrm{i\text{-}1}} & y_{\mathrm{i}} & . & . & y_{\mathrm{i+j\text{-}2}} \end{vmatrix} \quad Y_{\mathrm{f}} = \begin{vmatrix} y_{\mathrm{i}} & y_{\mathrm{i+1}} & . & . & y_{\mathrm{i+j\text{-}1}} \\ y_{\mathrm{i+1}} & y_{\mathrm{i+2}} & . & . & y_{\mathrm{i+j}} \\ . & . & . & . & . \\ . & . & . & . & . \\ y_{\mathrm{2i\text{-}1}} & y_{\mathrm{2i}} & . & . & y_{\mathrm{2i+j\text{-}2}} \end{vmatrix} \tag{3.12}$$

$$U_{\mathrm{p}} = \begin{vmatrix} u_0 & u_1 & . & . & u_{\mathrm{j\text{-}1}} \\ . & . & . & . & . \\ . & . & . & . & . \\ . & . & . & . & . \\ u_{\mathrm{i\text{-}1}} & u_{\mathrm{i}} & . & . & u_{\mathrm{i+j\text{-}2}} \end{vmatrix} \quad U_{\mathrm{f}} = \begin{vmatrix} u_{\mathrm{i}} & u_{\mathrm{i+1}} & . & . & u_{\mathrm{i+j\text{-}1}} \\ u_{\mathrm{i+1}} & u_{\mathrm{i+2}} & . & . & u_{\mathrm{i+j}} \\ . & . & . & . & . \\ . & . & . & . & . \\ u_{\mathrm{2i\text{-}1}} & u_{\mathrm{2i}} & . & . & u_{\mathrm{2i+j\text{-}2}} \end{vmatrix} \tag{3.13}$$

Algorithm 1 Deterministic Subspace Identification Method

1: Collect input and output data from measurement
2: Calculate extended block Hankel matrix.
3: Calculate oblique projections O_{i} and $O_{\mathrm{i\text{-}1}}$

$$O_{\mathrm{i}} = Y_{\mathrm{f}}/_{\mathrm{U_f}} W_{\mathrm{p}} \tag{3.3}$$

$$O_{\mathrm{i\text{-}1}} = Y_{f^-}/_{\mathrm{U}_{f^-}} W_{p^+} \tag{3.4}$$

4: Calculate SVD of the weighted oblique projections

$$W_1 O_{\mathrm{i}} W_2 = USV^T \tag{3.5}$$

where

W_1 and W_2 : The identity weighting matrices

5: Determine the reduced order of the system

$$W_1 O_{\mathrm{i}} W_2 = USV^T = \begin{vmatrix} U_1 & U_2 \end{vmatrix} \begin{vmatrix} S_1 & 0 \\ 0 & S_2 \end{vmatrix} \begin{vmatrix} {V_1}^T \\ {V_2}^T \end{vmatrix} \tag{3.6}$$

6: Calculate the extended observability matrix Γ_{i} and $\Gamma_{\mathrm{i\text{-}1}}$

$$\Gamma_{\mathrm{i}} = {W_1}^{-1} U_1 {S_1}^{1/2} \tag{3.7}$$

$\Gamma_{\mathrm{i\text{-}1}}$= first $(i-1)m$ rows of Γ_{i}
7: Determine ${X_{\mathrm{i}}}^d$ and ${X_{\mathrm{i+1}}}^d$

$${X_{\mathrm{i}}}^d = \widehat{\Gamma}_{\mathrm{i}} O_{\mathrm{i}} \tag{3.8}$$

$${X_{\mathrm{i+1}}}^d = \widehat{\Gamma_{\mathrm{i\text{-}1}}} O_{\mathrm{i\text{-}1}} \tag{3.9}$$

where

$\widehat{\Gamma}_{\mathrm{i}}$: Moore-Penrose pseudo inverse operation of Γ_{i}

8: Solve linear equations to get A,B,C and D

$$\begin{vmatrix} {X_{\mathrm{i+1}}}^d \\ Y_{\mathrm{i|i}} \end{vmatrix} = \begin{vmatrix} A & B \\ C & D \end{vmatrix} \begin{vmatrix} {X_{\mathrm{i}}}^d \\ U_{\mathrm{i|i}} \end{vmatrix} \tag{3.10}$$

Algorithm 2 Stochastic Subspace Identification Method

1: Collect output data from measurement
2: Calculate extended block Hankel matrix only from outputs.
3: Calculate projections
4: Calculate SVD of the weighted projections
5: Determine the reduced order of the system
6: Calculate the extended observability matrix.
7: Determine X_{i} and $X_{\mathrm{i+1}}$
8: Solve linear equations to get A and C

$$\begin{vmatrix} A \\ C \end{vmatrix} = \begin{vmatrix} X_{\mathrm{i+1}} \\ Y_{\mathrm{i|i}} \end{vmatrix} \widehat{X_{\mathrm{i}}} \tag{3.11}$$

$$Y_{\mathrm{p+}} = \begin{vmatrix} y_0 & y_1 & . & . & y_{\mathrm{j\text{-}1}} \\ . & . & . & . & . \\ . & . & . & . & . \\ y_{\mathrm{i\text{-}1}} & y_{\mathrm{i}} & . & . & y_{\mathrm{i+j\text{-}2}} \\ y_{\mathrm{i}} & y_{\mathrm{i+1}} & . & . & y_{\mathrm{i+j\text{-}1}} \end{vmatrix} \quad Y_{\mathrm{f\text{-}}} = \begin{vmatrix} y_{\mathrm{i+1}} & y_{\mathrm{i+2}} & . & . & y_{\mathrm{i+j}} \\ . & . & . & . & . \\ . & . & . & . & . \\ . & . & . & . & . \\ y_{\mathrm{2i\text{-}1}} & y_{\mathrm{2i}} & . & . & y_{\mathrm{2i+j\text{-}2}} \end{vmatrix} \tag{3.14}$$

$$U_{\mathrm{p+}} = \begin{vmatrix} u_0 & u_1 & . & . & u_{\mathrm{j\text{-}1}} \\ . & . & . & . & . \\ . & . & . & . & . \\ u_{\mathrm{i\text{-}1}} & u_{\mathrm{i}} & . & . & u_{\mathrm{i+j\text{-}2}} \\ u_{\mathrm{i}} & u_{\mathrm{i+1}} & . & . & u_{\mathrm{i+j\text{-}1}} \end{vmatrix} \quad U_{\mathrm{f\text{-}}} = \begin{vmatrix} u_{\mathrm{i+1}} & u_{\mathrm{i+2}} & . & . & u_{\mathrm{i+j}} \\ . & . & . & . & . \\ . & . & . & . & . \\ u_{\mathrm{2i\text{-}1}} & u_{\mathrm{2i}} & . & . & u_{\mathrm{2i+j\text{-}2}} \end{vmatrix} \tag{3.15}$$

Then, using subspace identification technique, the extended observability matrix Γ_i is calculated based on projection algorithm as

$$E_{\mathrm{p}} = U_{\mathrm{p}} Y_{\mathrm{p}} \tag{3.16}$$

$$H_{1:j} = U_{\mathrm{f}} E_{\mathrm{p}} Y_{\mathrm{f}} \tag{3.17}$$

$$\mathbf{H_{1:j}} = \begin{bmatrix} U_f \\ E_p \\ Y_f \end{bmatrix} = \begin{bmatrix} L_{11} & 0 & 0 \\ L_{21} & L_{22} & 0 \\ L_{31} & L_{32} & L_{33} \end{bmatrix} \begin{bmatrix} Q_{11}^T \\ Q_{21}^T \\ Q_{31}^T \end{bmatrix} \tag{3.18}$$

$$(Y_f/U_f) * E_p = \Gamma_i X_i/U_f^{|} = L_{32} Q_{21}^T \tag{3.19}$$

where E_p represents the subspace of past input and output in block Hankel matrices U_p and Y_p. Eqn. (3.19) calculates the oblique projection of the future outputs on the past input/output along the future inputs. Column space of L_{32} is equal to the column space of extended observability matrix Γ_i. So only extracting L_{32} from the LQ decomposition of the whole subspace is enough to get the system characteristics. The projected matrix O will then be,

$$O = L_{32} \tag{3.20}$$

From (3.20), only L_{32} is needed for proper system identification when both input and output measurements are used. Calculate the SVD on L_{32} and select the reduced order n from singular values obtained from SVD,

$$L_{32} = USV^T = \begin{bmatrix} U_1 & U_2 \end{bmatrix} \begin{bmatrix} S_1 & 0 \\ 0 & S_2 \end{bmatrix} \begin{bmatrix} V_1^T \\ V_2^T \end{bmatrix} \approx U_1 S_1 V_1^T \tag{3.21}$$

where $U_1 = \Gamma_i$. Since Γ_i is defined as $\Gamma_i = \langle CCACA^2...CA^{i-1} \rangle^T$ which contains the information of system matrix, A can be calculated by $A = \Gamma_i^* \Gamma_i$. From eigenvalues of A matrix, the modes and their damping ratio can be calculated. In the first step of recursive algorithm, the LQ factorization is calculated recursively. In the second step, the extended observability matrix is calculated recursively to avoid computationally challenging SVD at each iteration. New 'p' data is coming after first data set.

3.2.6 Updating LQ factorization recursively

From the Hankel matrix generated previously, we can get

$$H_{1:j} = \begin{vmatrix} U_{\mathrm{f}} \\ E_{\mathrm{p}} \\ Y_{\mathrm{f}} \end{vmatrix} \tag{3.22}$$

$$H_{1:j} = L_1 Q_1 \tag{3.23}$$

$$G_1 Q_1 = \begin{bmatrix} \varepsilon & \sigma \\ 0 & \bar{Q}_1 \end{bmatrix} \tag{3.24}$$

$$\begin{aligned} (G_1 Q_1)^T (G_1 Q_1) &= \begin{bmatrix} \varepsilon & \sigma \\ 0 & \bar{Q}_1 \end{bmatrix}^T \begin{bmatrix} \varepsilon & \sigma \\ 0 & \bar{Q}_1 \end{bmatrix} \\ &= \begin{bmatrix} \varepsilon & \sigma \\ 0 & \bar{Q}_1 \end{bmatrix} \begin{bmatrix} \varepsilon & \sigma \\ 0 & \bar{Q}_1 \end{bmatrix}^T \\ &= I \end{aligned} \tag{3.25}$$

It can be proved that, $\varepsilon^T \varepsilon = I_p$ and $\sigma = 0$. So,

$$G_1 Q_1 = \begin{bmatrix} I_p & 0 \\ 0 & \bar{Q}_1 \end{bmatrix} \tag{3.26}$$

$$
\begin{aligned}
H_{1+p:j+p} &= [H_{p+1:j} \quad H_{j+1:j+p}] \\
&= [\bar{L_1}\bar{Q}_1 \quad H_{j+1:j+p}] \\
&= [H_{j+1:j+p} \quad \bar{L_1}] \begin{bmatrix} 0 & I_p \\ \bar{Q}_1 & 0 \end{bmatrix} \\
&= \bar{L_2}\bar{Q}_2 \\
&= (\bar{L_2}G_2)(G_2^T\bar{Q}_2) \\
&= L_2Q_2
\end{aligned} \tag{3.27}
$$

where G_1 and G_2 are the givens rotation matrix.

3.2.7 Updating the extended observability matrix recursively to avoid performing SVD

Once the LQ decomposition is updated recursively then the next step is to update the extended observability matrix Λ_i recursively without using SVD. This is performed using the propagator method [55]. The propagator can be determined recursively by solving a least square error minimization approach. The process is as follows. First, the system A matrix is developed for given data. The extended observability matrix Λ_i is developed. Then an identity matrix I_n is calculated, where n is the order of the system. Further a matrix is defined as $P_f^T = I_n$ and $L_f = I_n$. With this, the following matrices are calculated.

$$
\Gamma_f = \begin{bmatrix} I_n & P_f^T \end{bmatrix} \tag{3.28}
$$

where R_x = covariance of A matrix with

$$
R_{zf} = \Gamma_f \times R_x \times \Gamma_f^T \tag{3.29}
$$

$$
R_{zf1} = R_{zf}(1:n, 1:n) \tag{3.30}
$$

$$R_{zf2} = R_{zf}(n+1:2n, n+1:2n) \tag{3.31}$$

where λ = Forgetting factor, ζ = Instrument variable. After initialization and applying the given's rotation twice we get,

$$\begin{bmatrix} L_{11} & 0 & 0 & 0 \\ L_{21} & L_{22} & 0 & \bar{z_p} \\ L_{31} & L_{32} & L_{33} & \bar{z_f} \end{bmatrix} = \begin{bmatrix} L_{11} & 0 & 0 & 0 \\ L_{21} & L_{22} & 0 & 0 \\ L_{31} & L_{32} & L_{33} & \bar{\bar{z}}_f \end{bmatrix} \tag{3.32}$$

$$\bar{\bar{z}}_f = \begin{vmatrix} z_{\mathrm{f1}} \\ z_{\mathrm{f2}} \end{vmatrix} \tag{3.33}$$

$$g_f = \begin{vmatrix} R_{zf2}\zeta & z_{f2} \end{vmatrix} \tag{3.34}$$

$$\Lambda = \begin{vmatrix} -\zeta^T\zeta & \lambda \\ \lambda & 0 \end{vmatrix} \tag{3.35}$$

$$\psi = \begin{vmatrix} R_{zf1}\zeta & z_{f1} \end{vmatrix} \tag{3.36}$$

$$k = (\Lambda + \psi^T L_f \psi)^{-1} \psi^T L_f \tag{3.37}$$

$$P_f^T = P_f^T + (g_f - P_f^T\psi)k \tag{3.38}$$

$$R_{zf1} = \lambda R_{zf1} + Z_{f1}\zeta \tag{3.39}$$

$$R_{zf2} = \lambda R_{zf2} + Z_{f2}\zeta \tag{3.40}$$

$$L_f = \frac{1}{\lambda^2}(L_f - L_f\psi k) \tag{3.41}$$

where P_f is a linear operator called propagator which expresses the linearly dependant vectors of extended observability matrix Λ_i which is same as earlier mentioned Γ_i as a linear

combination of n independent vectors, $Z_f(t)$ is the observation vector, k is the gain vector and $R_{z_{f1}}$ is the expected value of observation vector. The recursive subspace identification framework is able to estimate behaviour of the power system in the presence of input excitation and noise. This helps to estimate system electro-mechanical modes accurately even in the presence of forced oscillations and at the same time can also classify oscillations between forced and natural electro-mechanical modes.

3.3 Experimental Results and Discussion

All of the aforementioned methods are applied on two test systems. The first one is a two-area power grid [56] and the second system is IEEE 68 bus test system which represents the NETS-NYPS system model. This system is used to show the scalability of the methods to perform well on large systems. Laboratory implementation of the algorithms in real-time is shown using Fig. 3.1.

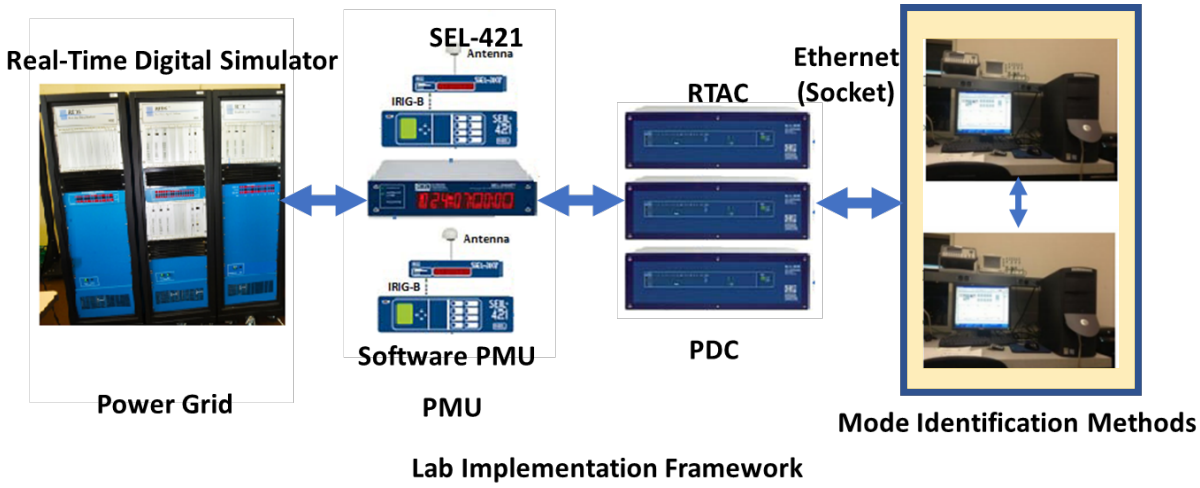

Fig. 3.1: Lab Implementation Procedure.

3.3.1 Test System I: Two Area Test System

Kundur's two area system consists of 9 buses and 4 generators and has two areas. The details are in [56]. The natural inter-area mode for this system is 0.62Hz.

3.3.1.1 Case I

Two cases are created in two area system. For the first case, the total simulation time is 600 seconds. A three-phase ringdown event is created on bus 5 at 5 seconds. The three-phase fault is chosen as this is the most extreme fault scenario in the power system. Then a step-change in load (50 MW) is applied at bus 5 at 200 seconds and lastly, a cyclic load of 0.8 Hz is applied at bus 5 at 400 seconds. The speed of generator 1 is taken as the output vector and the voltage of generator 1 is taken as the input vector for mode estimation. The methods that are applied on these input and output vectors to estimate modes are Prony, ERA, Matrix Pencil Method, non-recursive subspace identification (a non-recursive version of the discussed subspace identification), and recursive subspace identification method. Fig. ?? represents speed of generator 1 for case I.

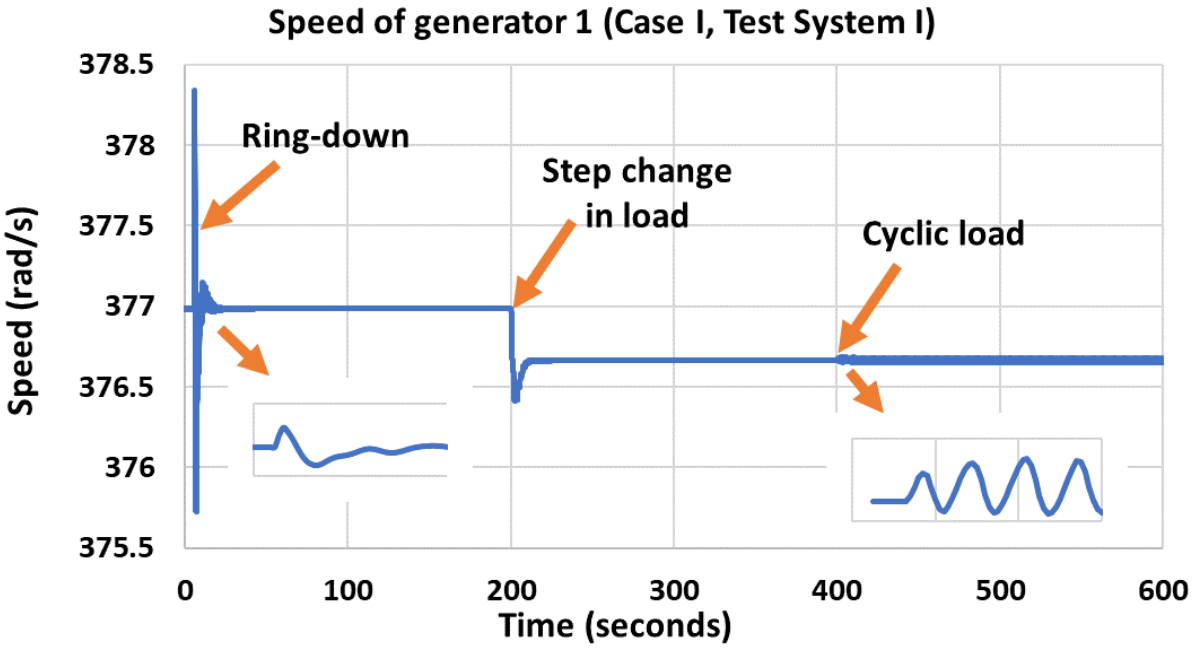

Fig. 3.2: Speed of generator 1 for case I (Test System I).

Table 3.1 and Table 3.2 shows the comparisons. Fig. 3.3 shows the results for mode estimation for case I using recursive SSI method. This result shows that recursive SSI method can identify both natural and forced mode with good accuracy.

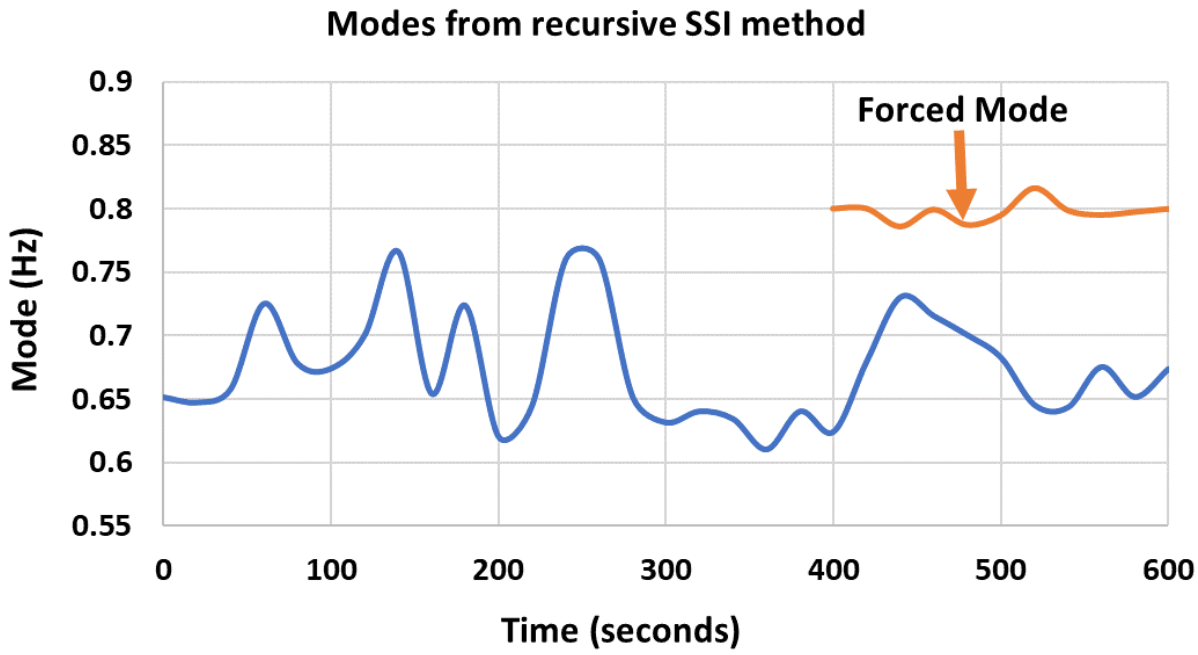

Fig. 3.3: Estimated mode from recursive SSI method for case I (Test System I)

3.3.1.2 Case II

For the second case, the total simulation time is 500 seconds. A three-phase ringdown event happens at bus 5 at 5 seconds and a step-change in load (50 MW) is applied at bus 5 at 200 seconds. A cyclic load of 0.6Hz is applied throughout the whole simulation. The purpose of this case is to find out if the methods are capable of identifying the modes when the forced mode is very close to the natural mode. The speed of generator 1 is taken as the output vector and the voltage of generator 1 is taken as the input vector for mode estimation. Fig. 3.4 represents speed of generator 1 for case II.

Fig. 3.5 shows the result for mode estimation of case II using the recursive SSI method. From this figure, it is clear that the forced mode of 0.6Hz and the natural mode of 0.62Hz are both identified by using this method. But the natural mode can not be identified between 20 seconds to 80 seconds. While using other methods on the same data, it is found that other methods also fail to identify natural mode at this time. Some methods such as Prony, Matrix Pencil, and non-recursive SSI fail to identify natural mode for an even longer period. Table 3.1 and Table 3.2 summarize the results.

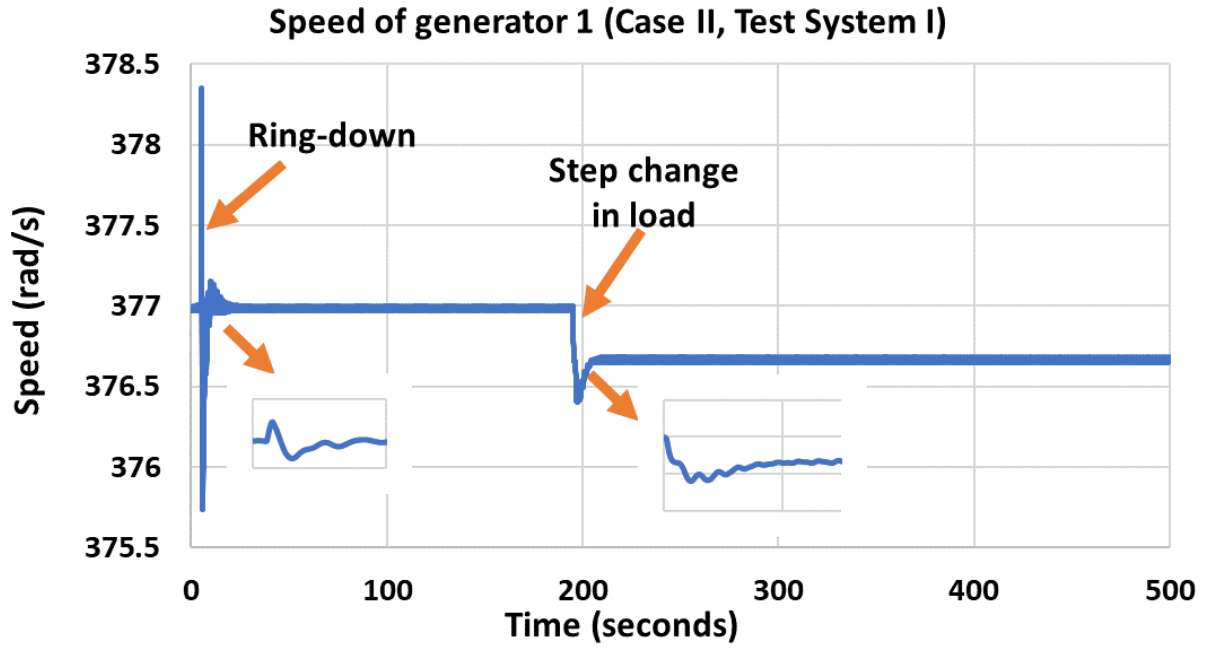

Fig. 3.4: Speed of generator 1 for case II (Test System I).

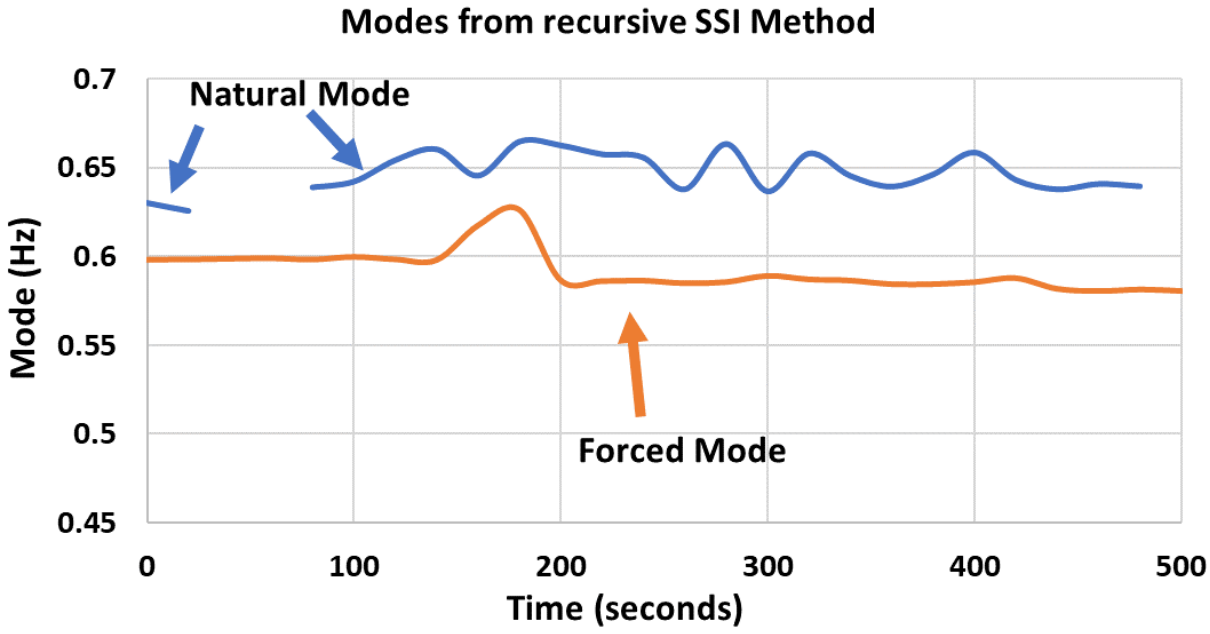

Fig. 3.5: Estimated mode from recursive SSI method for case II (Test System I)

3.3.2 Test System II: IEEE 68 Bus System

The IEEE 68 bus power grid is used as a larger system. The natural inter-area mode for this system is 0.60Hz. This system has 5 areas and consists of 68 buses and 16 generators.

Table 3.1: Kundur 2 area test system comparisons.

Case Studies	MP and Prony (Min-Max)	ERA (Min-Max)	SSI Non Recur. (Min-Max)	SSI Recur. (Min-Max)
Case I Natural Mode (Hz)	0.583-0.864 Dev. 32.5%	0.397-0.859 Dev. 53.7%	0.606-0.79 Dev. 23.3%	0.61-0.766 Dev. 20.3%
Case I Forced Mode (Hz)	0.769-0.801 Dev. 3.99%	0.769-0.811 Dev. 5.18%	0.635-0.72 Dev. 11.8%	0.786-0.816 Dev. 3.7%
Case II Natural Mode (Hz)	NA Dev. NA%	0.396-0.644 Dev. 38.5%	0.623-0.662 Dev. 5.89%	0.625-0.664 Dev. 5.08%
Case II Forced Mode (Hz)	0.582-0.654 Dev. 11.0%	0.578-0.627 Dev. 7.81%	0.57-0.621 Dev. 8.21%	0.581-0.62 Dev. 6.29%

Table 3.2: Summary of Case I and Case II of Test I

Case Number	Methods	Summary
Case I	MP and Prony	Natural mode: Not precise.
	ERA	Natural mode: Not precise.
	Non-recursive SSI	Forced: Not precise.
	Recursive SSI	Both mode: Precise.
Case 2	MP and Prony	Forced mode: Yes, Natural mode: No.
	ERA	Forced mode:Yes. Natural mode: Not precise.
	Non-recursive SSI	Forced mode:Yes. Natural mode: Not precise.
	Recursive SSI	Both mode: Precise.

Table 3.3: IEEE 68 bus system features.

Buses & Generators	68 Buses 16 Generators	Areas	5
Total Active Power Generation (MW)	17787.53	Total Active Load (MW)	17620.65
Total Reactive Power Generation (MVAR)	2496.53	Total Reactive Load (MVAR)	1671.76

3.3.2.1 Case I

For the first case, Three types of events are created in this case as well. The total simulation time is 600 seconds. A three-phase ringdown event happens near bus 14 at 5 seconds. Secondly, a step-change in load (50 MW) is applied at bus 17, 39, and 41 at around 200 seconds and finally, a cyclic load of 0.8 Hz is applied at bus 40 at 400 seconds. The speed

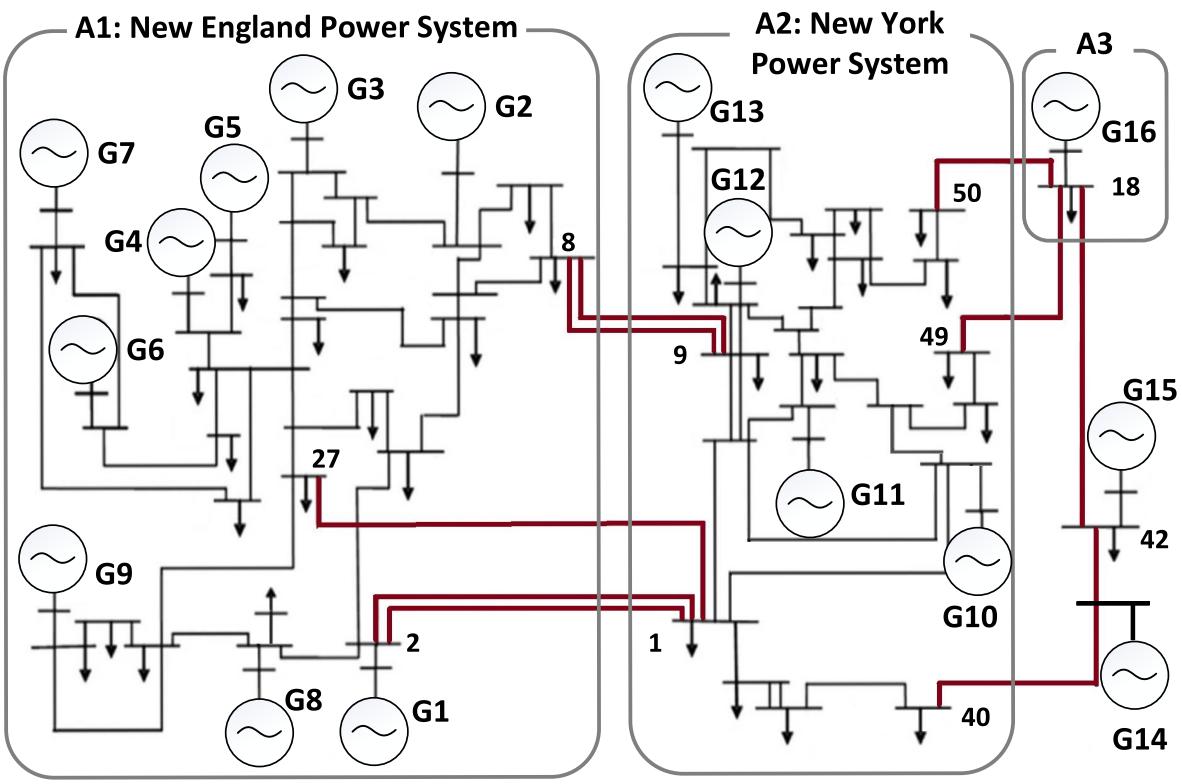

Fig. 3.6: IEEE 68 Bus study system.

of generator 14 is taken as the output vector and the voltage of generator 14 is taken as the input vector for mode estimation. Fig. 3.7 represents speed generator 14 for case I.

Fig. 3.8 shows the results for mode estimation for case I of test system II. Fig. 3.8 shows the estimated mode using the recursive SSI method. This result shows that the recursive SSI method can identify both natural and cyclic modes with better accuracy. Table 3.4 and 3.5 summarizes the result.

3.3.2.2 Case II

For the second case, the total simulation time is 500 seconds. A three-phase ringdown event is created on bus 14 at 5 seconds. Secondly, a step-change in load (50 MW) is applied at bus 17, 39, and 41 at around 200 seconds. A cyclic load of 0.6Hz is applied throughout the whole simulation. The speed of generator 14 is taken as the output vector and the voltage of generator 14 is taken as the input vector for mode estimation. Fig. 3.9 represents speed

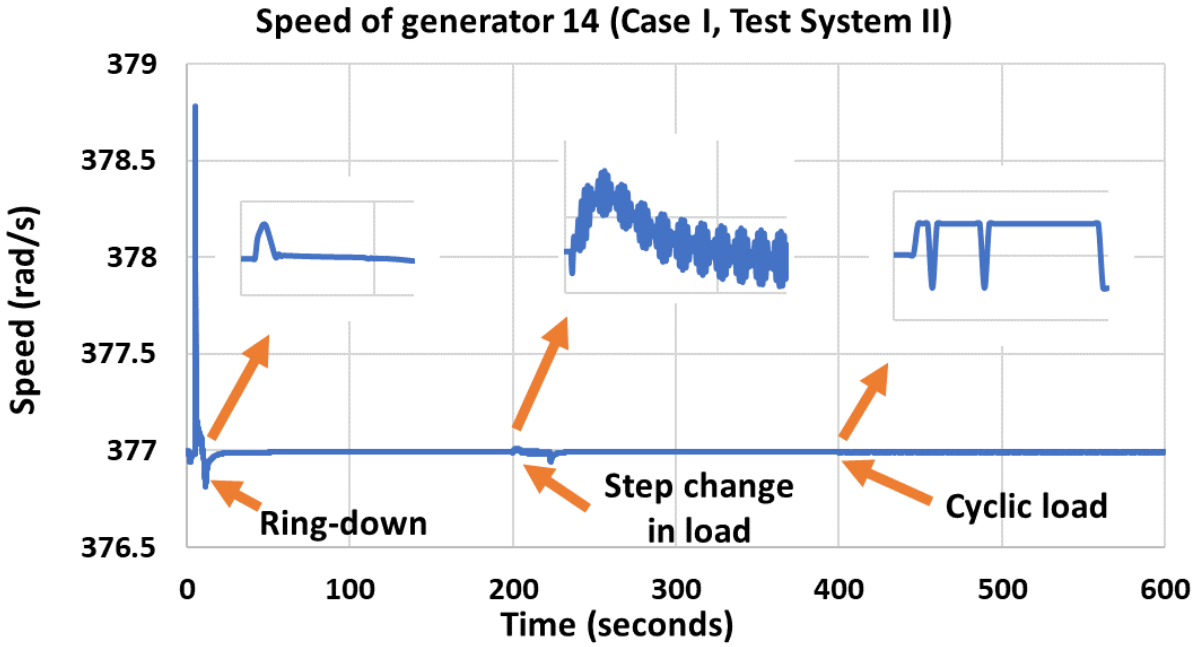

Fig. 3.7: Speed of generator 14 for case I (Test System II).

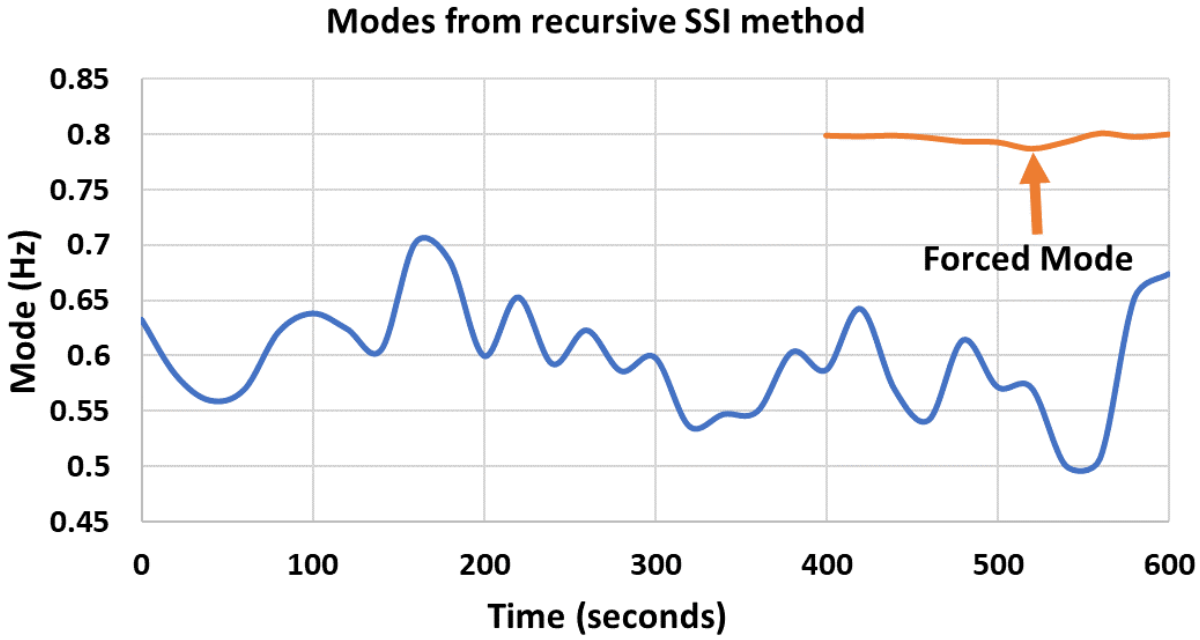

Fig. 3.8: Estimated mode from recursive SSI method for case I (Test System II)

of generator 14 for case II.

Fig. 3.10 shows the result for mode estimation of case II using the recursive SSI method. The recursive SSI method can identify both modes with better accuracy throughout the whole simulation time. Among the other methods, ERA is capable of identifying both

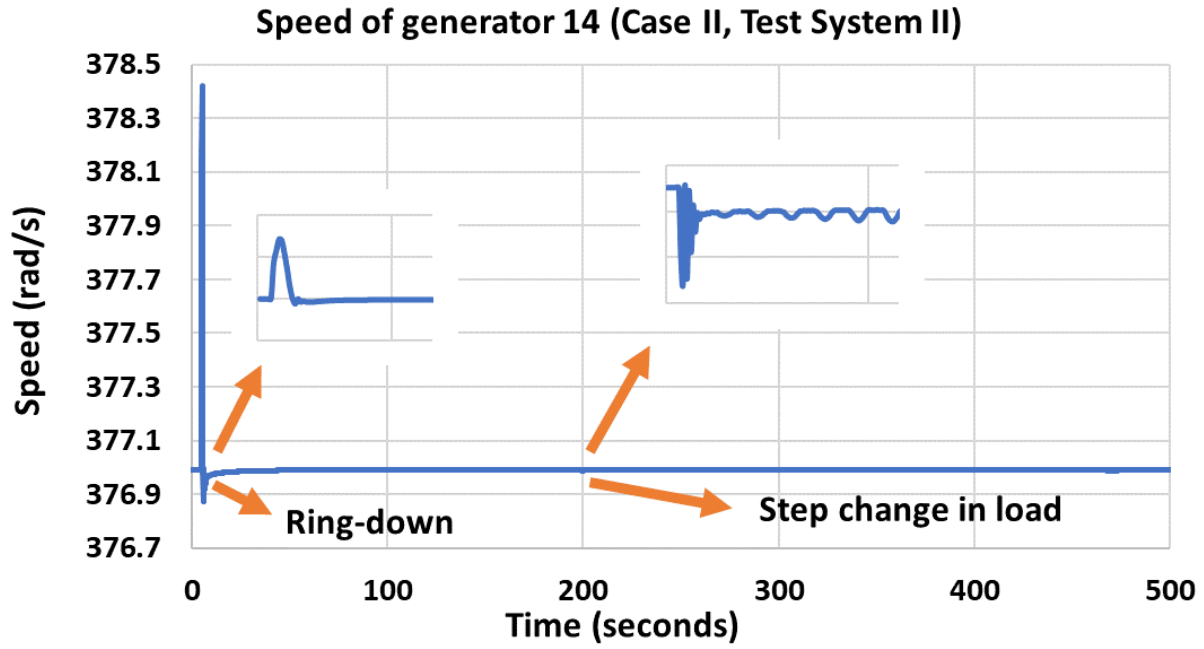

Fig. 3.9: Speed of generator 1 for case II (Test System II).

modes the whole time but the accuracy of natural mode is not as good as recursive SSI. Other methods fail to identify both modes the whole time. Table 3.4 and 3.5 summarizes the result.

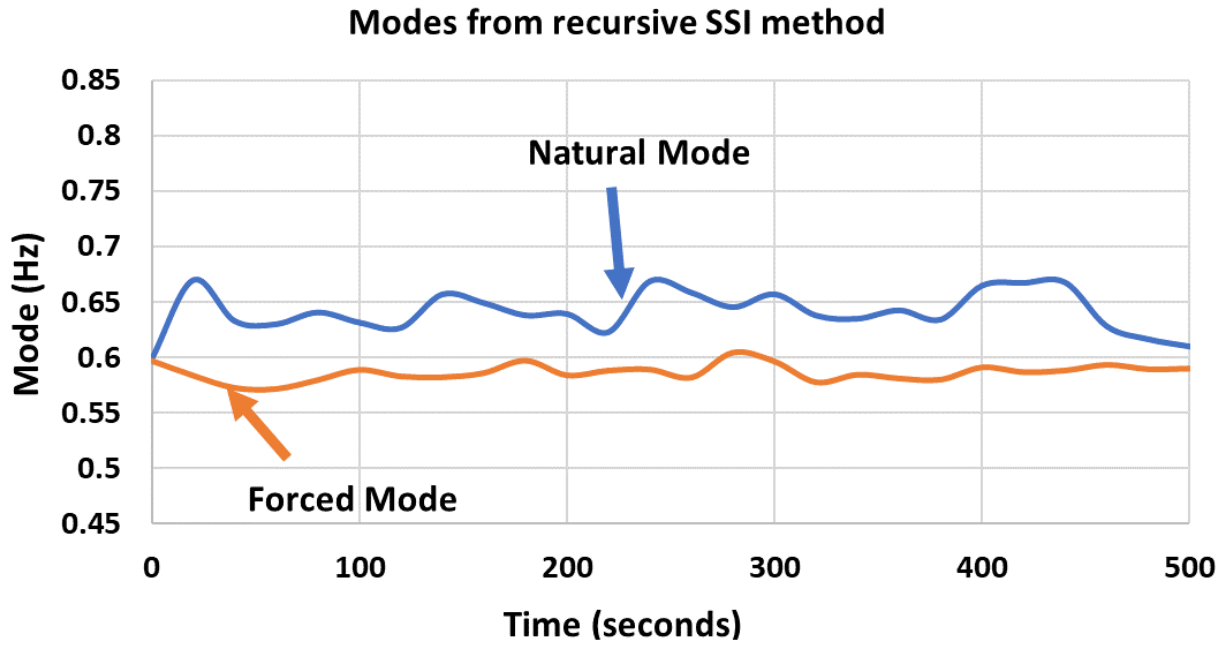

Fig. 3.10: Estimated mode from recursive SSI method for case II (Test System II)

Table 3.4: IEEE 68 bus system test system comparisons.

Case Studies	MP and Prony (Min-Max)	ERA (Min-Max)	SSI Non Recur. (Min-Max)	SSI Recur. (Min-Max)
Case I Natural Mode (Hz)	0.336-0.787 Dev. 57.3%	0.287-0.899 Dev. 68.7%	0.403-0.779 Dev. 48.3%	0.501-0.701 Dev. 28.5%
Case I Forced Mode (Hz)	0.776-0.841 Dev. 7.7%	0.789-0.806 Dev. 2.1%	0.776-0.82 Dev. 5.4%	0.787-0.801 Dev. 1.7%
Case II Natural Mode (Hz)	NA Dev. NA%	0.559-0.812 Dev. 31.1%	0.27-0.799 Dev. 66.2%	0.596-0.669 Dev. 10.9%
Case II Forced Mode (Hz)	0.52-0.61 Dev. 14.7%	0.586-0.655 Dev. 10.5%	0.583-0.679 Dev. 14.1%	0.571-0.603 Dev. 5.3%

Table 3.5: Summary of Case I and Case II of Test II

Case Number	Methods	Summary
Case I	MP and Prony	Natural mode: Not precise.
	ERA	Natural mode: Not precise.
	Non-recursive SSI	Forced: Not precise.
	Recursive SSI	Both mode: Precise.
Case 2	MP and Prony	Forced mode: Yes, Natural mode: No.
	ERA	Forced mode:Yes. Natural mode: Not as precise as recursive SSI.
	Non-recursive SSI	Forced mode:Yes. Natural mode: Not precise.
	Recursive SSI	Both mode: Precise.

The required time for estimating modes by using every method is also calculated. Fig. 3.11 shows the required time for each method to estimate the modes for case II of test system II. This figure shows that the Matrix pencil method takes the lowest time while the non-recursive SSI method takes the longest time.

3.4 Summary

In this chapter, a comparative study of various mode identification methods is presented on two test systems including the recursive forced and natural mode identification method from [30]. Both natural mode identification and forced mode identification study have been done with different methods. As it can be seen from Table 3.2 and 3.5, the recursive method

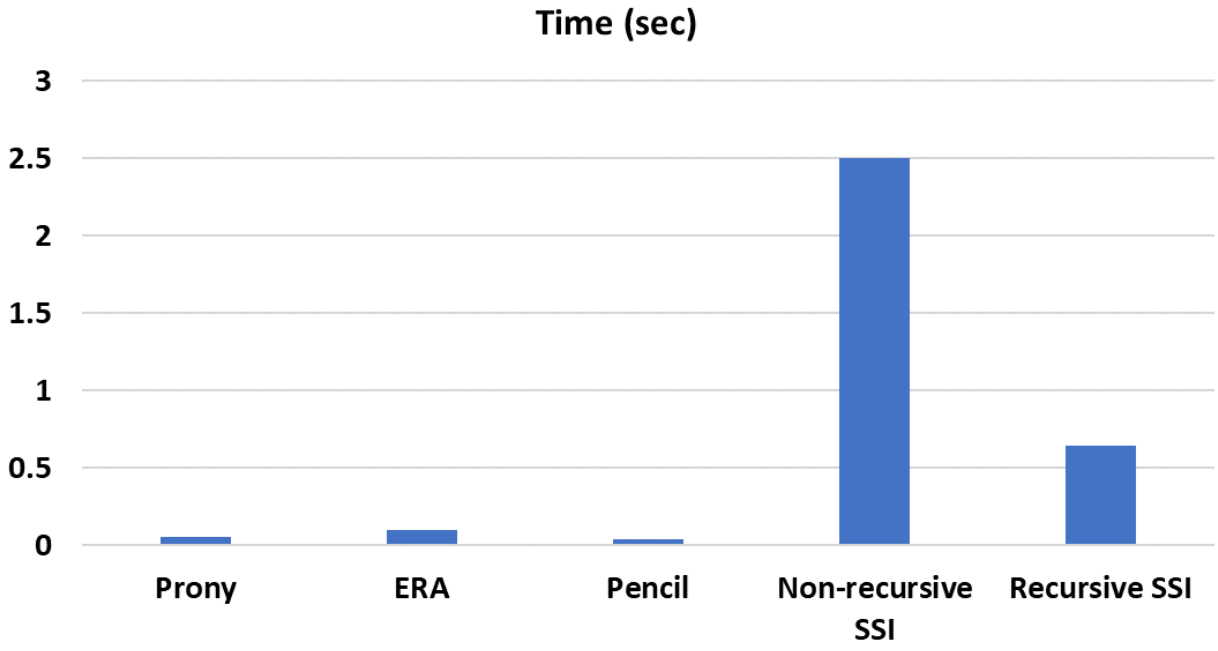

Fig. 3.11: Required simulation time for every method for case II (Test System II)

can accurately measure natural and forced mode (lesser deviation from the min-max) when compared to other methods. Thus it can be concluded that recursive SSI has better performance overall for identifying both natural mode and forced mode under different conditions. After identifying the low frequency mode and their damping ratio, the next chapter will explore a control methodology to improve damping ratio of low damped or unstable modes in power system grid.

CHAPTER 4: An Online Wide-Area Direct Coordinated Control Architecture For Power Grid Transient Stability Enhancement Based On Subspace Identification

4.1 Introduction and main contributions

Control of the power grid during transient and dynamic conditions is very important and critical for system stability and reliability. Recent changes in power grid operations with the advent of integrating renewable energy-based power generating sources make stability assessment and improvement a much critical aspect. Conventional stability assessment mainly deals with rotor angle oscillations and the dynamic behavior of synchronous machines. In the transient stability conditions, large-signal models can assess system stability criteria especially when subject to disturbances such as faults considering full dynamics of generators and assuming the rest of the power grid represented in a reduced form at the generator terminals [57, 58]. Then numerical methods are used to assess the impact of disturbances on overall system stability. Several methods have been assessed to evaluate the system stability even for large scale systems [59–61]. Numerical methods are computationally complex when dealing with large scale grid stability assessment [57, 58, 62].

An alternate solution is the assessment of stability using direct methods. Direct methods provide a coherent solution to assess system stability much like an index just by looking at the energy transfer between generators and the grid during transients. The result is a faster and accurate solution that can give a qualitative index on system stability and thus the health. During faults, such an index can be used to assess the post-fault conditions of the system even when the generator behavior is unknown. The only criteria are that the post fault system information should be available for such an analysis. Direct methods can be used for Transient Stability Assessment (TSA) without depending on numerical solution methods and thus can be used for analysis and control even though the multiple generator

control using such methods is not possible. The most widely used direct method is based on Lyapunov stability criteria [63]. The concept is that during the energy transfer from kinetic to the potential there will be a balance and the system reaches a stability point. With the help of the Lyapunov theory, the stability of the system can be assessed as a scalar function called the Lyapunov function.

Various studies have been conducted to investigate the application and efficiency of transient stability analysis via the direct method. The feasibility of Lyapunov functions for power system transient stability analysis by controlling the unstable equilibrium point (UEP) method is explored in [64]. Ref. [65] uses the Lyapunov function for estimating transient stability considering the load dynamics. Ref. [66], uses direct methods to analyze the transient stability of power systems close to voltage collapse. An investigation of the implications of stability analysis on structure-preserving models of power systems is presented in [67]. In all the mentioned researches, off-line studies are required to use direct methods.

Control of relevant generators for managing grid stability during or after the abnormal conditions is a very important aspect [32–34]. Identifying the faults, selection of important generators for control, and providing an appropriate control action considering the whole system dynamics in mind is a very challenging and important task. Even though several wide-area control designs are proposed in the literature, almost all of them don't show methods that can control relevant generators or they cannot be implemented online. Earlier we have proposed a control architecture for Static Var Compensator (SVC) for a single generator based on the direct energy function [68]. The generator considered is the one close to the fault assuming that the fault is known. This chapter is an extension of [30, 68, 69]. In this chapter, based on the Potential and Kinetic Energy (PE and KE) calculation, a unique method is proposed that can select and control a single or a group of generators to mitigate the power grid inter-area oscillations. The online control architecture designed provides optimal control such that the grid stability is improved.

The main contributions of this chapter are:

- A unique approach for energy function based identification and control that can be applied to the multi-machine system, thus scalable.
- An unique wide-area optimal control designed for multiple generators that can prioritize generator contribution to improve stability.
- A unique method to identify and detect relevant generators for control just by using measurements from the grid and provide a control model.
- The proposed architecture is feasible and performed online and proven on the real-time simulator.

The rest of the chapter is organized as follows: In section 4.2, preliminaries on energy function theory are discussed. Section 4.3, 4.4 and 4.5 discusses the proposed methodology. Section 4.6 discusses real-time simulation results implementation framework. Section 4.7 concludes the chapter.

4.2 Preliminaries on Energy Function Theory

Consider a power grid with n generators and m buses without generators. During power balance, current flowing into or from a bus can be represented as

$$[I] = [Y][V] \tag{4.1}$$

$$I_i = \sum_{j=1}^{n+m} y_{ij} V_i \tag{4.2}$$

and corresponding power as

$$S_i = V_i I_i^* \tag{4.3}$$

Then a general load (power) flow can be represented as

$$I_i = \sum_{j=1}^{n+m} Y_{ij} V_j = \sum_{j=1}^{n+m} |Y_{ij}|\,|V_j| \sphericalangle(\Theta_{ij} + \delta_j) \tag{4.4}$$

$$P_{ei} = \sum_{j=1}^{n+m} |V_i|\,|V_j|\,|Y_{ij}|\,cos(\Theta_{ij} - \delta_i + \delta_j) \tag{4.5}$$

$$Q_{ei} = -\sum_{j=1}^{n+m} |V_i|\,|V_j|\,|Y_{ij}|\,sin(\Theta_{ij} - \delta_i + \delta_j) \tag{4.6}$$

where Y represents the transfer matrix of the network at steady-state, I_i, P_{ei}, and Q_{ei} are current, active power, and reactive power injected to the grid from bus i, respectively. V_i is the voltage of bus i, and δ_i is the angle of its voltage. Θ_{ij} is the angle of Z_{ij}, when Z_{ij} is the $ijth$ element of $Zbus$.

Generator models can be implemented using a classical representation in the form of swing equations as

$$\frac{\mathrm{d}^2\delta_\mathrm{i}}{\mathrm{d}t^2} = \frac{\pi f}{H_i}(P_{m_i} - P_{e_i}) - D_i\frac{\mathrm{d}\delta_i}{\mathrm{d}t}, \quad i = 1, 2, \cdots, n \tag{4.7}$$

$$\frac{\mathrm{d}\delta_i}{\mathrm{d}t} = \omega_i, \quad i = 1, 2, \cdots, n \tag{4.8}$$

where δ_i is the generator angle with respect to synchronous frame, ω_s is the reference speed, ω_i is the speed of generator i, D_i is the damping factor, and H_i is the inertia constant of generator i. Replacing P_{ei} based on the load flow equations, we get

$$\frac{\mathrm{d}^2\delta_\mathrm{i}}{\mathrm{d}t^2} = \frac{\pi f}{H_i}\left(P_{m_i} - \sum_{j=1}^{2n+m} |V_i|\,|V_j|\,|Y_{ij}|\,cos(\Theta_{ij} - \delta_i + \delta_j)\right) - D_i\frac{\mathrm{d}\delta_i}{\mathrm{d}t}, \quad i = 1, 2, \cdots, n \tag{4.9}$$

4.2.1 Energy Function Representation

To derive an energy function for a power system, the swing equation should be integrated [58]. Let $\frac{\pi f}{H_i} = M_i$. Multiplying both sides of (4.9) by $\frac{\mathrm{d}\delta_i}{\mathrm{d}t}$ and then performing a time integration results in

$$\sum_{i=1}^{n} \frac{1}{2} M_i \omega_i^2 \Big]_{\omega_i^a}^{\omega_i^b} = \sum_{i=1}^{n} (P_{m_i} - \left|V_i^2\right| G_{ii})\delta_i \Big]_{\delta_i^a}^{\delta_i^b}$$

$$- \int_a^b \sum_{i=1}^{n-1} \sum_{j=i+1}^{n} D_{ij} cos\delta_{ij} \partial(\delta_i + \delta_j) - \int_a^b \sum_{i=1}^{n} D_i (\frac{\mathrm{d}\delta_i}{\mathrm{d}t})^2 dt$$

$$-\int_a^b \sum_{i=1}^{n} \sum_{j=n+1}^{2n+m} C_{ij} sin\delta_{ij} \partial\delta_i - \int_a^b \sum_{i=1}^{n} \sum_{j=n+1}^{2n+m} D_{ij} cos\delta_{ij} \partial\delta_i \tag{4.10}$$

where ω is the angular speed, G_{ii} is the conductance, $C_{ij} = |V_i|\,|V_j|\,|Y_{ij}|\,sin\Theta_{ij}$, $D_{ij} = |V_i|\,|V_j|\,|Y_{ij}|\,cos\Theta_{ij}$, and, a, b are the angle limits. In (4.10), the path-dependent term cannot be calculated without numerical methods, since the trajectory of the parameters is not known specifically during abnormal operating conditions such as faults. Also, most of the existing formulations consider the system to be loss-less, thus D_{ij} is assumed to be zero.

The expression for the energy function is the difference between the transient Kinetic Energy (KE) and the total potential energy (PE). This can be written as

$$V = KE - PE \tag{4.11}$$

This function has been used to assess the first swing stability of the power system especially up to the first one second. During a fault, the machine gains KE and PE will keep changing. After the fault, the gained KE is transferred to PE and the system reaches a stable or unstable equilibrium point. In critical cases, the kinetic energy is equal to the potential energy ($KE = PE$), in stable situations the kinetic energy is less than the potential energy ($KE < PE$), and instability occurs if the kinetic energy is greater than the potential energy ($KE > PE$) [58, 70]. Thus V_{cr} can be represented as $V_{cr} = V_{PE}^{max}$.

4.3 Proposed Methodology

For a generalized approach based on energy function, three problems need to be addressed. First, the power grid needs to be represented as a multiple machine system. Second, a method should be developed to model a multi-machine power grid and calculate PE. Third, accurate representation of KE and PE along with their extremes (V_{cr}) need to be analyzed to evaluate the stability as this depends on the fault location. The challenge though is, a) to calculate the KE and PE in an online environment, b) to identify the generators that contribute most towards system stability, c) to develop an identification model for controlling

generators of interest, d) to develop control architecture that can balance PE for multiple generators in the system and, and e) to control multiple generators if required. In this chapter, an energy function monitoring and framework is proposed to address all the above-mentioned challenges. The methodology is a real-life implementable that can be used to control generators to improve system stability.

4.3.1 Measurement Based Energy Function Model of Power Grid

The first step is to develop a measurement-based energy function for each generator in the power grid considering (4.10). For each generator in the system, we can represent (4.10) as

$$KE_i = \frac{1}{2} M_i \omega_i^2 \tag{4.12}$$

$$PR_i = -(P_{m_i} - \left|V_i^2\right| G_{ii})\delta_i \tag{4.13}$$

$$P_{Mag_i} = -\int_a^b \sum_{j=1, j\neq i}^{2n+m} C_{ij} sin\delta_{ij} \partial\delta_i \tag{4.14}$$

$$P_{Loss_i} = -\int_a^b \sum_{j=1, j\neq i}^{n} D_{ij} cos\delta_{ij} \partial(\delta_i + \delta_j)$$

$$-\int_a^b D_i (\frac{\mathrm{d}\delta_i}{\mathrm{d}t})^2 dt - \int_a^b \sum_{i=1}^{n} \sum_{j=n+1}^{2n+m} D_{ij} cos\delta_{ij} \partial\delta_i \tag{4.15}$$

This can be written as

$$PE_i = PR_i + P_{Mag_i} + P_{Loss_i} \tag{4.16}$$

where KE_i and PE_i are the kinetic and potential energy of generator i. PR_i, P_{Mag_i}, and P_{Loss_i} represent rotor position energy, magnetic energy, and loss energy related to machine i, respectively. From this, the total energy in the system can be represented with a measurement based power grid model.

4.3.2 Method for calculating PE and KE from measurement

Our approach is to calculate PE for each generator from the angle and speed at each generator bus (either from PMU measurements of or through prediction if PMU's are not available), and the mechanical power for each generator. We propose to utilize the modern Energy Management System (EMS) with synchronised phasor measurements to measure δ and ω which is feasible to implement. In case of non-availability of PMUs, an angle and speed prediction method is utilized during the fault condition. Also, the generator mechanical power can be obtained through power grid supervisory control and data acquisition system (SCADA). The voltage of non-generator buses is assumed to be 1 pu. Based on this approach, the related energy terms can be approximated via the following equations. These approximations are useful because it reduces the calculation and process time and helps a faster response from control. For the remainder of this section, we have three assumptions. First, the R/X ratio is minimum so the G_{ij} and D_{ij} is neglected. This is very reasonable and realistic for transmission systems. Second, the voltage of non-generator buses is 1pu. This assumption can be relaxed based on the voltage magnitude estimation. It will not change the proposed architecture. Third, during fault, Pm is assumed as constant. With this realistic assumptions, from (4.12) we get

$$KE_{\mathrm{i}} = 0.5 \times M_{\mathrm{i}} \times \omega_{\mathrm{i}} \times (1 - \omega_{\mathrm{PUi}})^2 \tag{4.17}$$

Equation (4.13) can be approximated as

$$PR_i = (\delta_{\mathrm{i}} - \delta) \times (Pm_{\mathrm{i}} - G_{ii}) \tag{4.18}$$

Since $C_{ij} = |V_i|\,|V_j|\,|Y_{ij}|\,sin\Theta_{ij}$, P_{Mag_i} can be re-written as,

$$P_{Mag_i} = |V_i|\,|V_j|\,|Y_{ij}|\,sin\Theta_{ij}cos(\delta_i) \tag{4.19}$$

Again, considering a network neglecting resistance and knowing $Pe_i = |V_i|\,|V_j|\,|B_{ij}|\,sin(\Theta_{ij})$, (4.19) can be expressed as

$$P_{Mag_i} = cos(\delta_{\mathrm{i}} - \delta) \times Pe_{\mathrm{i}} \tag{4.20}$$

Further, knowing that $Pe_i = Pm_i - \frac{H_i}{\pi f} * \frac{\mathrm{d}^2\delta_{\mathrm{i}}}{\mathrm{d}t^2}$

$$P_{Mag_i} = cos(\delta_{\mathrm{i}} - \delta) \times (Pm_i - \frac{H_i}{\pi f} * \frac{\mathrm{d}^2\delta_{\mathrm{i}}}{\mathrm{d}t^2}) \tag{4.21}$$

As mentioned earlier, neglecting network resistances (R/X ratio for transmission system being small) G_{ij}, $D_{ij} = V_i V_j G_{ij} = 0$ and equation (4.15) can be written

$$P_{Loss_i} = -D_i w_i^2 \Delta t \tag{4.22}$$

At unstable equilibrium points (UEP) we get,

$$P_{Mag_i}^{UEP} = cos(\pi - (\delta_{\mathrm{i}} - \delta)) \times Pe_{\mathrm{i}} \tag{4.23}$$

$$PR_i^{UEP} = (\pi - (\delta_{\mathrm{i}} - \delta)) \times (Pm_{\mathrm{i}} - G_{ii}) \tag{4.24}$$

Then PE_i from measurements can be written as

$$PE_{\mathrm{i}} = -(P_{Loss_i} + P_{Mag_i} + PR_i - PR_i^{UEP} - P_{Mag_i}^{UEP}) \tag{4.25}$$

where M_{i} is moment of inertia of generator i, ω_{i} is rotational speed of generator i, ω_{PUi} is per unit speed of generator i, δ_{i} is rotor mechanical angle of generator i, δ is rotor mechanical angle of swing generator, Pm_{i} is mechanical power output of governor of generator i. Thus, from (4.17) - (4.25), KE and PE of generator i can be calculated through measurements if we can measure δ_i, ω_i and Pm_i.

4.3.3 PE and KE calculation from prediction algorithm or PMUs

We propose using PMUs at the generator buses for measuring δ and ω. In the event of measurement delay or unavailability, we propose a prediction method as follows. From [71], δ, ω can be predicted as follows

$$\omega(t_0 + \Delta t) = \omega(t_0) + \left(\frac{P_m - P_e}{M}\right)\Delta t - \frac{D}{M}\Delta\delta \tag{4.26}$$

$$\delta(t_0 + \Delta t) = \delta(t_0) + \left[\omega(t_0)\Delta t + \left(\frac{P_m - P_e}{M} - \frac{D}{M}\omega(t_0)\right)\frac{\Delta t^2}{2!}\right] * 2\pi f \tag{4.27}$$

where t_0 is the initial time and Δt is the time step. Equations (4.26) and (4.27) along with (4.17) - (4.25) is used for online calculation of KE and PE for each generators and for control.

4.3.4 Subspace Identification For Power Grid Model

In the previous section, we proposed a method to measure PE, KE, and P_{mi}. The next step is to develop a dynamic model of the grid using measurements. The dynamic model of the power grid using (4.25) and Pm_i for all the generator of interest can be designed using a subspace identification method [22]. The advantage of the proposed approach is that one can develop a state-space representation of generator dynamics in the power grid using measurements. Also, the subspace identification method gives an appropriately reduced-order n of the system without losing the required accuracy. The general procedure of subspace identification is as follows.

Let the input-output stream data from the measurements be represented as u and y (In this chapter, P_{mi} and PE are used as input and output measurement respectively) , then for $(y_0, y_1, ..., y_{\mathrm{M}})$ and $(u_0, u_1, ..., u_{\mathrm{M}})$ measurements where $y_{\mathrm{k}} \in R^{M\times 1}, u_{\mathrm{k}} \in R^{M\times 1}$ for

$k = 0, 1, 2, ..., M$, extended block Hankel matrices can be represented for each generator

$$Y_{\mathrm{p}} = \begin{vmatrix} y_0 & y_1 & . & . & y_{\mathrm{j\text{-}1}} \\ . & . & . & . & . \\ . & . & . & . & . \\ . & . & . & . & . \\ y_{\mathrm{i\text{-}1}} & y_{\mathrm{i}} & . & . & y_{\mathrm{i+j\text{-}2}} \end{vmatrix} \quad Y_{\mathrm{f}} = \begin{vmatrix} y_{\mathrm{i}} & y_{\mathrm{i+1}} & . & . & y_{\mathrm{i+j\text{-}1}} \\ y_{\mathrm{i+1}} & y_{\mathrm{i+2}} & . & . & y_{\mathrm{i+j}} \\ . & . & . & . & . \\ . & . & . & . & . \\ y_{\mathrm{2i\text{-}1}} & y_{\mathrm{2i}} & . & . & y_{\mathrm{2i+j\text{-}2}} \end{vmatrix} \tag{4.28}$$

$$U_{\mathrm{p}} = \begin{vmatrix} u_0 & u_1 & . & . & u_{\mathrm{j\text{-}1}} \\ . & . & . & . & . \\ . & . & . & . & . \\ . & . & . & . & . \\ u_{\mathrm{i\text{-}1}} & u_{\mathrm{i}} & . & . & u_{\mathrm{i+j\text{-}2}} \end{vmatrix} \quad U_{\mathrm{f}} = \begin{vmatrix} u_{\mathrm{i}} & u_{\mathrm{i+1}} & . & . & u_{\mathrm{i+j\text{-}1}} \\ u_{\mathrm{i+1}} & u_{\mathrm{i+2}} & . & . & u_{\mathrm{i+j}} \\ . & . & . & . & . \\ . & . & . & . & . \\ u_{\mathrm{2i\text{-}1}} & u_{\mathrm{2i}} & . & . & u_{\mathrm{2i+j\text{-}2}} \end{vmatrix} \tag{4.29}$$

$$Y_{\mathrm{p+}} = \begin{vmatrix} y_0 & y_1 & . & . & y_{\mathrm{j\text{-}1}} \\ . & . & . & . & . \\ . & . & . & . & . \\ y_{\mathrm{i\text{-}1}} & y_{\mathrm{i}} & . & . & y_{\mathrm{i+j\text{-}2}} \\ y_{\mathrm{i}} & y_{\mathrm{i+1}} & . & . & y_{\mathrm{i+j\text{-}1}} \end{vmatrix} \quad Y_{f^-} = \begin{vmatrix} y_{\mathrm{i+1}} & y_{\mathrm{i+2}} & . & . & y_{\mathrm{i+j}} \\ . & . & . & . & . \\ . & . & . & . & . \\ . & . & . & . & . \\ y_{\mathrm{2i\text{-}1}} & y_{\mathrm{2i}} & . & . & y_{\mathrm{2i+j\text{-}2}} \end{vmatrix} \tag{4.30}$$

$$U_{\mathrm{p+}} = \begin{vmatrix} u_0 & u_1 & . & . & u_{\mathrm{j\text{-}1}} \\ . & . & . & . & . \\ . & . & . & . & . \\ u_{\mathrm{i\text{-}1}} & u_{\mathrm{i}} & . & . & u_{\mathrm{i+j\text{-}2}} \\ u_{\mathrm{i}} & u_{\mathrm{i+1}} & . & . & u_{\mathrm{i+j\text{-}1}} \end{vmatrix} \quad U_{f^-} = \begin{vmatrix} u_{\mathrm{i+1}} & u_{\mathrm{i+2}} & . & . & u_{\mathrm{i+j}} \\ . & . & . & . & . \\ . & . & . & . & . \\ u_{\mathrm{2i\text{-}1}} & u_{\mathrm{2i}} & . & . & u_{\mathrm{2i+j\text{-}2}} \end{vmatrix} \tag{4.31}$$

where j is determined by $j = M - 2i + 2$, i is a pre-selected integer greater than order of the system n. $U_{\mathrm{p}}, U_{p^+}, U_{\mathrm{f}}, U_{f^-}$ are constructed with the input vector data in a similar way as $Y_{\mathrm{p}}, Y_{p^+}, Y_{\mathrm{f}}, Y_{f^-}$ respectively. The subscript p stands for *past* and the subscript f for $future$. The matrices Y_p and Y_f are past and future output matrices respectively. The matrices Y_p^+ and Y_f^- on the other hand are defined by shifting the border between past and future one block row down. W_{p} and W_{p^+} are constructed from extended block hankel

matrices.

$$W_{\mathrm{p}} = \begin{vmatrix} U_{\mathrm{p}} \\ Y_{\mathrm{p}} \end{vmatrix} \tag{4.32}$$

$$W_{p^+} = \begin{vmatrix} U_{p^+} \\ Y_{p^+} \end{vmatrix} \tag{4.33}$$

By oblique projection, O_{i} and $O_{\mathrm{i\text{-}1}}$ can be calculated as

$$O_{\mathrm{i}} = Y_{\mathrm{f}} /_{\mathrm{U_f}} W_{\mathrm{p}} \tag{4.34}$$

$$O_{\mathrm{i\text{-}1}} = Y_{f^-} /_{\mathrm{U}_{f^-}} W_{p^+} \tag{4.35}$$

Subsequently, a singular value decomposition (SVD) operation is performed as

$$W_1 O_{\mathrm{i}} W_2 = USV^T \tag{4.36}$$

where W_1 and W_2 are identity weighting matrices. From the singular values, n number of significant singular values is obtained which is the selected order of the reduced system. Subsequently, the order of the singular values in S is obtained by partitioning the SVD accordingly to obtain U_1 and S_1

$$W_1 O_{\mathrm{i}} W_2 = USV^T = \begin{vmatrix} U_1 & U_2 \end{vmatrix} \begin{vmatrix} S_1 & 0 \\ 0 & S_2 \end{vmatrix} \begin{vmatrix} {V_1}^T \\ {V_2}^T \end{vmatrix} \tag{4.37}$$

The extended observability matrix Γ_{i} and $\Gamma_{\mathrm{i\text{-}1}}$ will then be

$$\Gamma_{\mathrm{i}} = {W_1}^{-1} U_1 {S_1}^{1/2} \tag{4.38}$$

where $\Gamma_{\text{i-1}}$ is the first $(i-1)M$ rows of Γ_{i}. Then ${X_{\text{i}}}^d$ and ${X_{\text{i+1}}}^d$ is determined using

$$ {X_{\text{i}}}^d = \widehat{\Gamma}_{\text{i}} O_{\text{i}} \tag{4.39} $$

$$ {X_{\text{i+1}}}^d = \widehat{\Gamma_{\text{i-1}}} O_{\text{i-1}} \tag{4.40} $$

where $\widehat{\Gamma}_{\text{i}}$ is Moore-Penrose pseudo inverse operation of Γ_{i}. Then a set of linear equations is solved for A,B,C and D minimizing least square error

$$ \begin{vmatrix} {X_{\text{i+1}}}^d \\ Y_{\text{i|i}} \end{vmatrix} = \begin{vmatrix} A & B \\ C & D \end{vmatrix} \begin{vmatrix} {X_{\text{i}}}^d \\ U_{\text{i|i}} \end{vmatrix} \tag{4.41} $$

To be able to identify the frequency of interest from measurement data and to develop control, an appropriate sampling time is of great importance. If the frequency of interest is within f_o Hz, then based on Nyquist theorem,

$$ f_{\text{s}} \geqslant 2 \times f_o \tag{4.42} $$

where f_s is the sampling frequency. Then

$$ k = 1/f_{\text{s}} \tag{4.43} $$

where k is the sampling time. The timing diagram using system identification and proposed control algorithm and how it is implemented in this chapter is shown in Fig. 4.3.

4.4 Physical State-Space Representation and Identification

For control, the identified and physical states need to be mapped. This is performed as follows. Consider, the system model is available for the actual power grid. The dynamic model that we consider is a Differential Algebraic Equation (DAE) representation with generator

dynamics included as,

$$\Delta X_{t+1} = A_g \Delta X_t + B_g \Delta u_t \tag{4.44}$$

$$\mathrm{X}= \left[\Delta\delta, \Delta S_m, \Delta E'_q, \Delta E''_q, \Delta E'_d, \Delta E''_q, \Delta E_{fq}, \Delta V_r, \Delta V_f, \Delta V_a\right]$$

$$\mathrm{A}_g = \begin{vmatrix}
0 & \omega_B & 0 & 0 & 0 & 0 & 0 & 0 & 0 & 0 \\
0 & -\frac{D}{2H} & 0 & -\frac{I_{q0}}{2H} & 0 & -\frac{I_{d0}}{2H} & 0 & 0 & 0 & 0 \\
0 & 0 & -\frac{k_d}{T'_{d0}} & \frac{k_d-1}{T'_{d0}} & 0 & 0 & \frac{1}{T'_{d0}} & 0 & 0 & 0 \\
0 & 0 & \frac{1}{T''_{d0}} & -\frac{1}{T''_{d0}} & 0 & 0 & 0 & 0 & 0 & 0 \\
0 & 0 & 0 & 0 & -\frac{k_q}{T'_{q0}} & \frac{k_q-1}{T'_{q0}}0 & 0 & 0 & 0 & 0 \\
0 & 0 & 0 & 0 & \frac{1}{T''_{q0}} & -\frac{1}{T''_{q0}}0 & 0 & 0 & 0 & 0 \\
0 & 0 & 0 & 0 & 0 & 0 & -\frac{K_E}{T_E} & \frac{1}{T_E} & 0 & 0 \\
0 & 0 & 0 & 0 & 0 & 0 & 0 & -\frac{1}{T_A} & -\frac{K_A}{T_A} & -\frac{K_A}{T_A} \\
0 & 0 & 0 & 0 & 0 & 0 & -\frac{K_F K'_E}{T_E T_F} & \frac{K_F}{T_E T_F} & -\frac{1}{T_F} & 0 \\
0 & 0 & 0 & 0 & 0 & 0 & 0 & 0 & 0 & -\frac{1}{T_R}
\end{vmatrix}$$

where δ is the rotor angle in radians, ω_B is the rotor base angular speed in radians per second, S_m is the slip, H is the inertia constant in seconds, P_m is the mechanical power, D is the machine rotor damping, E'_d and E''_d is the transient and sub-transient emf due to flux linkage in d-axis damper coil respectively, E'_q and E''_q is the transient and sub-transient emf due to flux linkage in q-axis damper coil respectively, I_d and I_q are the d-axis and q-axis components of the stator current respectively, X_d, X'_d and X''_d are synchronous, transient

and sub-transient reactances along the d-axis respectively.

$$B_g = \begin{vmatrix} 0 & 0 & 0 \\ \frac{1}{2H} & \frac{(X''_d - X''_q)I_{q0} - E''_{d0}}{2H} & \frac{(X''_d - X''_q)I_{d0} - E''_{q0}}{2H} \\ 0 & 0 & 0 \\ 0 & \frac{X''_d - X'_d}{T''_{d0}} & 0 \\ 0 & 0 & 0 \\ 0 & 0 & \frac{X''_q - X'_q}{T''_{q0}} \\ 0 & 0 & 0 \\ 0 & 0 & 0 \\ 0 & 0 & 0 \\ 0 & 0 & 0 \end{vmatrix}, U = \begin{vmatrix} \Delta P_m \\ \Delta I_d \\ \Delta I_q \end{vmatrix}$$

Similarly, X_q, X'_q and X''_q are synchronous, transient and sub-transient reactances along the q-axis respectively, $\mathrm{k}_d = \frac{X_d - X''_d}{X'_d - X''_d}$, $k_q = \frac{X_q - X''_q}{X'_q - X''_q}$, T'_{d0} and T''_{d0} are d-axis open circuit transient and sub-transient time constants in seconds, Also, T'_{q0} and T''_{q0} are q-axis open circuit transient and sub-transient time constants in seconds. E_{fq} is the field excitation voltage, K_e is the exciter gain, K_F is the stabilizer gain and K_A is the regulator gain. T_E is the exciter time constant, T_R is the input filter time constant, T_F is the stabilizer time constant and T_A is the regulator time constant. V_R is the regulator emf, V_a is the input filter emf and V_F is the stabilizer emf. Considering multiple generators in the system, the overall system state-space can be represented along with the algebraic model $\bar{A}_s = diag(A_{g1}, A_{g2}, ...)$. Similarly, $\bar{B}_s = diag(A_{g1}, A_{g2}, ...)$, $\bar{C}_s = diag(A_{g1}, A_{g2}, ...)$, $\bar{D}_s = diag(A_{g1}, A_{g2}, ...)$.

Let us mention this as

$$\Delta x_{t+1} = A_s \Delta x_t + B_s \Delta u_t \tag{4.45}$$

where $A_s = \bar{A}_g - \bar{B_G}\bar{D_g}^{-1}\bar{C}_g$ Then a similarity transformation matrix T_m can be developed to convert the identified model to the actual system state-space representation. For this

first, the right eigenvector of the physical state model A_s is found for a given system. This is stored in the form of T_m in a model dictionary. The similarity transformation can be used to compare the identified model (A_k) with the actual physical state. Also, the T_m will convert the A_s to a Canonical Jordan form. The transformed matrix from the identified model can then be represented as

$$A_T = T_m * A_k * T_m^{-1} \tag{4.46}$$

The flowchart for identified and physical state comparison is illustrated in Fig. 4.1 In the

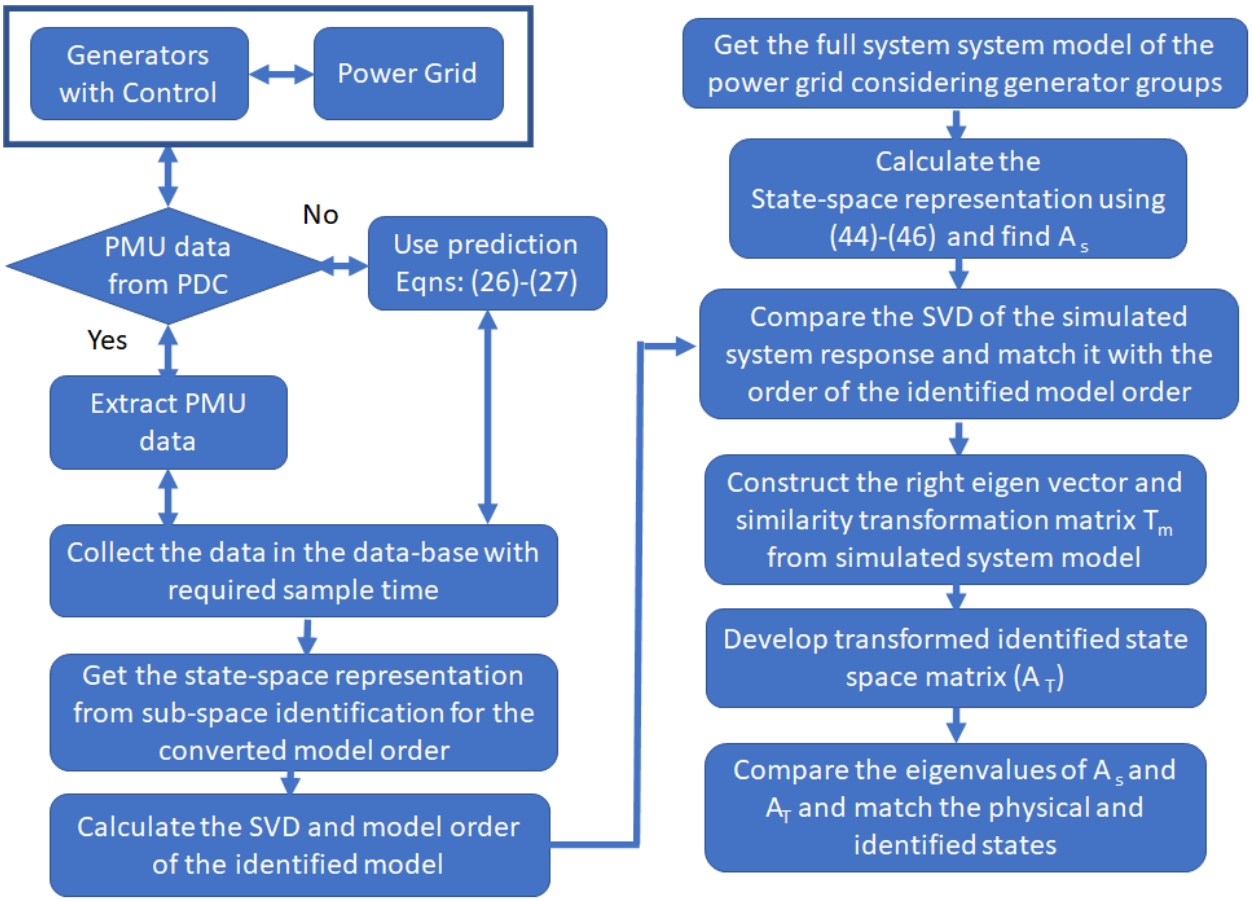

Fig. 4.1: Identified and physical state matching.

test cases, the error threshold is maintained for a system reduced order of 18.

4.4.1 Scalability and Multiple Interarea modes

In the case of a group of inter-area modes of oscillation, the proposed approach will identify the most participated in the generated groups and control those generators. For example, in case I there are two modes identified (0.154Hz and 0.1160Hz) without control and still, there are 4 generators selected for control purposes. After control, both mode's damping ratio is improved. For a larger system, first generator groups can be identified. From this, the most dominant generator can be controlled. Thus will alleviate the computational burden and at the same time feasible. Also, in our test cases, a reduced-order number is found as 18. For a large system, the approach is significantly effective due to the dominant generator identification as it will reduce the computational burden. It will help to identify relevant inter-area modes that contribute largely to oscillatory modes. In the event of having an apriori system knowledge, this information can be used to group the generators based on coherency and extract the modes and dominant machines from the proposed architecture. We have provided a section on how the model and state matching can be performed with the apriori information.

4.5 Trajectory Following Measurement Based Optimal Control

Consider the power grid dynamics in the form or a nonlinear system represented represented in the time varying form as

$$\begin{aligned} x_{t+1} &= f(x_t, u_t) \\ y_{t+1} &= h(x_t, u_t) \end{aligned} \tag{4.47}$$

For the above nonlinear system an iterative optimal control can be designed considering a cost function minimization

$$\begin{aligned} &\min_{x,u} \sum_{t=0}^{H} g(x_t, u_t) \\ &\text{s.t.} x_{t+1} = f(x_t, u_t) \forall t \end{aligned} \tag{4.48}$$

where i is the current time step and H is the time horizon. On this, we can control the state sequence to a feasible target x_t^*,u_t^* based on certainty equivalence law

$$\iff \exists u^* s.t. x_{t+1}^* = f(x_t^*, u_t^*) \tag{4.49}$$

The goal is to minimize the cost function iteratively for every discrete time step i such that the sum of the control inputs satisfies (4.49). From the above, we have

$$x_{t+1} = f(x_t^i, u_t^i) + \frac{\partial f}{\partial x}(x_t^i, u_t^i)(x_t - x^i) + \frac{\partial f}{\partial u}(x_t^i, u_t^i)(u_t - u_t^i) \tag{4.50}$$

From (4.50), for a time horizon $0, 1, ...H$

$$\Delta x_{t+1} = \Delta f(x_t^*, u_t^*) + \frac{\partial f}{\partial x}(x_t^*, u_t^*)\Delta x_t + \frac{\partial f}{\partial u}(x_t^*, u_t^*)\Delta u_t \tag{4.51}$$

where $\Delta x_{t+1} = x_{t+1} - x_{t+1}^*$, $\Delta x_t = x_t - x_t^i$, $\Delta u_t = u_t - u_t^i$ From the above we can write

$$\Delta x_{t+1} = A_k \Delta x_t + B_k \Delta u_t \tag{4.52}$$

where $A_k = \frac{\partial f}{\partial x}(x_t^i, u_t^i)$ and $B_k = \frac{\partial f}{\partial u}(x_t^i, u_t^i)$. Let, $z_t = \Delta x_{t+1}$ and $v_t = \Delta u_t$, then

$$z_{t+1} = A_k z_t + B_k v_t \tag{4.53}$$

Then the cost minimization function will be

$$\begin{aligned} &\min_{x,u} \sum_{t=0}^{H} z_t^T Q z_t + v_t^T R v_t \\ &\text{s.t.} z_{t+1} = A_k z_t + B_k v_t \forall t \end{aligned} \tag{4.54}$$

The controller signal from the optimal controller will be

$$v_t = G_k z_t \tag{4.55}$$

In the discrete time horizon, the architecture can be represented as in algorithm 2.

The overall procedure for developing a dynamic state-space representation and controlling multiple generators in an online environment is explained in algorithm 1 and algorithm 2. Fig. 6.3 represents the overall flow diagram.

4.5.1 Damping Ratio Improvement Index

Damping ratio improvement index (σ) is an index to show the overall improvement in the damping ratio of the dominant modes identified while using controller vs using no controller. The dominant modes are of the same weight for the calculation of the stability improvement index. If there are two dominant modes, then each of the mode's weight will be 0.5. The damping ratio improvement will also be accounted for. The equation for calculating stability improvement index is as follows:

$$\sigma = \sum_{i=1}^{Z} \frac{1}{Z} * Normalized\ damping\ improvement \tag{4.56}$$

Here, Z = Number of dominant modes. In real life, PMUs are used to get measurements from the system. While RTU (Remote Terminal Unit) based SCADA can communicate at a slower rate (2-4 samples every second), PMU based SCADA can provide real-time data at higher rates (Up to 60 samples per second) and with higher accuracy. PMU data are also time-stamped with GPS (Global Positioning System). PMU measurements are then sent to PDC (Phasor Data Concentrator) in real-time based on IEC 61850 protocol. From PDC, the measurements are being used for the synchrophasor application framework, energy management system (EMS), and dynamic security assessment. From these measurements, through our proposed control architecture, the wide-area optimal control signals can be sent

back to generators of the system in real-time (see [1] the details of field-deployed PMU based EMS).

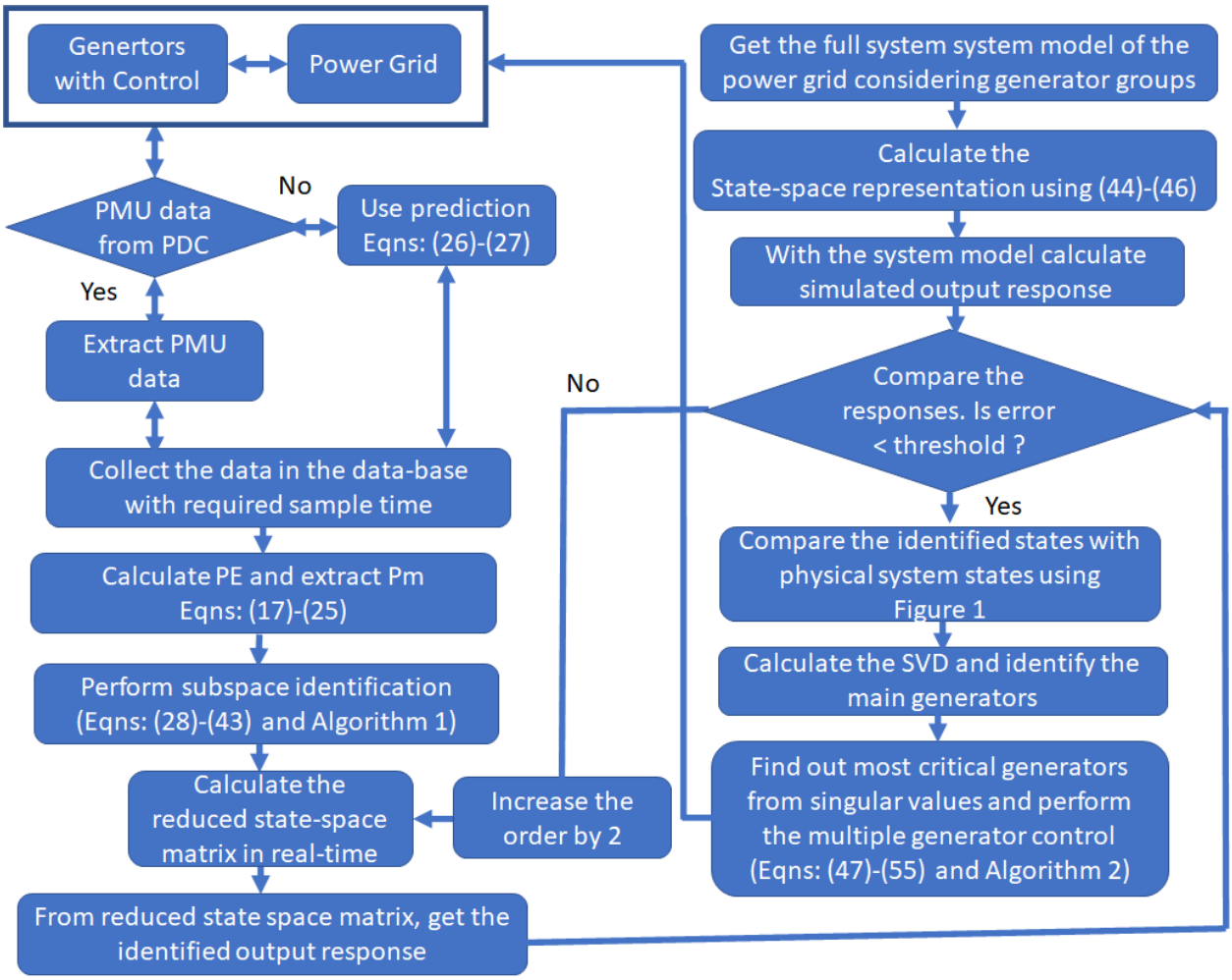

Fig. 4.2: Overall flow diagram of the proposed algorithm.

4.6 Real-Time Simulation Results

The proposed technique is designed and tested on a the dynamic IEEE 68 bus test system discussed in [72] using Real-Time Digital Simulator (RTDS). The power grid dynamic model consists of five different areas including New England test system (NETS) which is a reduced equivalent model of New England area in the US, and the New York power system (NYPS). The one line diagram and the implementation schematic of the proposed architecture is shown in Fig. 4.3. Table 4.1 describes the main characteristics of the test system.

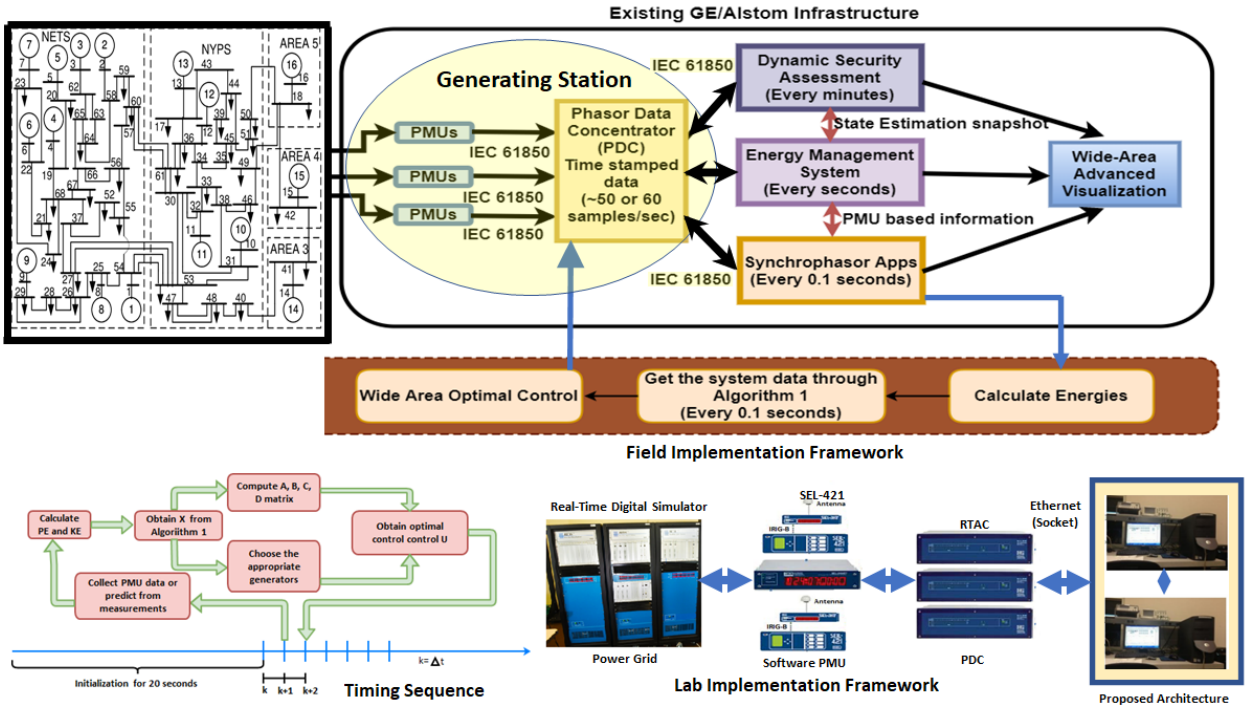

Fig. 4.3: Proposed control architecture implementation schematic based on [1], timing diagram, and lab implementation framework.

Table 4.1: IEEE 68 Bus System Features

Buses & Generators	68 Buses 16 Generators	Areas	5
Total Active Power Generation (MW)	17787.53	Total Active Load (MW)	17620.65
Total Reactive Power Generation (MVAR)	2496.53	Total Reactive Load (MVAR)	1671.76

The test system along with the controller is implemented in a real-time simulator with all the dynamics captured as in real-life and the data used from real-life implementations. The real-time power grid is running in the closed-loop with a control algorithm and the data is exchanged using an ethernet port connection through a socket (GTNET-SKT). The transfer and receipt of data occur between real-time simulator and controller implemented in Matlab in real-time. PMUs are connected to all the generators to collect speed, generator angle, and mechanical power data and voltage. Then the PE and KE are calculated for all the generators. Fig. 4.3 shows the lab implementation framework which also shows the

connection between RSCAD® and MATLAB® through GTNET-SKT®.

For data collection, choosing appropriate sampling time to find and control the expected mode is very important. Sampling time is selected based on the oscillation frequency of interest. We are concerned about local and inter-area oscillation frequencies which span between 0 Hz to 2 Hz. Based on the Nyquist theorem, f_{s} should be greater than or equal to 4 Hz. For the simulation, f_{s} is considered as 10 Hz and k is 0.1 second. Data window length is chosen as 200 which implicates that, the identification and control architecture works with 200 data at a time. The data window is updated every 0.1 seconds. For every data window, the identification method identifies the system as a linear system and produces a control signal for selected generators. For analysis, two different fault conditions and a one-step change in load conditions are considered. Results and comparisons for each case are discussed next. The fault condition tests are conducted for three separate scenarios - without any controller, with a power system stabilizer (PSS), and with the proposed controller. The load change condition is conducted for two scenarios - without any controller and with the proposed controller.

4.6.1 Case I

In this case, a symmetrical three-phase fault is applied on bus 17 at $t = 0.9$ seconds. Fault duration is 6 cycles and the fault is removed at $t = 1.0$ seconds. The generator dynamics are with full controllers including governors and excitation systems. The data is collected from PMU measurements and the KE and PE are calculated. From PE and Pm_{i}, A, B, C and D matrix is found by using subspace identification method. The appropriate reduced order for all the generators from magnitudes of singular values is determined as 18 using online measurements (Fig. 4.4). Fig. 4.6 shows the comparison of the responses between the actual system and the reduced-order system which shows the negligible difference. This proves that online model reduction is effective and captures the full system dynamics. The magnitude of the singular values is also important for determining the most critical generators due to the fault. Fig. 4.5 shows maximum singular values obtained from SVD of the speed of

all generators during and after the fault. We can observe that the most critical generators (Generator 10, 11, 12, and 13) are located in the same area (NYPS), where the symmetrical fault is applied. As a result, these four generators are controlled simultaneously.

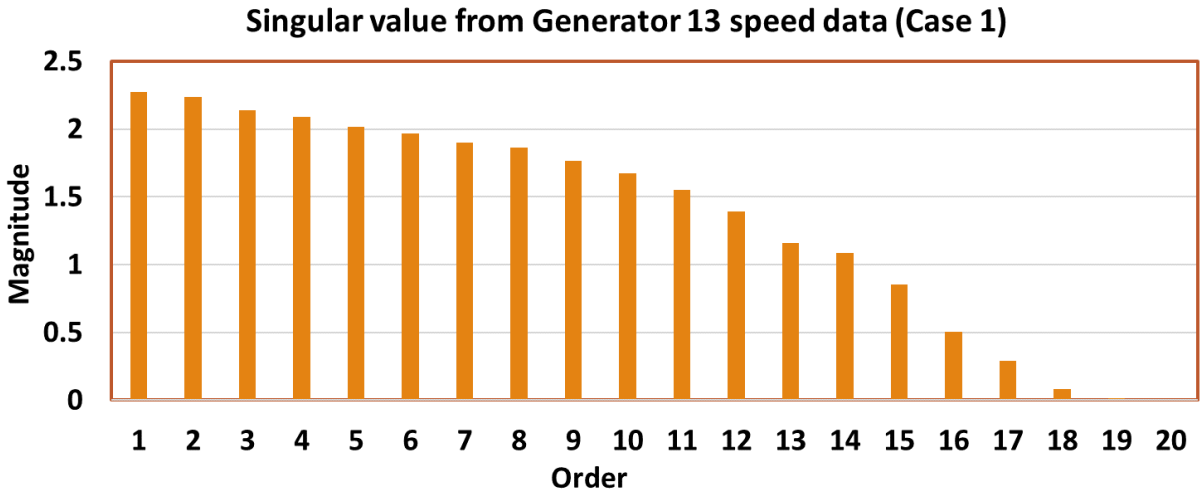

Fig. 4.4: Order reduction from singular values for Case 1.

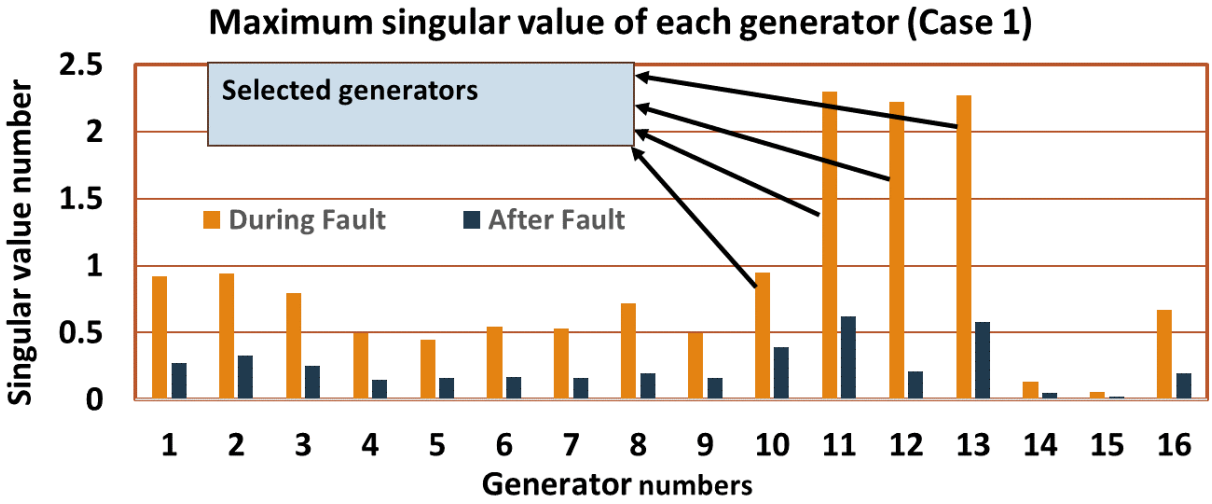

Fig. 4.5: Maximum singular value of generators for Case 1.

The closed-loop controller provides four control signals simultaneously to four selected generators. These control signals are then implemented in the real-time simulator using GTNET-SKT and applied to the exciters of these 4 generators. Fig. 4.7 shows a comparison

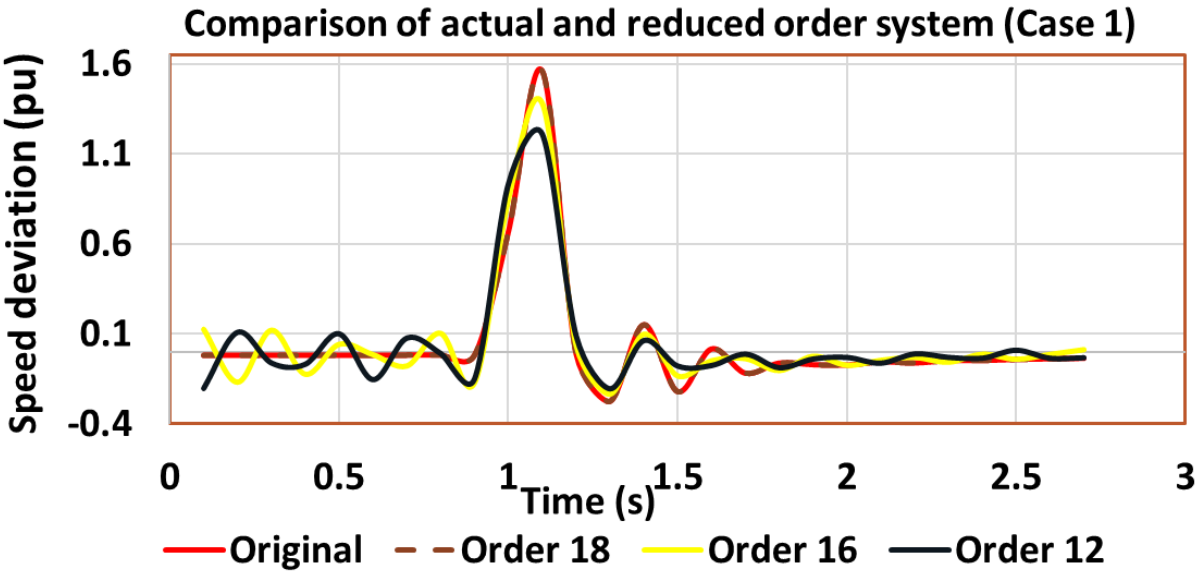

Fig. 4.6: Comparison between actual and reduced order system response.

of the speed of the selected generators with no control, with PSS, and with proposed control. Fig. 4.8 shows percentage error between measured and predicted speed and angle during the fault period. The percentage error is very low and the predicted speed and angle values can be used if PMU data is unavailable during the fault. This shows prediction accuracy. Fig. 4.9 shows a percentage change in energy function difference of the same generators with the proposed controller as well as the control signal output for the selected generators. From this figure, it is evident that while using the proposed controller, the difference between KE and PE is increased which means an improvement of stability margin.

Fig. 4.10 shows a comparison of supplied reactive power and change in voltage at the faulted bus after applying the proposed controller. From the eigenvalues obtained from system matrix A (For with controller, with PSS, and without controller), it is evident that by applying the proposed controller, the damping ratio of the dominant modes is improved. Table 4.2 summarizes the dominant modes' frequency and damping ratio.

To measure the performance improvement, the area under the curve of the speed graph is considered (For with proposed controller, with PSS and without controller). The reduced area under the curve means less oscillation and an improvement. Table 4.3 summarizes the

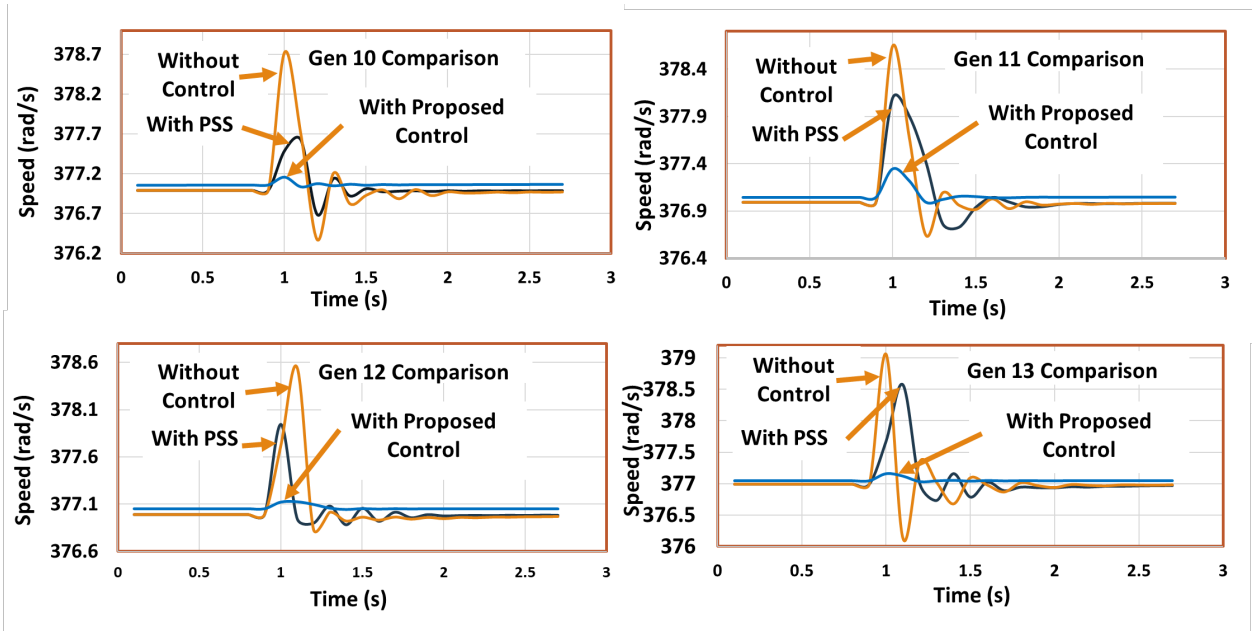

Fig. 4.7: Comparison of generator speed for Case 1.

Table 4.2: Summary of Damping Ratio Improvement for Case 1

List	Without controller	With PSS	With controller
Mode 1 (Hz)	0.154	Unidentified	0.145
Damping Ratio of mode 1 (%)	8.86	NA	13.15
Mode 2 (Hz)	0.1160	0.1116	0.1160
Damping Ratio of mode 2 (%)	3.72	34.71	42.07
Damping Ratio improvement index (σ)	NA	0.500	0.968

results.

4.6.2 Case II

In this case, a symmetrical three-phase fault is applied on bus 62 at $t = 0.9$ seconds. The fault is removed at $t = 1.0$ seconds. The controllers are working similarly as case I. The reduced system order is 18 in this case too. In this case, the fault location is in NETS area the most affected generators due to the fault are generators 2, 3, 4 and 7 (Fig.4.11).

Fig. 4.12 shows comparison of speed of the selected generators with no control, with PSS

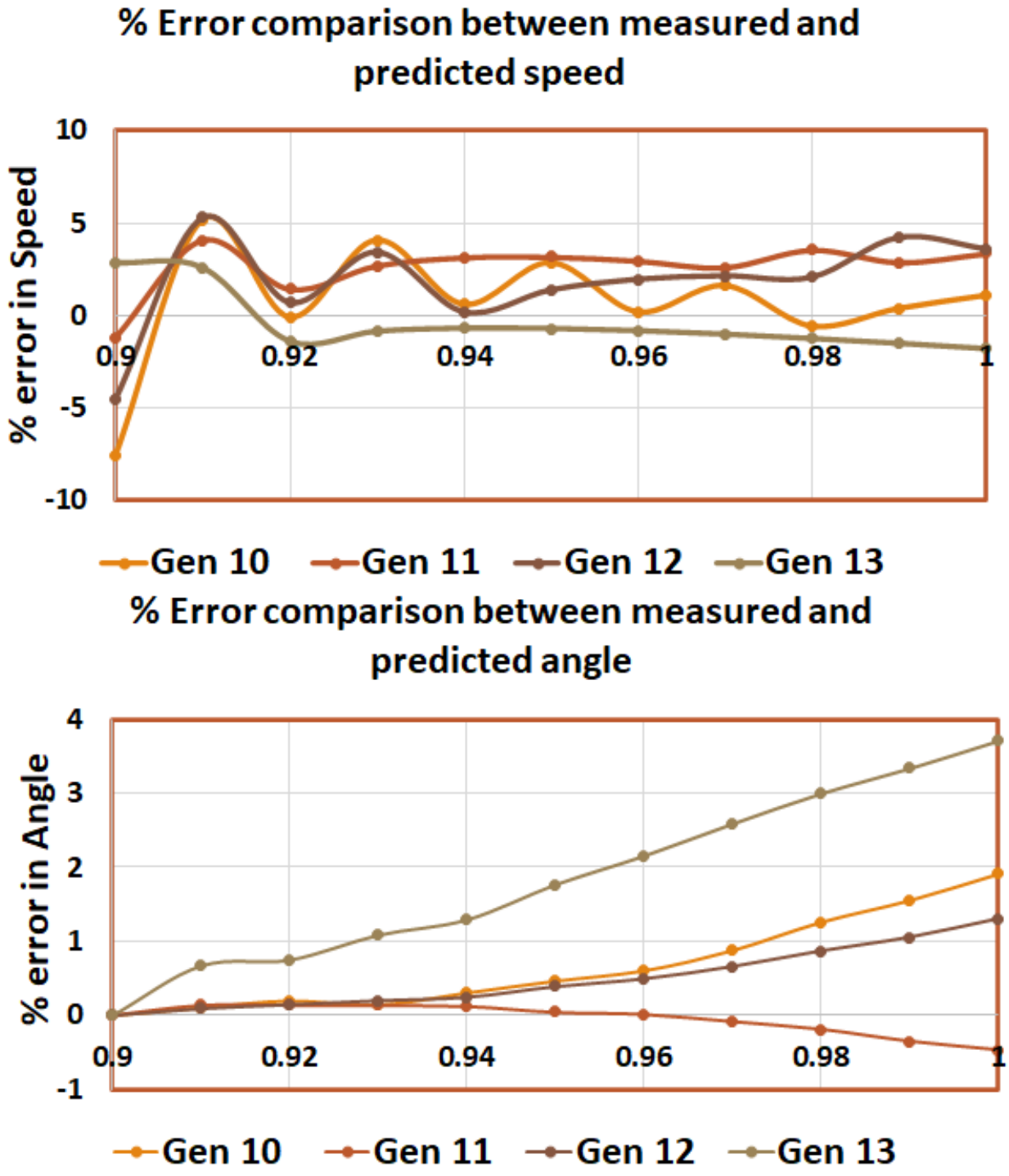

Fig. 4.8: Comparison of % error in speed and angle during the fault.

and with proposed control. Fig. 4.13 shows percentage change in energy function difference of the same generators with the proposed controller as well as the control signal output for the selected generators.

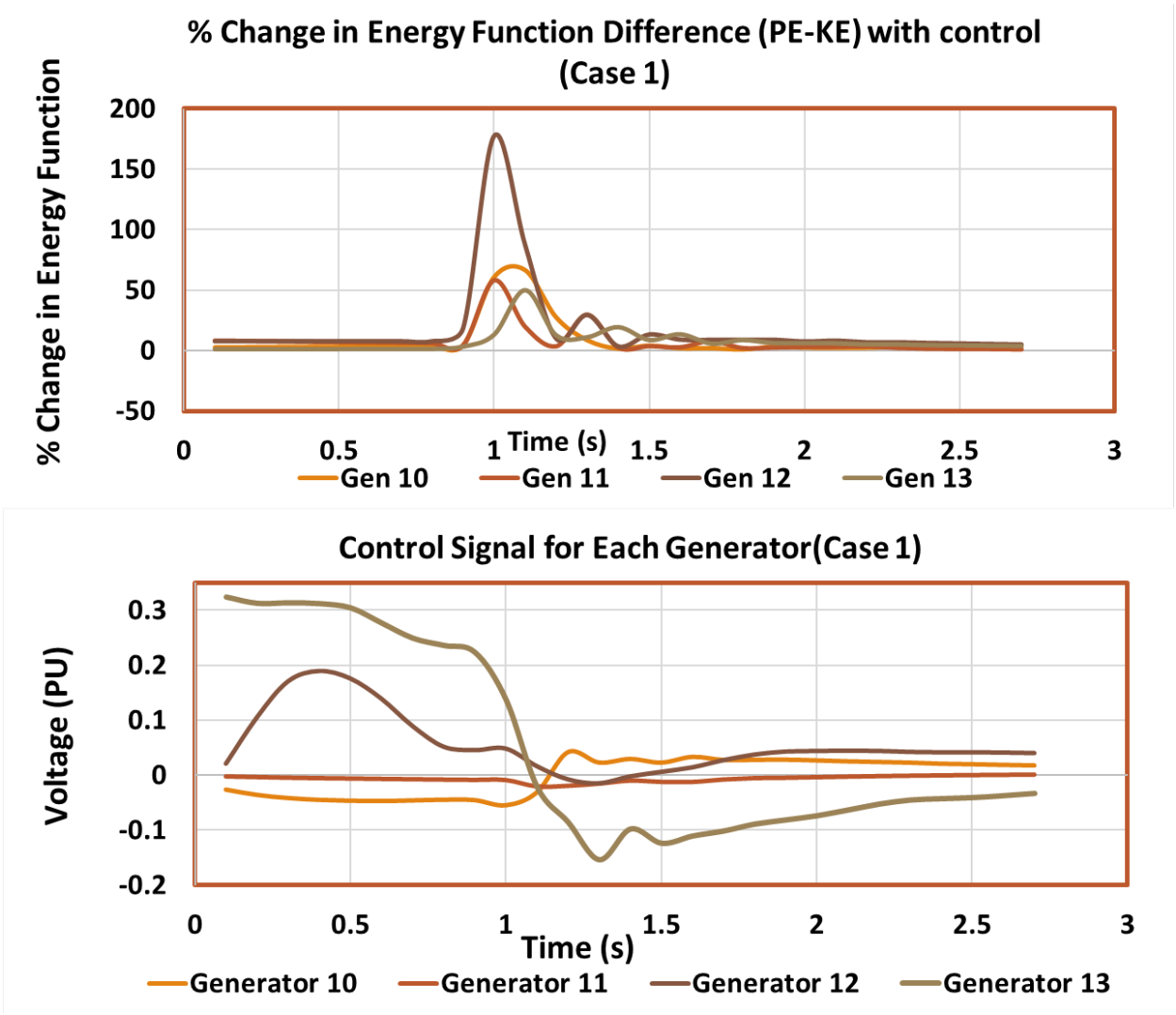

Fig. 4.9: % Change in Energy Function difference with control and control signals for selected generators for Case 1.

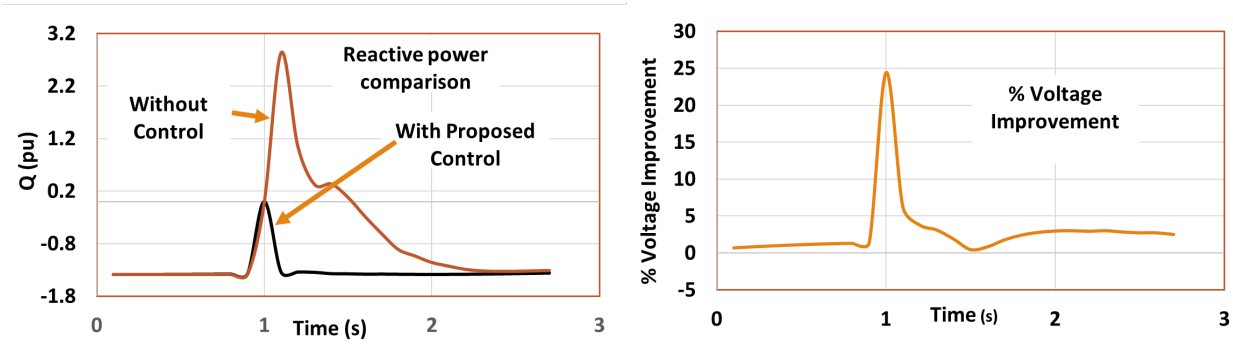

Fig. 4.10: Comparison of Supplied Reactive power and % change in Voltage at the faulted bus for Case 1.

Table 4.3: Summary of Controller Performance for Case 1

Generator	Gen 10	Gen 11	Gen 12	Gen 13
Area under curve (Without Controller)	4.8263	4.32	4.1726	4.7421
Area under curve (With PSS)	2.3036	4.3347	2.0252	4.3743
Area under curve (With proposed Controller)	0.22	0.8704	0.3194	0.3366
% Improvement (PSS)	52.2698	-0.3403	51.4643	7.7561
% Improvement (Controller)	95.4416	79.8518	92.3453	92.9019

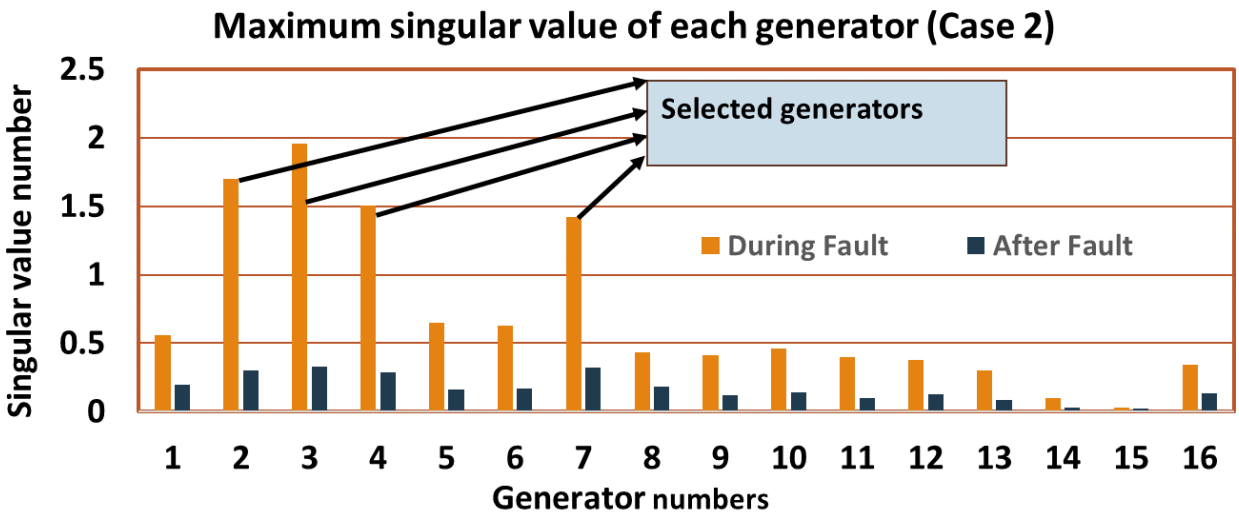

Fig. 4.11: Maximum singular value of each generator during and after fault for Case 2.

In Fig. 4.14, shows comparison of supplied reactive power and change in voltage at the faulted bus after applying the proposed controller is shown. From the eigenvalues obtained from system matrix A, it is evident that by applying the proposed controller, the damping ratio of the dominant modes is improved. Table 4.4 summarizes the dominant modes' frequency and damping ratio.

To measure the performance improvement, the area under the curve of the speed graph is considered. The reduced area under the curve means less oscillation and an improvement. Table 4.5 summarizes the results.

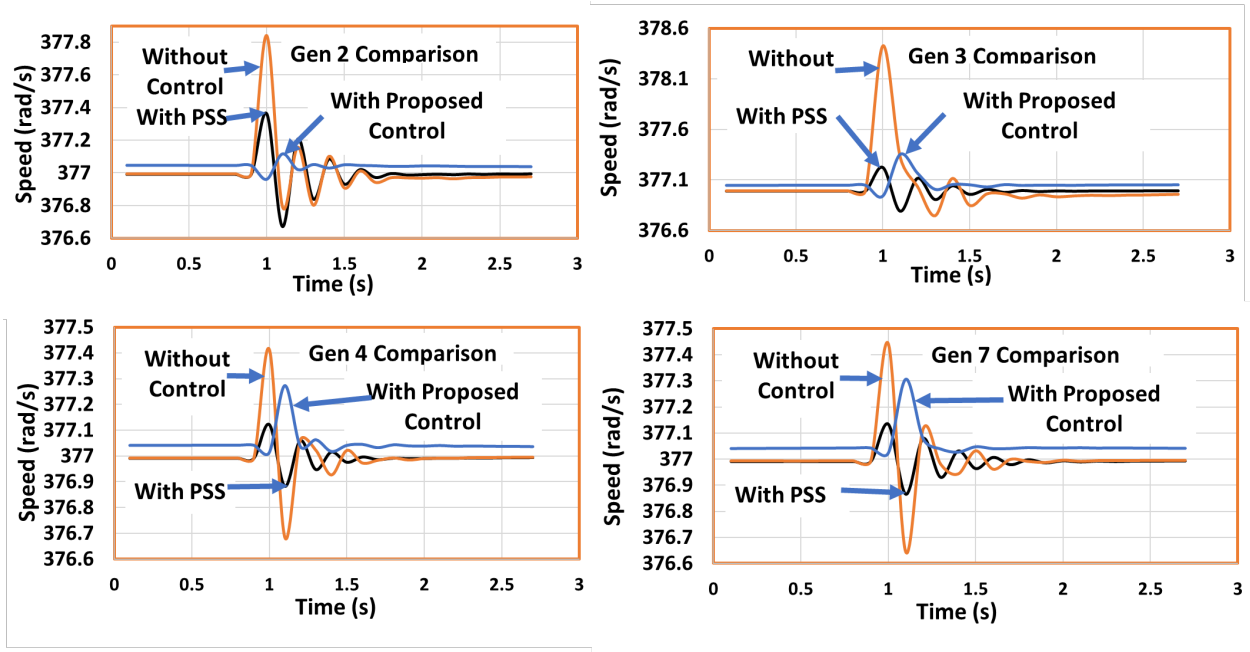

Fig. 4.12: Comparison of generator speed for Case 2.

Table 4.4: Summary of Damping Ratio Improvement for Case 2

List	Without controller	With PSS	With controller
Mode (Hz)	0.114	0.1352	0.15
Damping Ratio (%)	2.31	15.27	16.49
Damping Ratio improvement index (σ)	NA	0.914	1.00

Table 4.5: Summary of Controller Performance for Case 2

Generator	Gen 2	Gen 3	Gen 4	Gen 7
Area under curve (With PSS)	1.3769	0.8307	0.4432	0.5672
Area under curve (With proposed Controller)	0.2379	0.7953	0.4711	0.5440
% Improvement (PSS)	34.6728	75.7778	58.5717	52.2317
% Improvement (Controller)	88.7128	76.8100	55.9637	54.1856

4.6.3 Case III

A step change in load (increase of 150 MW) is created at bus 62 at 0.9 second for this case. Bus 62 is placed next to generator 3 and so generator 3 is much more affected than

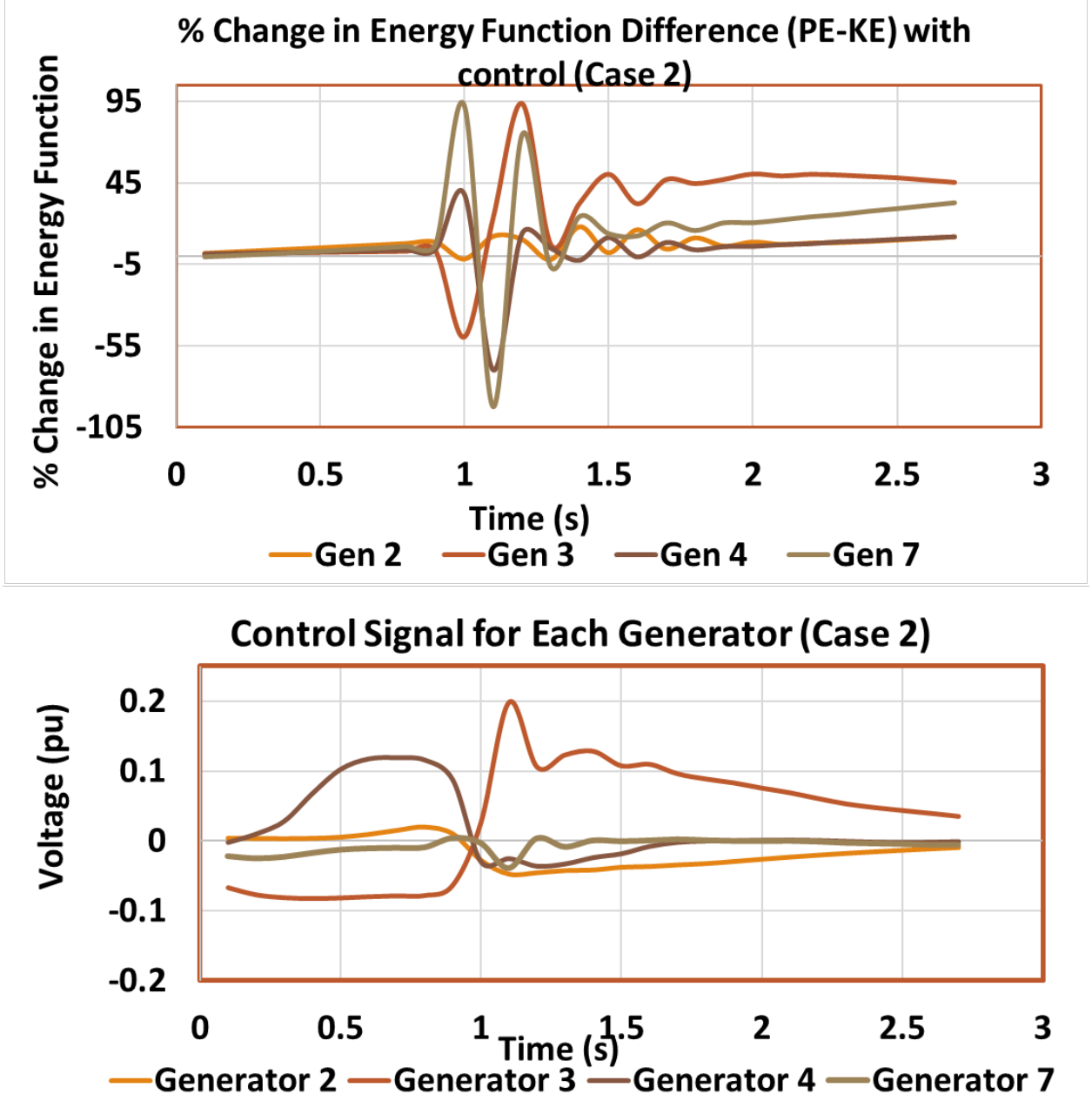

Fig. 4.13: % Change in Energy Function difference with control and control signals for selected generators for Case 2.

other generators for this case. Fig. 4.15 shows comparison of speed of generator 3 with and without control for this case. Fig. 4.16 shows comparison of supplied reactive power and change in voltage at generator 3 while using controller. Table 4.6 shows the dominant modes and damping ratio summary for this case. Table 4.7 shows the improvement by using area

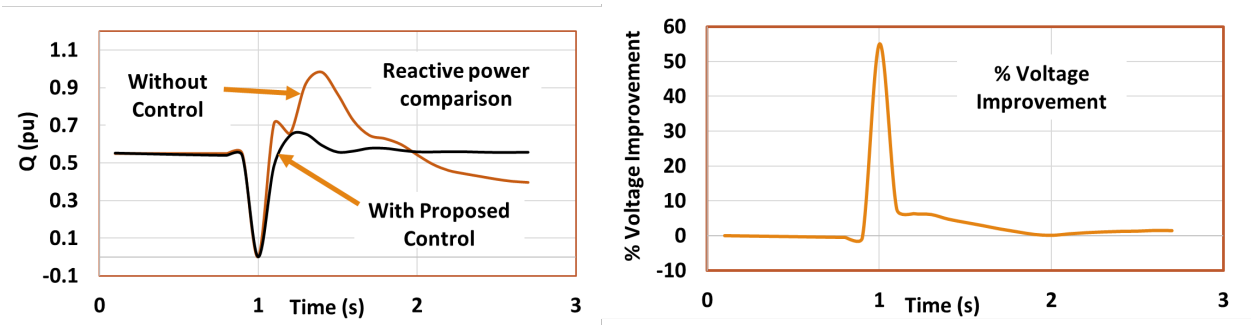

Fig. 4.14: Comparison of supplied reactive power and % change in voltage at the faulted bus for Case 2.

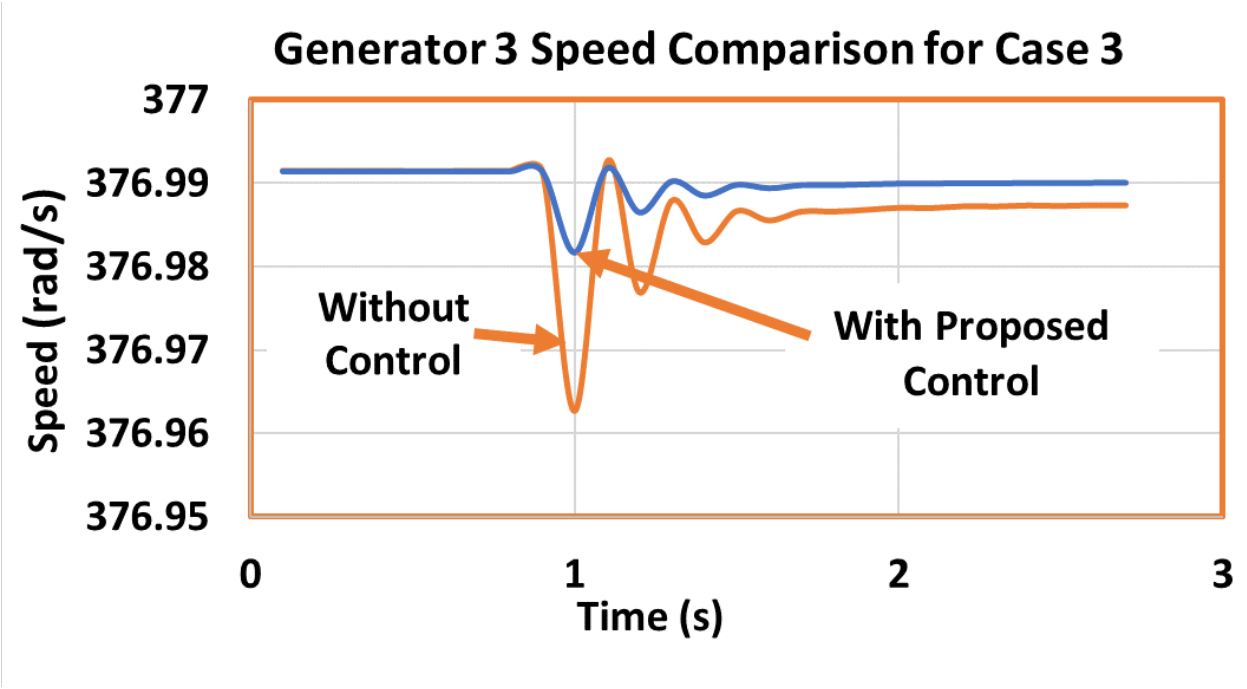

Fig. 4.15: Comparison of speed with and without control for Case 3.

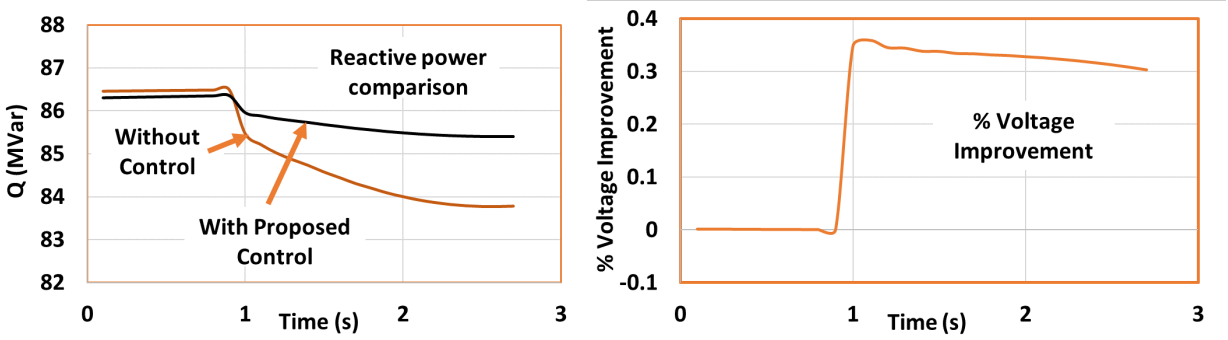

Fig. 4.16: Comparison of reactive power and % change in voltage for Case 3.

under curve while using controller.

4.6.4 Critical Clearing Time Improvement

To maintain transient stability, a power system fault must be cleared quickly enough so that the fault-on transient remains inside the stability boundary. The critical clearing time is the maximum such clearing time, and if the critical clearing time is exceeded, stability is lost by generators losing synchronism. For testing, critical clearing time improvement by our proposed controller for Case 1 and case 2, a three-phase fault of higher duration is applied. For Case 1, a three-phase fault with 41 cycle duration is created at bus 17 at 0.9 seconds. Without control, 41 cycle three-phase fault causes instability at generator 13 whereas, with the proposed controller, the system remains stable. It showcases the stability margin improvement using the proposed controller. Fig. 4.17 shows the comparison of the speed of generator 13 with no controller and with the proposed controller under 41 cycle fault. Generator 13 becomes unstable under 52 cycle three-phase fault applied at the same location while using the proposed controller. Table 4.8 summarize the quantitative improvement in critical clearing time.

Table 4.6: Summary of Damping Ratio Improvement for Case 3

List	Without controller	With controller
Mode (Hz)	0.1141	0.1060
Damping Ratio (%)	40.1057	63.3592

Table 4.7: Summary of Controller Performance for Case 3

Generator	Gen 3
Area under curve (Without Controller)	0.0846
Area under curve (With proposed Controller)	0.0287
% Improvement (Controller)	66.08

For case 2, a three phase fault with 22 cycle duration is created at bus 62 at 0.9 second. Without control, 22 cycle three phase fault causes instability at generator 3 whereas with proposed controller, the system remains stable. Fig. 4.18 shows comparison of the speed of

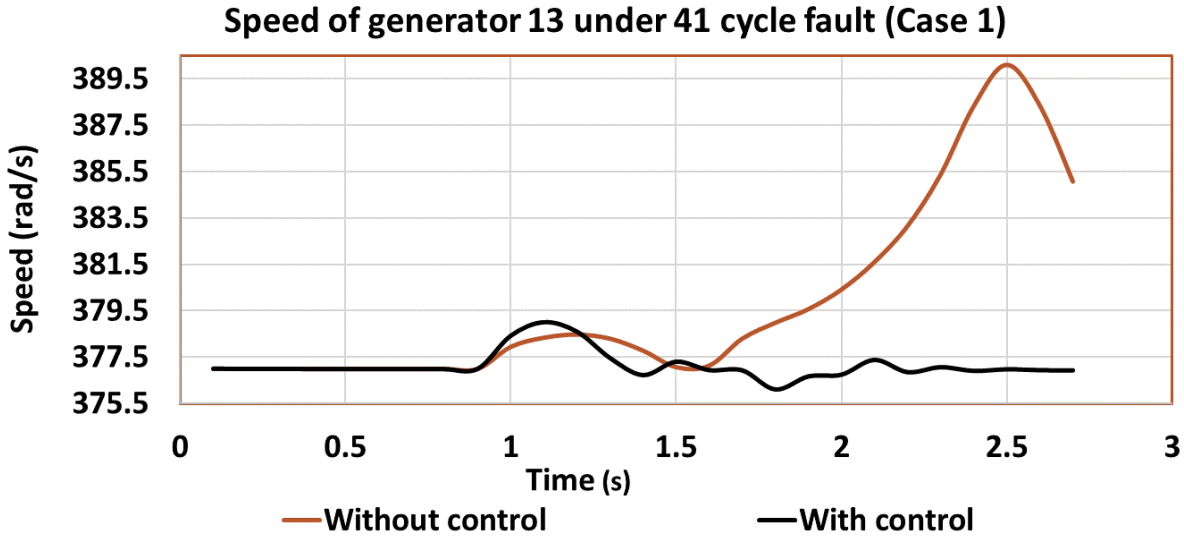

Fig. 4.17: Speed of generator 13 under 41 cycle fault for Case 1.

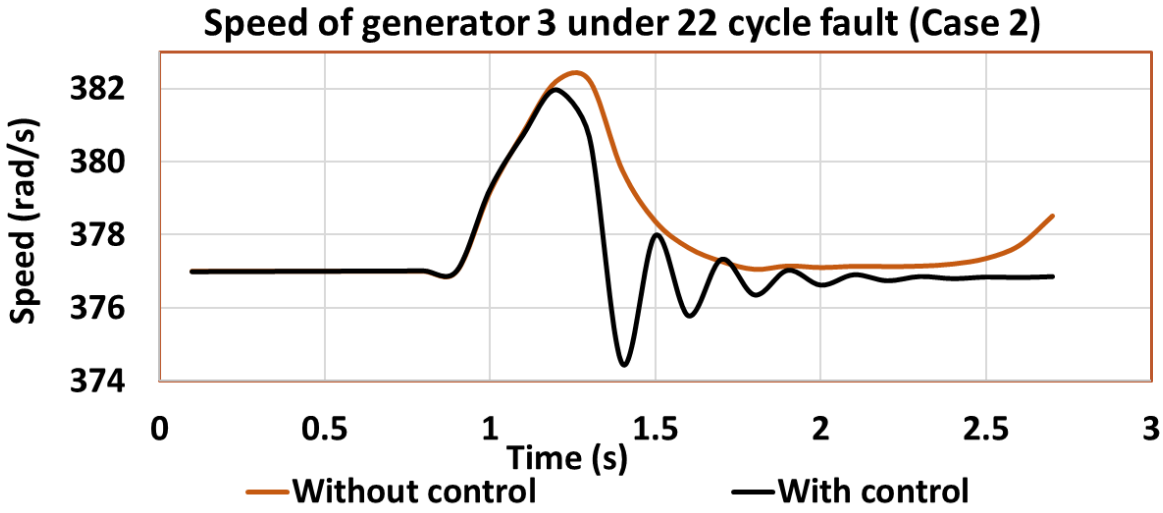

Fig. 4.18: Speed of generator 3 under 22 cycle fault for Case 2.

Table 4.8: Summary of Critical Clearing Time Improvement

List	Case 1		Case 2	
	Without Controller	With Controller	Without Controller	With Controller
Critical Clearing Time (sec)	0.683	0.867	0.367	0.45
% Improvement	NA	26.94	NA	22.615

Table 4.9: Comparisons with state-of-the-art controllers

Damping	Case 1		Case 2	
	With [73] Controller	Proposed Controller	With [74] Controller	Proposed Controller
% Improvement	16.6	26.94	20.6	22.615

generator 3 with no controller and with proposed controller under 22 cycle fault. Generator 3 becomes unstable under 27 cycle three phase fault applied at the same location while using proposed controller. State-of-the-art comparisons with two other papers ([73], [74]) are provided. Although in these two papers, different types of event and controller is applied, critical clearing time improvement is comparable to our proposed method. The quantitative analysis in the Table 4.9 shows the advantage of the proposed architecture.

4.7 Summary

In this chapter, a novel architecture to improve the stability margin and damping ratio of dominant modes by controlling the PE of generators following an event is proposed. The proposed control methodology works in an online environment which is an advantage. The methodology is tested on three different cases which include both transient change and step load change. From the experimental results, it is clear that the stability margin can be improved by the proposed architecture as much as 80%. Also with the proposed architecture critical clearing time is improved by 30%. The proposed control methodology offers the choice to control the most critical generators out of all generators in the power system by using a reduced-order system matrix which helps to improve computational time. The architecture is dynamic, and it can be implemented in real-time. Although, the proposed control method alongside measurement identification method is applied in a real-time environment, the sampling time was highly restricted due to highly computationally extensive algorithm like performing SVD and LQ factorization for every data window. As shown in Chapter 3 of this research work, recursive subspace identification methods can improve required simulation time compared to non-recursive subspace identification method, in the next chapter,

recursive subspace identification method will be applied alongside dynamic control algorithm to make the process more efficient.

Algorithm 3 Dynamic Energy Function Induced Energy Function Base Sub-Space Identification Algorithm

Step: 1 Initialize with N number of steady state data

Step: 2 Collect measurement data from generators at k^{th} time and calculate PE and Pm

Step: 3 Develop extended Hankel matrices U_p, U_p+, U_f, U_f-, Y_p, Y_p+, Y_f, Y_f-, W_p and W_p+ based on N data available at k^{th} time.

Step: 4 Use the oblique projection $O_i = Y_{\mathrm{f}}/_{\mathrm{U_f}} W_{\mathrm{p}}$ and $O_{\mathrm{i\text{-}1}} = Y_{\mathrm{f\text{-}}}/_{\mathrm{U_{f\text{-}}}} W_{\mathrm{p+}}$

Step: 5 Perform SVD of the weighted oblique projection $W_1 O_{\mathrm{i}} W_2 = USV^T$ where W_1 and W_2 are the identity weighting matrices

Step: 6 Select the system order comparing with modeled system and select the dominant generators using SVD

Step: 7 Calculate the output error

while *output error* $<$ *Threshold* **do**
  Partition the SVD into two groups for $\mathrm{U_1}$, $\mathrm{S_1}$ and $\mathrm{U_2}$, $\mathrm{S_2}$ using

$$W_1 O_{\mathrm{i}} W_2 = USV^T = \begin{vmatrix} U_1 & U_2 \end{vmatrix} \begin{vmatrix} S_1 & 0 \\ 0 & S_2 \end{vmatrix} \begin{vmatrix} {V_1}^T \\ {V_2}^T \end{vmatrix}$$

  repeat
    SVD partition
  until *for all n generator group*;
  if *new fault occurs* **then**
    Go to Step: 5
  else
    Go to Step: 6
  Go to Step: 7

Step: 8 Get the extended observability matrix Γ_{i} and $\Gamma_{\mathrm{i\text{-}1}}$ as

$$\Gamma_{\mathrm{i}} = {W_1}^{-1} U_1 {S_1}^{1/2}$$

Step: 9 Determine ${X_{\mathrm{i}}}^d$ and ${X_{\mathrm{i+1}}}^d$ as

$${X_{\mathrm{i}}}^d = \widehat{\Gamma}_{\mathrm{i}} O_{\mathrm{i}}$$

$${X_{\mathrm{i+1}}}^d = \widehat{\Gamma_{\mathrm{i\text{-}1}}} O_{\mathrm{i\text{-}1}}$$

where $\widehat{\Gamma}_{\mathrm{i}}$ is Moore-Penrose pseudo inverse operation of Γ_{i}, i is $\subset N$ and $\Gamma_{\mathrm{i\text{-}1}}$ is first $(i-1)M$ rows of Γ_{i}

Algorithm 4 Dynamic Optimal Control Algorithm

Step: 1 Solve the set of linear equations for A_k, B_k, C_k and D_k in a least square sense

$$\begin{vmatrix} {X_{\mathrm{i+1}}}^d \\ Y_{\mathrm{i|i}} \end{vmatrix} = \begin{vmatrix} \mathrm{A}_k & \mathrm{B}_k \\ \mathrm{C}_k & \mathrm{D}_k \end{vmatrix} \begin{vmatrix} {X_{\mathrm{i}}}^d \\ U_{\mathrm{i|i}} \end{vmatrix}$$

Step: 2 Calculate state matrix X_k from A_k, B_k, C_k and D_k.

Step: 3 Get steady state matrices X^* and U^*. Calculate Z_k as:

$$Z_k = X_k - X^*$$

Step: 4 Set $Q_k = C_k(C_k)^T$ and $R = \rho * I$ and initialize $P_{\mathrm{k\text{-}1}} = Q_k$

Step: 5 Solve P_{k}

$$P_{\mathrm{k}} = Q_k + A_k^T P_{\mathrm{k\text{-}1}} A_k - A_k^T P_{\mathrm{k\text{-}1}} B_k (R + B_k^T P_{\mathrm{k\text{-}1}} B_k)^{-1}$$
$$B_k^T P_{\mathrm{k\text{-}1}} A_k$$

Step: 6 Solve G_k for k^{th} time

$$G_{\mathrm{k}} = -(R + B_k^T P_{\mathrm{k}} B_k)^{-1} B_k^T P_{\mathrm{k}} A_k$$

Step: 7 For k^{th} time ; optimal $v_{\mathrm{k\ CTRL}}$ is given by,

$$v_{\mathrm{k\ CTRL}} = -G_{\mathrm{k}} Z_{\mathrm{k}}$$

Step: 8 Get $\mathrm{U_{k\ CTRL}}$ from the following equation:

$$U_{kCTRL} = U^* + v_{\mathrm{k\ CTRL}}$$

CHAPTER 5: A Novel Hybrid Deterministic-Stochastic Recursive Subspace Identification for Electro Mechanical Mode Estimation, Classification and Control

5.1 Introduction and main contributions

Power system develops various electro-mechanical oscillations during its normal operations [56] which are its inherent properties. However, these oscillations must be damped effectively so that the system can be kept stable. Oscillations that are not damped can not only cause system instability but will in turn lead to power grid blackouts [75]. Preventive action of oscillation detection, classification, and damping is even more important now than before due to the integration of renewable energy resources and other operational constraints of the modern power grid. On the positive side, such actions are possible due to the advent of modern Energy Management Systems (EMS) based on Phasor Measurement Units (PMUs). For the operators to take preventive action even with online measurements such as PMUs, there is a need to develop online grid models that can represent grid models. Further, the models should be able to detect and classify oscillations. Model-based methods that have been discussed in classical stability theory [56] is not suitable for online applications. Additionally, such models cannot capture dynamic changes and changing oscillatory modes during internal and external disturbances. Recently, significant progress has been made in the research field of measurement-based estimation of electro-mechanical modes from PMU data. Recent development and implementation of Phasor Measurement Units (PMUs) enable a provision to design measurement-based identification of the oscillatory modes [76]. The methods used for analysis include Prony, eigenvalue realization, matrix pencil algorithm. The signals used for the analysis consist of ambient signals, ring-down signals, and probing signals. Common methods that use ambient signals are subspace identification, mode-meter, and Yule-Walker algorithms. The main challenge for using these methods is that most of

them deal with offline data sets. Also, it is difficult to represent classical analysis methods such as Singular Value Decomposition (SVD) using online data. Another challenge for real-time computation is the complexity related to computing. For real-time implementation, recursive algorithms are proposed in the literature including time-series [77], least-square, and subspace identification [78], [79]. Such algorithms are computationally faster and can capture changing operating conditions. In particular, subspace identification methods are robust. Authors in [78] proposed an adaptive subspace identification method for identifying electro-mechanical oscillations from ambient signals using covariances. Authors in [79] uses the ringdown signal for identifying oscillation characteristics and proposes a solution to damp it.

Algorithms that can take time-series data and provides output through recursive computation can be suitable for online applications. Time-series methods [77] and forms of subspace identification methods [78], [79] is examples of such architectures. Recently [78] proposed adaptive subspace identifications through stochastic covariance (SSI-COV) representations using ambient signals. Non-recursive method data-driven methods are also popular (SSI-data), especially when identifying oscillation characteristics using ring-down signals [79]. Theoretically, both SSI-Data and SSI-COV should give the same estimate for an infinite amount of data but, due to the availability of limited data in practical applications the estimation from both methods might vary. It has been noted that oscillations in the power grid vary depending on the inputs (such as load changes, faults, external disturbances). The impact of these oscillations is also critically different based on the network topology and the disturbances (such as forced vs natural [80]). Thus, detecting the type of oscillations and classifying them is extremely critical. For example, if natural oscillation has low damping and if the frequencies are close to the force oscillation frequencies, identification and classifications become extremely difficult. Recently, in [81] a method that can estimate both natural (ambient changes or faults) and forced (cyclic load changes) oscillations. However, the method did not discuss mode separation. Mode identification, classification and

mitigation is critical for power grid reliability [82], [83], [8, 26, 84–98].

In [30], we proposed a combined deterministic-stochastic online identification method. In that work, we showed that a recursive architecture can be used to capture power grid oscillation modes either occurring internally or coming from outside. We have also shown that such an architecture can be implemented in real-time. In this chapter, we propose a recursive combined-deterministic stochastic subspace identification (RCDSSI) algorithm that provides oscillation characteristics and classifies input/forced modal information for all types of signals such as, ambient, ring-down, and cycling signals. The approach is based on subspace identification using a recursive algorithm and provides varying model order avoiding QR and Singular Value Decomposition (SVD). In this approach, the power grid measurements are used as both input and output data set to develop measurement-based models of the grid. Then, an approach based on oblique and orthogonal projection is designed recursively to find the system state-space considering grid oscillations. The approach also uses a system observability matrix recursively that avoids the need for SVD. Compared to other work in the literature, the main contribution and novelty of our work is that the architecture can

- Provide oscillation monitoring of the power grid considering internal and external disturbance and classify natural and forced-modes of oscillations.
- The approach is implementable online and can estimate and classify the oscillation modes.
- The proposed approach is computationally robust and adjusts the power grid model order dynamically without being to calculate the SVD.
- Approach also provides an oscillation damping framework and can be implemented in real-grid applications.

Compared to earlier work [30], the novelty and the main contribution of this chapter is as follows

- The proposed method avoids numerically exhaustive steps like QR decomposition or Singular Value Decomposition (SVD) and recursive system identification is performed. In non-recursive identification process, these computationally extensive process happen for every data window and make online application a lot more complex. The proposed algorithm is faster, efficient, and computationally robust and more suitable for online detection and control.

- The architecture provides a dynamic and reduced order of the system A matrix considering the modes of oscillation thus reducing the computational burden. The dynamic and adaptive order selection also helps to identify the oscillation modes effectively.

- The proposed algorithm can identify the forced and natural modes of oscillations even if they occur at the same frequency (in case of resonance). The algorithm can identify mode of interest and calculate their damping ratio at the same time. With the help of the state matrix obtained from the algorithm, an optimal control strategy is also applied to improve damping scenario of the mode of interest.

- It can sequentially identify the most dominant generator for control depending on the dynamic changes in the system and thus can be most optimal at any time.

The chapter is organized as follows. Section 5.2 discussed the preliminaries of sub-space identification and section 5.3 discusses the proposed approach. Section 5.4 discusses the implementation results and section 5.5 concludes the chapter.

5.2 Preliminaries on Subspace Identification

Generally, power systems are nonlinear but with small disturbance, it can be approximated as a dynamically changing linear model. Finding the system matrices from the measured input and output vectors is the problem that is solved by subspace system identification. The subspace identification process can be divided into two sub-categories: Deterministic subspace identification and Stochastic subspace identification. In the deterministic subspace

identification method, both input and output vectors are known and available and the noise vectors are zero. In the stochastic subspace identification method, only output vectors are known from measurements and the system matrices are estimated from only output vectors.

5.2.1 Deterministic and Stochastic Subspace Identification

The approach of deterministic subspace identification is as follows. First, the data is collected from the measurement both for output $(y_0, y_1, ..., y_{\mathrm{M}})$ and input $(u_0, u_1, ..., u_{\mathrm{M}})$ vectors where, $y_{\mathrm{k}} \in R^{M\times 1}, u_{\mathrm{k}} \in R^{M\times 1}$ for $k = 0, 1, 2, ..., M$.

$$Y_{\mathrm{p}} = \begin{vmatrix} y_0 & y_1 & . & . & y_{\mathrm{j\text{-}1}} \\ . & . & . & . & . \\ . & . & . & . & . \\ . & . & . & . & . \\ y_{\mathrm{i\text{-}1}} & y_{\mathrm{i}} & . & . & y_{\mathrm{i+j\text{-}2}} \end{vmatrix} \quad Y_{\mathrm{f}} = \begin{vmatrix} y_{\mathrm{i}} & y_{\mathrm{i+1}} & . & . & y_{\mathrm{i+j\text{-}1}} \\ y_{\mathrm{i+1}} & y_{\mathrm{i+2}} & . & . & y_{\mathrm{i+j}} \\ . & . & . & . & . \\ . & . & . & . & . \\ y_{\mathrm{2i\text{-}1}} & y_{\mathrm{2i}} & . & . & y_{\mathrm{2i+j\text{-}2}} \end{vmatrix} \tag{5.1}$$

$$U_{\mathrm{p}} = \begin{vmatrix} u_0 & u_1 & . & . & u_{\mathrm{j\text{-}1}} \\ . & . & . & . & . \\ . & . & . & . & . \\ . & . & . & . & . \\ u_{\mathrm{i\text{-}1}} & u_{\mathrm{i}} & . & . & u_{\mathrm{i+j\text{-}2}} \end{vmatrix} \quad U_{\mathrm{f}} = \begin{vmatrix} u_{\mathrm{i}} & u_{\mathrm{i+1}} & . & . & u_{\mathrm{i+j\text{-}1}} \\ u_{\mathrm{i+1}} & u_{\mathrm{i+2}} & . & . & u_{\mathrm{i+j}} \\ . & . & . & . & . \\ . & . & . & . & . \\ u_{\mathrm{2i\text{-}1}} & u_{\mathrm{2i}} & . & . & u_{\mathrm{2i+j\text{-}2}} \end{vmatrix} \tag{5.2}$$

$$Y_{\mathrm{p+}} = \begin{vmatrix} y_0 & y_1 & . & . & y_{\mathrm{j\text{-}1}} \\ . & . & . & . & . \\ . & . & . & . & . \\ y_{\mathrm{i\text{-}1}} & y_{\mathrm{i}} & . & . & y_{\mathrm{i+j\text{-}2}} \\ y_{\mathrm{i}} & y_{\mathrm{i+1}} & . & . & y_{\mathrm{i+j\text{-}1}} \end{vmatrix} \quad Y_{\mathrm{f\text{-}}} = \begin{vmatrix} y_{\mathrm{i+1}} & y_{\mathrm{i+2}} & . & . & y_{\mathrm{i+j}} \\ . & . & . & . & . \\ . & . & . & . & . \\ . & . & . & . & . \\ y_{\mathrm{2i\text{-}1}} & y_{\mathrm{2i}} & . & . & y_{\mathrm{2i+j\text{-}2}} \end{vmatrix} \tag{5.3}$$

$$U_{\mathrm{p+}} = \begin{vmatrix} u_0 & u_1 & . & . & u_{\mathrm{j\text{-}1}} \\ . & . & . & . & . \\ . & . & . & . & . \\ u_{\mathrm{i\text{-}1}} & u_{\mathrm{i}} & . & . & u_{\mathrm{i+j\text{-}2}} \\ u_{\mathrm{i}} & u_{\mathrm{i+1}} & . & . & u_{\mathrm{i+j\text{-}1}} \end{vmatrix} \quad U_{\mathrm{f\text{-}}} = \begin{vmatrix} u_{\mathrm{i+1}} & u_{\mathrm{i+2}} & . & . & u_{\mathrm{i+j}} \\ . & . & . & . & . \\ . & . & . & . & . \\ u_{\mathrm{2i\text{-}1}} & u_{\mathrm{2i}} & . & . & u_{\mathrm{2i+j\text{-}2}} \end{vmatrix} \tag{5.4}$$

Then an extended block Hankel Matrices j is determined by $j = M - 2i + 2$, where i is a pre-selected integer greater than order of the system 'N'. $Y_{\mathrm{p}}, Y_{\mathrm{p+}}, Y_{\mathrm{f}}, Y_{\mathrm{f\text{-}}}, U_{\mathrm{p}}, U_{\mathrm{p+}}, U_{\mathrm{f}}, U_{\mathrm{f\text{-}}}$ from the input and output vectors as follows. The subscript p stands for *past* and the subscript f for $future$. The matrices Y_p and Y_f are past and future output matrices respectively. The matrices Y_p^+ and Y_f^- on the other hand are defined by shifting the border between past and future one block row down. Similarly, U_p, U_f, U_p^+ and U_f^- matrix are constructed from input vectors. Then organizing the matrices as

$$W_{\mathrm{p}} = \begin{vmatrix} U_{\mathrm{p}} \\ Y_{\mathrm{p}} \end{vmatrix}, W_{p^+} = \begin{vmatrix} U_{p^+} \\ Y_{p^+} \end{vmatrix} \tag{5.5}$$

we can use the oblique projection as

$$O_{\mathrm{i}} = Y_{\mathrm{f}} /_{\mathrm{U_f}} W_{\mathrm{p}}, O_{\mathrm{i\text{-}1}} = Y_{f^-} /_{\mathrm{U}_{f^-}} W_{p^+} \tag{5.6}$$

From the SVD, then, the n number of significant singular values which is the selected order of the reduced system can be found. After determining the order, by partitioning the SVD accordingly we can obtain obtain U_1, S_1 and V_1 as

$$W_1 O_{\mathrm{i}} W_2 = USV^T = \begin{vmatrix} U_1 & U_2 \end{vmatrix} \begin{vmatrix} S_1 & 0 \\ 0 & S_2 \end{vmatrix} \begin{vmatrix} {V_1}^T \\ {V_2}^T \end{vmatrix} \tag{5.7}$$

where U_1, S_1 and V_1 is the reduced U, S and V matrices in accordance with reduced order n and W_1 and W_2 is the identity weighting matrices. U and V are complex unitary matrix and S is rectangular diagonal matrix which contains singular values. Further, we can prepare an extended observability matrix Γ_{i} and $\Gamma_{\mathrm{i\text{-}1}}$ as

$$\Gamma_{\mathrm{i}} = {W_1}^{-1} U_1 {S_1}^{1/2} \tag{5.8}$$

where $\Gamma_{\text{i-1}}$= first $(i-1)M$ rows of Γ_{i}. The determined states of the system ${X_{\text{i}}}^d$ and ${X_{\text{i+1}}}^d$ can then be found as

$$ {X_{\text{i}}}^d = \widehat{\Gamma}_{\text{i}} O_{\text{i}}, {X_{\text{i+1}}}^d = \widehat{\Gamma_{\text{i-1}}} O_{\text{i-1}} \tag{5.9} $$

where $\widehat{\Gamma}_{\text{i}}$ is Moore-Penrose pseudo inverse operation of Γ_{i} From which, A, B, C and D can be determined as

$$ \begin{vmatrix} {X_{\text{i+1}}}^d \\ Y_{\text{i|i}} \end{vmatrix} = \begin{vmatrix} A & B \\ C & D \end{vmatrix} \begin{vmatrix} {X_{\text{i}}}^d \\ U_{\text{i|i}} \end{vmatrix} \tag{5.10} $$

In the stochastic subspace identification, only the outputs are used such that

$$ O_{\text{i}} = Y_{\text{f}}/Y_{\text{p}}, O_{\text{i-1}} = Y_{f^-}/Y_{p^+} \tag{5.11} $$

Then using (7) we can get determine X_{i} and $X_{\text{i+1}}$ as

$$ X_{\text{i}} = \widehat{\Gamma}_{\text{i}} O_{\text{i}}, X_{\text{i+1}} = \widehat{\Gamma_{\text{i-1}}} O_{\text{i-1}} \tag{5.12} $$

From which A and C in a least square sense as

$$ \begin{vmatrix} A \\ C \end{vmatrix} = \begin{vmatrix} X_{\text{i+1}} \\ Y_{\text{i|i}} \end{vmatrix} \widehat{X_{\text{i}}} \tag{5.13} $$

5.3 Proposed Methodology

The objective is to identify the power system model as

$$ x_{\text{k+1}} = Ax_{\text{k}} + Bu_{\text{k}} + w_{\text{k}} \tag{5.14} $$

$$ y_{\text{k}} = Cx_{\text{k}} + Du_{\text{k}} + v_{\text{k}} \tag{5.15} $$

where x_k is the state vector, u_k is the input vector (measured and available), y_k is the output vector (measured and available), w_k and v_k are unknown disturbances, A is the state matrix, B is the input matrix, C is the output Matrix, D is the feedthrough matrix. To accomplish this through measurements, first, from the measurements, Hankel matrices are formed as shown in (1)-(4). In order to capture appropriate dynamics, the data selection window design is critical. The optimal selection of data window depends on the oscillation modes of interest. The window length can be calculated knowing the oscillation period (see Fig. 5.1). It has been proven that a minimum window length of $2i$ is good to capture system dynamics effectively especially for the low frequency oscillations. Using subspace identification technique, the extended observability matrix Γ_i is calculated based on projection algorithms as

$$\underset{\mathbb{R}^{i\times j}}{H_{1:j}} = \begin{bmatrix} Y_p \\ Y_f \end{bmatrix} = \begin{bmatrix} L_{11} & 0 \\ L_{21} & L_{22} \end{bmatrix} \tag{5.16}$$

$$Y_f/Y_p = L_{21}Q_{11}^T; L_{21}Q_{11}^T = \Gamma_i X_i \tag{5.17}$$

where $H_{1:j}$ is the Hankel matrix with first j data, L_{ij} is the lower triangular matrix of LQ decomposition and Q_{ij} represents the orthogonal matrix.

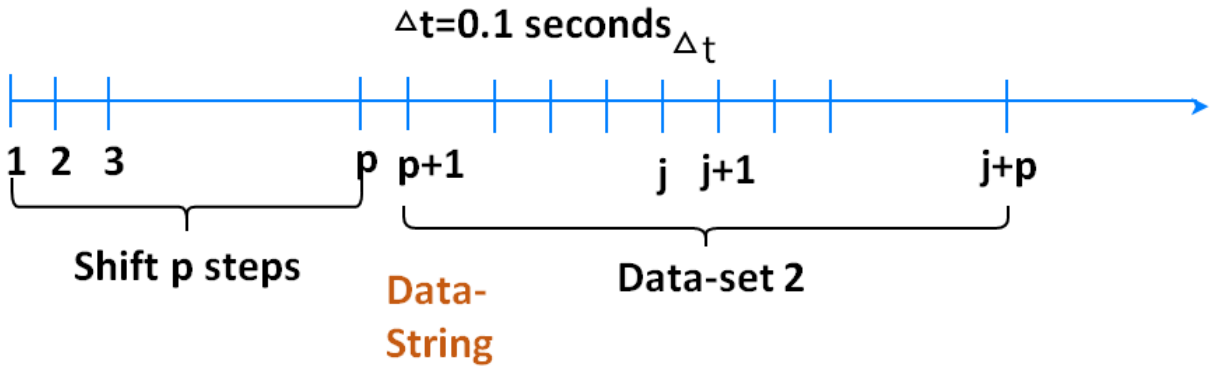

Fig. 5.1: Data time stamp for recursive algorithm.

Eqn. (5.16) shows that the extended observability matrix Γ_i can be calculated from the

column space of $\mathbf{L_{21}}$. In case of deterministic subspace identification,

$$E_{\mathrm{p}} = \begin{vmatrix} U_{\mathrm{p}} \\ Y_{\mathrm{p}} \end{vmatrix}, H_{1:j} = \begin{vmatrix} U_{\mathrm{f}} \\ E_{\mathrm{p}} \\ Y_{\mathrm{f}} \end{vmatrix} \tag{5.18}$$

$$\mathbf{H_{1:j}} = \begin{bmatrix} U_f \\ E_p \\ Y_f \end{bmatrix} = \begin{bmatrix} L_{11} & 0 & 0 \\ L_{21} & L_{22} & 0 \\ L_{31} & L_{32} & L_{33} \end{bmatrix} \begin{bmatrix} Q_{11}^T \\ Q_{21}^T \\ Q_{31}^T \end{bmatrix} \tag{5.19}$$

$$(Y_f/U_f) * E_p = \Gamma_i X_i/U_f^{|} = L_{32} Q_{21}^T \tag{5.20}$$

where E_p represents the subspace of past input and output in block Hankel matrices U_p and Y_p. Eqn. (5.20) calculates the oblique projection of the future outputs on the past input/output along the future inputs. Column space of L_{32} is equal to the column space of extended observability matrix Γ_i. So only extracting L_{32} from the LQ decomposition of the whole subspace is enough to get the system characteristics. The projected matrix O will then be,

$$O = \begin{cases} L_{21}, \text{if only output measurements are used} \\ L_{32}, \text{if both input and output are used} \end{cases} \tag{5.21}$$

From (5.21), only L_{32} is needed for proper system identification when both input and output measurements are used. From here, conventionally, one can calculate the SVD on L_{32} and select the reduced order n from the singular values as,

$$L_{32} = \begin{bmatrix} U_1 & U_2 \end{bmatrix} \begin{bmatrix} S_1 & 0 \\ 0 & S_2 \end{bmatrix} \begin{bmatrix} V_1^T \\ V_2^T \end{bmatrix} \approx U_1 S_1 V_1^T \tag{5.22}$$

where $U_1 = \Gamma_i$. Since Γ_i is defined as $\Gamma_i = \langle \text{C} \;\; \text{CA} \;\; CA^2 \;\; ... \;\; CA^{i-1} \rangle^T$ which contains the system matrix information, and A can be calculated by $A = \Gamma_i^* \Gamma_i$.Further, Eigenvalues can be calculated from A matrix. From eigenvalues, the modes and their damping ratio can be calculated.

5.3.1 Proposed Recursive Algorithm

The proposed recursive algorithm has two steps. In the first step the LQ factorization is calculated recursively. In the second step, the extended observability matrix is calculated to avoid computationally challenging SVD at each iteration.

5.3.1.1 Updating LQ factorization recursively

From the Hankel matrix in (19) and (20), we can get

$$H_{1:j} = L_1 Q_1, G_1 Q_1 = \begin{bmatrix} \varepsilon & \sigma \\ 0 & \bar{Q_1} \end{bmatrix} \tag{5.23}$$

where $(G_1 Q_1)^T (G_1 Q_1) = I$

It can be proved that, $\varepsilon^T \varepsilon = I_p$ and $\sigma = 0$. So, $G_1 Q_1 = \begin{bmatrix} I_p & 0 \\ 0 & \bar{Q_1} \end{bmatrix}$ and $H_{1:j} = [H_{1:p} \quad \bar{L_1}] \begin{bmatrix} I_p & 0 \\ 0 & \bar{Q_1} \end{bmatrix}$.

This brings

$[H_{j+1:j+p} \quad \bar{L_1}] \begin{bmatrix} 0 & I_p \\ \bar{Q_1} & 0 \end{bmatrix} = L_2 Q_2$ where G_1 and G_2 are the givens rotation matrix.

5.3.1.2 Updating the extended observability matrix recursively to avoid performing SVD

Once the LQ decomposition is updated recursively then the next step is to update the extended observability matrix Λ_i recursively without using SVD. This is performed using the propagator method [55]. The propagator can be determined recursively by solving a least square error minimization approach. The process is as follows. First, the system A matrix and Λ_i is developed for given data. Then an identity matrix I_n is calculated, where n is the order of the system. Further a matrix is defined as $P_f^T = I_n$ and $L_f = I_n$. This can be

represented as

$$\Gamma_f = \begin{bmatrix} I_n & P_f^T \end{bmatrix} \tag{5.24}$$

where R_x = covariance of A matrix with $R_{zf} = \Gamma_f \times R_x \times \Gamma_f^T, R_{zf1} = R_{zf}(1:n, 1:n), R_{zf2} = R_{zf}(n+1:2n, n+1:2n)$, λ = forgetting factor, and ζ = Instrument variable. After initialization we get,

$$\begin{aligned} H_{1:j} &= \begin{bmatrix} U_f & U_{f,p} \\ E_p & E_{f,p} \\ Y_f & Y_{f,p} \end{bmatrix} \\ &= \begin{bmatrix} L_{11} & 0 & 0 & U_{f,p} \\ L_{21} & L_{22} & 0 & E_{f,p} \\ L_{31} & L_{32} & L_{33} & Y_{f,p} \end{bmatrix} \begin{bmatrix} Q_{11}^T & 0 \\ Q_{21}^T & 0 \\ Q_{31}^T & 0 \\ 0 & 1 \end{bmatrix} \end{aligned} \tag{5.25}$$

Applying Given's rotation twice we get

$$\begin{bmatrix} L_{11} & 0 & 0 & 0 \\ L_{21} & L_{22} & 0 & \bar{z_p} \\ L_{31} & L_{32} & L_{33} & \bar{z_f} \end{bmatrix} = \begin{bmatrix} L_{11} & 0 & 0 & 0 \\ L_{21} & L_{22} & 0 & 0 \\ L_{31} & L_{32} & L_{33} & \bar{\bar{z}}_f \end{bmatrix} \tag{5.26}$$

where $\bar{\bar{z}}_f = \begin{vmatrix} z_{\mathrm{f1}} \\ z_{\mathrm{f2}} \end{vmatrix}, g_f = \begin{vmatrix} R_{zf2}\zeta & z_{f2} \end{vmatrix}, \Lambda = \begin{vmatrix} -\zeta^T\zeta & \lambda \\ \lambda & 0 \end{vmatrix}$

$$\psi = \begin{vmatrix} R_{zf1}\zeta & z_{f1} \end{vmatrix}; k = (\Lambda + \psi^T L_f \psi)^{-1} \psi^T L_f \tag{5.27}$$

$$P_f^T = P_f^T + (g_f - P_f^T\psi)k; R_{zf1} = \lambda R_{zf1} + Z_{f1}\zeta \tag{5.28}$$

$$R_{zf2} = \lambda R_{zf2} + Z_{f2}\zeta; L_f = \frac{1}{\lambda^2}(L_f - L_f\psi k) \tag{5.29}$$

where P_f is a linear operator called propagator which expresses the linear dependant vectors of extended observability matrix Λ_i which is the same as earlier mentioned Γ_i as a linear combination of n independent vectors, $Z_f(t)$ is the observation vector, k is the gain vector, $R_{z_{f1}}$ is the expected value of observation vector. ζ is the damping ratio and λ is the forgetting factor.

The proposed RCDSSI framework can estimate the behavior of the power system in the presence of input excitation and noise. This helps to estimate system electro-mechanical modes accurately even in the presence of forced oscillations at the same time can also classify oscillations between forced and natural electro-mechanical modes.

5.3.1.3 Updating Model Order

One of the main features of the proposed algorithm is its ability to change the model order based on the modes of oscillation. The approach is as follows. First, from the initial data set, the initial order is chosen as the reduced order of the system that can represent the original system without losing much accuracy. For the order update, the norm of modes of interest is used. If the number of the mode of interest increases (calculated based on the proposed identification), and the norm (here mode of interest is between 0 to 1 Hz) increases by a threshold value from the previous condition, the order of the system is decreased by 2. Else, if the norm decreases from before more than the threshold value, a higher number of system orders is necessary to capture the mode, and hence the order is increased by 2.

5.3.2 Dynamic Optimal Damping Control Design

The damping controller is designed based on optimal control theory with the quadratic cost function defined as

$$J = \sum_{k=1}^{M-1} ({X_{\mathrm{k}}}^T Q X_{\mathrm{k}} + {u_{\mathrm{k\ CTRL}}}^T R u_{\mathrm{k\ CTRL}}) + ({X_{\mathrm{M}}}^T Q X_{\mathrm{M}}) \tag{5.30}$$

where X_k is state matrix which is calculated from A, B, C and D matrix obtained from subspace identification. Q ad R are given state cost and input cost matrices. To minimize

Algorithm 5 Dynamic Optimal Control Algorithm

1: Solve the set of linear equations for A_k, B_k, C_k and D_k in a least square sense. The A_k matrix is similar to A_s matrix mentioned previously.

$$\begin{vmatrix} {X_{\mathrm{i+1}}}^d \\ Y_{\mathrm{i|i}} \end{vmatrix} = \begin{vmatrix} \mathrm{A}_k & \mathrm{B}_k \\ \mathrm{C}_k & \mathrm{D}_k \end{vmatrix} \begin{vmatrix} {X_{\mathrm{i}}}^d \\ U_{\mathrm{i|i}} \end{vmatrix}$$

2: Calculate state matrix X_k from A_k, B_k, C_k and D_k.
3: From A_k matrix, find the dominant mode and damping ratio of each generator.
4: Using the threshold (Below 5%) of damping ratio, find out the most affected generators.
5: Set $Q_k = C_k(C_k)^T$ and $R = \rho * I$ and initialize $P_{\mathrm{k\text{-}1}} = Q_k$
6: Solve P_{k}

$$P_{\mathrm{k}} = Q_k + A_k^T P_{\mathrm{k\text{-}1}} A_k - A_k^T P_{\mathrm{k\text{-}1}} B_k (R + B_k^T P_{\mathrm{k\text{-}1}} B_k)^{-1}$$
$$B_k^T P_{\mathrm{k\text{-}1}} A_k$$

7: Solve G_k for k^{th} time

$$G_{\mathrm{k}} = M * (-(R + B_k^T P_{\mathrm{k}} B_k)^{-1} B_k^T P_{\mathrm{k}} A_k)$$

where, M represents damping ratio
8: For k^{th} time ; optimal $u_{\mathrm{k\ CTRL}}$ is given by,

$$u_{\mathrm{k\ CTRL}} = -G_{\mathrm{k}} X_{\mathrm{k}}$$

J, $u_{\mathrm{k\ CTRL}}$ is solved as shown in algorithm 1. Here, $u_{\mathrm{k\ CTRL}}$ is the excitation voltage of the generator. Fig. 5.2 represents the overall flow diagram.

5.3.3 Mapping with system states

For control, the identified and physical states need to be mapped. This is performed as follows. Consider, the system model is available for the actual power grid. The dynamic model that we consider is a Differential Algebraic Equation (DAE) representation with generator dynamics included as,

$$\Delta X_{t+1} = A_g \Delta X_t + B_g \Delta u_t \tag{5.31}$$

where X represent the power grid states including generator internal voltage, current, terminal voltage, speed, angle and the system power flows. Considering multiple generators in the system, the overall system state-space can be represented along with the algebraic model $\bar{A}_s = diag(A_{g1}, A_{g2}, ...)$. Similarly, $\bar{B}_s = diag(A_{g1}, A_{g2}, ...)$, $\bar{C}_s = diag(A_{g1}, A_{g2}, ...)$,

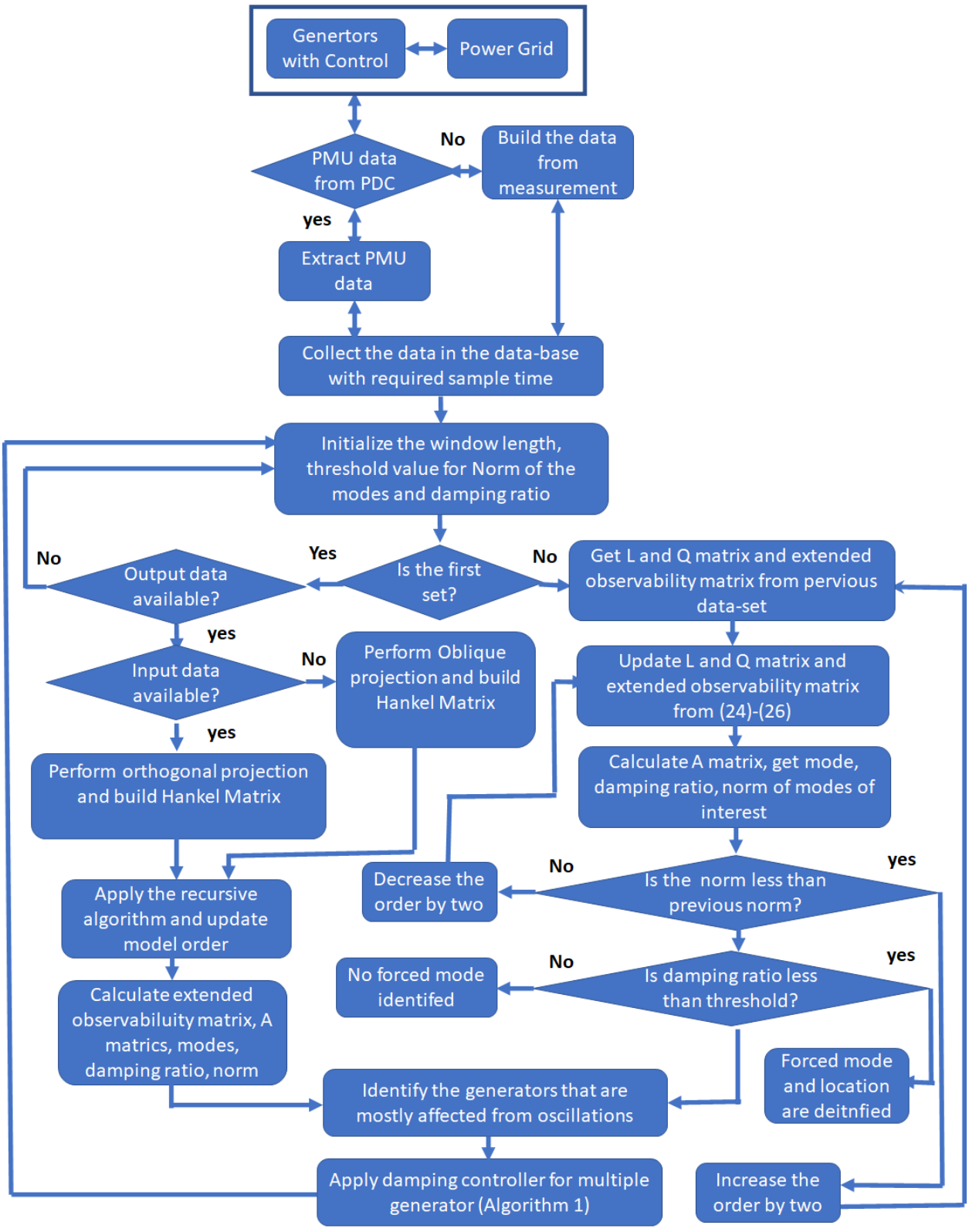

Fig. 5.2: Overall flowchart of the proposed architecture.

$\bar{D_s} = diag(A_{g1}, A_{g2}, ...)$. Let us mention this as

$$\Delta x_{t+1} = A_s \Delta x_t + B_s \Delta u_t \tag{5.32}$$

where $A_s = \bar{A_g} - \bar{B_G} \bar{D_g}^{-1} \bar{C_g}$. Then a similarity transformation matrix T_m can be developed to convert the identified model to the actual system state-space representation as

$$A_T = T_m * A_k * T_m^{-1} \tag{5.33}$$

Further equations regarding state space matrix and states of a power system with exciters can be found in Appendix A.

5.4 Experimental Results and Discussion

Fig. 5.3 shows the experimental setup. The complete model is built in Real-Time Digital Simulators (RTDS). PMU measurements are integrated both with software and hardware PMUs. A workstation is dedicated as Phasor Data Concentrator (PDC). The proposed architecture is implemented in MATLAB in another computer-integrated to PDC. The hardware and the RTDS along with the algorithm are integrated with Ethernet socket connection through RTDS/GTNET socket. First, the input and output vectors are collected from PMUs through PDC. Then these data are being used to produce the final controller output through our proposed algorithm in MATLAB. These controller outputs are then being sent to the selected generators through RTDS/GTNET socket to RTDS.

Cases on two real-life systems modeled in RTDS are presented in this chapter. The first one is a two-area power grid [56]. This is a widely used system to study inter-area oscillation. The second system is IEEE 68 bus test system which represents the NETS-NYPS system model. This system is used to show the scalability of the proposed algorithm to perform well on large systems. A control architecture is also applied to the IEEE 68 bus system using the proposed identification technique.

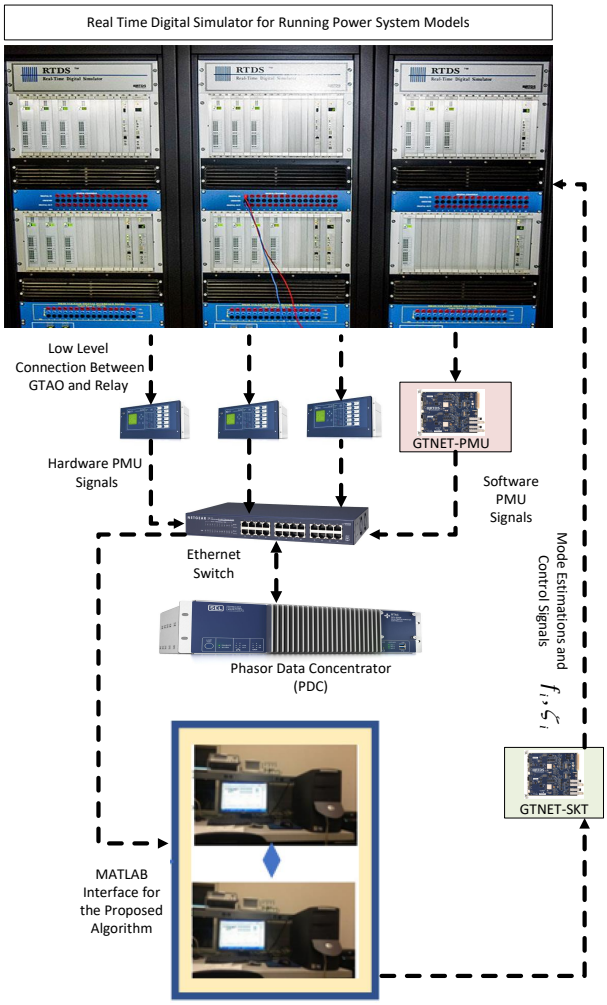

Fig. 5.3: Experimental implementation set-up.

5.4.1 Case I: Two Area Test System

The two area power grid is shown in Fig. 5.4. The characteristics of two area system is mentioned in Table 5.1. The details are in [56].

Table 5.1: Kundur 2 area test system features.

Buses & Generators	9 Buses 4 Generators	Areas	2
Total Active Power Generation (MW)	2819.00	Total Active Load (MW)	2743.00
Total Reactive Power Generation (MVAR)	798.00	Total Reactive Load (MVAR)	750.00

In Case 1, three types of events are sequentially created. First, a three-phase ringdown

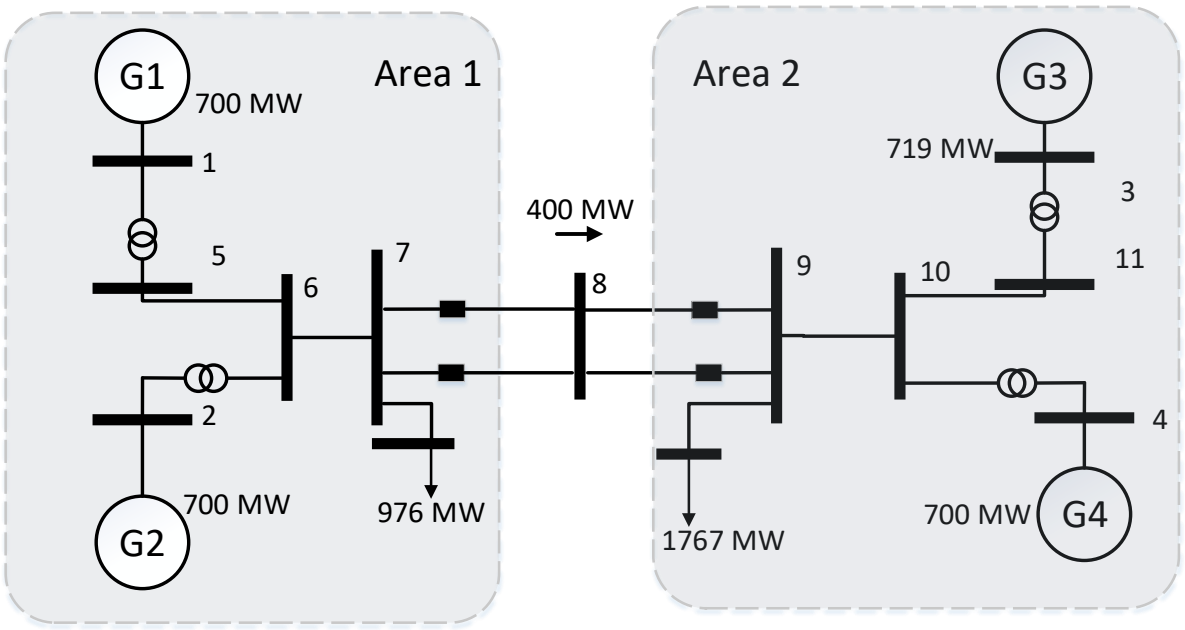

Fig. 5.4: Two-area four-machine test system.

event happens at bus 5 at 5 seconds. The three-phase fault is chosen as this is the most extreme fault scenario in the power system. Second, a step-change in load (50 MW increase) is applied at bus 5 at 200 seconds and third, a cyclic load of 0.6 Hz is applied at bus 5 at 400 seconds to represent a forced mode. The cyclic load oscillation frequency is selected as 0.6 Hz because it is very close to the natural mode of the system and to check if the proposed algorithm can detect both forced mode and natural mode when they are very close to each other. Some white noise is applied throughout the whole simulation period so that the modes are always excited. The speed and voltage data of generator 1 are taken as output vectors and input vectors for mode estimation. Both non-recursive subspace identification and some other established methods such as Prony analysis, Eigenvalue Realization Algorithm (ERA), and Matrix Pencil (MP) methods are applied to compare against the proposed recursive subspace identification method.

5.4.1.1 Ability to track both natural and forced modes

Fig. 5.5 and Fig. 5.6 represents speed and voltage of generator 1 for case I under these events. Identified mode from non-recursive subspace identification and the proposed method is represented in Fig. 5.7. From figure 5.7, it can be seen that, up to 400 seconds, both recursive and non-recursive methods of subspace identification work closely but after 400 seconds, when the cyclic load is introduced, the non-recursive subspace identification method was not able to identify the natural mode properly due to the resonance created from natural mode and forced mode. However, the proposed algorithm can detect both natural and forced modes with better accuracy. Table 5.2 represents the comparisons of the proposed method with the closest in the literature.

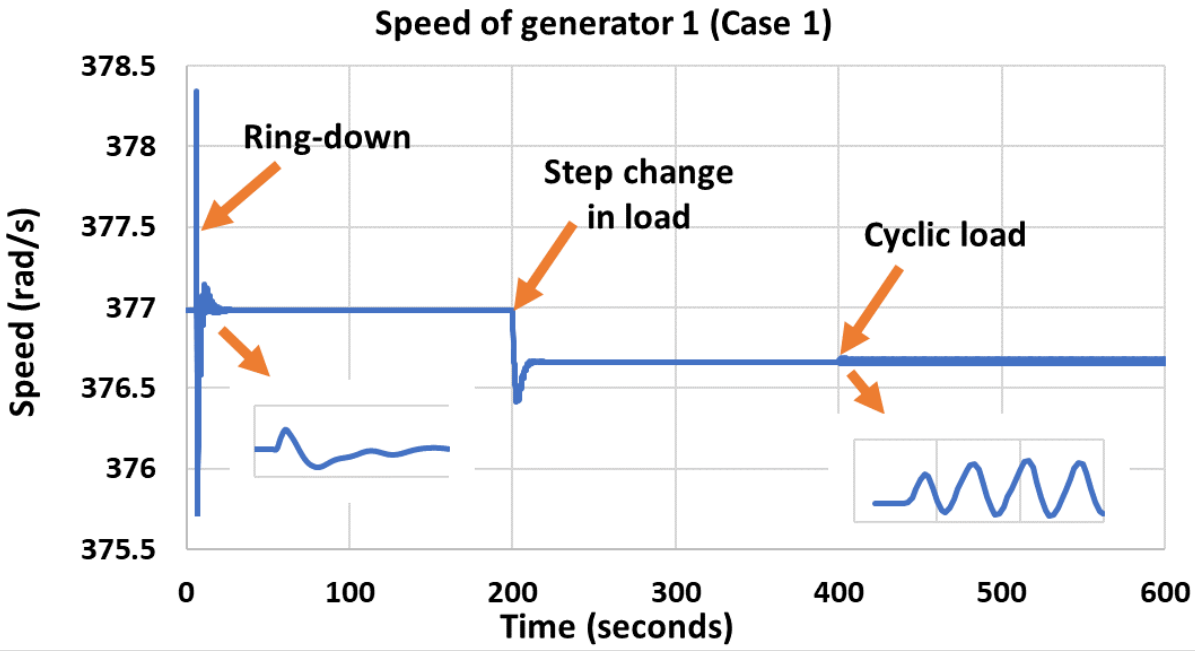

Fig. 5.5: Speed of generator 1 for case I.

5.4.1.2 Ability to select model order and controllable generators

The SVD for generator 1 is presented in Fig. 5.8 as obtained from the proposed methodology. It can be seen that the first 20 singular values from SVD are higher in magnitude and the other singular values are low in magnitude. With the threshold, an order of 20 is

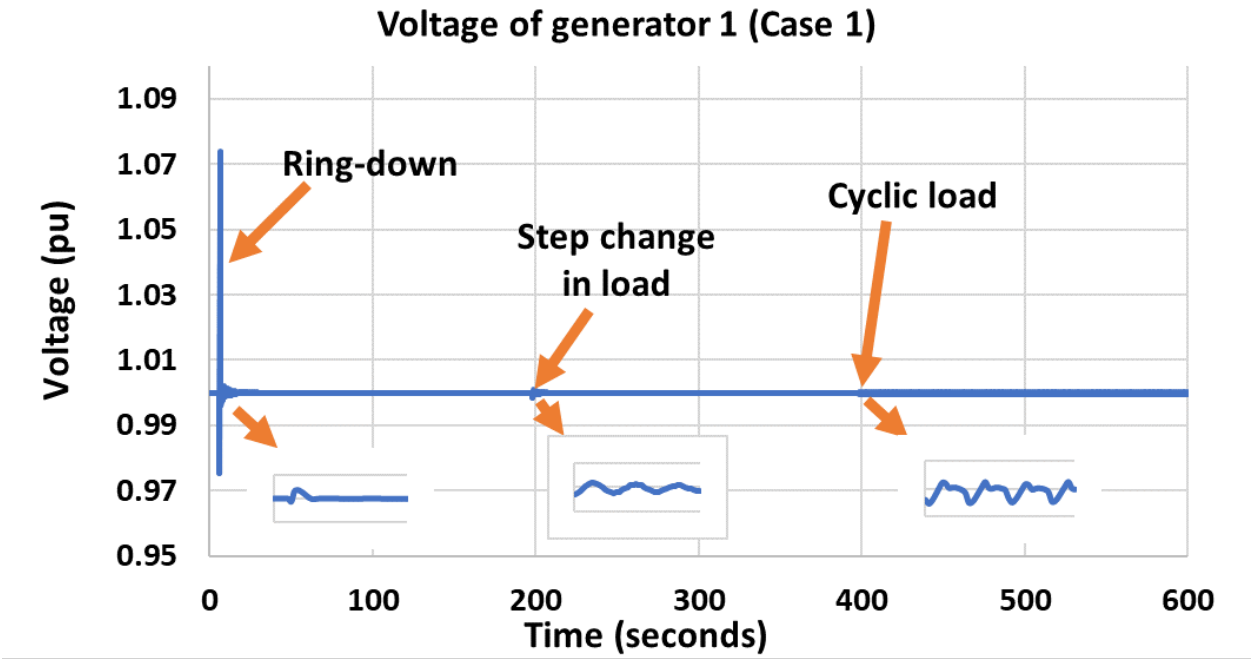

Fig. 5.6: Voltage of generator 1 for case I.

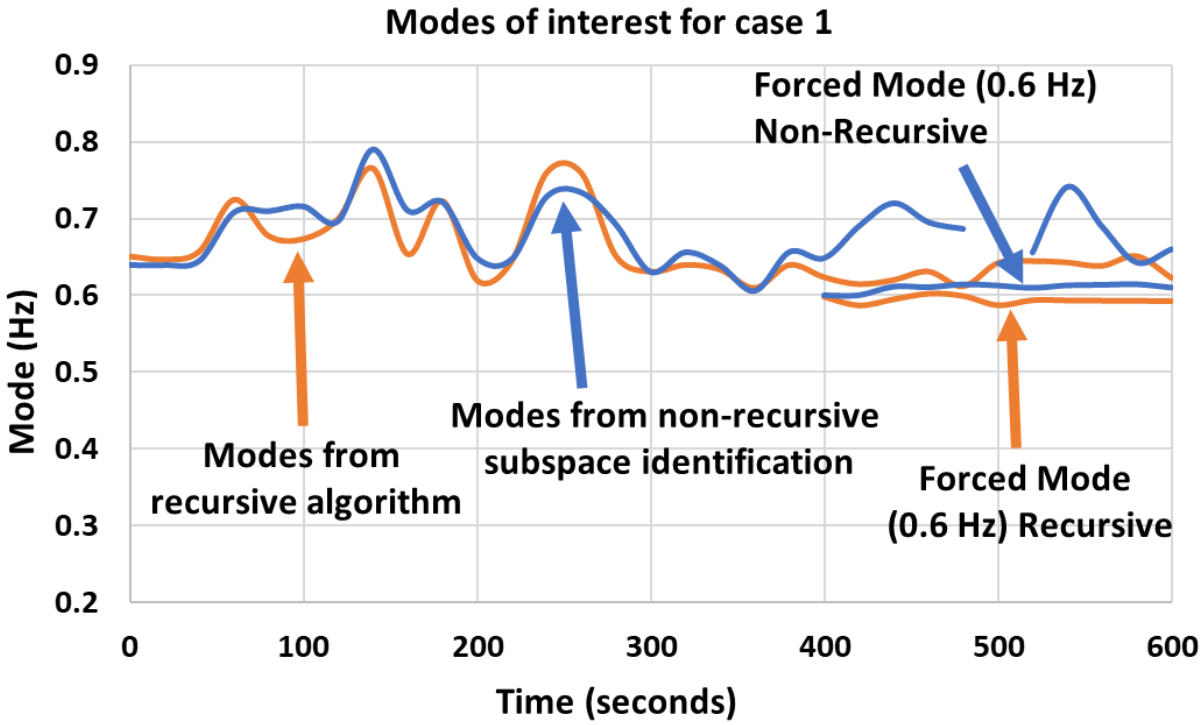

Fig. 5.7: Modes of generator 1 for case I.

identified. For checking if 20 is a good option for reduced-order, system response is generated from the reduced-order system matrix and compared with the original system response during the ring-down event. Fig. 5.8 shows diagram for singular values and Fig. 5.9 shows the comparison of actual and reduced system response. It can be seen that the online order selection is appropriate.

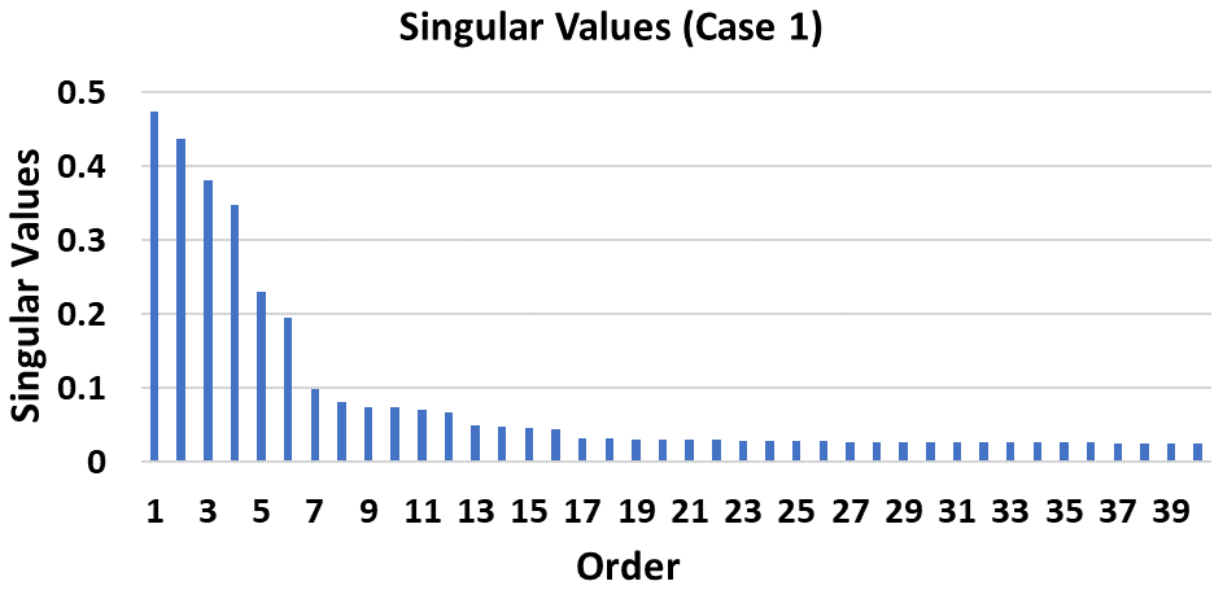

Fig. 5.8: Singular values of generator 1 for case I.

The cyclic mode of 0.6 Hz can be found from every generator's speed data. Finding the location of forced oscillation is very important as a forced mode usually occurs from malfunction and they can collapse the whole power grid. Fig. 5.10 shows that for generator 1, the mode 0.6 Hz has a damping ratio of 0.09% which is below the threshold of 0.1% set at the beginning of identification to find the location of forced mode. As in the created event for the case I, the cyclic mode is applied very close to generator 1 and the result shows that for generator 1 the damping ratio is very low. This proves that the proposed approach can identify the location of forced mode and identify the most controllable generators.

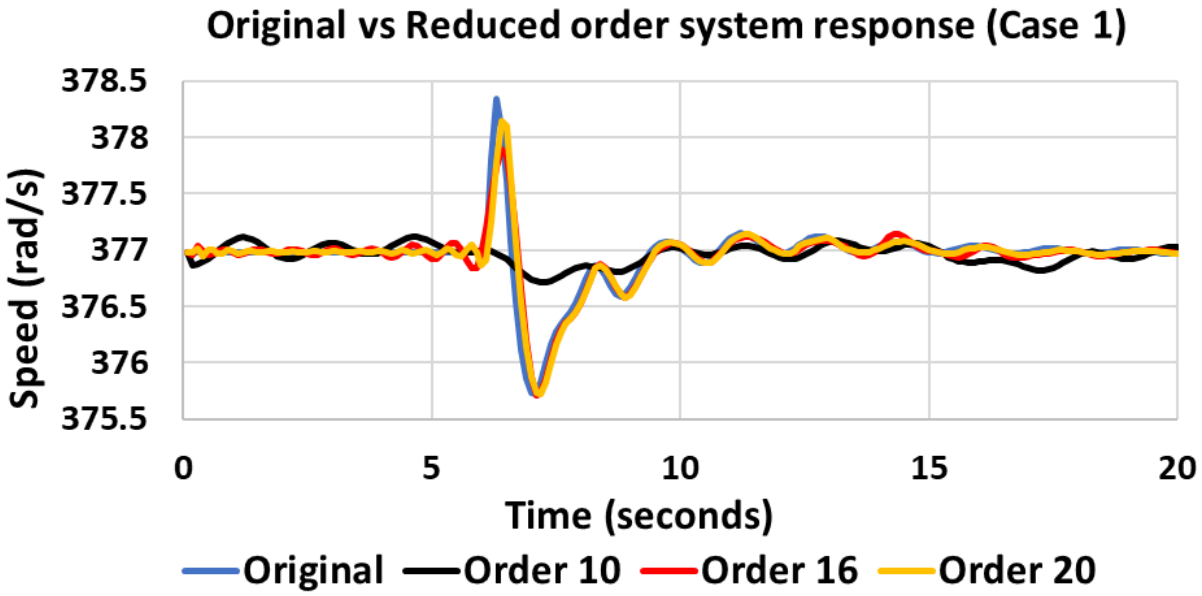

Fig. 5.9: Comparison of actual and reduced order system response of generator 1 for case I.

5.4.2 Case II: IEEE 68 Bus Test System

The IEEE 68 bus power grid is shown in Fig. 5.11. The characteristics of the IEEE 68 bus system are mentioned in Table 5.3. This case study presents how the proposed method works for a large-scale power system where different modes are excited at different times. The tie lines in the 68 bus system are marked red in Fig. 5.11. For this test case along with mode identification, dynamic control is also applied in an online environment to control most affected generators in the ring-down period.

5.4.2.1 Mode Identification

Three types of events are created in this case as well. The total simulation time is 1500 seconds. First, a three-phase ring down event (fault) happens near bus 14 at 15 seconds. Second, a step-change in load (50 MW) is applied at bus 17, 39, and 41 at 470 seconds and finally, a cyclic load of 0.6 Hz is applied at bus 40 at 960 seconds. Random white noise is applied throughout the whole simulation period besides these events. The speed and voltage data of generator 14 are taken as the input vector for mode estimation. Along with the proposed method, other mentioned methods in the previous case are also applied in this

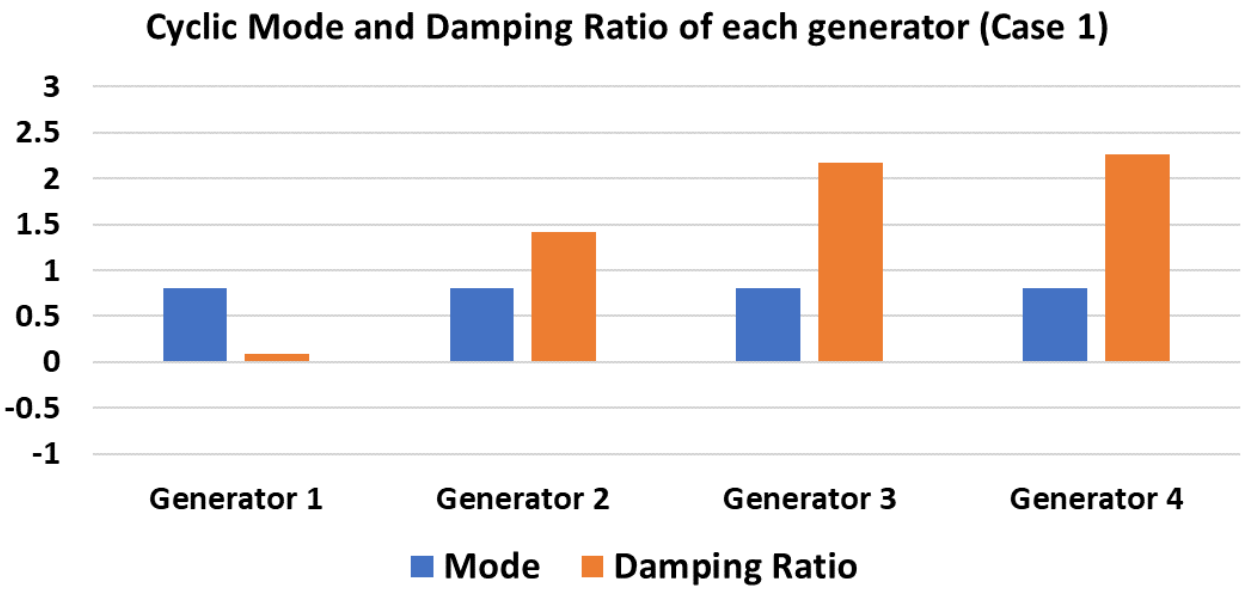

Fig. 5.10: Forced mode location for Case I.

Table 5.2: Estimated modes: Two area system (Case I), IEEE 68 bus system (Case II).

Systems Under Consideration		Case I		Case II	
Event	Methods	Freq. (Hz)	Damp. (%)	Freq. (Hz)	Damp. (%)
Ringdown	Prony, MP	0.624	11.24	0.581	0.52
	ERA	0.621	10.58	0.576	0.43
	SSI	0.632	11.89	0.595	0.38
	Recursive SSI	0.635	11.19	0.591	0.35
Load Change	Prony, MP	0.609	10.87	0.584	6.35
	ERA	0.642	11.25	0.595	7.24
	SSI	0.63	10.45	0.57	5.89
	Recursive SSI	0.61	10.57	0.55	6.12
Cyclic Load	Prony, MP (Natural)	NA	NA	NA	NA
	Prony, MP (Forced)	0.604	0.12	0.602	0.06
	ERA (Natural)	0.664	8.26	0.52	1.04
	ERA (Forced)	0.609	0.084	0.606	0.052
	SSI (Natural)	0.678	9.61	0.457	2.25
	SSI (Forced)	0.594	0.085	0.592	0.074
	Rec. SSI (Natural)	0.615	9.04	0.62	1.18
	Rec. SSI (Forced)	0.591	0.09	0.595	0.045

case. Fig. 5.12 and Fig. 5.13 represents speed and voltage of generator 14 for case II under these events. Identified modes from non-recursive subspace identification and the proposed method are represented in Fig. 5.14. From Fig. 5.14, it can be seen that the proposed

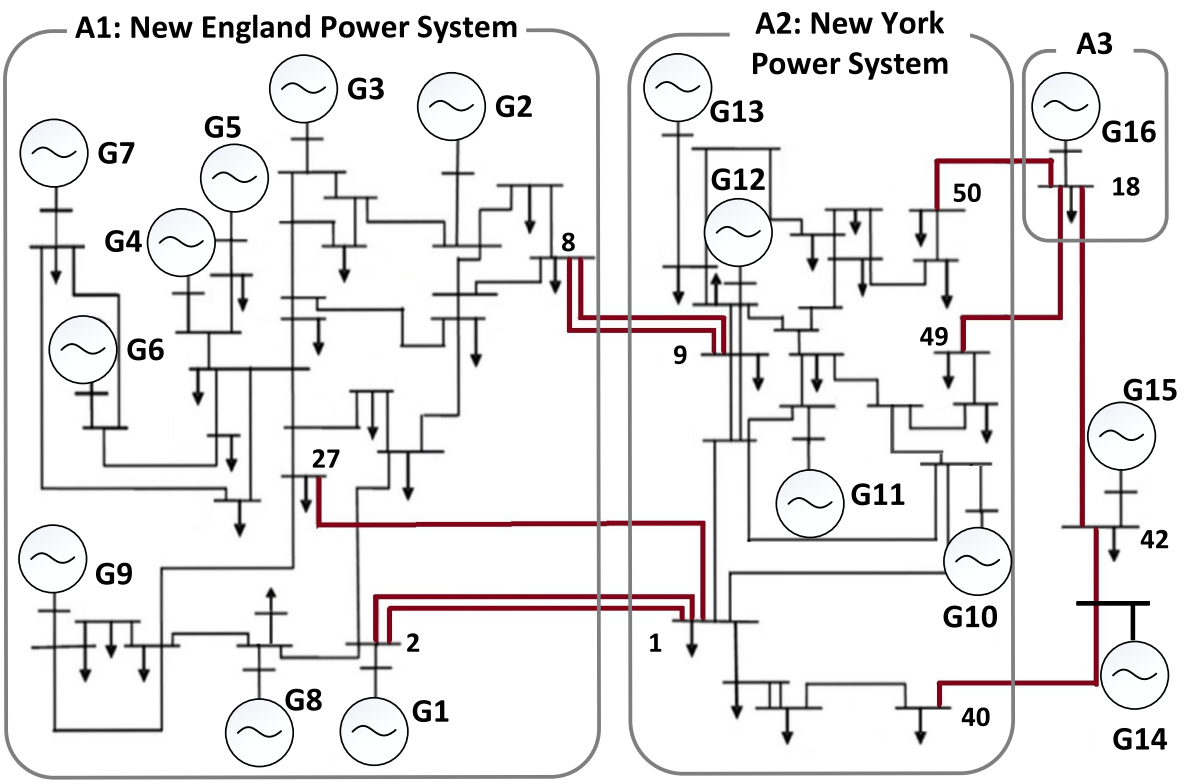

Fig. 5.11: IEEE 68 Bus study system.

Table 5.3: IEEE 68 bus system features.

Buses & Generators	68 Buses 16 Generators	Areas	5
Total Active Power Generation (MW)	17787.53	Total Active Load (MW)	17620.65
Total Reactive Power Generation (MVAR)	2496.53	Total Reactive Load (MVAR)	1671.76

recursive algorithm outperforms the non-recursive counterpart in detecting natural mode when the forced mode is close while the proposed method can detect both modes.

5.4.2.2 Dynamic Model Order Updates, Optimal Generator Selection and Efficiency Studies

From the first set of data, order 24 is selected as the reduced-order for Case II. Fig. 5.15 shows the norm of the mode of interest for case II while using a constant 24 as reduced-order throughout the whole simulation. It can be seen that a time progresses norm asymptotically

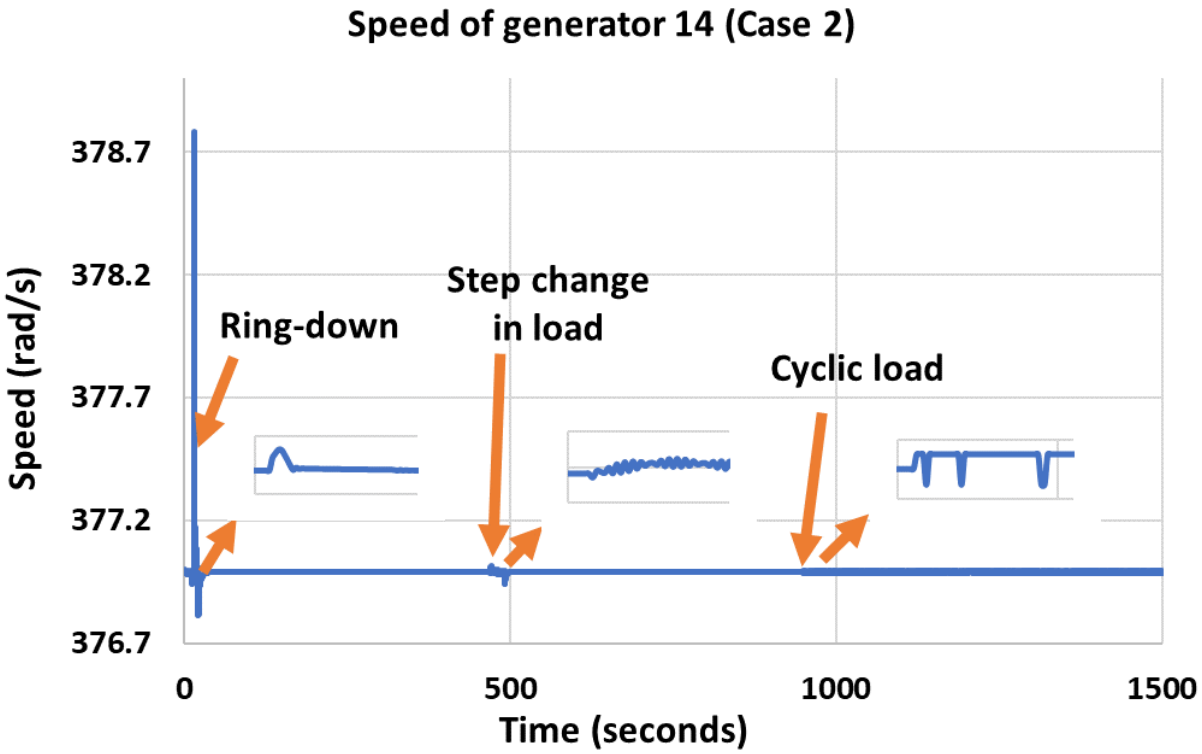

Fig. 5.12: Speed of generator 14 for case II.

moves to zero which represents that no mode can be identified at that time using this order. This is mainly due to additional noise and bad damping in the system. This proves the need for the adaptive model order. Fig. 5.16 shows the adaptive order automatically obtained in real-time with the proposed architecture. Fig. 5.17 represents the norm of modes while using this adaptive order. It can be seen that the adaptive order changes from 24 to 32 and then to 28.

The location of forced mode is found to be at generator 14 similarly as mentioned in case I. Fig.5.18 represents the location.

For the proposed method, the simulation time is improved when compared to the non-recursive method of mode identification. Fig. 5.19 shows the improvement of simulation time for each order and the improvement is better for a higher-order system and Table 5.2 represents the comparisons of the proposed method with the closest in the literature.

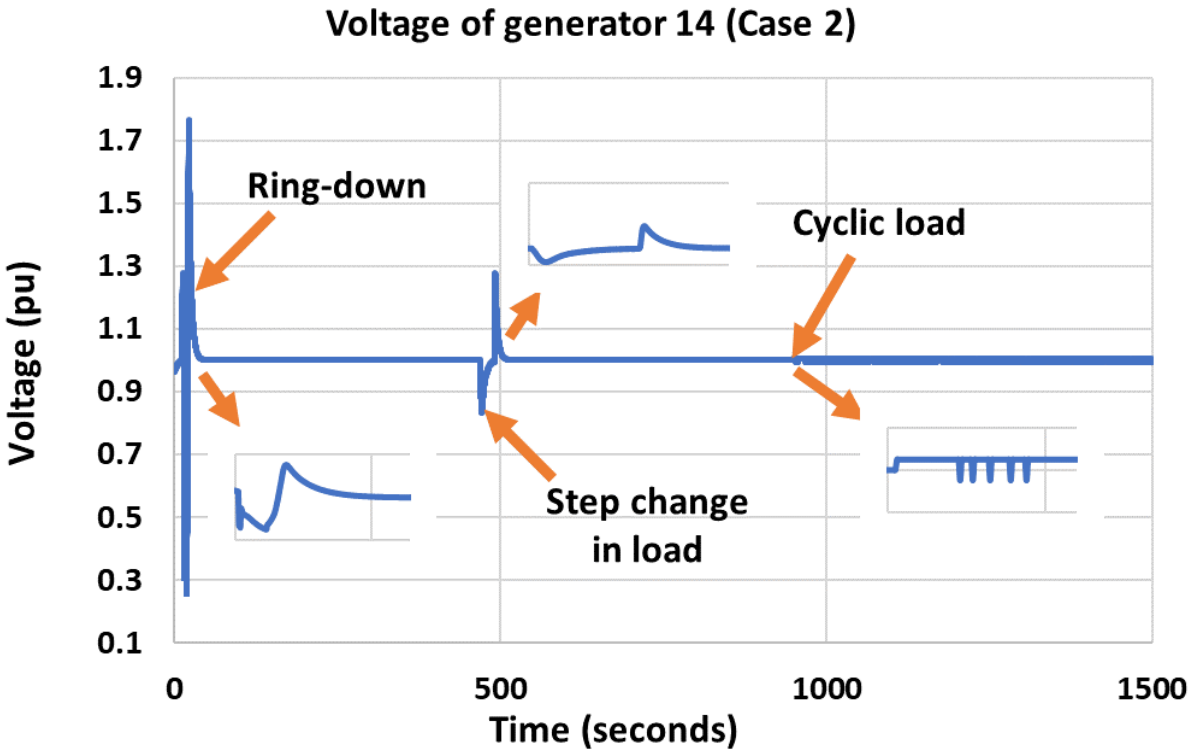

Fig. 5.13: Voltage of generator 14 for case II.

5.4.2.3 Adaptability and Optimal Damping Control Studies

For the controller implementation, a total simulation of 300 seconds is simulated. Two kinds of events were created to showcase the performance and adaptability of the controller. Also, the proposed controller's performance is compared with PSS which is the established controller for power systems. The first event is a three-phase fault near generator 14 at 15 seconds. Second, at 215 seconds, a line between bus 41 and bus 42 is removed to change the operating equilibrium point of the system and to check the controller's performance in a new equilibrium point. Fig. 5.20 shows the speed data and Fig. 5.21 represents the voltage data of generator 14 for this event. The speed and voltage of generator 14 are selected as output and input data for the proposed controller to generate control output. For the three-phase fault, based on the mode of interest and lowest damping ratio (under the threshold of 5% damping), the controller chose generators 1, 2, and 14 as the most affected generators and send the control signal to control these generators. For the line removal part, using the same

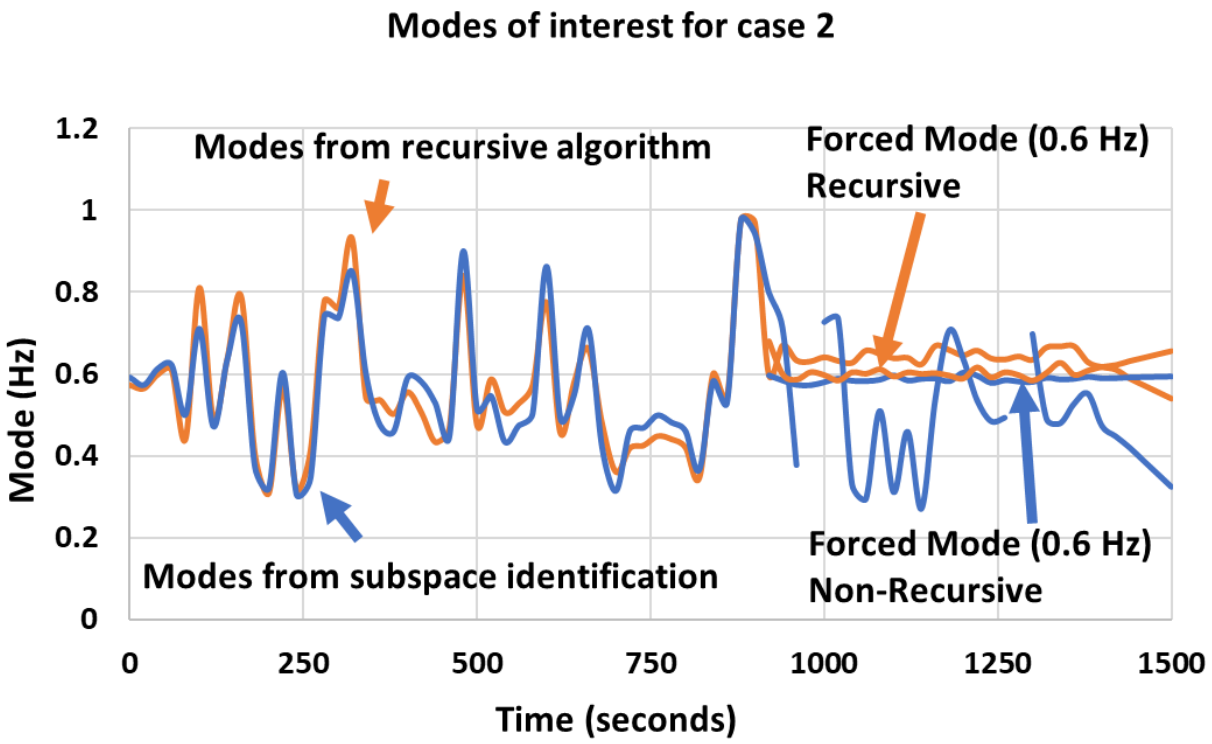

Fig. 5.14: Modes of generator 14 for case II.

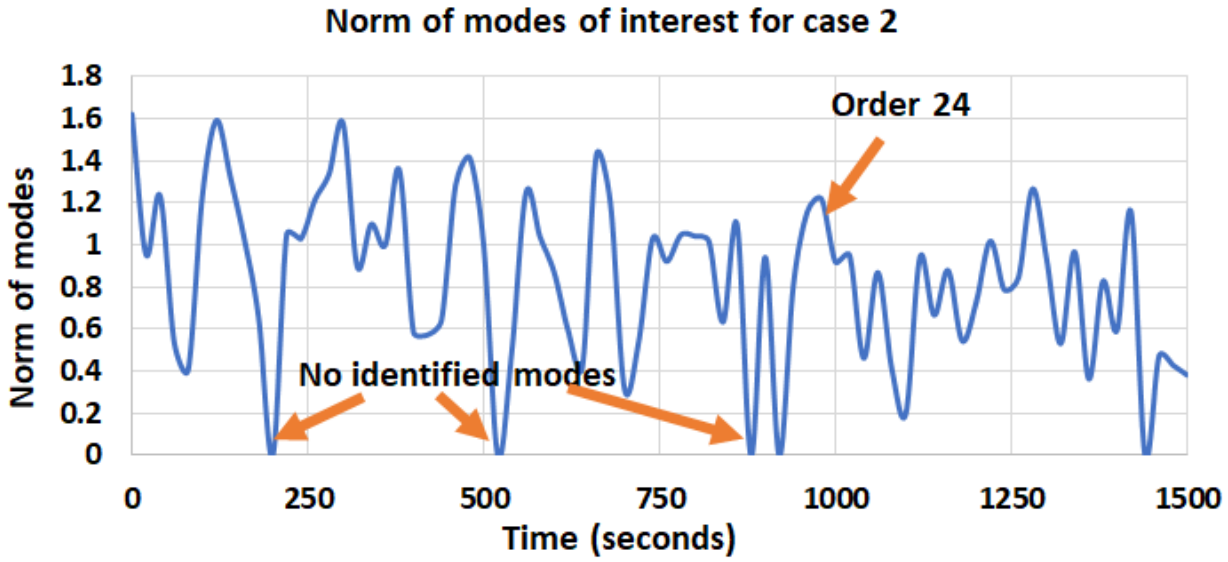

Fig. 5.15: Norm of mode of interest of Case II with constant order 24.

threshold for damping, generator 14 and 15 were chosen by the controller. Fig. 5.22 shows the choice of generators based on the damping ratio by the proposed controller. Fig. 5.23

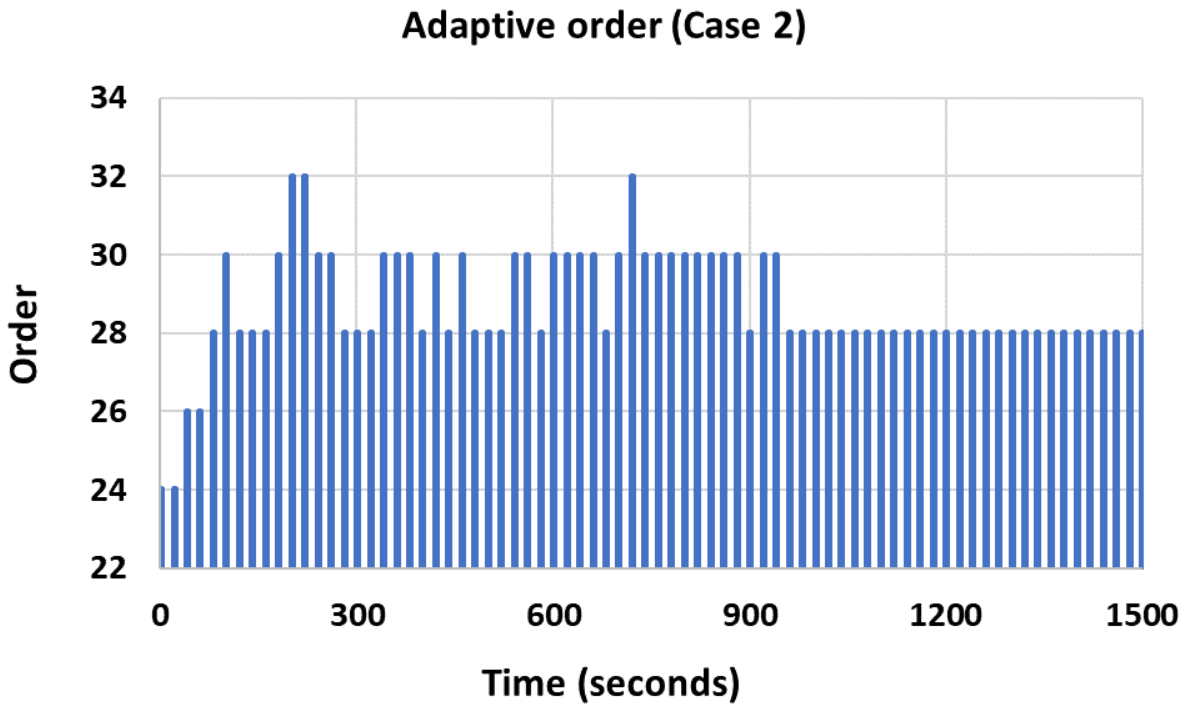

Fig. 5.16: Adaptive order for Case II.

shows the change of the operating point due to line removal event. It can be seen that the estimated mode of interest is shifted to around 1.60Hz.

To showcase the performance of proposed controller and compare it against no controller and PSS during the ring-down event, damping ratio and controller performances are summarized in Table 5.4- 5.9.

From the eigenvalues obtained from system matrix A (For with controller, with PSS, and without controller) during the ring-down event, it is evident that by applying the proposed controller, the damping ratio of the dominant modes is improved. Table 5.4 summarizes the dominant modes' frequency and damping ratio. To measure the performance improvement, the area under the curve of the speed graph is considered (For with proposed controller, with PSS, and without controller). The reduced area under the curve means less oscillation and an improvement. Table 5.5 summarizes the results. The results show that the proposed architecture improves the damping by more than 20% when compared to the exist-

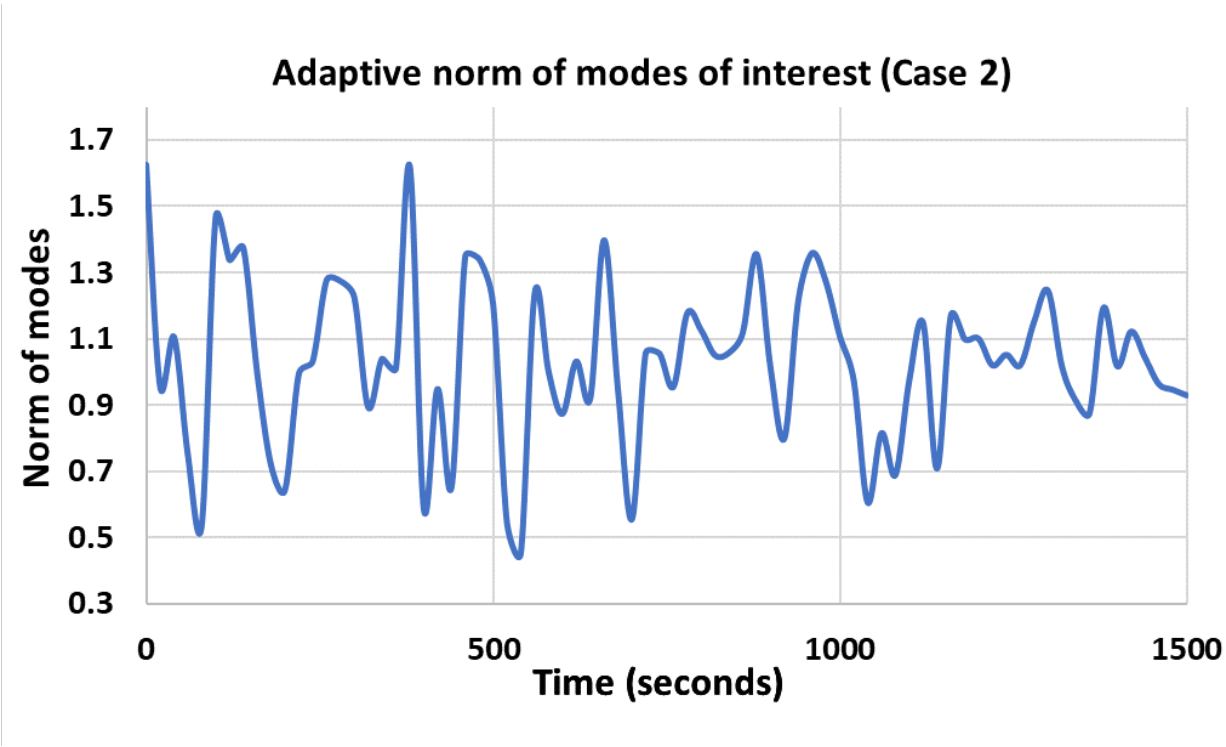

Fig. 5.17: Adaptive norm for Case II.

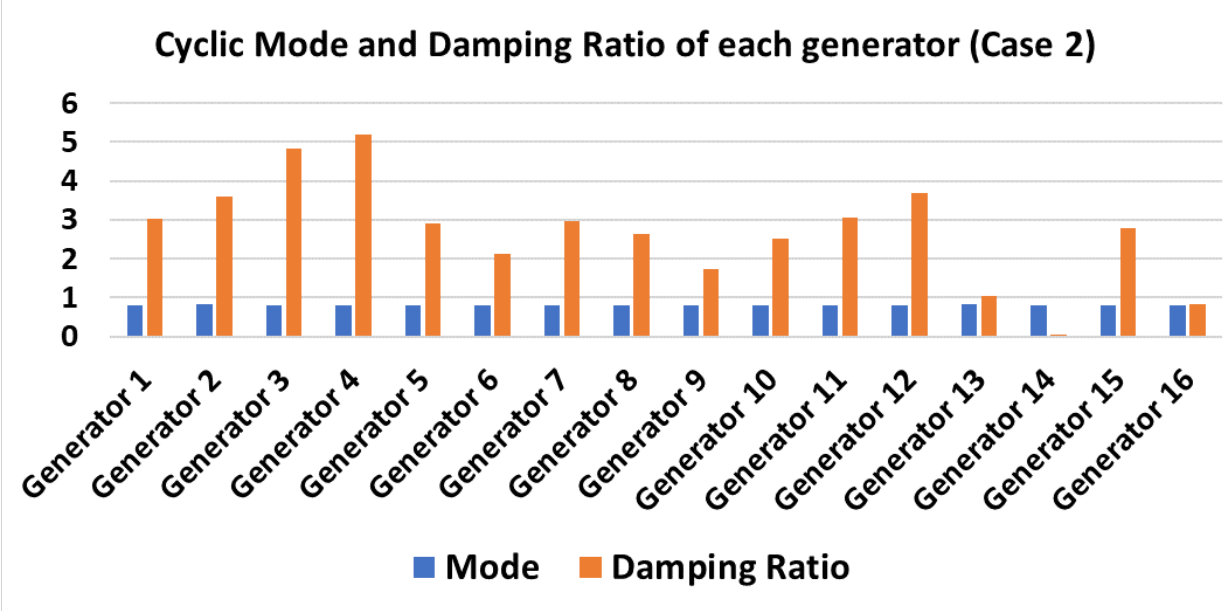

Fig. 5.18: Forced mode location for Case II.

ing architectures and is also capable of estimating and classifying the modes with improved computational efficiency.

For the second event at 215 seconds (line removal between bus 41 and bus 42), the op-

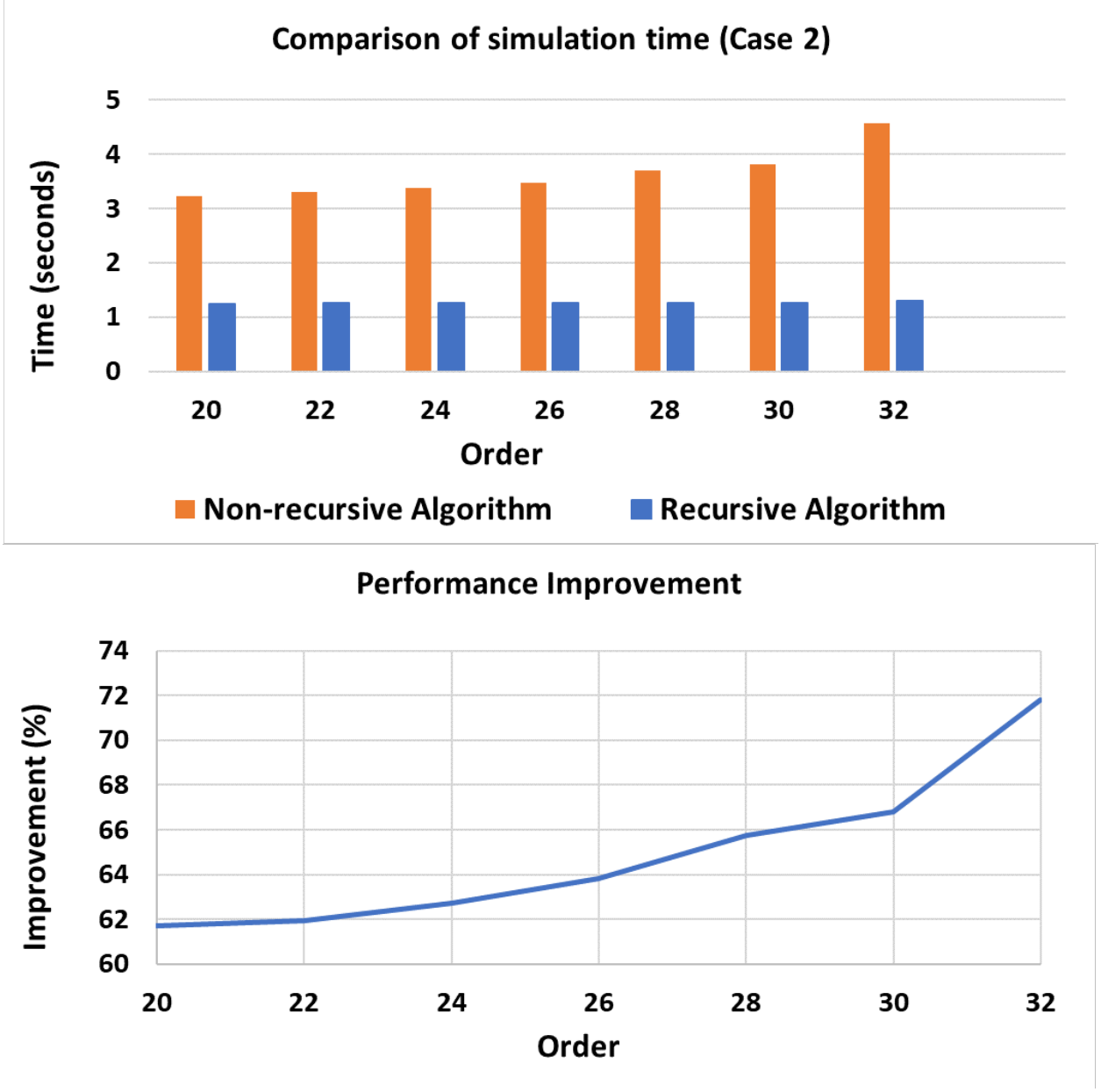

Fig. 5.19: Simulation time improvement for Case II.

erating point of the system is changed and the chosen generators are generators 14 and 15. Table 5.6 and 5.7 demonstrate the improvement. From the tables, it can be seen that as expected (PSS settings can not change dynamically) the proposed architecture outperforms the PSS, and when a new operating point arises, PSS provides poor damping.

To showcase if the selection of generators is working well, for the line removal part, controller outputs were sent to generators 1 and 2, which were the chosen generators for the

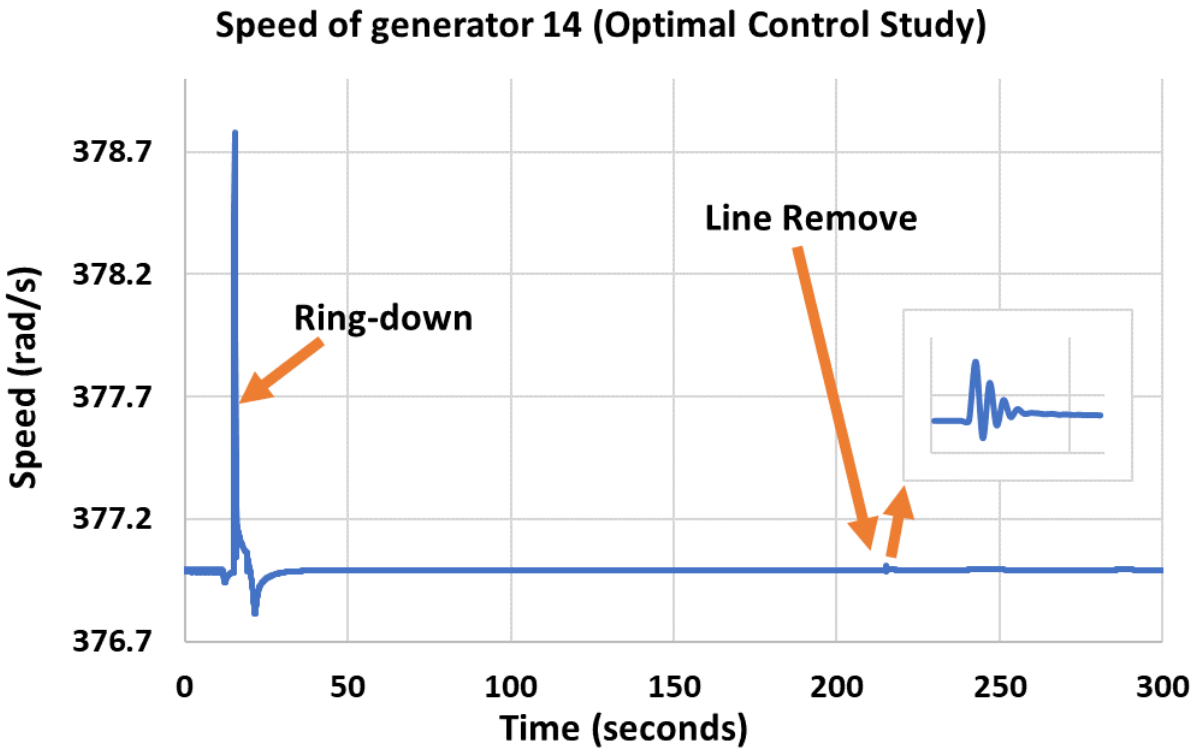

Fig. 5.20: Speed of generator 14 for control purpose

Table 5.4: Summary of Damping Ratio Improvement during ring-down event

List	Without controller	With PSS	With controller
Mode 1 (Generator 1) (Hz)	0.679	0.6422	0.6227
Damping Ratio of mode 1 (%)	2.9824	4.8777	10.6144
Mode 2 (Generator 2) (Hz)	0.7055	0.7976	0.7674
Damping Ratio of mode 2 (%)	1.014	1.4827	6.4128
Mode 3 (Generator 14) (Hz)	0.591	0.61544	0.5929
Damping Ratio of mode 3 (%)	0.35	1.3531	5.0357

ring-down event. The purpose of this is to check whether the performance of the proposed controller is good or bad if the generator location is not changed in accordance with the new event (line removal). Table 5.8 and 5.9 showcases that the controller performances with this

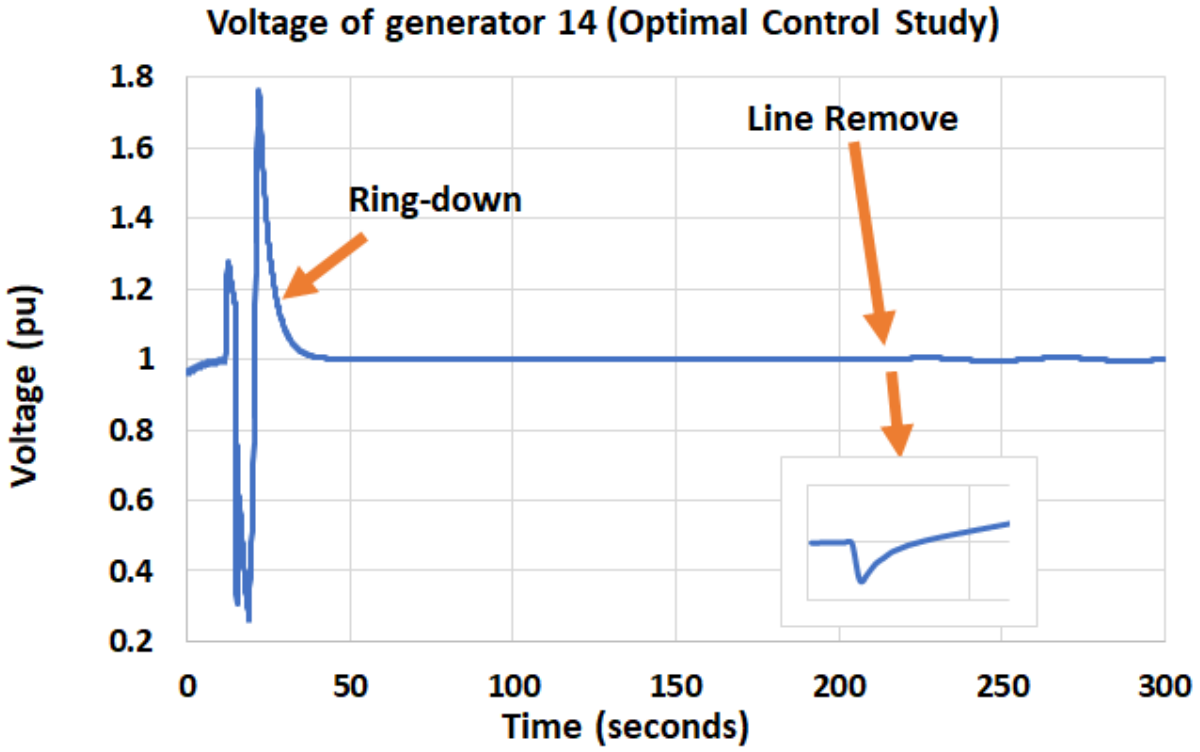

Fig. 5.21: Voltage of generator 14 for control purpose

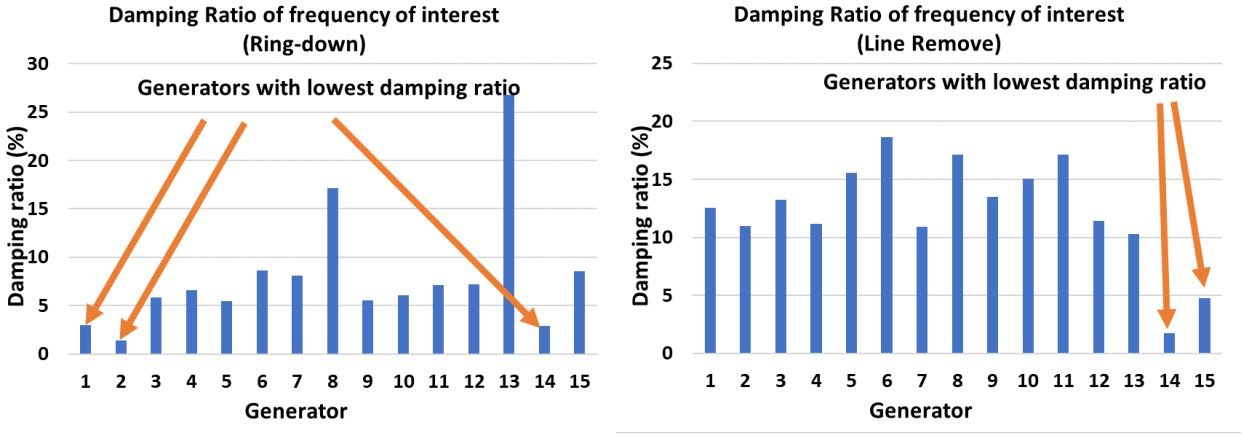

Fig. 5.22: Choice of Generators

selection is not good. Hence, it can be concluded that the adaptive selection of generators based on the proposed architecture is a critical need for controlling the right generator(s). All the quantitative assessment is included in the Tables IV- Table IX.

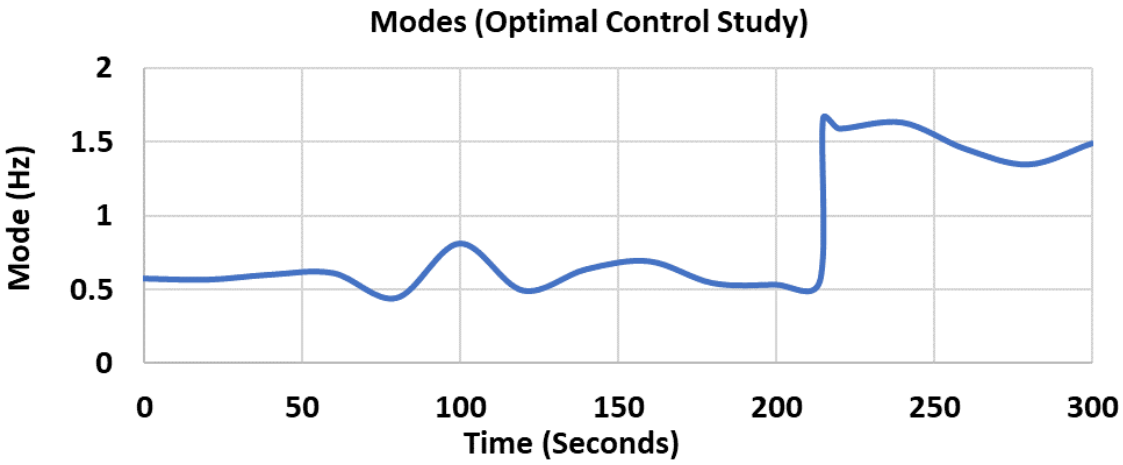

Fig. 5.23: Change of operating point due to line removal

Table 5.5: Summary of Controller Performance during ring-down event

Generator	Gen 1	Gen 2	Gen 14
Area under curve (Without Controller)	0.3337	0.2321	13.885
Area under curve (With PSS)	0.3475	0.2303	14.5975
Area under curve (With proposed Controller)	0.283	0.2105	10.5379
% Improvement (PSS)	-4.135	0.776	-5.1314
% Improvement (Controller)	15.193	9.306	24.106

Table 5.6: Summary of Damping Ratio Improvement during line removal event

List	Without controller	With PSS	With controller
Mode 1 (Generator 14) (Hz)	1.556	1.9241	1.610
Damping Ratio of mode 1 (%)	1.7431	1.3409	5.8954
Mode 2 (Generator 15) (Hz)	1.738	1.53	1.5783
Damping Ratio of mode 2 (%)	4.7546	4.233	13.2456

Table 5.7: Summary of Controller Performance during line removal event

Generator	Gen 14	Gen 15
Area under curve (Without Controller)	0.0790	0.0772
Area under curve (With PSS)	0.0813	0.0785
Area under curve (With proposed Controller)	0.069	0.0717
% Improvement (PSS)	-2.91	-1.68
% Improvement (Controller)	12.66	7.12

Table 5.8: Summary of Damping Ratio Improvement during line removal event

List	Without controller	With PSS	With controller
Mode 1 (Generator 1) (Hz)	1.1688	1.1952	1.0737
Damping Ratio of mode 1 (%)	12.57	-0.0547	13.121
Mode 2 (Generator 2) (Hz)	0.9955	0.8653	0.8852
Damping Ratio of mode 2 (%)	10.96	3.02684	9.16

Table 5.9: Summary of Controller Performance during line removal event

Generator	Gen 1	Gen 2
Area under curve (Without Controller)	0.0063	0.0016
Area under curve (With PSS)	0.0065	0.0016
Area under curve (With proposed Controller)	0.0064	0.0015
% Improvement (PSS)	-3.17	0
% Improvement (Controller)	-1.58	6.25

5.5 Summary

In this chapter, a novel recursive hybrid deterministic-stochastic subspace identification based power grid electro-mechanical mode-estimation and classification are proposed. The proposed architecture can effectively identify, natural oscillations from ambient and ring

down events and the force oscillations from cyclic events. The architecture can also classify them if it happens at the same frequency. Furthermore, the proposed architecture is computationally efficient as it changes the model order efficiently depending on changing system dynamics. The feasibility of the architecture is tested on a real-time digital simulator with realistic system information and the results noted that the architecture can classify oscillations effectively identify the modes of oscillations, improve the damping ratio by more than 20% when compared to state-of-the-art methods. Most importantly, the architecture can control the most vulnerable generators and improve the percentage damping by more than 20%. Until this chapter, improving damping ratio of low frequency oscillatory modes is done through generator selection based on singular values. While this method can choose upto 4 different generators which are more impacted by the oscillation, locating the oscillation source has not been explored in previous chapters. Oscillation source location is as important as controlling and identifying the undamped mode. The next chapter of this research work will explore and propose a new method for oscillation source location based on measurement data.

CHAPTER 6: A Novel Oscillation Source Location Identification Approach Utilizing Lyapunov Energy Functions and Measurement Based Identification Method

6.1 Introduction and main contributions

Power systems are really complex in nature. Accurate knowledge and estimation of the electro-mechanical modes in power system is of great importance to control a power grid since a system wide outage can be caused by one single unstable mode of oscillation. As a result, advanced and accurate mathematical tools are necessary to identify the system dynamics as well as oscillatory modes' information and to design the stabilizers and controllers to improve damping scenario of poorly damped oscillatory modes. With the increasing deployment of a large number of PMUs throughout the power grid, measurement based identification methods have been becoming popular recently. Model based frequency studies have been established for a long time [52]. However, model based studies cannot anticipate every kind of events in real-time when the system is extremely dynamic and has stochastic changes. Recently, several methods have been developed to estimate power system modes from measurement data [6, 7, 10, 11, 19, 22, 99, 100].

PMU based wide-area measurement system (WAMS) improves observabiity of power system dynamics in real-time and also helps power system operators and engineers with useful stability related information. The oscillatory modes which are well damped are not of major concern as they indicate that the system is going back to its normal steady state operation and approaching back to equilibrium. However, sustained oscillatory modes or the oscillatory modes which are not damped properly can damage or reduce power transfer limit in the network and can even result in failure of any electrical equipment. Sustained oscillations in power system can occur from improper operating condition, faulty equipment, malfunctioning controller of generating units or any periodic disturbances. Since, these sustained

oscillatory modes can become a major problem threatening the security of large-scale interconnected power systems, it is very important to have accurate knowledge of any sustained oscillatory mode as son as possible whether it is poorly damped natural oscillations or forced oscillations. This accurate knowledge of sustained oscillatory modes refer to the frequency and the damping ratio of the modes as well as the source location of these modes so that proper control mechanism to lower the risk of a large scale blackout or instability issue can be deployed easily.

Various methods of finding oscillation source location (OSL) have been conducted over the time. Among them travelling wave based methods, damping torque based methods, mode shape estimation based methods and energy based methods are noteworthy. Traveling wave based methods utilize the principle of the electro-mechanical wave propagation [35] to locate the oscillation source. This method depends on the detection of arrival time of the oscillation at different locations and actual wave speed map [36]. If the speed map is available and arrival time can be detected accurately, the method can be applied accurately. A similar method in [37] utilizes the PMU data to locate the source. Least mean square method is used in this procedure to estimate time differences of oscillation arrival times between different locations. In the damping torque based methods, the generator with negative damping torque coefficient is identified as the oscillation source as negative damping contributes to lowering damping and increasing oscillation. If multiple generating units have negative damping torque, the location is determined based on the slope of negative damping torque coefficient. How this damping torque concept can be extended from a single machine infinite bus (SMIB) system to a multimachine system can also determine the source location identification method. [38–41]. Mode shape estimation based methods locate the oscillation source by estimating the mode shape using measurements from different locations and then identifies the source based on the mode shape [42–45]. The energy based methods are mostly used to identify oscillation source location in recent years [46–50, 101]. Energy based methods are capable of identifying oscillation source locations and they have a similar working principle as damping torque

methods. This method works on the principle of dissipating energy and the method monitors energy flow throughout the whole network and identifies the generator as the source which injects energy into the network as the source. Injecting energy or producing energy is also an indication of negative damping torque coefficient.

In this chapter, a measurement based identification method has been applied on PMU measurement data to identify poorly damped natural mode and forced mode. Then Lyapunov based energy functions are used to calculate energy functions of a power system and to identify oscillation source location based on the energy calculated. All these methods are combined in a way that they can be implemented online. The advantage of the proposed method is that it can identify modes and their damping ratio as well as provide reduced order system matrix which can help to perform a control scheme to improve damping scenario. Compared to other work in the literature, the main contribution and novelty of our work is that the architecture can

- Provide oscillation monitoring of the power grid considering internal and external disturbance and classify natural and forced-modes of oscillations.
- The approach combines Sub-space Identification methods with Lyapunov energy function method to identify oscillation source location.
- The proposed approach is computationally robust and prone to noise.

6.2 Direct Energy Method of OSL Identification

For a multibus network, the bus current equation can be represented as follows:

$$Y_{BUS}V_{BUS} - I_G + I_L = 0 \tag{6.1}$$

Where, Y_{BUS} is bus admittance matrix, V_{BUS} is voltage matrix containing voltage of every buses, I_G is vector of generator phasor currents (n-dimensional) and I_L is vector of load phasor currents (n-dimensional)

All the generator buses are numbered first and m denotes the total number of generator buses. By using the above equation, an energy conservation law can be derived for power systems. To begin with, we will take complex integrals of both sides of the bus current equation in 6.1.

$$W =_c \int_{V_{BUS_0}}^{V_{BUS}} [(Y_{BUS}V_{BUS} - I_G + I_L)^*]^T dV_{BUS} \tag{6.2}$$

Where, integral path c is given by the system trajectory.

Equation 6.2 can be rewritten in the summation form as follows:

$$W =_c \int_{V_{BUS_0}}^{V_{BUS}} [\sum_{i=1}^{N}(\sum_{j=1}^{N} Y_{ij}^* V_j^*)dV_i - \sum_{i=1}^{m} I_{Gi}^* dV_i + \sum_{i=1}^{N} I_{Li}^* dV_i] \tag{6.3}$$

On the other hand, we have the following general relationships:

$$\mathbf{V_i} = V_i e^{j\theta_i} \tag{6.4}$$

$$I_{Gi}^* = \frac{P_{Gi} + jQ_{Gi}}{V_i} e^{-j\theta_i} \tag{6.5}$$

$$I_{Li}^* = \frac{P_{Li} + j(Q_{Li} - Q_{Ci})}{V_i} e^{-j\theta_i} \tag{6.6}$$

$$Y_{BUS} = [G_{ij} + jB_{ij}] \tag{6.7}$$

$$d\mathbf{V_i} = e^{j\theta_i} dV_i + jV_i e^{j\theta_i} d\theta_i \tag{6.8}$$

By substituting eqaution 6.4-6.8 into equation 6.3 we can derive the following equations for its imaginary part:

$$W_{IMAG} = -[\frac{1}{2}\sum_{i=1}^{N} B_{ii}V_i^2 + \frac{1}{2}\sum_{i=1}^{N}\sum_{j\neq 1}^{N} B_{ij}V_iV_jcos\theta_{ij}]$$

$$+\sum_{i=1}^{N}\sum_{j=1}^{N} {}_c\int_{(V_0,\theta_0)}^{(V,\theta)} G_{ij}(V_jsin\theta_{ij}dV_i + V_iV_jcos\theta_{ij})d\theta_i$$

$$-\sum_{i=1}^{m} {}_c\int_{(V_0,\theta_0)}^{(V,\theta)} (P_{Gi}d\theta_i + \frac{Q_{Gi}}{V_i}dV_i)$$

$$+\sum_{i=1}^{N} {}_c\int_{(V_0,\theta_0)}^{(V,\theta)} (P_{Li}d\theta_i + \frac{Q_{Li}-Q_{Ci}}{V_i}dV_i) \tag{6.9}$$

Theorem 1:

The energy integral of generator output power can be represented by a complex line integral of current and voltage phasors as follows:

$${}_c\int_{(V,\theta)}^{(V_0,\theta_0)} (P_{Gi}d\theta_i + \frac{Q_{Gi}}{V_i}dV_i) =_c \int_{V_{Gi0}}^{V_{Gi}} Im(\mathbf{I_{Gi}}^* d\mathbf{V_{Gi}}) \tag{6.10}$$

Where,

$$\mathbf{V_{Gi}} = V_i e^{j\theta_i}$$

P_{Gi} and Q_{Gi} are real and reactive power output from generator.

Theorem 2:

If the stator/network transients are negligible for generator i, the following holds:

$${}_c\int_{(V,\theta)}^{(V_0,\theta_0)} (P_{Gi}d\theta_i + \frac{Q_{Gi}}{V_i}dV_i) =_c \int_{\delta_{0i}}^{\delta_i} P_{ei}d\delta_i$$

$$+_c\int_{V_{Gi0}}^{V_{Gi}} (I_{di}dV_{qi} - I_{qi}dV_{di}) \tag{6.11}$$

On the other hand, we have the following generator power relation:

$$P_{ei} = P_{mi} - M_i\omega_i' - D_i\omega_i \tag{6.12}$$

Where, D_i is generator damping coefficient.

By combining equation 6.11 and 6.12, we get,

$$
\begin{aligned}
{}_c\int_{(V,\theta)}^{(V_0,\theta_0)}(P_{Gi}d\theta_i+\frac{Q_{Gi}}{V_i}dV_i) &= {}_c\int_{\delta_{0i}}^{\delta_i}P_{mi}d\delta_i \\
-\frac{1}{2}M_i(\omega_i^2-\omega_{i0}^2)-\int D_i\omega_i^2dt &+ {}_c\int_{V_{Gi0}}^{V_{Gi}}(I_{di}dV_{qi}-I_{qi}dV_{di})
\end{aligned}
\tag{6.13}
$$

By combining equation 6.9 and 6.13, we get,

$$
\begin{aligned}
&\sum_{i=1}^{m}\frac{1}{2}M_i\omega_i^2+\sum_{i=1}^{N}[-\frac{1}{2}B_{ii}V_i^2-\frac{1}{2}\sum_{j\neq 1}^{N}B_{ij}V_iV_jcos\theta_{ij}] \\
&+\sum_{i=1}^{N}{}_c\int_{\theta_0}^{\theta}G_{ii}(V_i^2d\theta_i+\sum_{i=1}^{N}\sum_{j\neq 1}^{N}G_{ijc}\int_{(V_0,\theta_0)}^{(V,\theta)}(V_iV_jcos\theta_{ij}d\theta_i \\
&+V_jsin\theta_{ij}dV_i)-\sum_{i=1}^{m}[{}_c\int_{\delta_{0i}}^{\delta_i}P_{mi}d\delta_i+{}_c\int_{V_{g0i}}^{V_{gi}}(I_{di}dV_{qi}-I_{qi}dV_{di})] \\
&+\sum_{i=1}^{N}[{}_c\int_{\theta_0}^{\theta}P_{Li}d\theta_i+{}_c\int_{V_0}^{V}\frac{Q_{Li}-Q_{Ci}}{V_i}dV_i)]+\sum_{i=1}^{N}[\int D_i\omega_i^2dt]=C
\end{aligned}
\tag{6.14}
$$

Where, C is a contant reflecting the initial energy at the operating (θ_0, V_0).

By exempting the time integral term in the above equation, we can obtain an energy function for a power system as follows:

$$
\begin{aligned}
E=&\sum_{i=1}^{m}\frac{1}{2}M_i\omega_i^2+\sum_{i=1}^{N}[-\frac{1}{2}B_{ii}V_i^2-\frac{1}{2}\sum_{j\neq 1}^{N}B_{ij}V_iV_jcos\theta_{ij}] \\
&+\sum_{i=1}^{N}{}_c\int_{\theta_0}^{\theta}G_{ii}(V_i^2d\theta_i)+\sum_{i=1}^{N}\sum_{j\neq 1}^{N}G_{ijc}\int_{(V_0,\theta_0)}^{(V,\theta)}(V_iV_jcos\theta_{ij}d\theta_i \\
&+V_jsin\theta_{ij}dV_i)-\sum_{i=1}^{m}[{}_c\int_{\delta_{0i}}^{\delta_i}P_{mi}d\delta_i+{}_c\int_{V_{g0i}}^{V_{gi}}(I_{di}dV_{qi}-I_{qi}dV_{di})] \\
&+\sum_{i=1}^{N}[{}_c\int_{\theta_0}^{\theta}P_{Li}d\theta_i+{}_c\int_{V_0}^{V}\frac{Q_{Li}-Q_{Ci}}{V_i}dV_i)]
\end{aligned}
\tag{6.15}
$$

From eqn. 6.15, we get,

$$PR_i = -(P_{m_i}\delta_i) \tag{6.16}$$

$$P_{Mag_i} = -\int_a^b \sum_{j=1,j\neq i}^{2n+m} |V_i|\,|V_j|\,|Y_{ij}|\,sin\Theta_{ij}cos(\delta_{ij}) \tag{6.17}$$

$$P_{Loss_i} = -\int_a^b \sum_{j=1,j\neq i}^{n} D_{ij}cos\delta_{ij}\partial(\delta_i+\delta_j)$$

$$-\int_a^b D_i(\frac{\mathrm{d}\delta_i}{\mathrm{d}t})^2dt - \int_a^b \sum_{i=1}^{n}\sum_{j=n+1}^{2n+m} D_{ij}cos\delta_{ij}\partial\delta_i \tag{6.18}$$

This can be written as

$$PTotal_i = PR_i + P_{Mag_i} + P_{Loss_i} \tag{6.19}$$

For applying these equations in real time and from PMU measurement, some assumptions are necessary. Damping coefficient D_{ij} is considered as 1 unless otherwise mentioned. Mechanical power P_m is considered to be equal to electrical power output P_e. Taking these assumptions and the deviations from steady state into considerations, we get:

$$\Delta PR_i = -\Delta P_{e_i}\Delta\delta_i \tag{6.20}$$

$$\Delta P_{Mag_i} = \Delta Q_{e_i}\Delta cos(\delta_{ij}) \tag{6.21}$$

$$\Delta P_{Loss_i} = -\Delta\omega_i^2 T_s$$

$$= -(2\pi\Delta f_i)^2 T_s \tag{6.22}$$

This can be written as

$$PTotal_{t+1} = PTotal_t + \Delta PR_i + \Delta P_{Mag_i} + \Delta P_{Loss_i} \tag{6.23}$$

6.2.1 Load modelling

In the development of strict Lyapunov functions of the form commonly used in power system analysis, it is necessary to assume reactive power load to have a dynamic response of the form shown in Fig. 6.1. To ensure that a strict Lyapunov function is obtained, it is necessary to restrict the reactive power transient response to,

$$Q_{ti}(V_i) = Q_{ti}^0 ln(\frac{V_i}{\psi_i}) \tag{6.24}$$

Combining load modeling with former equations, the final equations for the proposed algorithm becomes,

$$\Delta PR_i = -\Delta P_{e_i} \Delta \delta_i \tag{6.25}$$

$$\Delta P_{Mag_i} = \Delta Q_{e_i} \Delta cos(\delta_{ij}) \Delta ln(V_i) \tag{6.26}$$

$$\begin{aligned} \Delta P_{Loss_i} &= -\Delta \omega_i^2 T_s \\ &= -(2\pi \Delta f_i)^2 T_s \end{aligned} \tag{6.27}$$

This can be written as

$$PTotal_{t+1} = PTotal_t + \Delta PR_i + \Delta P_{Mag_i} + \Delta P_{Loss_i} \tag{6.28}$$

6.3 Challenges in Actual Power System

In real life implementation of the proposed algorithm, several challenges were faced.

6.3.1 Selection of PMU measurements

Any transmission line, transformer or generator that has PMU measurements of voltage, current and frequency/angle, can be used to estimate the DEF flow in that element. The most efficient are measurements in transmission elements connecting generators to the system

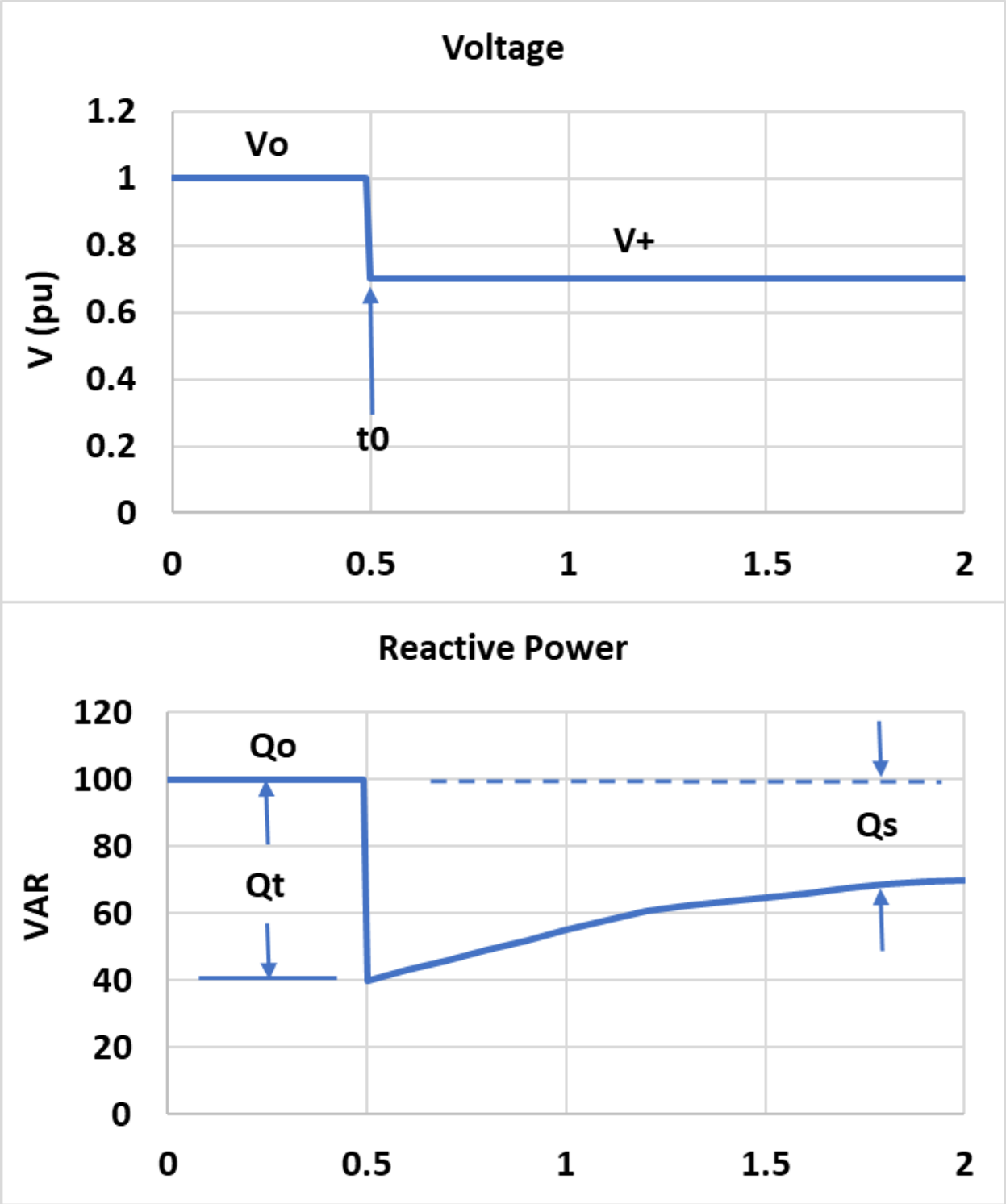

Fig. 6.1: Voltage vs reactive power in load

because a generator is usually the most likely source of sustained oscillations.

6.3.2 Frequency identification of sustained oscillations

Finding the frequency or mode of interest is very important for applying this method. Low frequency oscillation can create system wise collapse if remains uncontrolled. To find the mode of interest, subspace identification is applied with the proposed algorithm. Subspace identification method can not only find the mode of interest but also can provide system matrices which are helpful to find damping ratio and control purposes. With subspace identification, differentiating between natural and forced mode is also possible.

6.3.3 Data pre-processing

Ideal steady-state conditions in actual power systems practically do not exist so the de-trending process is required in order to estimate steady-state quantities. After de-trending, the PMU data are then passed through a bandpass filter which needs to be tuned according to the dominant mode found from subspace identification process.

6.3.4 Finding appropriate sample time

Selecting an appropriate sampling time is absolutely necessary for both subspace identification technique and proposed algorithm. If the sampling time is very small, subspace identification process needs to handle large data size and makes the whole process not suitable for online implementation. And if the sampling time is too large, it can not contain the necessary data to capture the event.

6.3.5 Calculating slope of the linear approximation

Slope of all the generator's linear approximation of total energy curve needs to be calculated. If data is taken for a small time after the event, sometimes the result is misleading. So an adequate amount of data is required for choosing the source location. A threshold is set in our method to find the appropriate length of data required. When 10 consecutive data sample's slope is under the set threshold, the algorithm stops running.

6.4 Test System, Cases and Results

6.4.1 Test System I

For this chapter, WECC 179 bus power system is used as a test system. This power system has 29 generators and 526 lines. The test system is shown in Fig.6.29.

For our proposed method, PMU data consists of the generator's voltage and angle data, each generator's adjacent bus's voltage data and the current flowing through the generators and their adjacent buses are collected. Total data for 40 seconds as collected where sampling time is 0.0333 seconds. These data are then used to identify the oscillation source location in the system by using proposed method executed in MATLAB. The flowchart of the proposed method is shown in Fig. 6.3.

6.4.2 Test Cases

Two types of test cases are created to check the proposed method's functionality. These two types are : Natural mode cases and Forced mode cases. For each type of cases, there are 3 different events created.

6.4.2.1 Natural Mode Cases

For natural mode cases, the proposed method is applied on 3 different cases each containing a natural poorly damped mode created by a three phase short circuit at different buses. These cases are represented as ND_x, where x refers to 1, 2 and 3.

- Case ND1: A three phase short circuit is added at bus 159 at 0.5 second and cleared at 0.55 second. The PMU data are collected and the total power is calculated through the proposed algorithm. The slope of the linear approximation of all generator's total power is calculated and Bus 45's slope is found to be the highest. The natural mode and it's damping ratio is found as $1.4122Hz$ and 0.12%. Curve of total power from the generator's for this case is shown in Fig. 6.4.

- Case ND2: A three phase short circuit is added at bus 79 at 0.5 second and cleared

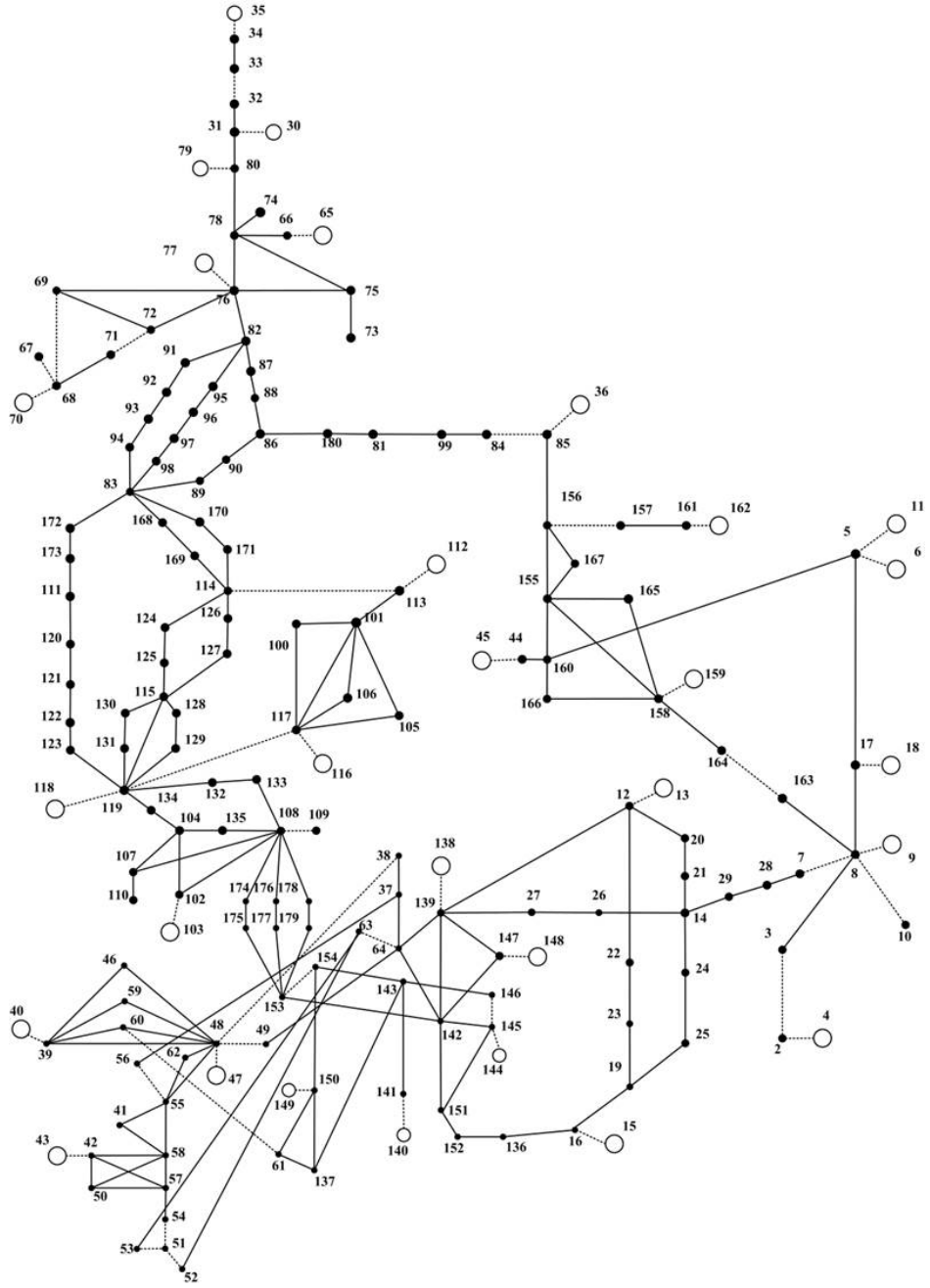

Fig. 6.2: Test System.

at 0.55 second. The PMU data are collected and the total power is calculated through the proposed algorithm. The slope of the linear approximation of all generator's total power is calculated and Bus 65's slope is found to be the highest. The natural mode and it's damping ratio is found as $0.374Hz$ and 0.052%. Curve of total power from the generator's for this case is shown in Fig. 6.5.

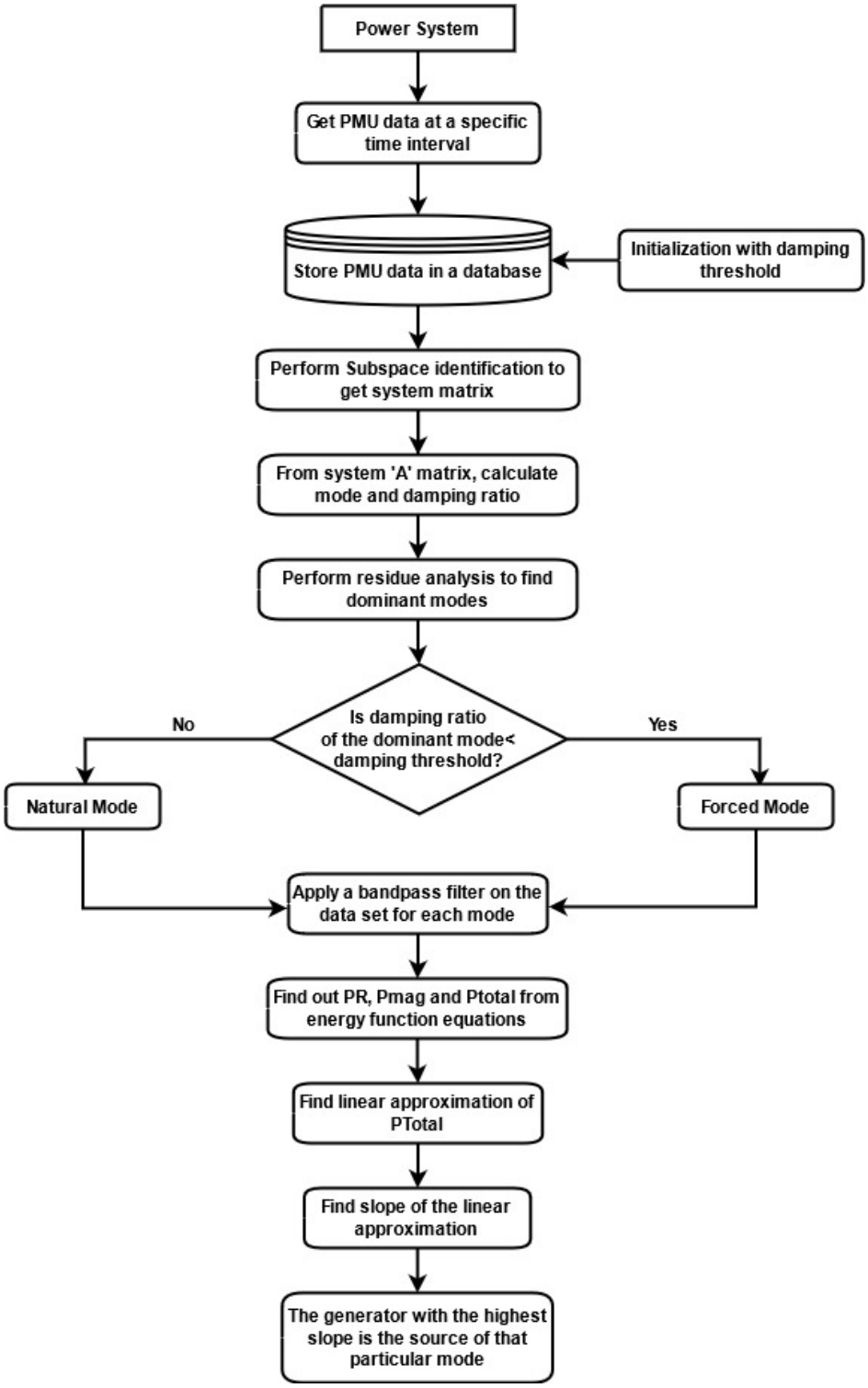

Fig. 6.3: Overall flow diagram.

- Case ND3: A three phase short circuit is added at bus 159 at 0.5 second and cleared at 0.51 second. The PMU data are collected and the total power is calculated through

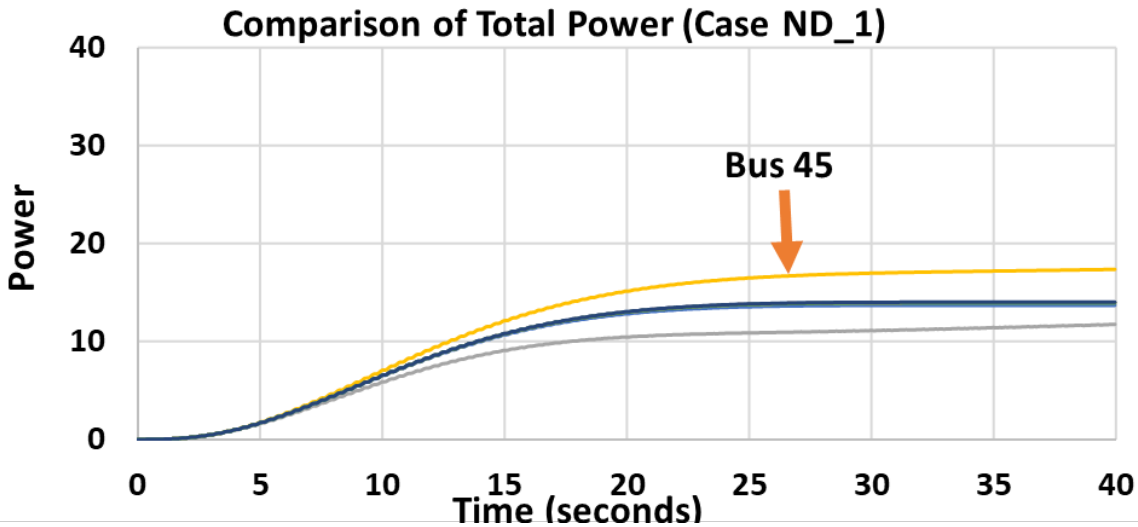

Fig. 6.4: Total power graph for case ND1

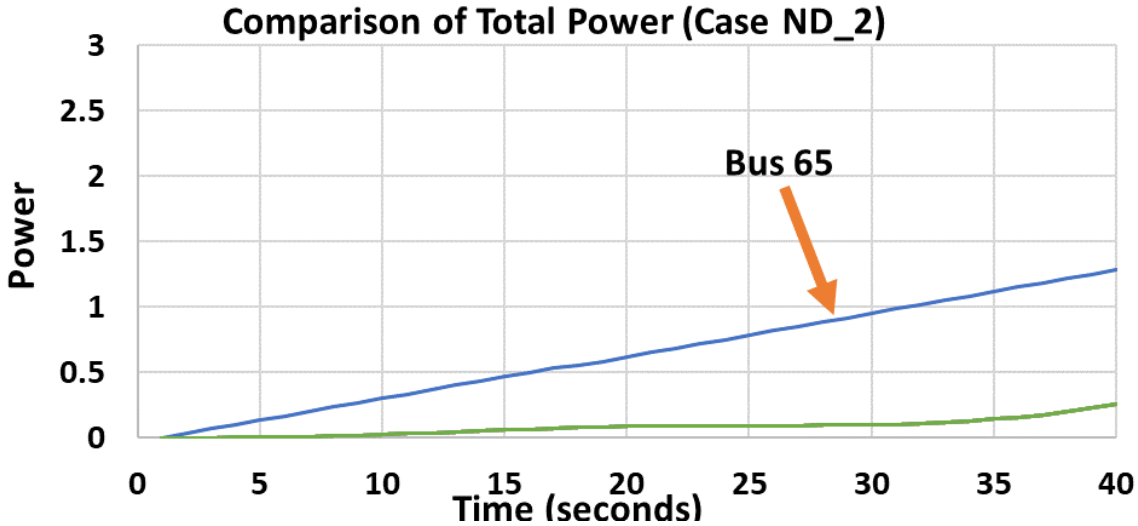

Fig. 6.5: Total power graph for case ND2

the proposed algorithm. The slope of the linear approximation of all generator's total power is calculated and Bus 45 and Bus 159's slope is found to be the highest. So, in this case, two sources with comparable contribution created a single unstable mode. The natural mode and it's damping ratio is found as $1.409Hz$ and -0.46%. Curve of total power from the generator's for this case is shown in Fig. 6.6.

The summary of natural mode cases are summarized in Table 6.1 and 6.2.

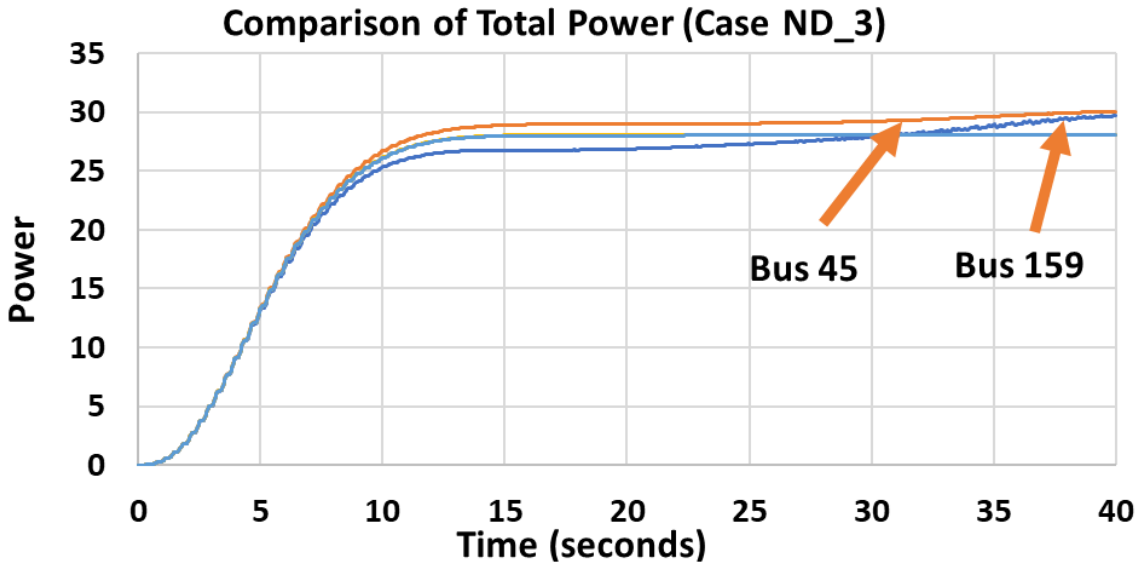

Fig. 6.6: Total power graph for case ND3

Table 6.1: Summary of Mode Identification for Natural mode cases

Cases	Mode(Hz)	Damping Ratio(%)	Mode(Hz)	Damping Ratio(%)
Case 1	1.41	0.01	1.4122	0.12
Case 2	0.37	0.02	0.374	0.052
Case 3	1.41	-0.93	1.409	-0.46

Table 6.2: Summary of Oscillation Source Location for Natural mode cases

Cases	Mode(Hz)	Fault Location	Oscillation Source Location
Case 1	1.4122	159	45
Case 2	0.374	79	65
Case 3	1.409	159	45,159

6.4.2.2 Forced Mode Cases

For forced mode cases, the proposed method is applied on 3 different cases each containing a forced mode created by a three phase short circuit at different buses. These cases are represented as FD_x, where x refers to 1, 2 and 3.

- Case FD1: Forced oscillation is injected into excitation system as a sinusoidal signal at generator 79 with a frequency 0.86Hz to cause resonance. The PMU data are collected and the total power is calculated through the proposed algorithm. The slope of the

linear approximation of all generator's total power is calculated and Bus 79's slope is found to be the highest. The Forced mode and it's damping ratio is found as $0.8611Hz$ and 0.014%. Curve of total power from the generator's for this case is shown in Fig. 6.7.

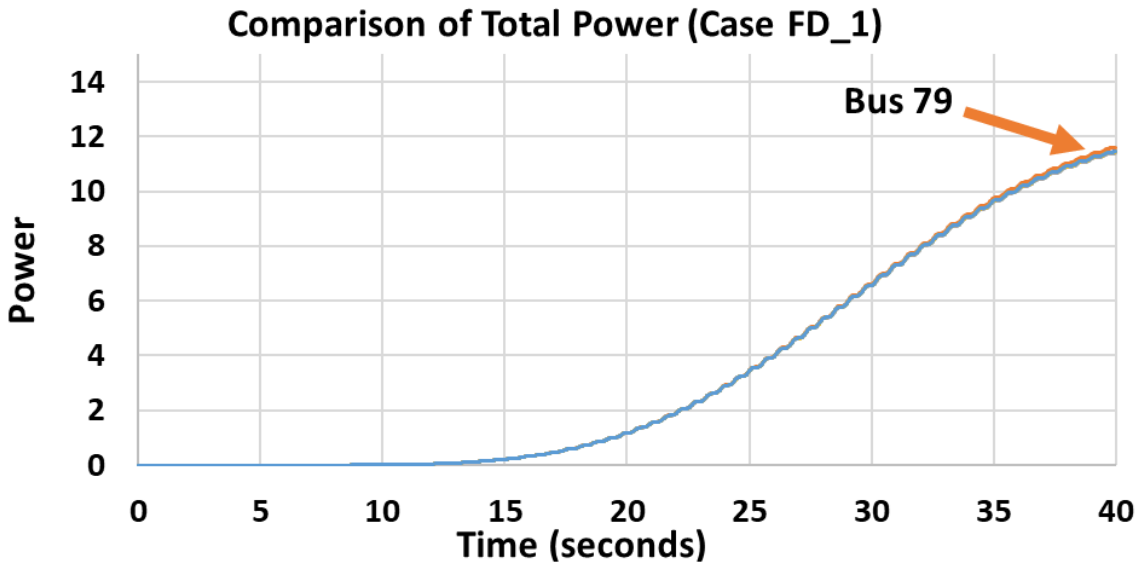

Fig. 6.7: Total power graph for case FD1

- Case FD2: Forced oscillation is injected into excitation system as a sinusoidal signal at generator 79 with a frequency 0.81Hz. The PMU data are collected and the total power is calculated through the proposed algorithm. The slope of the linear approximation of all generator's total power is calculated and Bus 79's slope is found to be the highest. The forced mode and it's damping ratio is found as $0.812Hz$ and 0.024%. Curve of total power from the generator's for this case is shown in Fig. 6.8.

- Case FD3: Forced oscillation is injected into excitation system as a sinusoidal signal at generator 79 with a frequency 0.89Hz. The PMU data are collected and the total power is calculated through the proposed algorithm. The slope of the linear approximation of all generator's total power is calculated and Bus 45 and Bus 79's slope is found to be the highest. So, in this case, two sources with comparable contribution created a

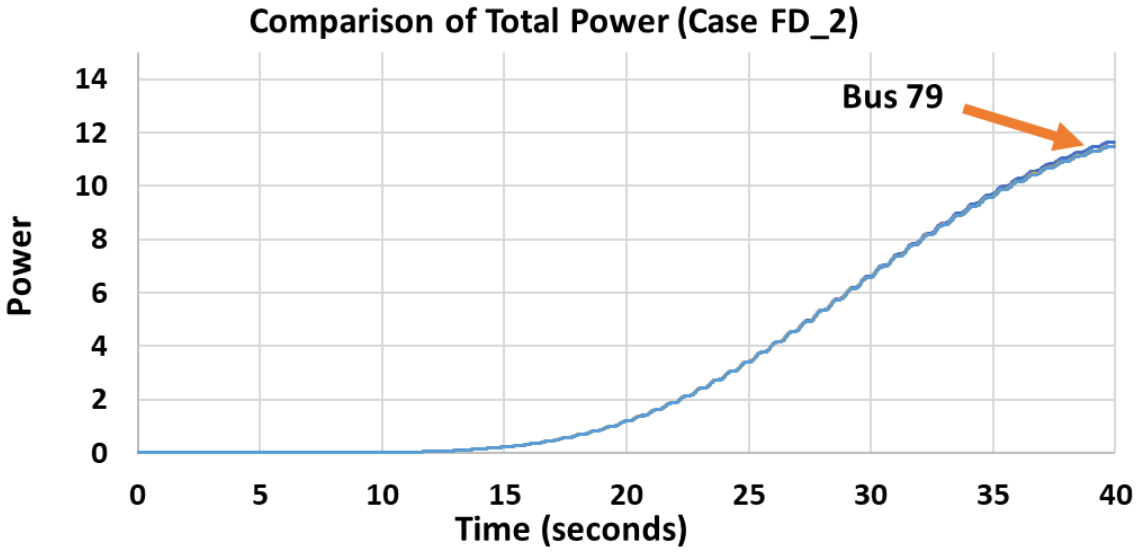

Fig. 6.8: Total power graph for case FD2

single unstable mode. The forced mode and it's damping ratio is found as $0.886Hz$ and 0.009%. Curve of total power from the generator's for this case is shown in Fig. 6.9.

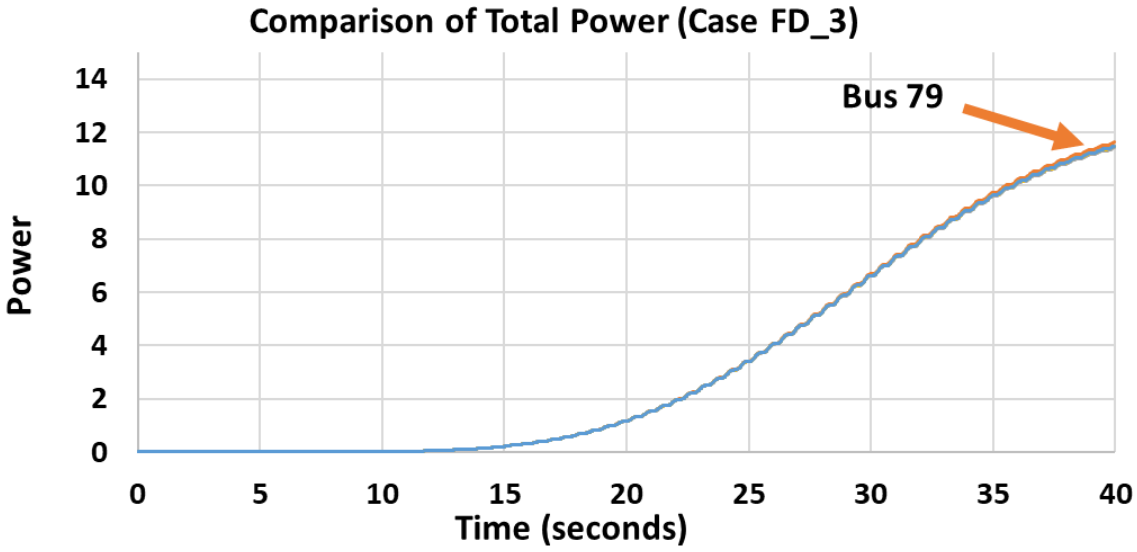

Fig. 6.9: Total power graph for case FD3

The summary of forced mode cases are summarized in Table 6.3 and 6.4.

Table 6.3: Summary of Mode Identification for Forced mode cases

Cases	Mode(Hz)	Damping Ratio(%)	Mode(Hz)	Damping Ratio(%)
Case 1	0.86	0.00	0.8611	0.014
Case 2	0.81	0.00	0.812	0.024
Case 3	0.89	0.00	0.886	0.009

Table 6.4: Summary of Oscillation Source Location for Forced mode cases

Cases	Mode(Hz)	Oscillation Source Location
Case 1	0.8611	79
Case 2	0.812	79
Case 3	0.886	79

6.4.3 Test System II: IEEE 68 Bus

The IEEE 68 bus power grid is used as a larger system. The natural inter-area mode for this system is 0.60Hz. This system has 5 areas and consists of 68 buses and 16 generators.

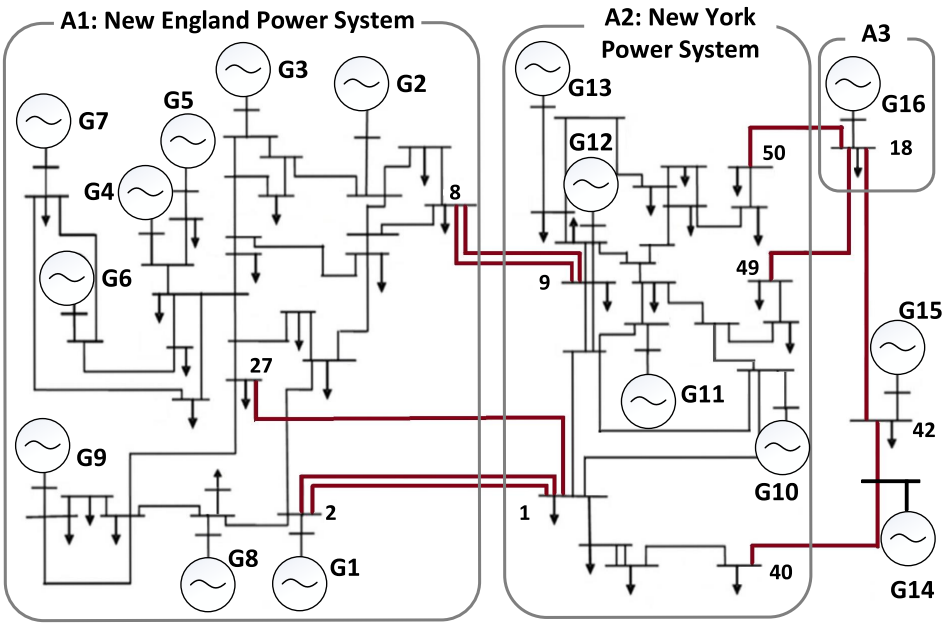

Fig. 6.10: IEEE 68 Bus study system.

6.4.4 Small signal stability study

Our test case IEEE 68 bus system has no PSS on any of the generators. Table 6.6 shows the dominant modes participation factor in our test cases. It shows that 0.404 Hz is participated

Table 6.5: IEEE 68 bus system features.

Buses & Generators	68 Buses 16 Generators	Areas	5
Total Active Power Generation (MW)	17787.53	Total Active Load (MW)	17620.65
Total Reactive Power Generation (MVAR)	2496.53	Total Reactive Load (MVAR)	1671.76

with generator 13.

Table 6.6: Small signal stability analysis of IEEE 68 bus system without PSS

Mode (Hz)	Damping ratio (%)	States	Participation factor
0.404	-0.438	Delta (13)	1
		SM (13)	0.741
		SM (15)	0.556
		SM (14)	0.524

6.4.5 Base Case

For test case, a 10 cycle fault is applied on bus 68 and measurement from all buses and generators are collected through PMUs. The fault is applied at 3 seconds and this event caused a 0.40 Hz interarea oscillatory mode to occur. Fig. 6.11 represents the speed of all 16 generators under the fault and Fig. 6.12 represents voltage of all 16 generators.

Fig. 6.13 represents base case energy graph obtained from dissipated energy flow algorithm and Fig. 6.14 represents base case energy graph obtained from proposed algorithm. Both algorithm detects generator 13 as the source location of the mode based on slopes calculated from both algorithm which are represented in Fig. 6.15 and Fig. 6.16.

6.4.6 Load Increase Case 1

For this case, an increased load of 10% is applied and also a line resistance increase of 10% is applied to increase loss. A 10 cycle fault is applied on bus 68 and measurement from all buses and generators are collected through PMUs. The fault is applied at 3 seconds and this event caused a 0.40 Hz interarea oscillatory mode to occur. Fig. 6.17 represents the speed of all 16 generators under the fault and Fig. 6.18 represents voltage of all 16 generators.

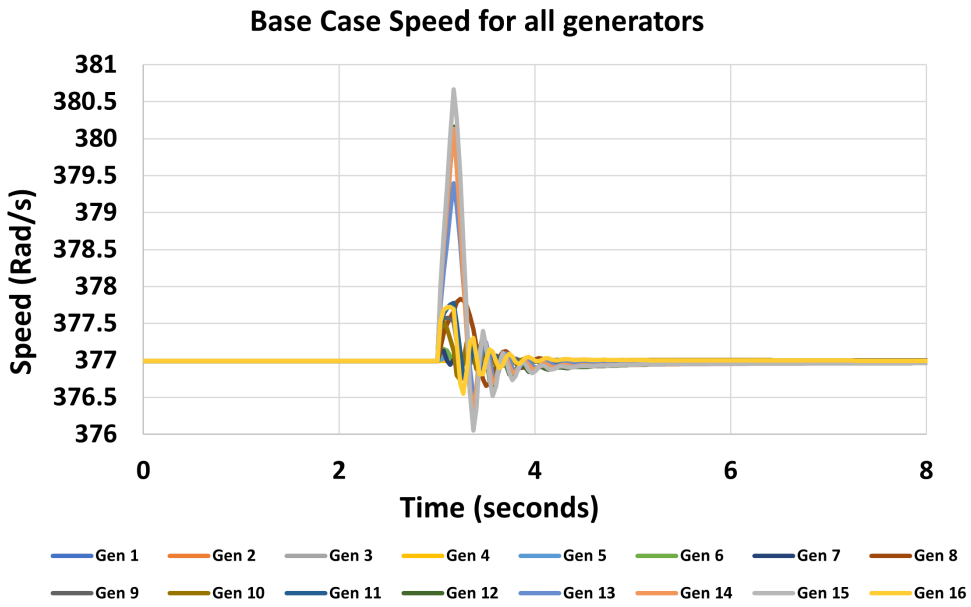

Fig. 6.11: Base Case Speed of all generators

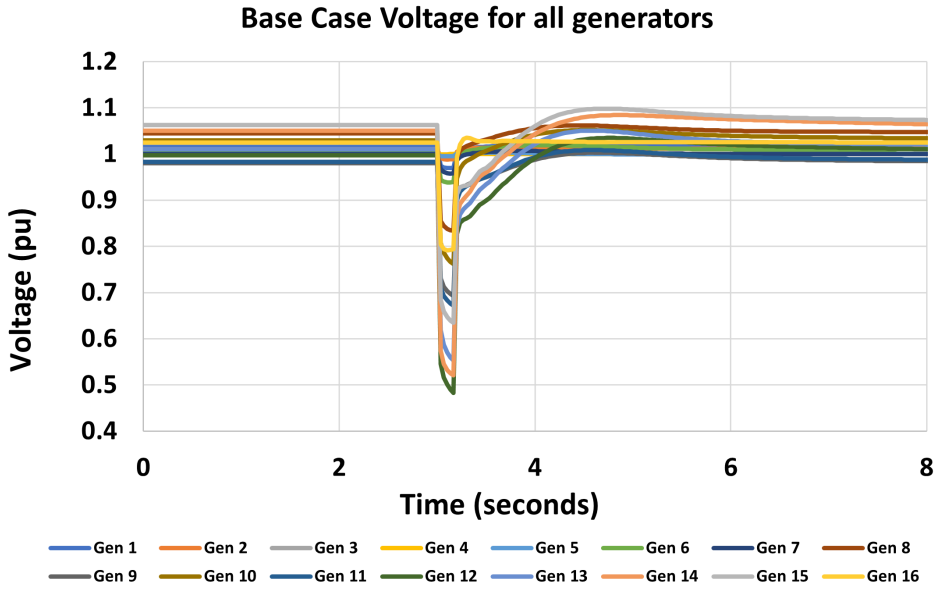

Fig. 6.12: Base Case Voltage of all generators

Fig. 6.19 represents base case energy graph obtained from dissipated energy flow algorithm and Fig. 6.20 represents base case energy graph obtained from proposed algorithm. DEF algorithm detects generator 16 as the source location while proposed algorithm detects generator 13 as the source location of the mode based on slopes calculated from both

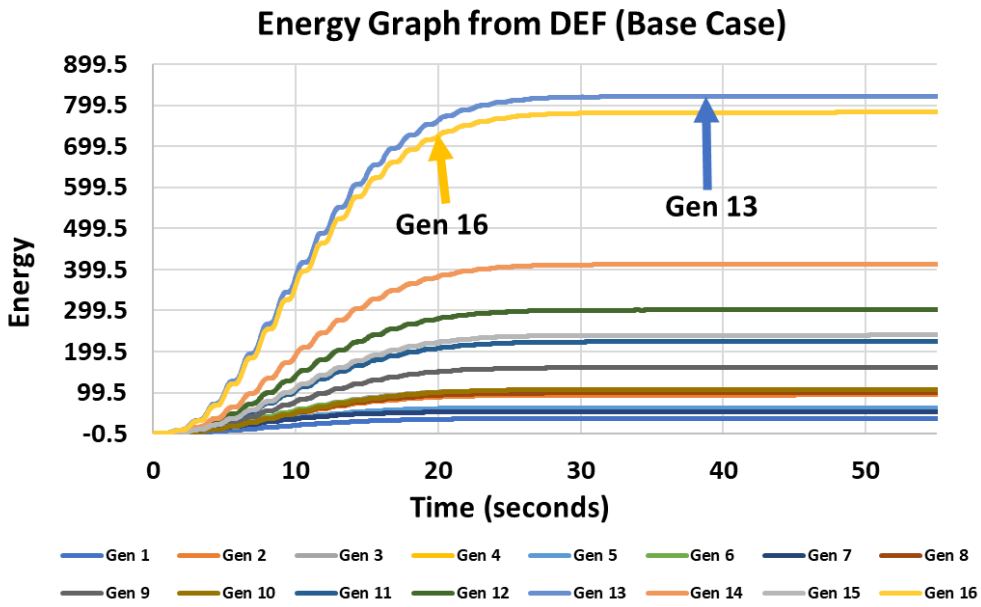

Fig. 6.13: Base Case Dissipated Energy of all generators from DEF

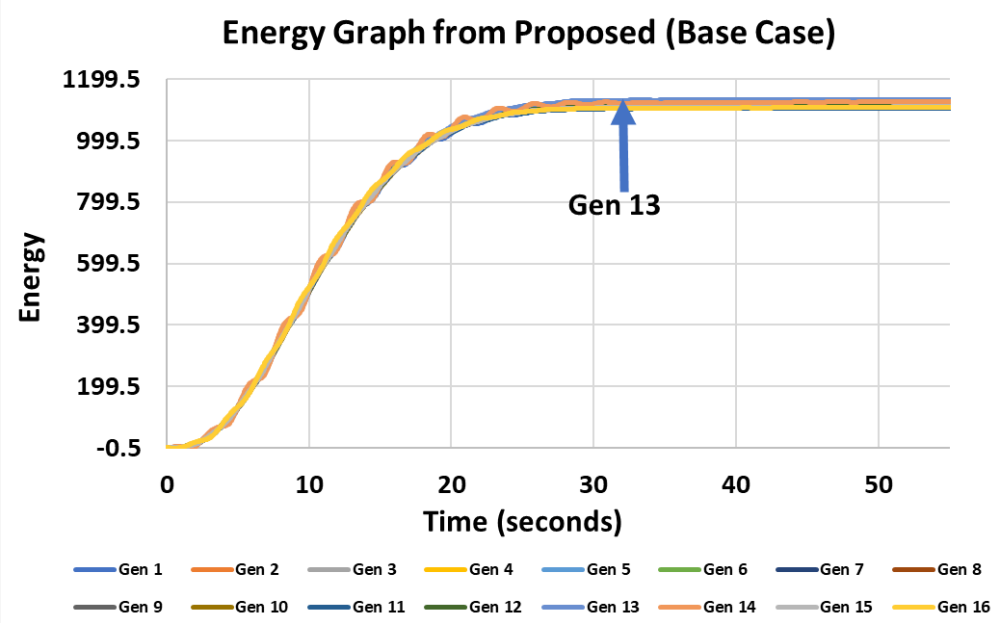

Fig. 6.14: Base Case Energy of all generators from Proposed Algorithm

algorithm which are represented in Fig. 6.21 and Fig. 6.22.

6.4.7 Load Increase Case 2

For this case, an increased load of 15% is applied and also a line resistance increase of 15% is applied to increase loss. A 10 cycle fault is applied on bus 68 and measurement from all

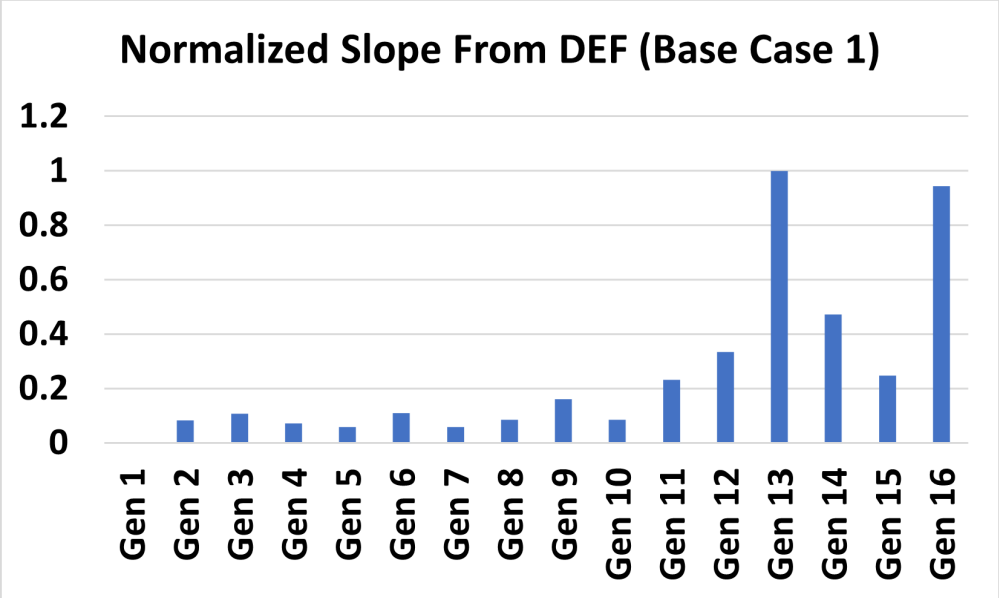

Fig. 6.15: Base Case Slope of all generators from DEF

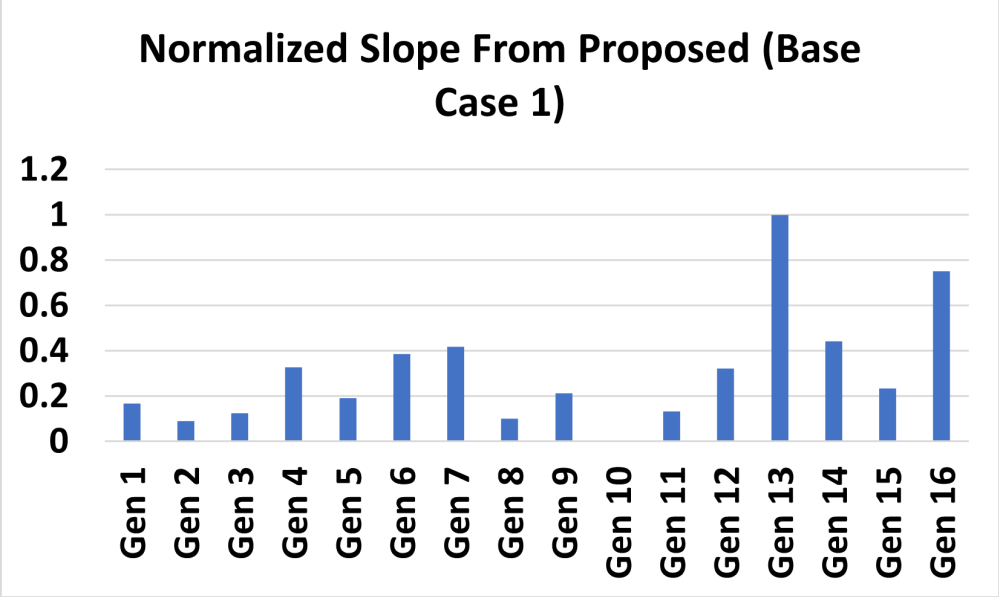

Fig. 6.16: Base Case Slope of all generators from Proposed Algorithm

buses and generators are collected through PMUs. The fault is applied at 3 seconds and this event caused a 0.40 Hz interarea oscillatory mode to occur. Fig. 6.23 represents the speed of all 16 generators under the fault and Fig. 6.24 represents voltage of all 16 generators.

Fig. 6.25 represents base case energy graph obtained from dissipated energy flow algorithm and Fig. 6.26 represents base case energy graph obtained from proposed algorithm.

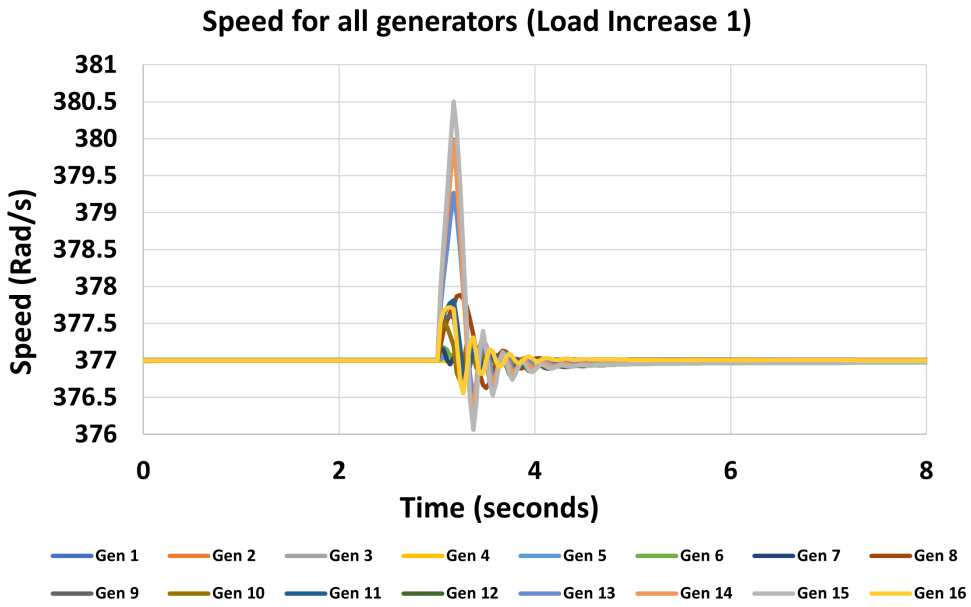

Fig. 6.17: Load Increase Case 1 Speed of all generators

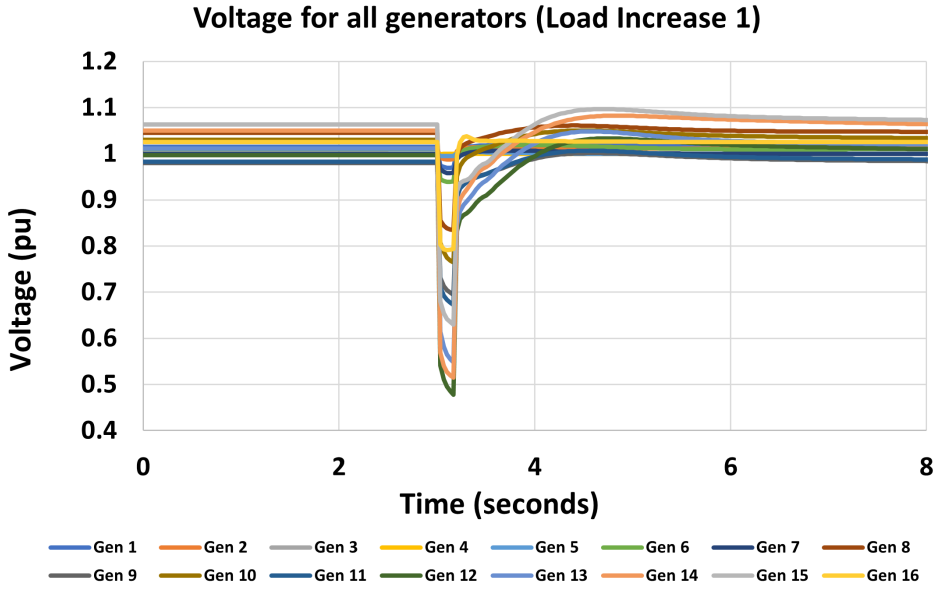

Fig. 6.18: Load Increase Case 1 Voltage of all generators

DEF algorithm detects generator 16 as the source location while proposed algorithm detects generator 13 as the source location of the mode based on slopes calculated from both algorithm which are represented in Fig. 6.27 and Fig. 6.28.

Table 6.7 and Table 6.8 summarizes the result of source location identification of all 3

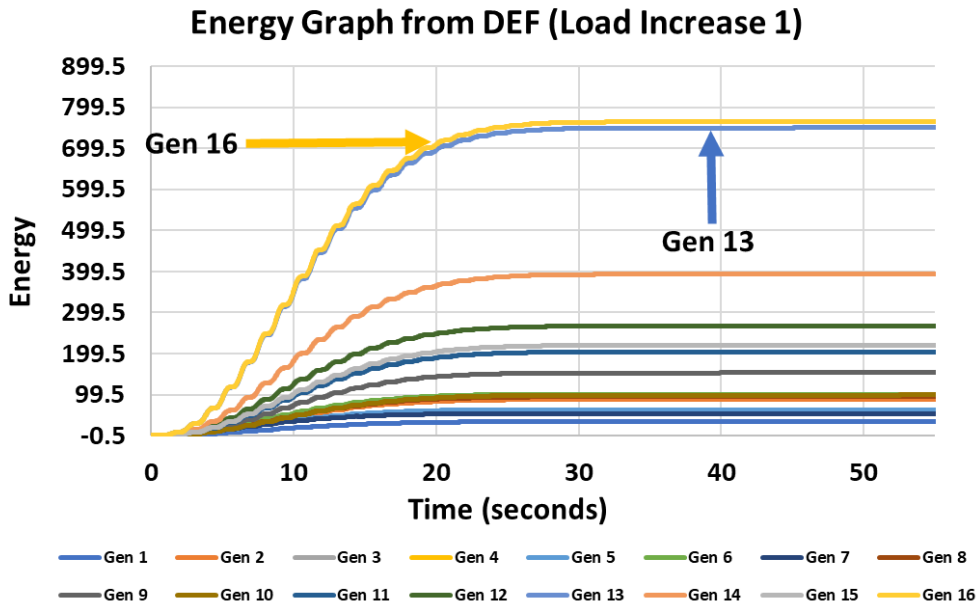

Fig. 6.19: Load Increase Case 1 Dissipated Energy of all generators from DEF

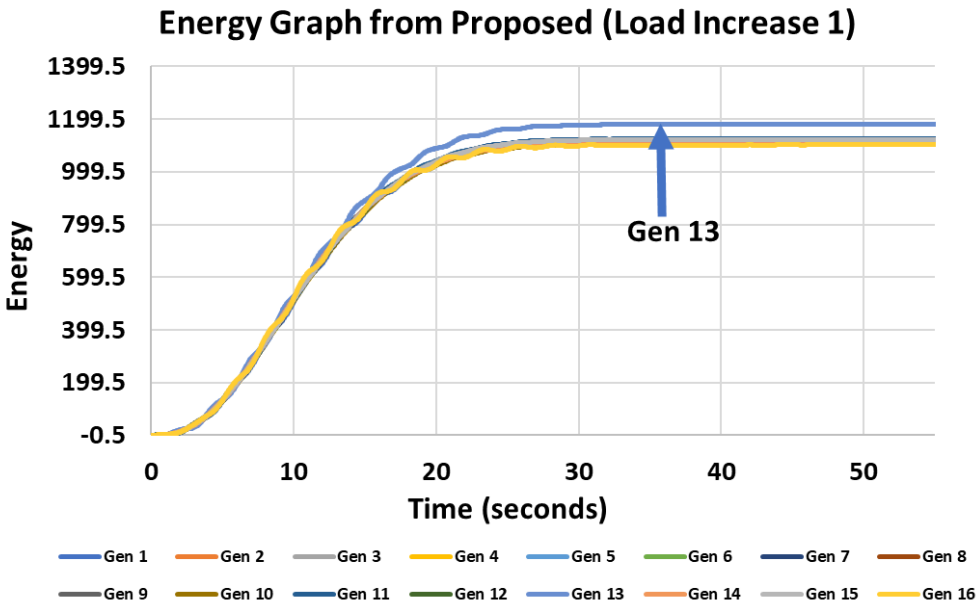

Fig. 6.20: Load Increase Case 1 Energy of all generators from Proposed Algorithm

cases of IEEE 68 bus from both algorithm.

6.4.8 Test System III: PESGM Oscillation Source Location Competition Test System

This test case was used in 2021 PESGM OSL contest. The test case was generated by simulating a WECC 240 bus test system [102] developed by NREL based on preference. The

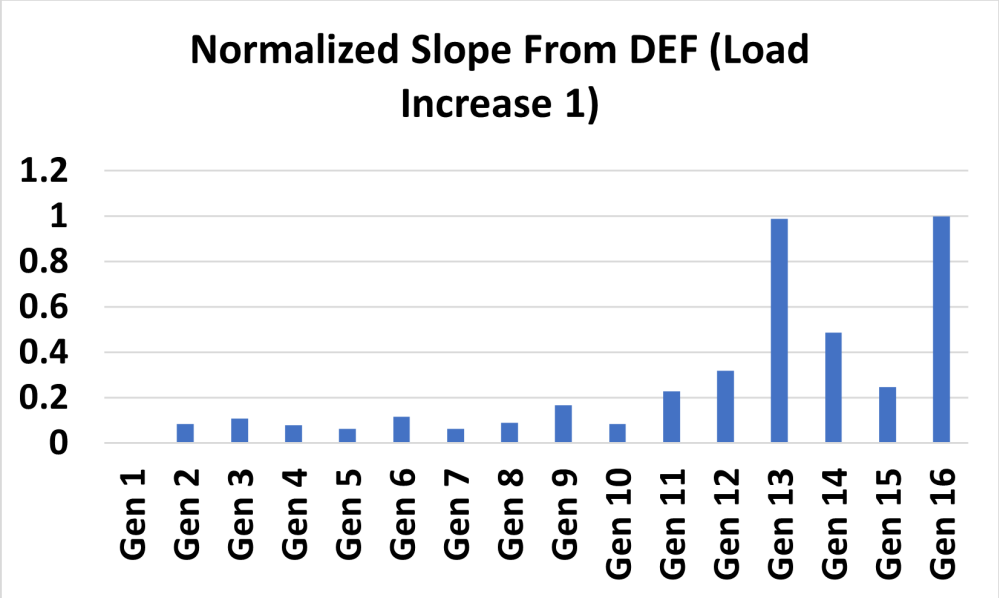

Fig. 6.21: Load Increase Case 1 Slope of all generators from DEF

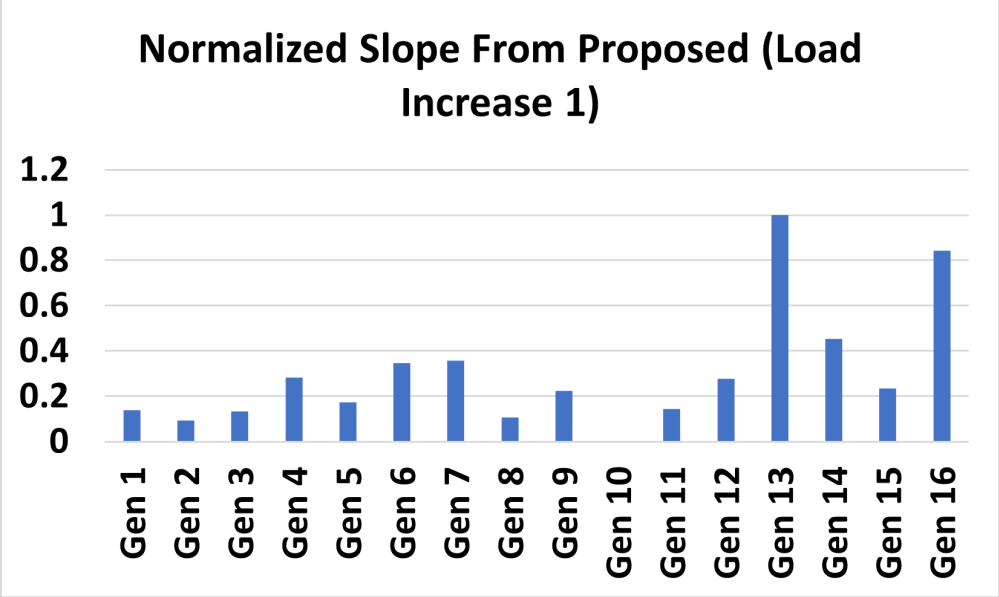

Fig. 6.22: Load Increase Case 1 Slope of all generators from Proposed Algorithm

Table 6.7: Summary of Oscillation Source Location for IEEE 68 bus cases from DEF

Cases	Mode(Hz)	Oscillation Source Location
Base Case	0.4011	Generator 13
Load Increase 1	0.4025	Generator 16
Load Increase 2	0.4068	Generator 16

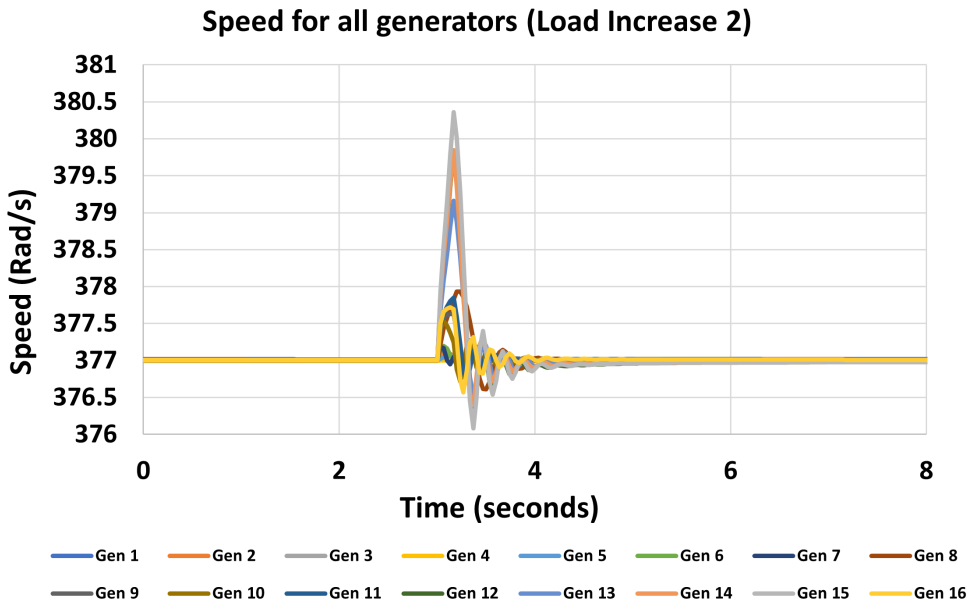

Fig. 6.23: Load Increase Case 2 Speed of all generators

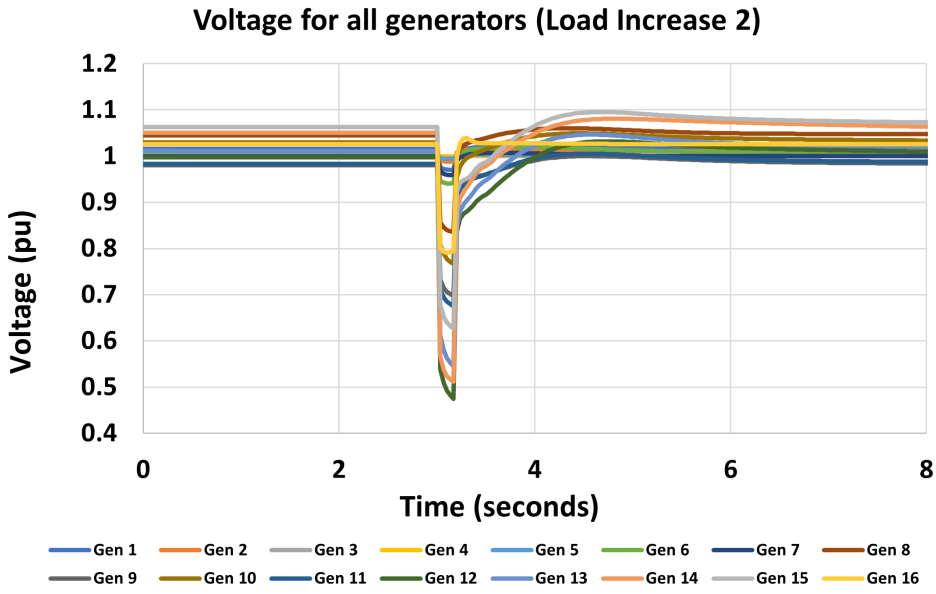

Fig. 6.24: Load Increase Case 2 Voltage of all generators

Table 6.8: Summary of Oscillation Source Location for IEEE 68 bus cases from Proposed Method

Cases	Mode(Hz)	Oscillation Source Location
Base Case	0.4011	Generator 13
Load Increase 1	0.4025	Generator 13
Load Increase 2	0.4068	Generator 13

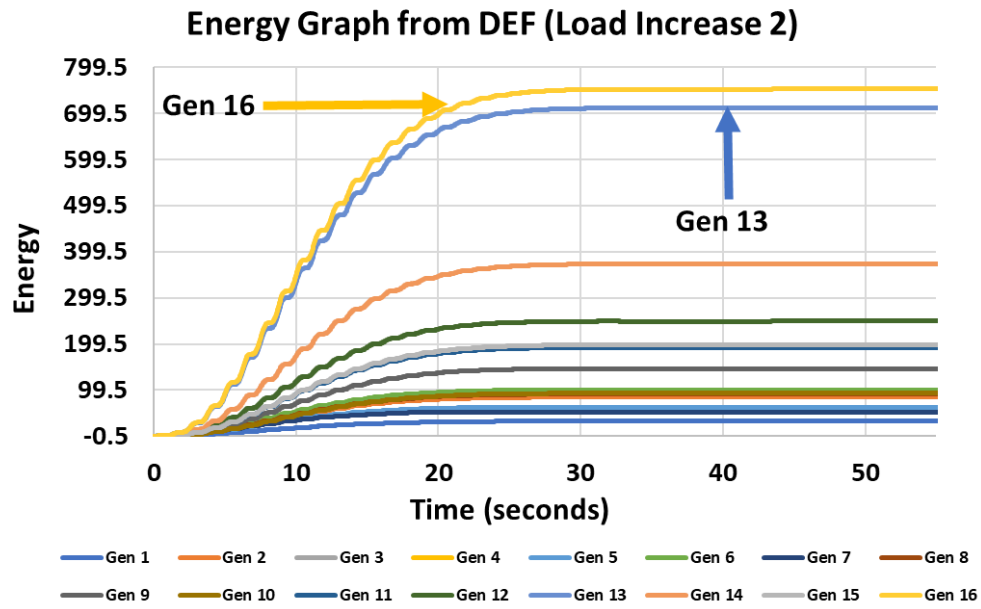

Fig. 6.25: Load Increase Case 2 Energy of all generators from DEF

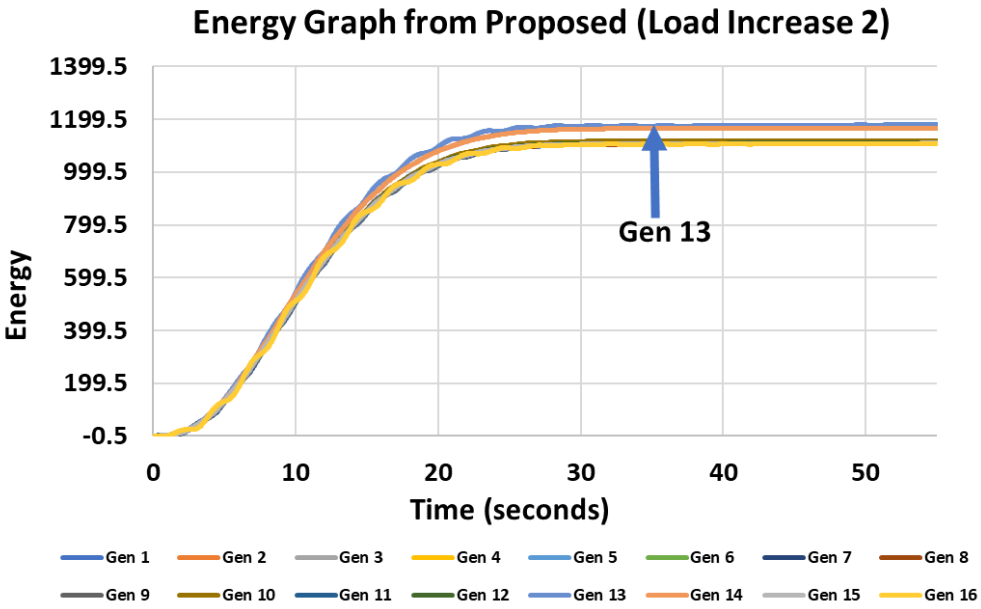

Fig. 6.26: Load Increase Case 2 Energy of all generators from Proposed Algorithm

system has 243 buses, 146 generating units at 56 power plants (including 109 synchronous machines and 37 renewable generators), 329 transmission lines, 122 transformers, 7 switched shunts and 139 loads. Fig. 6.29 shows one line diagram of the test case system.

Measurement data (Voltage, Current, Rotor speed) from different buses were given for

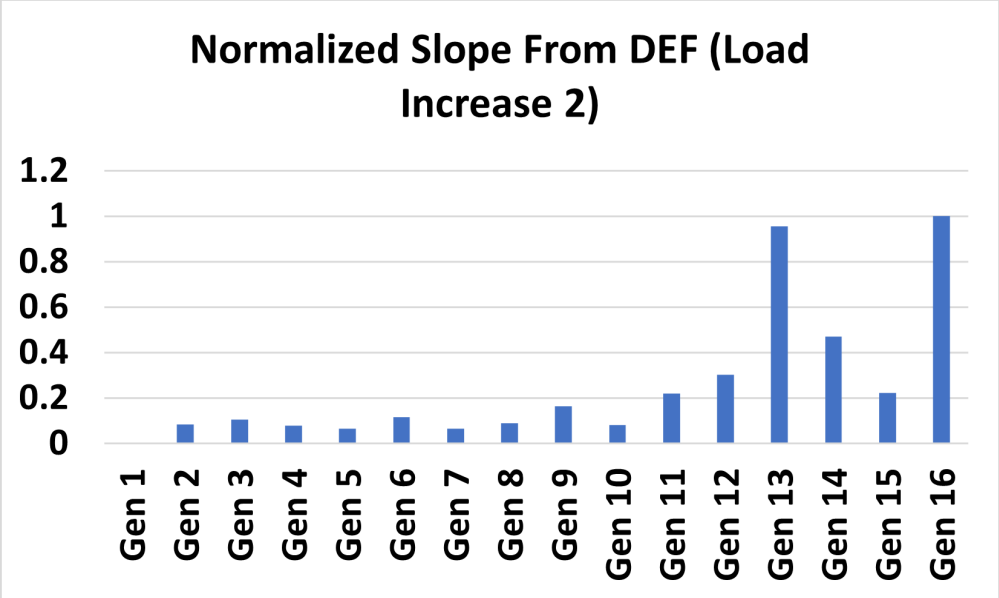

Fig. 6.27: Load Increase Case 2 Slope of all generators from DEF

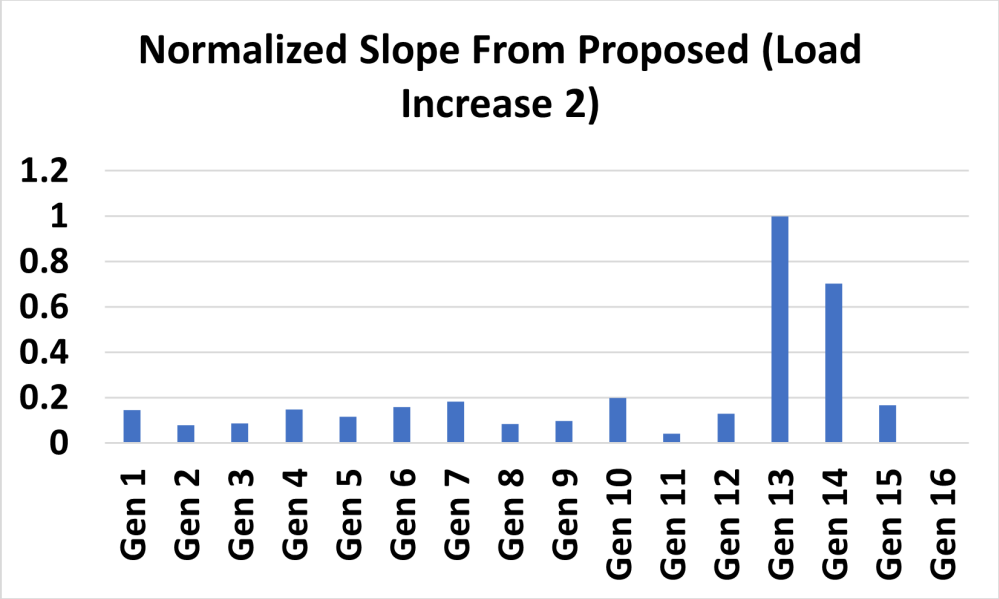

Fig. 6.28: Load Increase Case 2 Slope of all generators from Proposed Algorithm

identifying oscillation mode and locating the oscillation source from given data was the purpose of the competition. There were 5 different events for which measurement data were provided. But it is worth mentioning that measurement data were only available from some buses and generators; not from all the buses and generators. The solution was given and the solution was matched with our identification using the algorithm mentioned in this chapter.

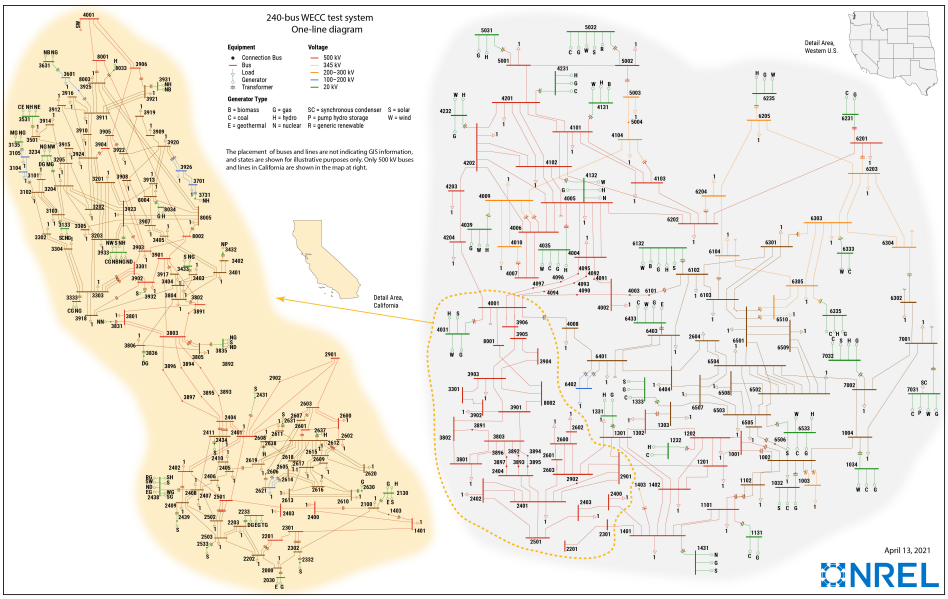

Fig. 6.29: Competition Test System.

The summary of the results are provided in Table 6.9 and 6.10.

Table 6.9: Summary of OSL Contest Solution

Case	Mode(Hz)	Type of Mode	Area Name	Bus
1	0.82	Natural	1-South	1431
2	1.19	Forced	2-California	2634
3	0.379	Forced	1-South	1131
4	1.27	Forced	3-North	7031
5	0.762,0.762	Forced,Natural	3-North	6533

Table 6.10: Summary of OSL Contest Solution by Proposed Algorithm

Case	Mode(Hz)	Type of Mode	Area Name	Bus
1	0.819	Natural	1-South	1431
2	1.189	Forced	2-California	2634
3	0.38	Forced	1-South	1131
4	1.27	Forced	3-North	7031
5	0.762,0.762	Forced,Natural	3-North	6533

This result is based on the slopes obtained from the linear approximation of the monitored generators' total power calculated through proposed algorithm in this chapter.

From Table 6.9 and 6.10, it is clear that mode and their type is precisely identified for

all cases of the competition test by proposed algorithm. In some cases, the area and the bus location is not matching. Those are the cases where measurement data are missing from those buses and generators. In those cases, the nearest bus is identified by proposed algorithm where measurement data was available. Also, the given solution detects the type of asset and controller (Governor/Exciter) from where the oscillatory mode is originated. Our proposed algorithm is not capable of identifying these yet.

6.5 Summary

The proposed algorithm in this chapter can identify mode, type of mode, origin area and origin location precisely when measurement data is available. If measurement data is not available, the proposed algorithm can identify the nearby buses in same area where measurement is available. For the case of unavailability of measurement data; another algorithm to extrapolate the missing data from available data using subspace identification system matrix is under work. Also, for identifying the controller type (Governor/Exciter) identification, model data along with measurement data is necessary. These challenges are acknowledged and in future work, these studies will also be included. Oscillatory modes in power system can also occur from inverter based resources (IBR) integration to existing grid. In the next chapter, different IBR connection architecture and their performance will be explored as well as low frequency oscillation identification methods will be applied on measurement data to find out power system oscillation due to IBR integration.

CHAPTER 7: Grid-forming Inverters Interfacing Battery Energy Storage Systems

7.1 Introduction and main contributions

Increasing the penetration of inverter-based generation in a power system results in reduced system inertia, which can lead to various stability issues. As a result, regulation of voltage and frequency are of considerable concern with the increased usage of non-synchronous generation. Grid-forming (GFM) inverters can provide options to help address these challenges [103, 104]. Battery energy storage systems (BESSs) are important for the economic and reliable operation of the grid, because of their capability for energy storage, bidirectional energy exchange, and fast output response [105]. With the increasing penetration of renewable energy sources on the grid, where these energy sources usually operate based on maximum power point tracking (MPPT) for economic purposes, the importance of BESSs is becoming more vital. Thus, grid-forming inverters that are interfaced with battery energy storage systems can play a significant role in modern power systems.

To achieve the required system performance, appropriate control strategies are needed for GFM inverters integrated with a BESS. Among several of the control methods for grid-forming, droop-based control is the most common. The droop-based control method provides regulation of voltage and frequency by mimicking the operation characteristics of a conventional synchronous machine. In this chapter, a detailed architecture of a GFM based inverter is discussed when a BESS along with a PV are connected to the grid. Several load change scenarios, fault scenarios, and grid connected/islanded operation scenarios are performed for two different test systems. In one test system, the BESS is connected to a single machine infinite bus (SMIB) and another test system contains a larger grid system (IEEE 13 bus) with a BESS integrated. Major BESS components and different BESS chemistry types are also briefly discussed. Finally, a measurement-based identification method, subspace identi-

fication, is applied on the DC-Link dynamics to identify modal information for all the cases on both test systems. Part of this work is published by the author in [106]. The main contribution of this chapter is as follows:

- Explore different inverter based resources especially BESS integration to modern power grid.
- To showcase grid forming and grid following architecture in power system network.
- To showcase performance of grid forming inverter in islanding mode of operation.
- To implement a measurement based identification method to identify oscillatory mode due to IBR integration to existing power grid.

Topics: inverter architecture (7.2), control architecture (7.3), BESS model (7.4), integrated BESS / GFM inverter model (7.5), large-scale BESS (7.6), application example (7.7), and simulation results (7.8).

7.2 Inverter Architecture

A conventional alternating-current (AC) power system grid mainly consists of synchronous generators, which have various control architectures that are commonly used. As an example, voltage regulation is obtained through excitation control of synchronous generators, whereas frequency control is achieved through governor control. Moreover, the inertia of the prime-mover and the rotor of the synchronous generator is required for stable operation of the power grid, as they help to keep voltage and frequency within acceptable limits during operational events, such as load changes and fault conditions. Synchronous generators also have an automatic voltage regulator mechanism and low output impedance. They also provide short circuit current or fault current contribution capability, which helps to keep the system stable, even after a fault and in clearing the fault [52].

However, with increasing demand for electric power consumption, variable distributed energy resources (DERs) are being integrated with conventional power grids. These DERs are mainly inverter based resources. Various DERs, such as photovoltaic (PV) and wind energy production, are becoming more and more common, as a result of reduced costs, availability of the resources, and the increasing demand for energy. One major challenge regarding the use of these DERs relates to the intermittent output characteristics of these resources, since the output from these DERs is directly dependent on the weather condition in the installation area. As a result of the intermittent nature, DERs often work on the maximum power point tracking (MPPT) principle. Consequently, the intermittent nature eventually results in reduced efficiency of the independent source. However, the overall efficiency of DERs can be improved by integration with the utility grid. A microgrid can offer higher reliability, improved power quality, reduced carbon emissions, and a cost-competitive solution over the traditional power distribution system. The connection of the microgrid or DERs to the utility grid is established through an inverter as the interfacing medium [107, 108].

Based on the interaction with the grid and controller implementation, inverters can be divided into two main groups: grid-following (GFL) and grid-forming (GFM) [103, 104, 109]. In GFL, inverter based resources are designed to follow the grid voltage and feed current per the existing voltage. As a result, they are focused on injecting active power into the grid with MPPT, whereas the reactive power supply is minimal. GFL can be further divided into two categories based on reactive power support: grid-feeding and grid-supporting. In the grid-feeding mode, reactive power support is zero. Whereas, in the grid-supporting mode, reactive power is provided to support grid voltage in any deviation. The behavior of the GFL architecture is similar to a current source. On the other hand, in the GFM architecture, inverters work as a voltage source. They are controlled to maintain voltage and frequency. As a result, they can perform in an islanded mode too. Figure 7.1 depicts the different categories of grid connected inverters, where P is active power, Q is reactive power, V is voltage, and f is frequency.

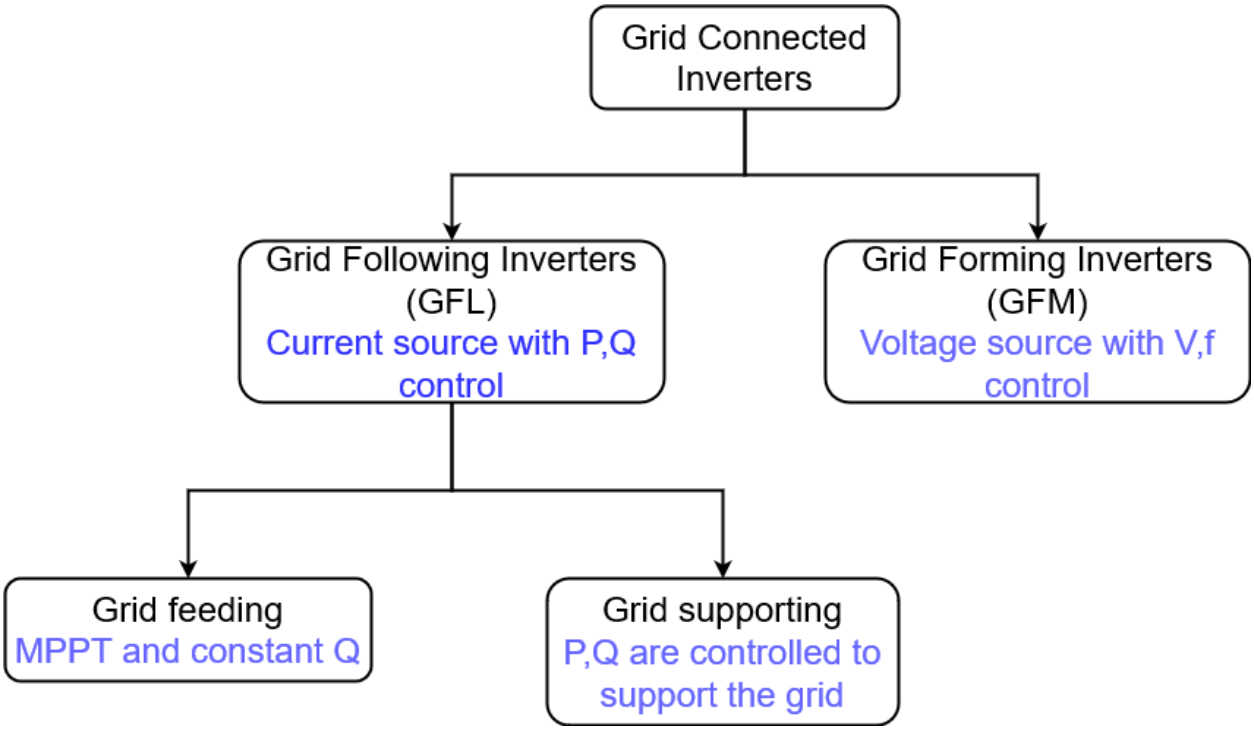

Fig. 7.1: Classification of grid connected inverters.

7.3 Control Architecture for Grid-forming (GFM) Inverter

As mentioned earlier, grid connected inverters can be classified into two major categories: GFL and GFM. This section details the control architecture for GFL and GFM inverters.

7.3.1 Grid-following (GFL) control

A grid-following inverter's behavior can be approximated as a controlled current source that injects current into an existing grid. It has a high impedance in parallel with the controlled current source. Figure 7.2 shows the general control architecture of GFL with the grid connection.

In GFL, the inverter is synchronized with the grid voltage via a phase locked loop (PLL) mechanism. It measures the voltage at the point of common coupling (PCC) and the phase of the voltage is obtained through the PLL using equation (7.1) [109].

$$\theta_{\text{PLL}} = \int \left[\omega_n + (K_p + K_i \int) V_{\text{PCC}} \right] \tag{7.1}$$

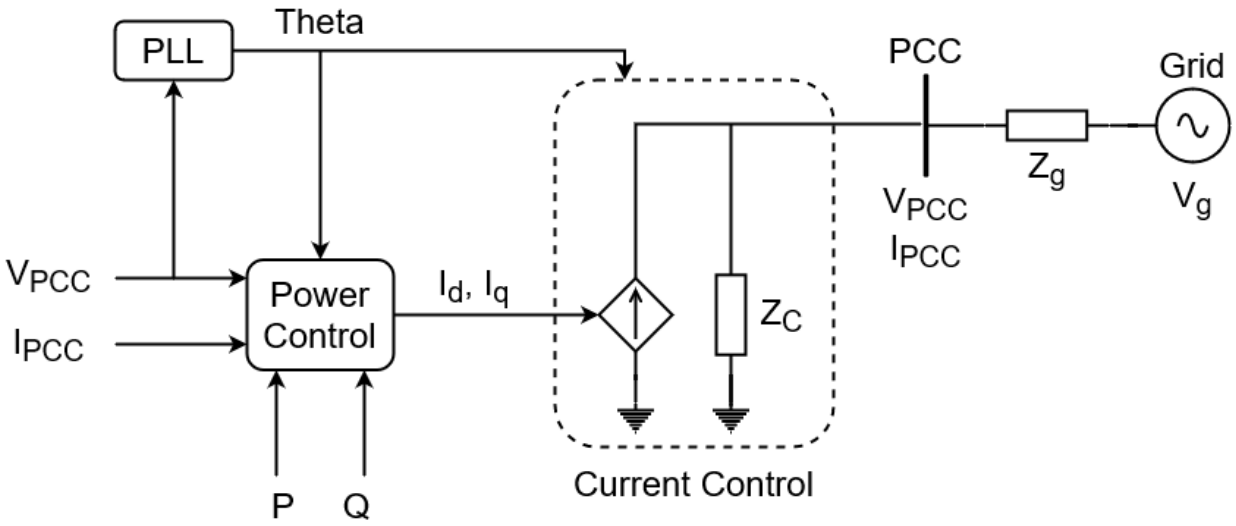

Fig. 7.2: General grid-following control architecture.

Here, ω_n is the angular speed (rad/s) and V_{PCC} is the PCC voltage. For the required direct and quadrature axis currents (I_d and I_q), voltage is changed accordingly. Active and reactive power support from GFL is achieved by controlling the injected I_d and I_q current. In GFL, synchronization is necessary throughout the entire time period to maintain synchronization with the grid, as GFL can only deliver real and reactive power, since it does not include any voltage and frequency regulation.

7.3.2 Grid-forming (GFM) control

Microgrids can perform with grid connection, as well, in an islanded mode of operation. While the grid is connection with the microgrid, voltage and frequency are regulated by the synchronous generators of the grid, but in an islanded mode, the microgrid needs to regulate its own voltage and frequency for stable operation. From this perspective, the GFM architecture is introduced and a notable volume of research has been conducted in this relatively new topic. While GFL behavior can be approximated as a controlled current source with a high impedance in parallel, GFM behavior can be approximated as a controlled voltage source with low impedance in series connection with the source. As a result, it can replicate a synchronous machine. For synchronization in the GFM architecture, at the beginning of operation, synchronization can be achieved in a similar fashion to a synchronous machine

and further synchronization is not required during normal operation. Figure 7.3 shows the general architecture for GFM with the grid connection.

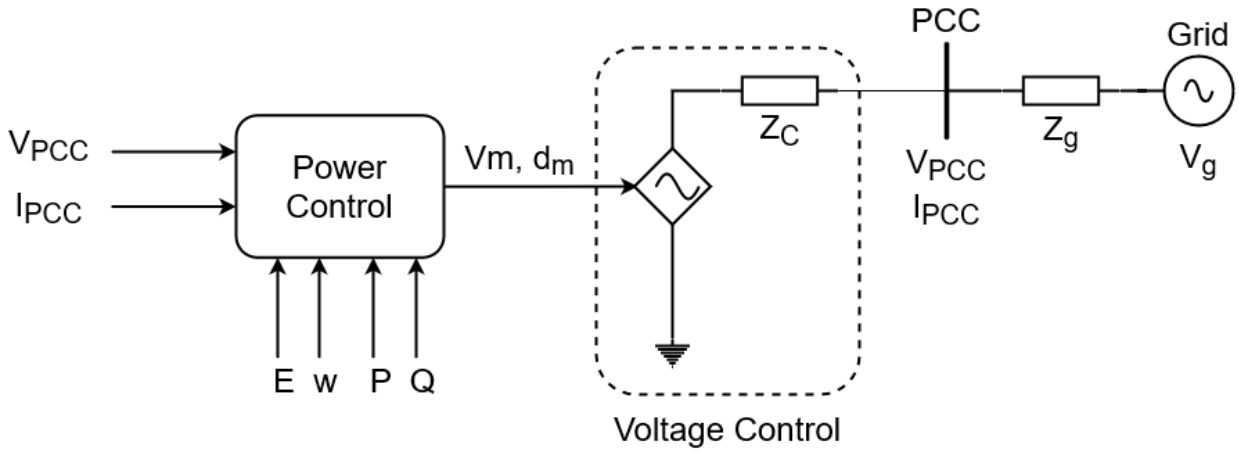

Fig. 7.3: General grid-forming control architecture.

In GFM, the PCC voltage is measured for regulating the power output. It is able to generate its own voltage and frequency reference in order to perform, even without the presence of the power grid. GFM architectures are recently being used as a solution for weaker grid conditions, as it provides a viable solution by creating its own voltage and frequency reference.

7.4 Battery Energy Storage System (BESS) Model

Modern power systems are accommodating an increasing number of variable renewable energy sources with existing grid systems, due to environmental interests, economic issues, and increasing energy consumption [107, 110]. Among these sources, solar and wind energy are currently the most common sources used around the world. However, these variable renewable energy sources are strongly dependent upon weather. Hence, their output is not consistent, since weather conditions vary all the time. Another significant concern about renewable energy sources is the reduction in mechanical inertia of the entire power system, which can result in large frequency swings during system disturbances, such as load changes and any type of fault, which in turn can lead the power system to instability [111, 112].

As one option to address these problems associated with variable renewable energy sources,

hybrid renewable energy systems are considered, which integrate different renewable energy sources in an optimal combination [113–115]. As another viable solution to these problems, various types of energy storage systems are also considered, because of their capability to absorb and release power when needed. Among the different types of energy storage systems, battery energy storage systems (BESSs) are being studied extensively [116], because of their energy storage capability, bidirectional energy exchange, geographical independence, and fast output response. In addition, a BESS can also improve power quality, as well as reliability of the system [117, 118]. Since the output of a BESS is direct-current (DC), an inverter based solution is required with necessary control (GFM/GFL) for integration with an alternating-current (AC) utility grid.

7.4.1 BESS Components

BESS components can be divided into three major parts, namely: components of the battery, components required for grid connection, and components required for reliable system operation.

Battery components consist of: a battery pack, which has multiple cells that are arranged in modules to achieve the desired voltage and current capacity, a battery management system (BMS), and a battery thermal management system (B-TMS). The BMS works in a way that maintains proper operation of the BESS within the specified range for the voltage and current, respectively. Also, it protects the BESS in terms of temperature and provides reliable and safe operation of the BESS. The BMS monitors the condition of battery cells, measures their parameters and states, such as state-of-charge (SOC) and state-of-health (SOH), and protects batteries from fires and other hazards. The BMS is also responsible for balancing varying SOC for series connected battery cells. The B-TMS maintains the temperature of the battery cells according to specifications.

Components required for grid connection consist of several items (e.g., power electronics, filters, etc.). Power electronics are required for connecting the BESS to the DC bus of the power grid. Filters are required for smoothing the ripples from the output of the BESS.

An inverter or a power conversion system (PCS) is required to convert DC power produced by the battery to AC power supplied to grid. For charging or discharging, a bidirectional inverter system is required.

An energy management system (EMS) and thermal management system are required for reliable system operation of BESS. The EMS manages the required power flow and distribution of power flow. It is responsible for energy flow of the battery system. The EMS coordinates between the BMS, PCS, and other components of the BESS, where it is able to efficiently manage power flow after analyzing the data. The thermal management system is responsible for system heating management.

7.4.2 Battery Chemistry Types

This section provides an overview of the primary battery types for possible consideration with a BESS [105,119,120]. A summary of advantages and disadvantages of different battery chemistry is provided in Table 7.1.

7.5 Integrated BESS with GFM Inverter Model

The section details model integration of the BESS with the GFM inverter. In this integrated system, a BESS is connected to a grid through DC-Link filters, three phase switching converters, AC filters, and a transformer. Both GFL and GFM control architectures for the BESS inverter are used in this chapter. A 1MW solar PV system is also used alongside the BESS, where the PV system is connected to the power grid via a similar fashion to that of the BESS. A one-line diagram of the system used in this chapter is shown in Figure 7.4. The different components of the BESS are discussed in the subsections below.

7.5.1 Integrated Model: BESS

The battery model used in this chapter is a Li-Ion model. The no load voltage of the battery, V_{nl}, is calculated based on the state-of-charge of the battery using a nonlinear equation, which is shown in equation (7.2) [104].

Table 7.1: Summary of typical battery chemistry types used with a BESS

Chemistry Type	Advantages	Disadvantages
Lead-Acid (PbA) (Mainly used in vehicles and other purposes where high values of load current is required)	Simple manufacturing procedure, Low cost for manufacturing, Low cost per watt hour of usage, High discharge current capability, Performs irrespective of temperature, No cell-wise BMS requirement	Poor weight to energy ratio, Slow charging Limited, life-cycle, Adverse environmental impact
Nickel-Cadmium (Ni-Cd) (Mainly used in portable computers, drills, and other small battery operated devices)	Rechargeable, Fast charging with low stress, Long shell life, Simple storage and transportation, Performs in low temperature, Economical pricing	High self discharge, Low cell voltage, Environmental impact,
Nickel-Metal Hydride (Ni-MH) (Combines positives from Ni-Cd batteries with energy storage features of metal alloys)	Higher capacity, Less voltage depression, Perform at very low temperature, Higher energy density	Shorter lifespan, Limited discharge current, High self discharge
Lithium-Ion (Li-Ion) (Widely used in all types of electronic devices)	High energy density, High load capabilities, Maintenance free high shell life, Simple charge algorithm, Shorter charge time	Degradation at higher temperatures, Requires protection circuit

$$V_{nl} = V_0 - V_k \frac{1}{SOC} + A^{-BC(1-SOC)} \tag{7.2}$$

were, V_{nl} is the no load voltage of the battery, V_0 is the battery constant voltage, SOC is the state-of-charge of the battery, V_k is the polarization voltage, C is the capacity of the battery in Ah, and A and B are constants. A, B, and V_k can be tuned for the desired performance from the battery. The BESS has a rated power of 1MW and a rated capacity of 1MWh. Each battery cell's voltage is 3.2V and each module has four cells in them. There are 72 modules

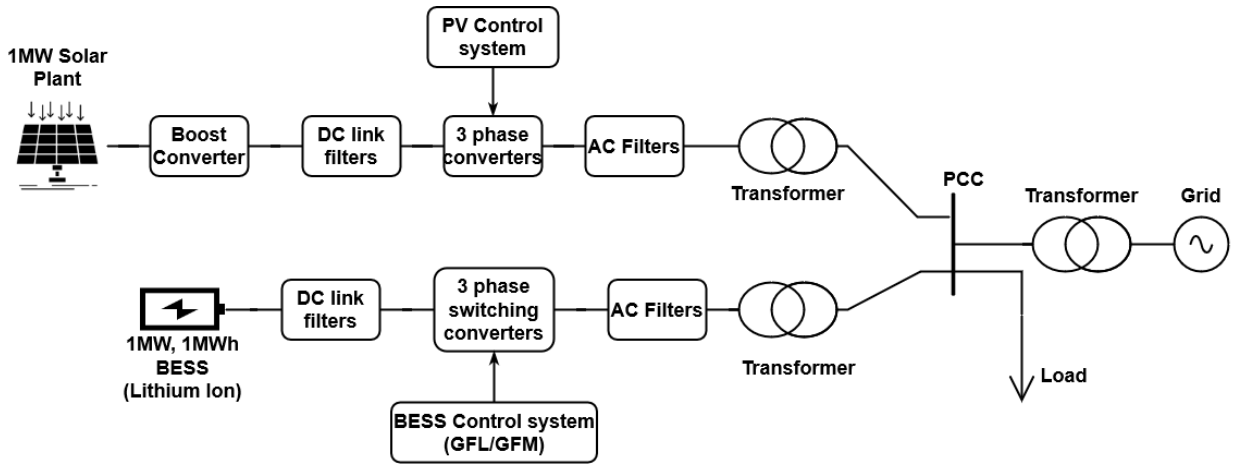

Fig. 7.4: BESS and PV integration to grid.

in series. Each cell's current capacity is 14Ah and there are 80 parallel connections. The nominal voltage of the BESS is 921.6V and the initial SOC is 50%. Aging and temperature effect of the BESS are ignored for this work.

7.5.2 Integrated Model: DC/AC filter

DC filters are positioned before the converter and AC filters are positioned after the converter. The purpose of both filters is to limit the ripple of the current and to add damping effect. Resistors and inductors of different values are connected in series and capacitors are connected in parallel to accomplish the desired output for both of the filters.

7.5.3 Integrated Model: DC-AC converter

Figure 7.4 shows how the DC-AC converter connects the battery to the grid through filters on both sides. A three phase two-level switching type converter is used with the detailed BESS model. Detailed BESS models are better for stability studies and mode identification. A reference voltage signal is passed through pulse width modulation (PWM) to produce a sinusoidal reference signal for the converter. The reference voltage signal is produced by the BESS control system block. The PWM carrier frequency is 2700Hz for this model.

7.5.4 Integrated Model: Solar (PV) panel

A photovoltaic (PV) panel is also used alongside the BESS for connecting to the grid (Figure 7.4). The PV panel is used to show the BESS performance with a PV panel presented. The PV panel is designed based on a MPPT mode and its rating is 1MW. Each PV cell's open circuit voltage is 51.9V and the short circuit current is 8.68A. Each module has 83 cells and 15 modules are connected in series per string. There are 190 parallel string in this representative PV model. The PV panel is then connected to a boost converter through DC filters. Then, a three phase converter is placed for connection between the DC and AC side, accordingly. A PV control block is used, which provides the necessary modulation signal for controlling the PV converter. Then, the PV system is connected to grid through an AC filter and a transformer.

7.6 Grid-connected/islanded large-scale BESS

A battery energy storage system can enhance the power system flexibility and can enable high level penetration of renewable energy to the grid. A BESS can operate in both grid connected mode or islanded mode. While connected to grid, a GFL architecture of the inverters is deployed and the BESS follows the grid and supports the grid by supplying or absorbing power, as applicable. While in islanded mode, the GFM architecture of BESS is enabled and the BESS can act as the frequency regulator of the islanded part of the grid. For integration with grid in the transmission network, a large-scale or utility-scale BESS is required. Configuration of a large-scale BESS integration into a transmission network is quite similar to Figure 7.4. Figure 7.5 [121] shows the configuration of a large-scale BESS interconnected at the transmission substation level. Several battery cells are connected in series and parallel to obtain the required voltage and current levels and the battery cells are then connected to the inverter, which can operate in both GFL/GFM modes, accordingly. A BMS works alongside the inverter, which can send the status information of several system parameter to the system operator and can also import set points determined by system

operator. The inverter is then connected to the low voltage side of the AC transformer. The high voltage side of the AC transformer is connected to transmission network through a tie-line, as depicted in Figure 7.5.

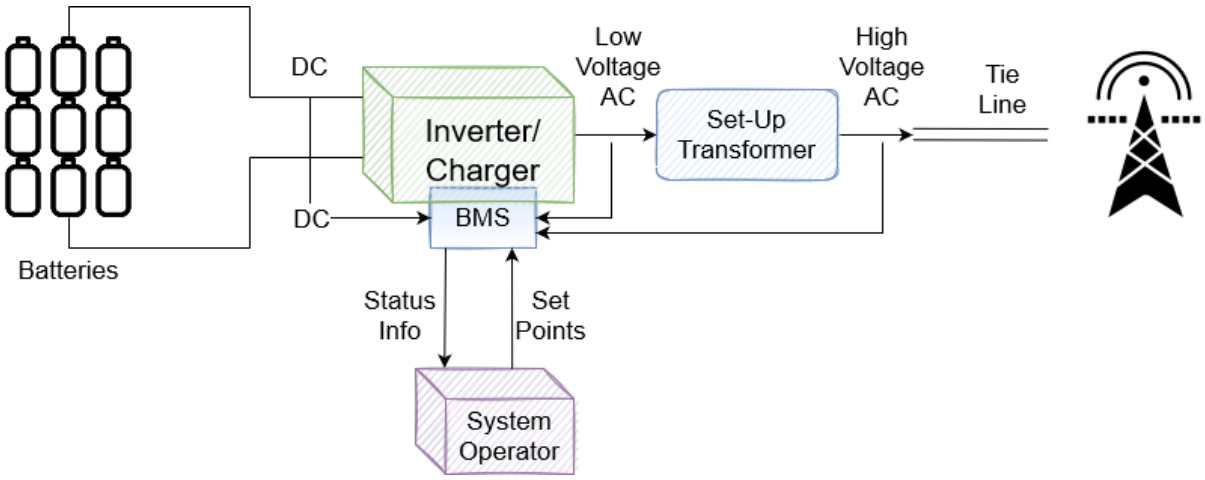

Fig. 7.5: Large-scale battery energy storage systems.

7.7 Application: Developing the model

This section provides an example application for the integrated BESS with a GFM inverter, presented in this chapter, which can be performed using a typical software platform (e.g., MATLAB/Simulink). The one-line diagram in Figure 7.4 is modeled in Simulink. A Li-Ion BESS model is used alongside a PV panel for integration to the grid. The control algorithm for grid-connected inverters consist of both grid-following and grid-forming architectures. The BESS has a rated power of 1MW and a rating of 1MWh. The PV panel is rated at 1MW power. The grid generator is rated as 1.3MVA machine and performs as a swing generator. The terminal voltage of the generator is 20kV and the transformer is used as a step down transformer to transform the voltage to 600V, which is the PCC voltage. Some fixed load and variable loads are connected to the PCC, which are modeled based on a constant Z model. The PV panel is modeled based on MPPT and the transformer with the PV panel transforms the voltage of the PV panel to 600V and then connects to the PCC. The BESS is modeled in a way that it can perform in both a GFL and GFM mode of control. The nominal voltage of the BESS is 922V and the transformer with the BESS transforms

the voltage to match the PCC voltage. Voltage and current can be measured at the PCC and other points and buses in the network, as needed. As an example application, Figure 7.6 shows the simulation test case of a BESS integrated with the grid modeled in Simulink.

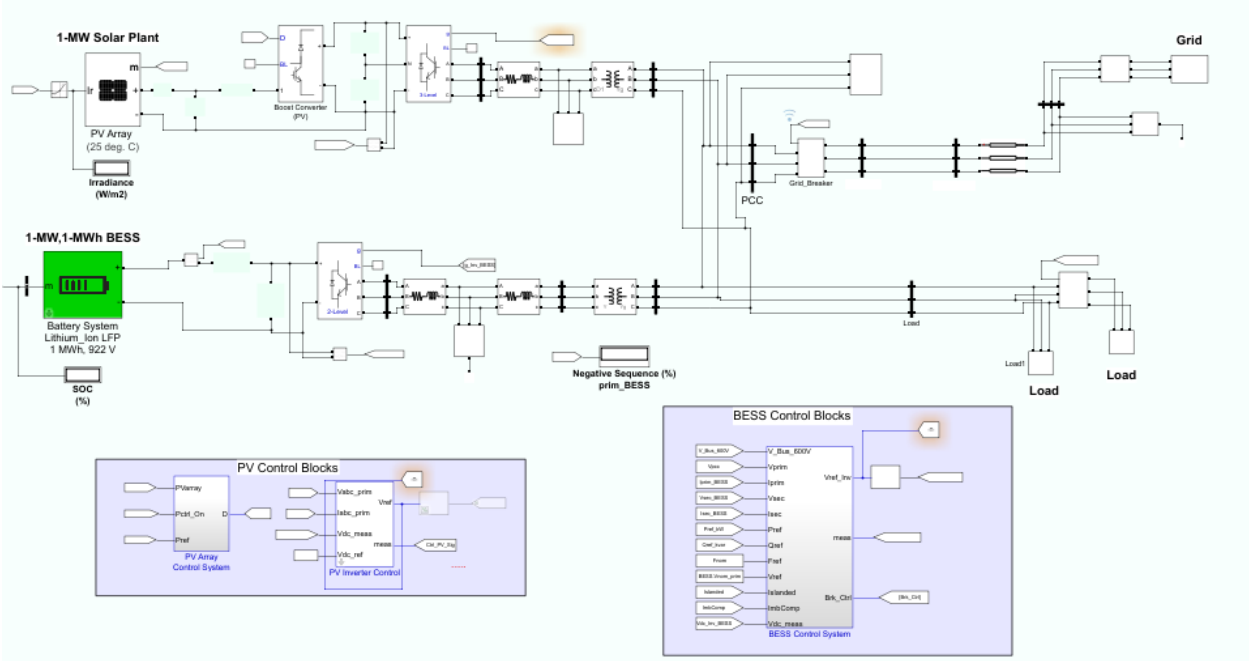

Fig. 7.6: Simulink model of a BESS integrated with the grid.

7.7.1 Detailed GFL Architecture

The voltage measurement at the PCC and current measurements after the AC filters are passed through an $abc - dq0$ transformation block, which provides dq-axis voltage and current. These dq-axis current and voltage values are then used to calculate the injected active and reactive power per equations (7.3) and (7.4), respectively [104].

$$P = \frac{3}{2}(V_d I_d - V_q I_q) \tag{7.3}$$

$$Q = \frac{3}{2}(V_d I_q - V_q I_d) \tag{7.4}$$

A PLL is required to calculate the phase angle θ_{PLL}, which is then transferred to $abc - dq$ blocks and the PWM block. P_{ref} and Q_{ref} are given as inputs to the current reference

generator block. This block generates current dq-axis reference set points I_{dref} and I_{qref} utilizing the calculated powers and reference powers per equations (7.5) and (7.6) [104]. Then, the current closed loop control block generates dq-axis voltage references $V_{ref_{dq}}$. Both $V_{ref_{dq}}$ and θ_{PLL} signals are then passed through a $dq0 - abc$ transformation block, which provides the abc-reference voltage $V_{ref_{abc}}$. Then, the $V_{ref_{abc}}$ signal is transferred to a PWM scheme to generate the modulation signal for the converter. Figure 7.7 represents the GFL architecture used for this work.

$$I_{dref} = \frac{2}{3}\frac{P_{ref}V_d + Q_{ref}V_q}{V_d^2 + V_q^2} \tag{7.5}$$

$$I_{qref} = \frac{2}{3}\frac{P_{ref}V_q + Q_{ref}V_d}{V_d^2 + V_q^2} \tag{7.6}$$

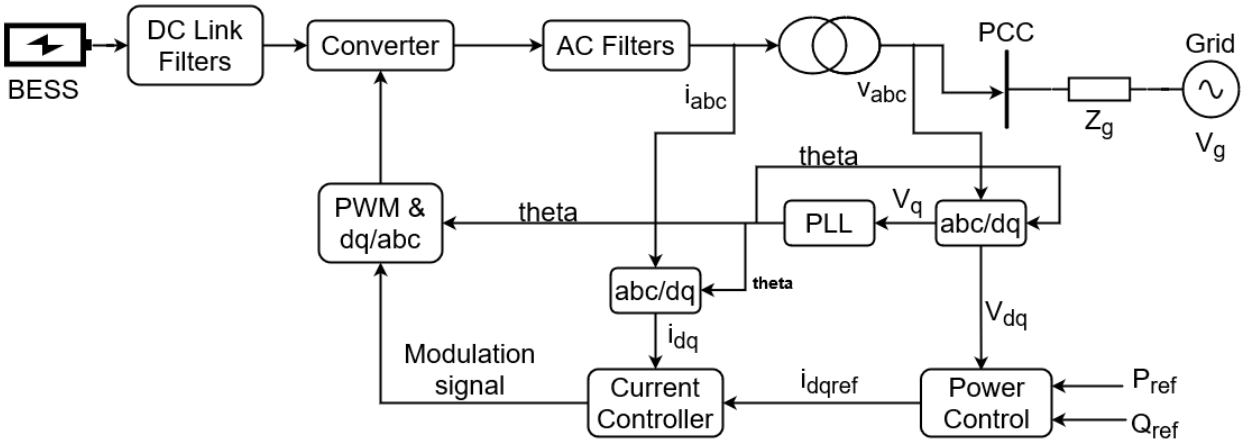

Fig. 7.7: Grid-following control architecture.

7.7.2 Detailed GFM Architecture

In the GFM architecture (Figure 7.8), no PLL is required to calculate phase angle. θ_{PLL} is generated using ω_{ref} and then transferred to $abc - dq$ blocks and PWM block. Voltage and current measurement are collected and passed through $abc - dq0$ blocks to generate dq-axis voltage and current, which are V_{dq} and I_{dq}, respectively. V_{dqref} and V_{dq} signals go into the voltage controller block to generate the I_{dqref} signal for the current controller block.

A proportion integral (PI) control block is then used to generate the I_{dqref} signal inside the voltage controller block. Figure 7.9 represents the voltage controller block.

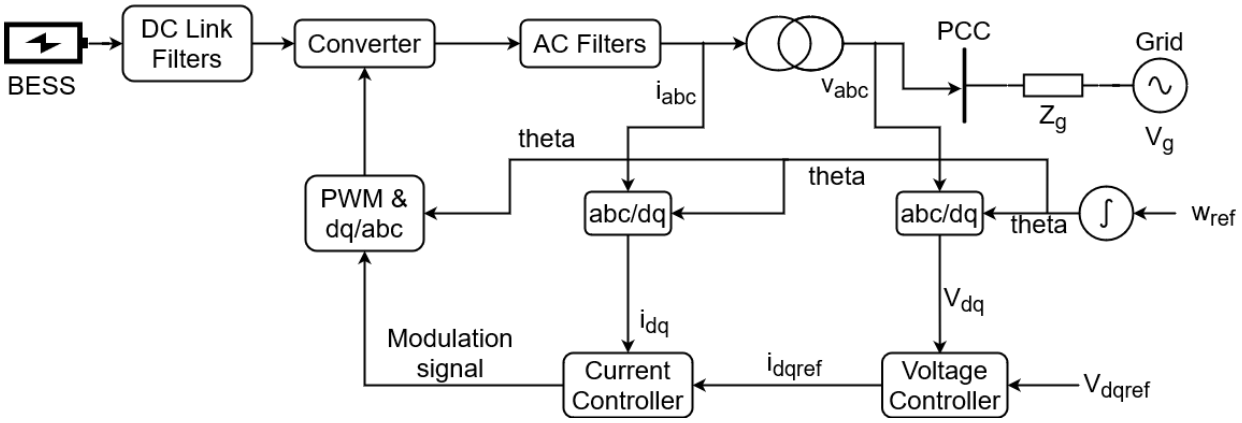

Fig. 7.8: Grid-forming control architecture.

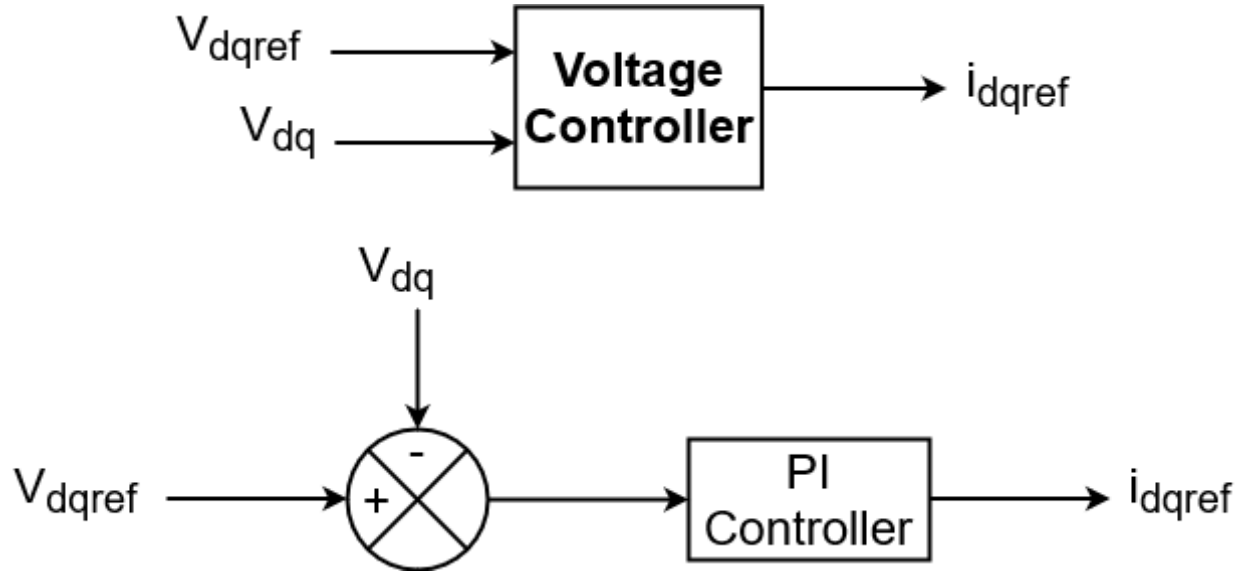

Fig. 7.9: Voltage controllers.

The current control block also has a feedforward block within it. The output from the voltage controller block is passed through the current closed-loop control to obtain the ï¬¬*nalmodulationsignal.Thefeedforwardtermsshouldbeusedtodecouplethetwoaxesandshouldbeconsidered* 1001[104]*representthefeedforwardequation*, *where*$V_{d_{ac-filter}}$ and $V_{q_{ac-filter}}$ are the dq-axes voltage obtained from the voltage measurement at the bus after the AC filter. V_{0d} and V_{0q} are the outputs of the feedforward block. The outputs from feedforward block and the PI

controller block are then added to generate the modulation signal. Figure 7.10 represents the current control block with the feedforward terms.

$$V_{0d} = V_{d_{ac-filter}}(1 - \omega^2 L_f C_f) + I_{dref} R_f - I_{qref} \omega L_f - V_{q_{ac-filter}} \omega R_f C_f \tag{7.7}$$

$$V_{0q} = V_{q_{ac-filter}}(1 - \omega^2 L_f C_f) + I_{dref} R_f + I_{dref} \omega L_f + V_{d_{ac-filter}} \omega R_f C_f \tag{7.8}$$

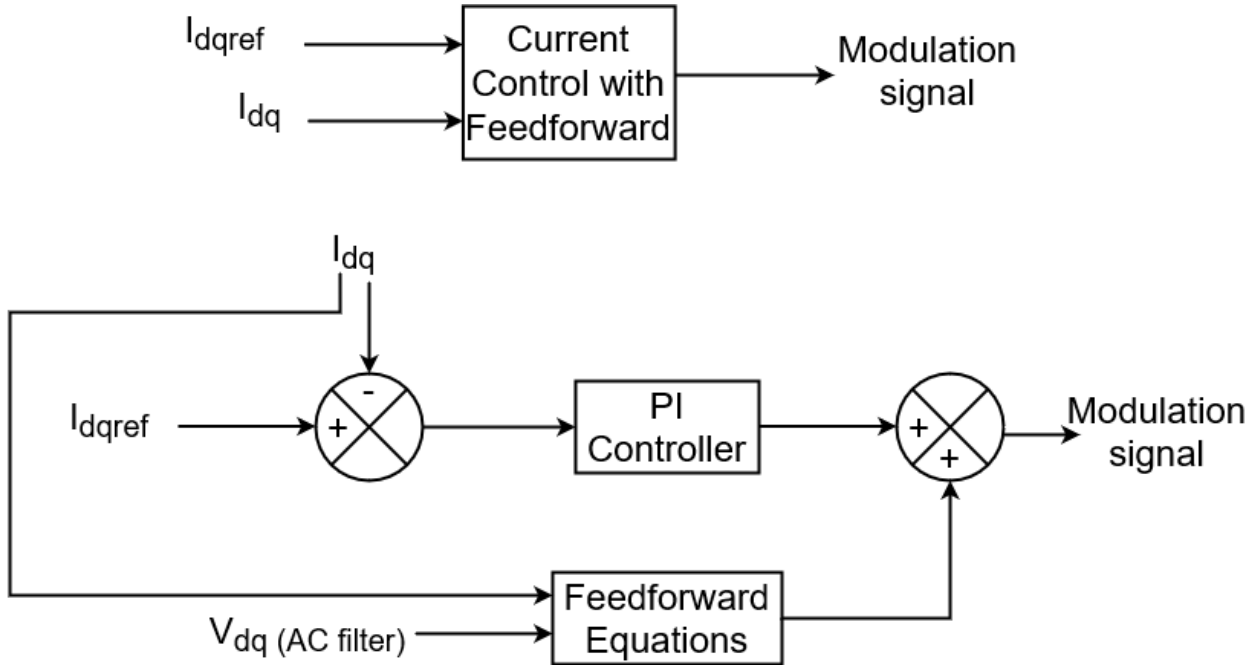

Fig. 7.10: Current controllers.

The outputs of the current controller are the modulation signals, which are transformed back to the abc-reference frame to obtain the sinusoidal control signals for the PWM scheme of the converter.

A droop controller is used to generate the ω_{ref} and V_{dqref} signals, which are used with the voltage control blocks and phase angle calculation. Droop control is also used for maintaining voltage and frequency within acceptable limits. Figure 7.11 represents the droop control block, which is used for this work. An active power controller is used for generating ω_{ref} and a reactive power controller is used for generating V_{dqref}.

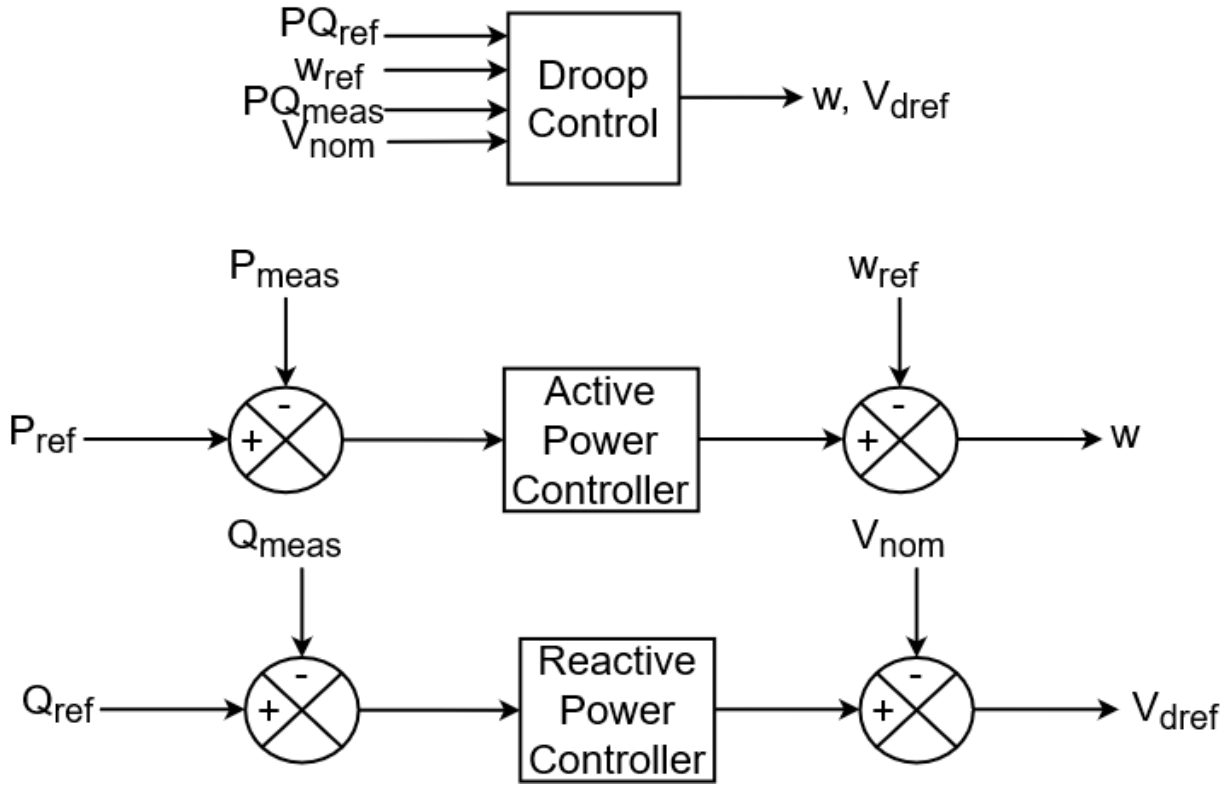

Fig. 7.11: Droop control.

7.8 Simulation Results

Two test systems are used for this chapter. In Test System 1, the BESS and PV system are connected to a generator that works as a swing generator for this system (see Figure 7.4). In Test System 2, a BESS and PV system are connected to a larger power system, which is an IEEE 13 bus system (see Figure 7.21). Both test systems are simulated in MATLAB/Simulink. The discrete timestep is 40μs. For each test system, four different cases or events are studied. For all cases, the DC-Link voltage dynamics measurement is captured for stability studies.

7.8.1 Test System 1: BESS with a single machine

For this test system (Test System 1), a BESS along with a PV system are connected to a single grid machine, which has a rating of 1.3MVA (Figure 7.4). The phase-to-phase RMS voltage is 20kV, which is then passed through a step-down transformer and transformed to

600V. The BESS and PV are connected to the PCC via transformers, where the PCC voltage is 600V. The total load connected at the PCC is 600kW and 100kVAR, respectively. Some variable load is also connected to create a load change event or step change in load during the study.

7.8.2 Cases on Test System 1

7.8.2.1 Case 1: Grid-Following and Grid-Forming

Case 1 (Test System 1) shows the transformation of the grid-connected inverter from grid-following mode to grid-forming mode. For this test case, the total simulation period is 6s. The total load connected at PCC is 600kW and 100kVAR, respectively. The grid connected generator is supplying the load initially (from 0s to 1s). No PV or BESS supply is present initially. From 1s to 3s, grid-following mode is activated with a reference power of -200kW at the BESS, where the BESS is charging by 200kW. Grid supplied power is increased by 200kW to charge the BESS. From 3s to 6s, grid-forming mode is activated. The grid is islanded and the BESS starts to supply the demanded load. The PV irradiance is 0W/m^2 for the total simulation period and the output power from the PV is also 0kW throughout the entire simulation period.

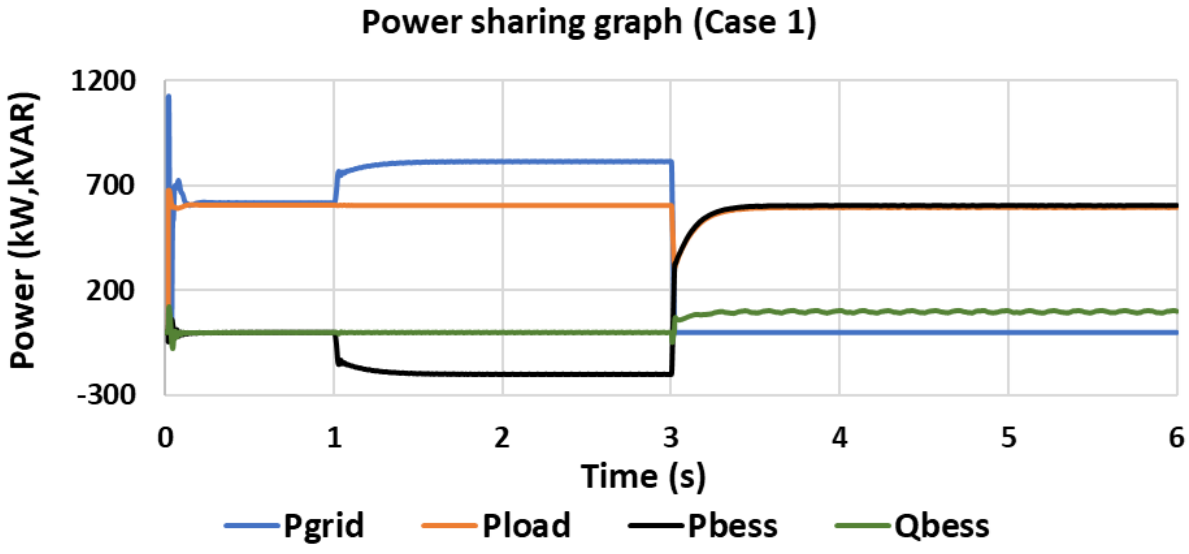

Fig. 7.12: Power sharing graph at PCC for Case 1 (Test System 1).

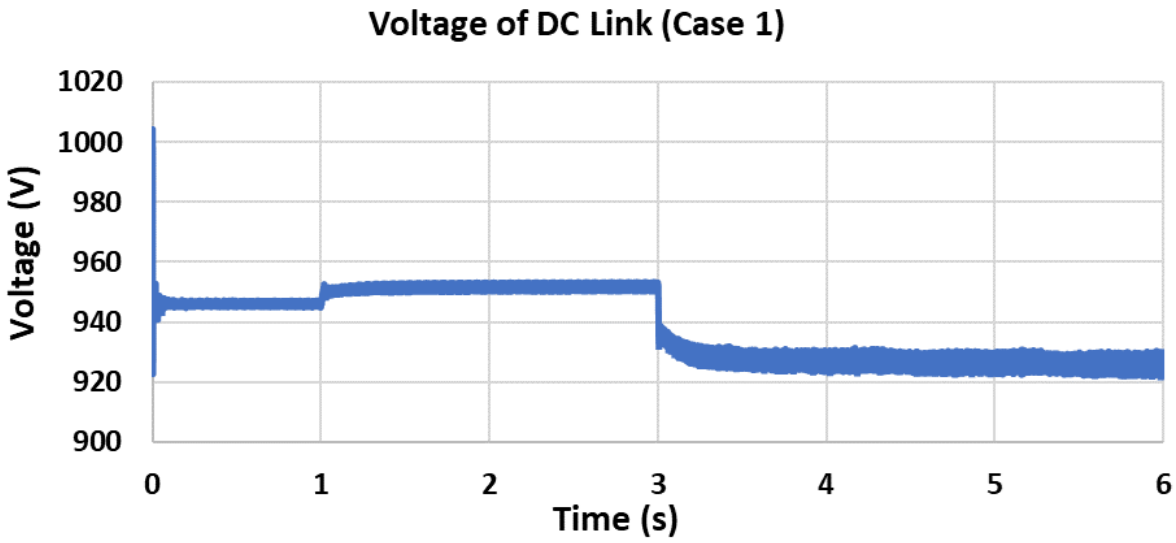

Fig. 7.13: DC-Link voltage dynamics for Case 1 (Test System 1).

Figure 7.12 shows the power shared by all sources at the PCC. Figure 7.13 depicts the DC-Link voltage dynamics from the BESS for this case.

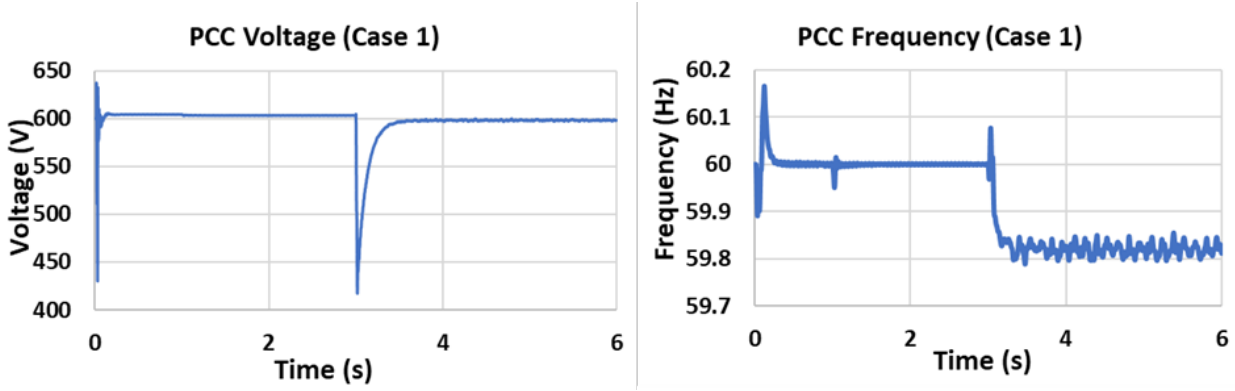

Fig. 7.14: PCC voltage and frequency for Case 1 (Test System 1).

The PCC voltage and frequency are shown in Figure 7.14. From this figure, in grid-following mode, the PCC voltage remains at 600V and the PCC frequency remains at 60Hz, but in grid-forming mode, the frequency varies between 59.80Hz-59.85Hz.

7.8.2.2 Case 2: Step change in load in GFM with PV supply

Case 2 (Test System 1) considers a step change in the load, while in GFM mode with the PV supply. For this test case, the total simulation period is 6s. The total initial load is

600kW and 100kVAR at the beginning of simulation. Irradiance of the PV plant is 200W/m^2 and the PV system is supplying 200kW throughout the entire simulation. Initially, the grid is supplying the additional 400kW and 100kVAR (from 0s to 1s). From 1s to 6s, grid-forming mode is activated. The BESS is supplying the 400kW and 100kVAR load, instead of the grid generator. At 3s, half of the active and reactive load is disconnected. As a result, the BESS is supplying 100KW and 50kVAR.

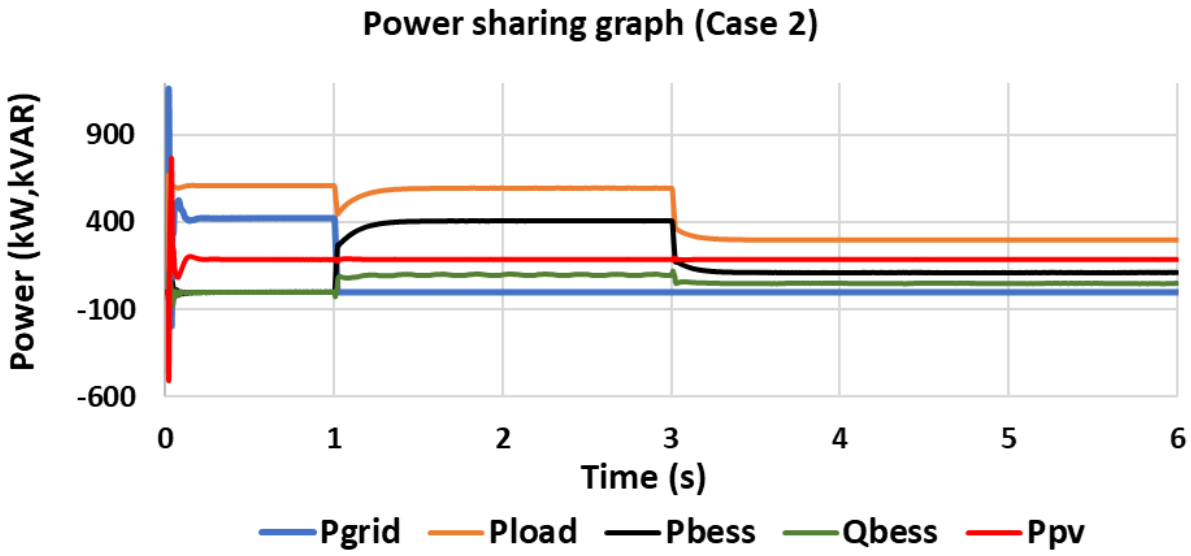

Fig. 7.15: Power sharing graph at PCC for Case 2 (Test System 1).

Figure 7.15 shows the power shared by all sources at the PCC. Figure 7.16 represents DC-Link voltage dynamics from the BESS.

The PCC voltage and frequency are shown in Figure 7.17. From this figure, initially, the PCC voltage remains at 600V and the PCC frequency remains at 60Hz. From 1s to 3s, the PCC frequency is around 59.875Hz and after 3s, the PCC frequency is around 59.97Hz.

7.8.2.3 Case 3: Fault at PCC in GFM with PV supply

Case 3 (Test System 1) considers a fault at the PCC, while in GFM mode with the PV supply. For this test case, the total simulation period is 6s. The total load is 600kW and 100kVAR at the beginning of the simulation. The PV system is supplying 200kW throughout the entire simulation. The power grid is initially supplying 400kW and 100kVAR. From 1s

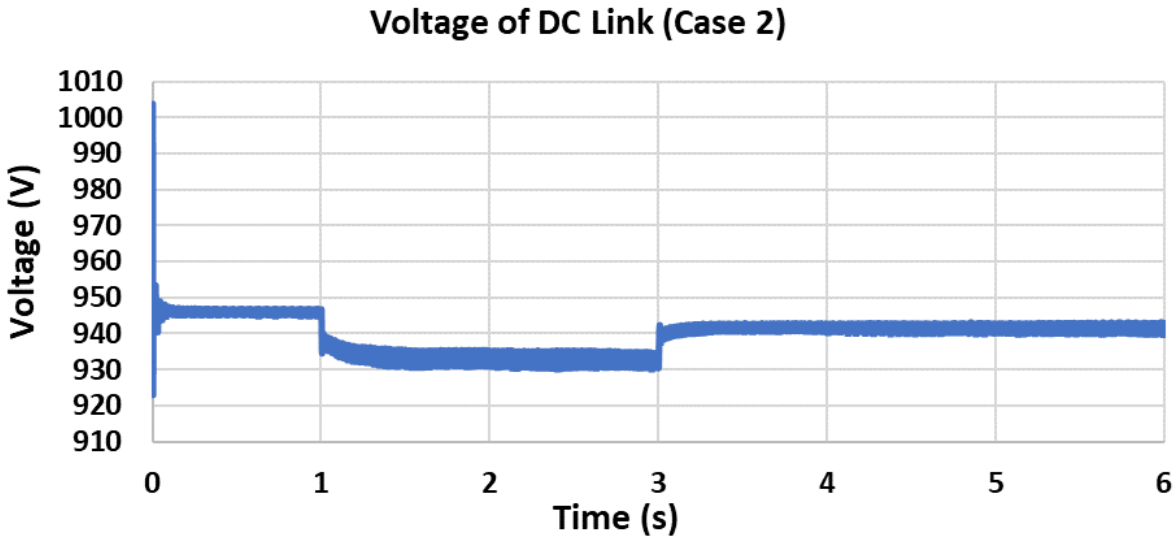

Fig. 7.16: DC-Link voltage dynamics for Case 2 (Test System 1).

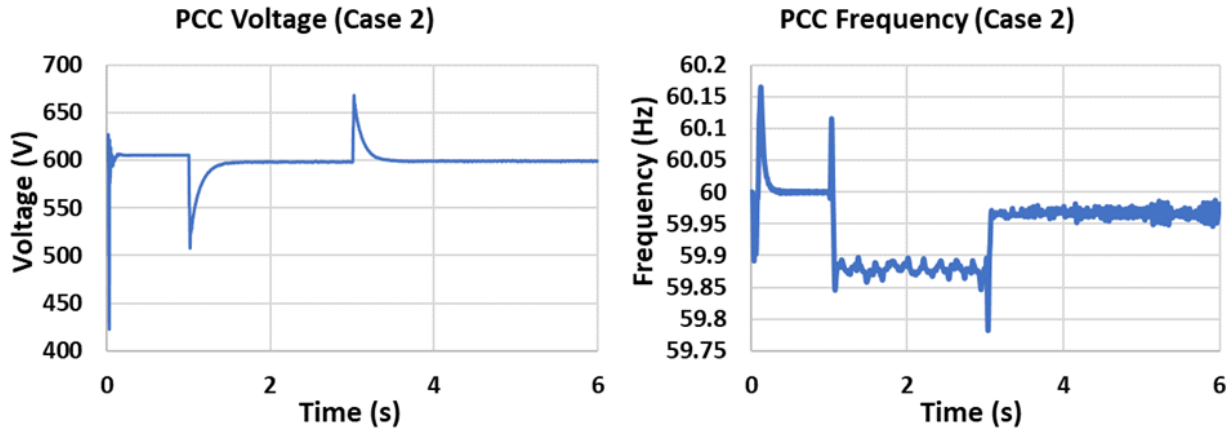

Fig. 7.17: PCC voltage and frequency for Case 2 (Test System 1).

to 6s, grid-forming mode is activated. The BESS supplies 400kW and 100kVAR to supply the load. At 3s, a three phase fault is applied for 0.167s. At 3.167s, the fault is cleared and whole system goes back to previous state. Three phase fault is applied to check stability under most stress.

Figure 7.18 shows the power shared by all sources at the PCC. Figure 7.19 depicts DC-Link voltage dynamics from the BESS.

The PCC voltage and frequency are shown in Figure 7.20. From this figure, initially, the

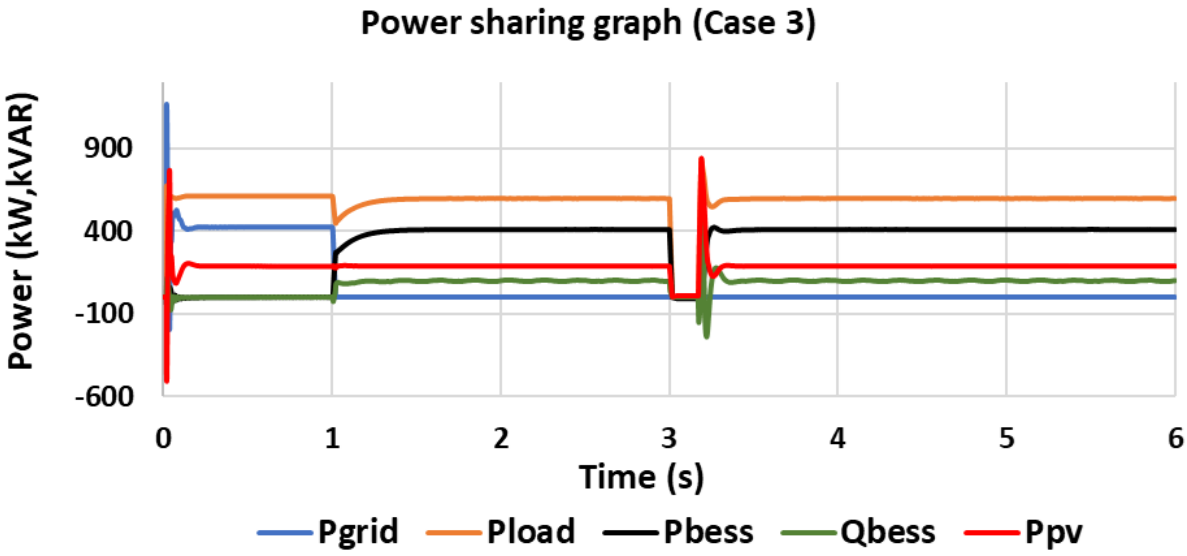

Fig. 7.18: Power sharing graph at PCC for Case 3 (Test System 1).

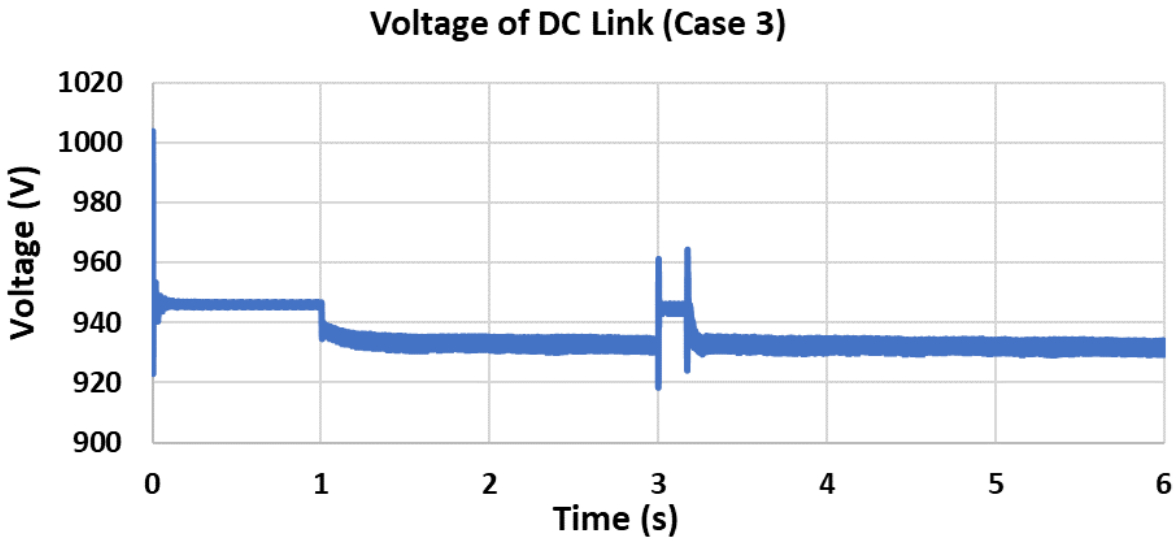

Fig. 7.19: DC-Link voltage dynamics for Case 3 (Test System 1).

PCC voltage remains at 600V and the PCC frequency remains at 60Hz. From 1s to 6s, the PCC frequency is around 59.87Hz.

For all cases considered with Test System 1, the DC-Link dynamics are measured and a mode identification method, called subspace identification [22], is applied on the measurement data to calculate the mode and damping ratio. The modal and damping ratio information helps to identify any unstable modes and apply proper control mechanism to

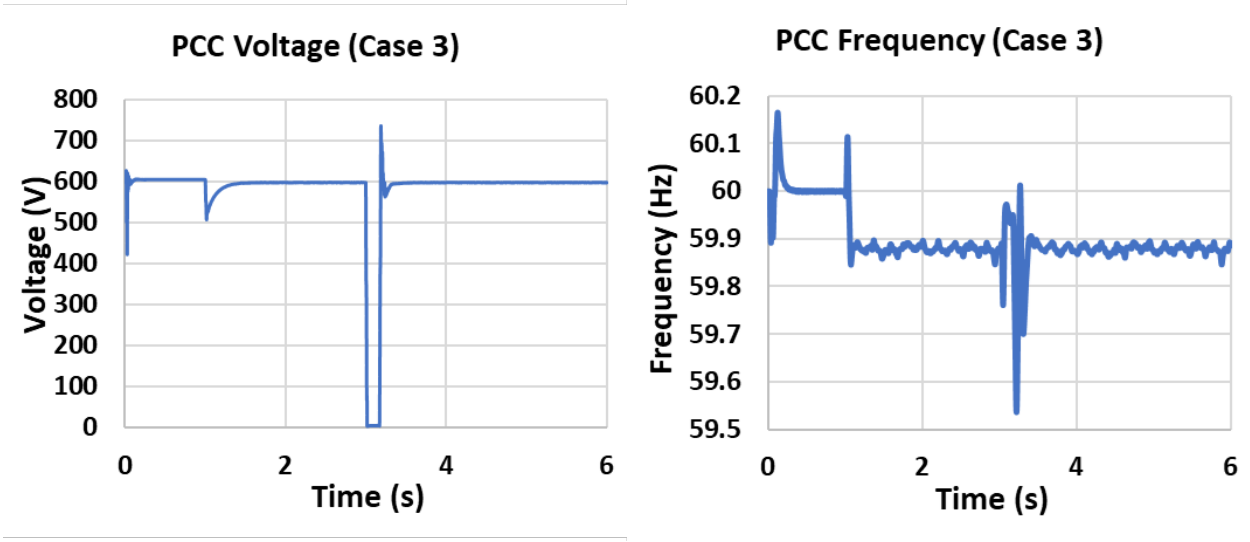

Fig. 7.20: PCC voltage and frequency for Case 3 (Test System 1).

stabilize the system. [122–124] The summary of identified modes of all cases are summarized in Table 7.2.

Table 7.2: Summary of Electro-mechanical Mode Identification for Test System 1

Cases	Steady state Mode (Hz) & Damping ratio (%)	GFL/GFM Mode (Hz) & Damping ratio (%)	Load change/Fault Mode (Hz) & Damping ratio (%)
Case 1	0.086 & 12.098	0.155 & -0.0008	0.155 & -0.0007
Case 2	0.086 & 12.098	0.155 & -0.0012	0.155 & -0.0076
Case 3	0.086 & 12.098	0.155 & -0.0012	0.155 & -0.0164

7.8.3 Test System 2: BESS and PV integrated with IEEE 13 bus

For Test System 2, the BESS and PV system are connected to bus 634 of the IEEE 13 bus system (see Figure 7.21). The phase-to-phase RMS voltage is 480V. The BESS and PV system are connected to the PCC via transformers, where the PCC voltage is 480V. The total load connected to the PCC is 400kW and 290kVAR, respectively.

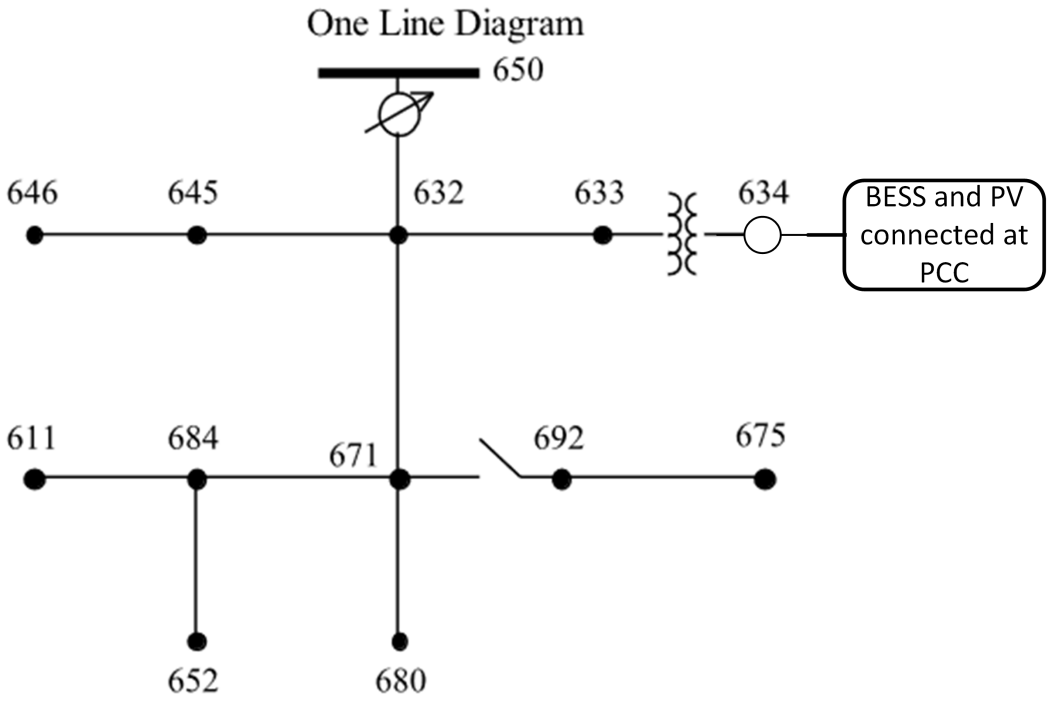

Fig. 7.21: IEEE 13 bus system.

7.8.4 Cases on Test System 2

7.8.4.1 Case 1: Grid-Following and Grid-Forming

Case 1 (Test System 2) considers the transformation of the grid-connected inverter with the IEEE 13 bus system from grid-following mode to grid-forming mode. The total simulation period is 5s. The total load is 400kW and 290kVAR, respectively. Initially, from 0s to 1s, the grid is supplying the load. From 1s to 3s, grid-following mode is activated with a reference power of -200kW at the the BESS, where the BESS is charging by 200kW. The grid supplied power is increased by 200kW to charge the BESS. From 3s to 5s, grid-forming mode is activated. The grid is islanded and the BESS starts to supply the load. The PV system irradiance is $0 W/m^2$ and output of the PV plant is 0kW for the entire simulation period.

Figure 7.22 shows the power shared by all sources at the PCC. Figure 7.23 depicts the DC-Link voltage dynamics from the BESS. In grid-following mode, the PCC voltage remains at 480V and the PCC frequency is 60Hz, whereas the PCC frequency is around 59.95Hz in

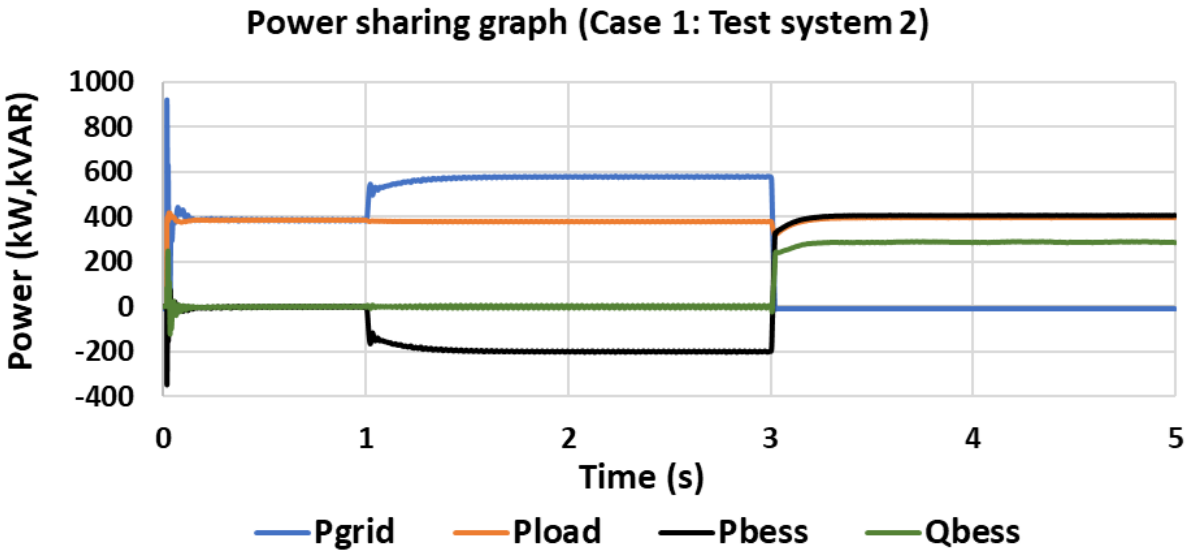

Fig. 7.22: Power sharing graph at PCC for Case 1 (Test System 2).

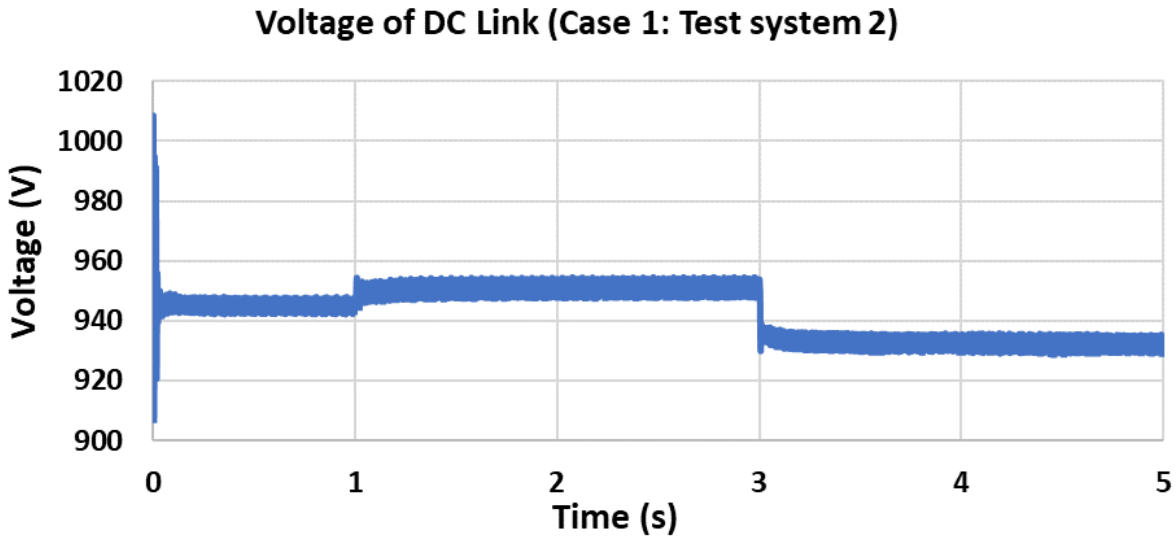

Fig. 7.23: DC-Link voltage dynamics for Case 1 (Test System 2).

GFM mode.

7.8.4.2 Case 2: Step change in load in GFM with PV supply

Case 2 (Test System 2) considers a step change in the load, while in GFM mode with the PV supply and IEEE 13 bus system. In this test case, the total simulation period is 5s. The total load is 400kW and 290kVAR at the beginning of the simulation. The PV system

is supplying 50kW throughout the entire simulation. The power grid is supplying 350kW and 290kVAR at the start. From 1s to 5s, grid-forming mode is activated. The BESS starts supplying the 350kW and 290kVAR load. At 3s, half of the load is disconnected. After 3s, the BESS is supplying the load, which is 150kW and 145kVAR.

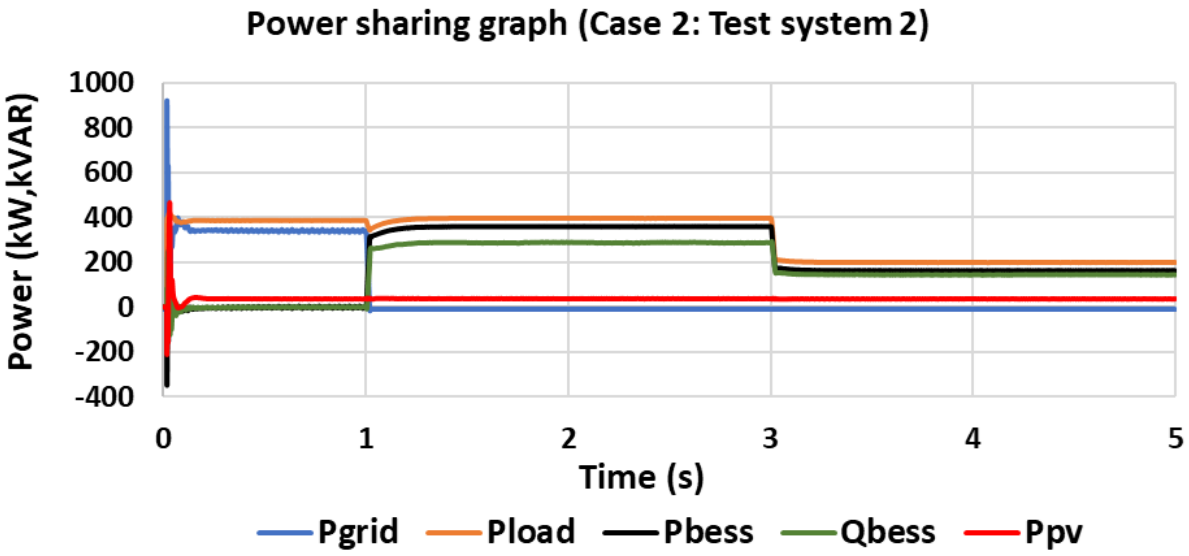

Fig. 7.24: Power sharing graph at PCC for Case 2 (Test System 2).

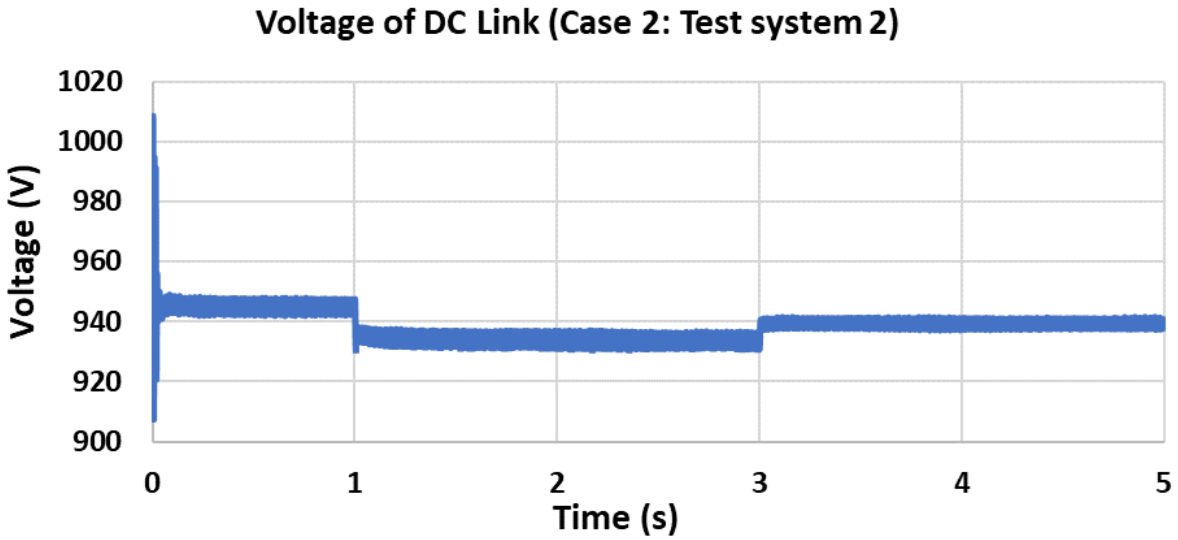

Fig. 7.25: DC-Link voltage dynamics for Case 2 (Test System 2).

Figure 7.24 shows the power shared by all sources at the PCC. Figure 7.25 depicts the

DC-Link voltage dynamics from the BESS. Initially, the PCC voltage remains at 480V and the PCC frequency remains at 60Hz. From 1s to 3s, the PCC frequency is around 59.95Hz and after 3s, the PCC frequency is around 59.97Hz.

7.8.4.3 Case 3: Fault at PCC in GFM with PV supply

Case 2 (Test System 2) considers a fault at the PCC, while in GFM mode with the PV supply and IEEE 13 bus system. In this case, the total simulation period is 5s. The total load is 400kW and 290kVAR at the beginning of the simulation. The PV is supplying 200kW throughout the entire simulation. Initially, the power grid is supplying 200kW and 290kVAR. From 1s to 5s, grid-forming mode is activated. The BESS supplies 200kW and 290kVAR, respectively, to supply the load. At 3s, a three phase fault is applied for 0.167s at the inverter side. At 3.167s, the fault is cleared and power system goes back to the previous state.

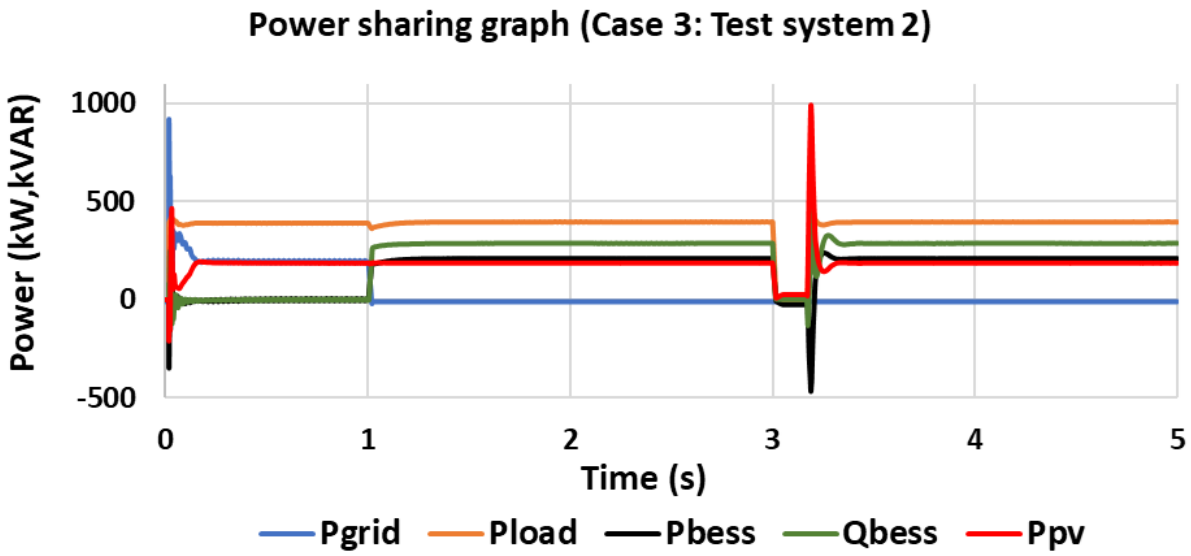

Fig. 7.26: Power sharing graph at PCC for Case 3 (Test System 2).

Figure 7.26 shows the power shared by all sources at the PCC. Figure 7.27 depicts DC-Link voltage dynamics from the BESS. Initially, the PCC voltage remains at 480V and the PCC frequency remains at 60Hz. From 1s to 5s, the PCC frequency is around 59.975Hz.

For all of the test cases considered with Test System 2, the DC-Link dynamics are measured. The associated modes and damping ratios are calculated through a subspace iden-

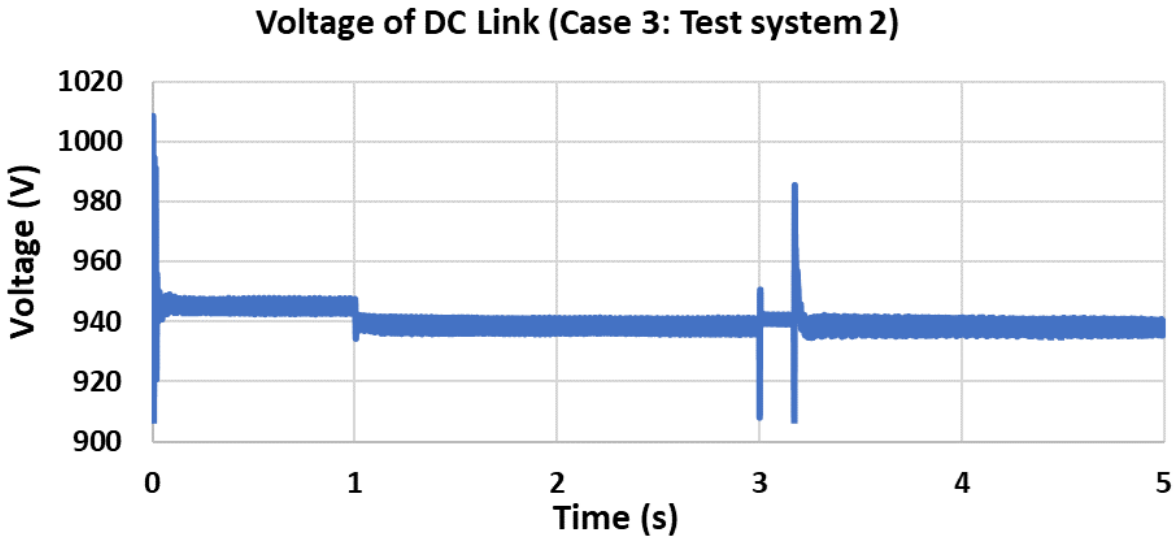

Fig. 7.27: DC-Link voltage dynamics for Case 3 (Test System 2).

tification method. The summary of the identified modes for all cases of Test System 2 are summarized in Table 7.3.

Table 7.3: Summary of Electro-mechanical Mode Identification for Test System 2

Cases	Steady state Mode (Hz) & Damping ratio (%)	GFL/GFM Mode (Hz) & Damping ratio (%)	Load change/Fault Mode (Hz) & Damping ratio (%)
Case 1	0.081 & 40.09	0.155 & 0.1153	0.155 & 0.0105
Case 2	0.081 & 40.09	0.155 & 0.0175	0.155 & -0.0035
Case 3	0.081 & 40.09	0.155 & 0.0381	0.155 & 0.01

7.9 Summary

This chapter presents a battery energy storage system, along with a photovoltaic system, that are connected to a power grid through both grid-following and grid-forming control architectures. This chapter also presents the basic fundamental differences between grid-following and grid-forming architectures for grid connected inverters. Grid-forming architectures for controlling grid-connected inverters are an emerging technology and can be utilized for maintaining stability in the grid by providing voltage and frequency support, especially in the weaker parts of the grids. With the increasing penetration of variable distributed en-

ergy resources into present AC utility grids, more inverter-based technologies are being used, where grid-forming with a battery energy storage system can offer a viable solution to enable integration of these inverter-based resources with the existing power grid by addressing performance challenges (e.g., reliability, stability, etc.). In this chapter, integration of a battery energy storage system is shown with a single machine, as well as a larger power grid system (IEEE 13 bus system), to showcase the capability of using grid-forming in larger grids. Also, oscillatory modes can be identified from measurement data collected from SCADA or phasor measurement units (PMUs) to find unstable modes and damping ratios, which can help to build a stability control architecture.

CHAPTER 8: Conclusions and Future Work

8.1 Conclusions

In this dissertation, a series of measurement-based methods for oscillation monitoring, identification, classification, and control for a modern power grid is introduced and each method is evaluated. The main conclusions are as follows.

- In the literature review chapter of this research work, various methods of identification such as model-based identification and measurement-based identification of power systems have been explored. Different state-of-the-art control methods for low-frequency oscillations in the power system to add damping to under-damped modes have also been reviewed. Based on the literature review, measurement based identification methods seem to have certain advantage over model based identification and to perform a real-time environment control architecture, an LQR based dynamic control is considered as a good option alongside measurement based identification method.

- In chapter 3 of this research work, a comparative study of different measurement-based identification methods have been studied on two different test system to showcase the scalability of the methods. All the methods have been implemented in a real-time environment and based on the comparative analysis, the recursive subspace identification method is more robust and efficient than other methods. Mode classification methods have also been explored in this chapter. Based on the comparative analysis in this chapter, subspace based identification methods are more advantageous than other methods because of their robustness and noise prone nature. Recursive based subspace identification is computationally more efficient than non-recursive method and also more accurate.

- In chapter 4, a non-recursive based identification method has been applied to measurement data from the power system and a dynamic control method has also been developed to work alongside the identification method to add damping to the network. The proposed methodology can select multiple generators based on identified modes to add damping and control any sustained low-frequency oscillations. The stability margin of the system can be improved by the proposed method as well as critical clearing time can be improved by almost 30%. The proposed method is implemented in a real-time environment. One disadvantage of using non-recursive identification method is that it is computationally extensive; hence the choice of sampling time and data window length is very limited while implementing the algorithm in real-time environment.

- In chapter 5, a novel framework for a recursive deterministic-stochastic subspace identification has been proposed which is more efficient than non-recursive identification methods in terms of computational time as well as performs better in ring-down or ambient data environments. The control method can add 20% more damping to sustained oscillatory modes than other most used methods. The recursive method is faster and accurate than the non-recursive method.

- In chapter 6, a Lyapunov energy-based oscillation source location method has been proposed and verified against dissipated energy flow algorithm on different test systems and for different types of events. For a larger power system (e.g. IEEE 68 bus), the proposed method performs better than DEF method. Also, the proposed method is tested for a much larger power system and the results are accurate. However, if measurement data is not available from every bus, the method can not pinpoint the oscillation source location to a certain bus but the proposed method can locate the area the oscillation source is located.

- In chapter 7, grid following and grid forming architecture of integrating inverter-based resources to the existing grid have been explored and studied in terms of a battery

energy storage system connected to a grid. Low-frequency oscillation due to inverter-based resource connection to existing grid technology has also been studied. It has been observed that integrating IBRs to existing grid through GFM architecture can introduce low frequency oscillation which is identifiable through measurement based identification methods. Controlling of such modes will be explored in future.

8.2 Future Work

- Future work includes improving the oscillation source location algorithm. Currently, the proposed algorithm can identify source locations only when measurement data from all buses in the system is available. In case of unavailable data from some buses and especially the source, the proposed algorithm identifies nearby buses as the source. Also, the proposed algorithm only works with measurement data. To identify the generator controller type (Governor/Exciter) from where the oscillation originated, model-based data should be used along with measurement data and this part of the algorithm will be worked on in the future.

- Using measurement data and subspace identification techniques, developing a quantitative measurement-based dynamic flexibility index will be analyzed in the future. This index will reflect how the system dynamics are affected by changing loading levels at different locations in the grid and also by intermittent injections from renewable energy sources.

- A dictionary-based approach will be explored for storing model-based state identification of a larger power grid system including different types of generating unit control methods based on this approach, the measurement-based identification method can utilize the dictionary data to pinpoint the location of different states in the power system.

List of Publications

Transactions

- **F. Al Hasnain**, A. Sahami, and S. Kamalasadan, âAn online wide-area direct coordinated control architecture for power grid transient stability enhancement based on subspace identification,â IEEE Transactions on Industry Applications, vol. 57, no. 3, pp. 2896â2907, 2021.

- **F. Al Hasnain**, S. J. Hossain, and S. Kamalasadan, âA novel hybrid deterministic-stochastic recursive subspace identification for electromechanical mode estimation, classification, and control,â IEEE Transactions on Industry Applications, vol. 57, no. 5, pp. 5476â5487, 2021.

Conference Papers

- **F. Al Hasnain**, S. J. Hossain, and S. Kamalasadan, âInvestigation and design of a measurement based electro-mechanical oscillation mode identification and detection in power grid,â in 2021 IEEE Power Energy Society General Meeting (PESGM), pp. 1â5, IEEE, 2021.

- **F. Al Hasnain**, S. Kamalasadan, and M. Smith, âElectro-mechanical mode identification of a bess integrated grid system through subspace identification method,â in 2022 IEEE Global Conference on Computing, Power and Communication Technologies (GlobConPT), pp. 1â6, 2022.

Book Chapter

- S. Kamalasadan, M. Smith, and **F. Al Hasnain**, "Grid-Forming Inverters Interfacing Battery Energy Storage Systems," In title of Book: Grid-Forming Power Inverters: Control and Applications (1st ed.). CRC Press. https://doi.org/10.1201/9781003302520

REFERENCES

[1] J. G. et.al., "i-pcgrid workshop presentations," 2011.

[2] L. Vanfretti and J. H. Chow, "Analysis of power system oscillations for developing synchrophasor data applications," in *2010 IREP Symposium Bulk Power System Dynamics and Control-VIII (IREP)*, pp. 1–17, IEEE, 2010.

[3] G. Liu, J. Quintero, and V. M. Venkatasubramanian, "Oscillation monitoring system based on wide area synchrophasors in power systems," in *2007 iREP symposium-bulk power system dynamics and control-VII. Revitalizing Operational Reliability*, pp. 1–13, IEEE, 2007.

[4] J. Y. Cai, Z. Huang, J. Hauer, and K. Martin, "Current status and experience of wams implementation in north america," in *2005 IEEE/PES Transmission & Distribution Conference & Exposition: Asia and Pacific*, pp. 1–7, IEEE, 2005.

[5] J. W. Pierre, D. J. Trudnowski, and M. K. Donnelly, "Initial results in electromechanical mode identification from ambient data," *IEEE Transactions on Power Systems*, vol. 12, no. 3, pp. 1245–1251, 1997.

[6] G. Prony and J. d. Paris, "L'ecole polytechnique, vol. 1," *Cahier*, vol. 2, pp. 24–76, 1795.

[7] J. F. Hauer, C. Demeure, and L. Scharf, "Initial results in prony analysis of power system response signals," *IEEE Transactions on power systems*, vol. 5, no. 1, pp. 80–89, 1990.

[8] D. J. Trudnowski, J. Johnson, and J. F. Hauer, "Making prony analysis more accurate using multiple signals," *IEEE Transactions on power systems*, vol. 14, no. 1, pp. 226–231, 1999.

[9] J. Hauer, "Application of prony analysis to the determination of modal content and equivalent models for measured power system response," *IEEE Transactions on Power Systems*, vol. 6, no. 3, pp. 1062–1068, 1991.

[10] J.-N. Juang and R. S. Pappa, "An eigensystem realization algorithm for modal parameter identification and model reduction," *Journal of guidance, control, and dynamics*, vol. 8, no. 5, pp. 620–627, 1985.

[11] I. Kamwa, R. Grondin, E. Dickinson, and S. Fortin, "A minimal realization approach to reduced-order modelling and modal analysis for power system response signals," *IEEE Transactions on Power Systems*, vol. 8, no. 3, pp. 1020–1029, 1993.

[12] J. Sanchez-Gasca, "Computation of turbine-generator subsynchronous torsional modes from measured data using the eigensystem realization algorithm," in *2001 IEEE Power Engineering Society Winter Meeting. Conference Proceedings (Cat. No. 01CH37194)*, vol. 3, pp. 1272–1276, IEEE, 2001.

[13] R. S. Pappa and J.-N. Juang, "Some experiences with the eigensystem realization algorithm," 1988.

[14] J.-N. Juang, *Applied system identification*. Prentice-Hall, Inc., 1994.

[15] F. Bazan, "Eigensystem realization algorithm (era): reformulation and system pole perturbation analysis," *Journal of sound and vibration*, vol. 1, no. 274, pp. 433–444, 2004.

[16] Q. Qin, H. Li, L. Qian, and C.-K. Lau, "Modal identification of tsing ma bridge by using improved eigensystem realization algorithm," *Journal of sound and vibration*, vol. 247, no. 2, pp. 325–341, 2001.

[17] J.-N. Juang and R. S. Pappa, "Effects of noise on modal parameters identified by the eigensystem realization algorithm," *Journal of Guidance, Control, and Dynamics*, vol. 9, no. 3, pp. 294–303, 1986.

[18] R. A. De Callafon, B. Moaveni, J. P. Conte, X. He, and E. Udd, "General realization algorithm for modal identification of linear dynamic systems," *Journal of engineering mechanics*, vol. 134, no. 9, pp. 712–722, 2008.

[19] Y. Hua and T. K. Sarkar, "Matrix pencil method for estimating parameters of exponentially damped/undamped sinusoids in noise," *IEEE Transactions on Acoustics, Speech, and Signal Processing*, vol. 38, no. 5, pp. 814–824, 1990.

[20] T. K. Sarkar and O. Pereira, "Using the matrix pencil method to estimate the parameters of a sum of complex exponentials," *IEEE Antennas and Propagation Magazine*, vol. 37, no. 1, pp. 48–55, 1995.

[21] Y. Hua and T. K. Sarkar, "Generalized pencil-of-function method for extracting poles of an em system from its transient response," 1989.

[22] P. Van Overschee and B. De Moor, *Subspace identification for linear systems: TheoryâImplementationâApplications*. Springer Science & Business Media, 2012.

[23] R. Brincker and P. Andersen, "Understanding stochastic subspace identification," *Proceedings of the 24th IMAC, St. Louis*, vol. 126, 2006.

[24] A. Mohammadi, H. Khaloozadeh, and R. Amjadifard, "Small signal monitoring of power system using subspace system identification," *International Journal of Computers Communications & Control*, vol. 7, no. 2, pp. 325–340, 2012.

[25] M. Mansouri, D. Westwick, and A. M. Knight, "A n4sid-based strategy to estimate the parameters of disturbances in power systems," in *2018 IEEE PES Innovative Smart Grid Technologies Conference Europe (ISGT-Europe)*, pp. 1–6, IEEE, 2018.

[26] S. N. Sarmadi and V. Venkatasubramanian, "Electromechanical mode estimation using recursive adaptive stochastic subspace identification," *IEEE Transactions on Power Systems*, vol. 29, no. 1, pp. 349–358, 2013.

[27] R. Eriksson and L. Soder, "Wide-area measurement system-based subspace identification for obtaining linear models to centrally coordinate controllable devices," *IEEE Transactions on Power Delivery*, vol. 26, no. 2, pp. 988–997, 2011.

[28] I. Kamwa and L. Gerin-Lajoie, "State-space system identification-toward mimo models for modal analysis and optimization of bulk power systems," *IEEE Transactions on Power Systems*, vol. 15, no. 1, pp. 326–335, 2000.

[29] N. Zhou, J. W. Pierre, and J. F. Hauer, "Initial results in power system identification from injected probing signals using a subspace method," *IEEE Transactions on Power Systems*, vol. 21, no. 3, pp. 1296–1302, 2006.

[30] S. J. Hossain and S. Kamalasadan, "Combined deterministic-stochastic online subspace identification for power system mode estimation and oscillation classification," in *2019 IEEE Industry Applications Society Annual Meeting*, pp. 1–9, 2019.

[31] S. J. Hossain and S. Kamalasadan, "Investigation on evaluating the unmodeled dynamics of power system and its effects on characterizing power system oscillations," in *2018 North American Power Symposium (NAPS)*, pp. 1–6, IEEE, 2018.

[32] S. Kamalasadan and A. A. Ghandakly, "A novel multiple reference model adaptive control approach for multimodal and dynamic systems," *Control and intelligent systems*, vol. 36, no. 2, pp. 119–128, 2008.

[33] A. Thakallapelli and S. Kamalasadan, "Alternating direction method of multipliers (admm) based distributed approach for wide-area control," in *2017 IEEE Industry Applications Society Annual Meeting*, 2017.

[34] S. Thakallapelli, Abilash: Kamalasadan, "Alternating direction method of multipliers (admms) based distributed approach for wide-area control," *IEEE Transactions on Industry Applications*, vol. 55, no. 3, pp. 3215–3227, 2019.

[35] J. Thorp, C. Seyler, and A. Phadke, "Electromechanical wave propagation in large electric power systems," *IEEE Transactions on Circuits and Systems I: Fundamental Theory and Applications*, vol. 45, no. 6, pp. 614–622, 1998.

[36] P. N. Markham and Y. Liu, "Electromechanical speed map development using fnet/-grideye frequency measurements," in *2014 IEEE PES General Meeting | Conference Exposition*, pp. 1–5, 2014.

[37] L. Q. T. L. H. X. ZHU Zhenshan, LIU Dichen and Z. Qiang, "Disturbance source location of forced power oscillation based on lms time delay estimation method," *AEPS*, vol. 39, p. 58, 2 2015.

[38] R. T. Alden and A. A. Shaltout, "Analysis of damping and synchronizing torques part i-a general calculation method," *IEEE Transactions on Power Apparatus and Systems*, vol. PAS-98, no. 5, pp. 1696–1700, 1979.

[39] A. A. Shaltout and R. T. Alden, "Analysis of damping and synchronizing torques part ii-effect of operating conditions and machine parameters," *IEEE Transactions on Power Apparatus and Systems*, vol. PAS-98, no. 5, pp. 1701–1708, 1979.

[40] A. Shaltout and K. Abu Al-Feilat, "Damping and synchronizing torque computation in multimachine power systems," *IEEE Transactions on Power Systems*, vol. 7, no. 1, pp. 280–286, 1992.

[41] Y. Li, Y. Huang, J. Liu, W. Yao, and J. Wen, "Power system oscillation source location based on damping torque analysis," *Dianli Xitong Baohu yu Kongzhi/Power System Protection and Control*, vol. 43, pp. 84–91, 07 2015.

[42] L. Dosiek, N. Zhou, J. W. Pierre, Z. Huang, and D. J. Trudnowski, "Mode shape estimation algorithms under ambient conditions: A comparative review," *IEEE Transactions on Power Systems*, vol. 28, no. 2, pp. 779–787, 2013.

[43] M. Wang and H. Sun, "An analysis method for forced power oscillation source detection," vol. 34, pp. 6209–6215, 12 2014.

[44] S. Maslennikov, B. Wang, Q. Zhang, a. Ma, a. Luo, a. Sun, and E. Litvinov, "A test cases library for methods locating the sources of sustained oscillations," in *2016 IEEE Power and Energy Society General Meeting (PESGM)*, pp. 1–5, 2016.

[45] R. B. Myers and D. J. Trudnowski, "Effects of forced oscillations on spectral-based mode-shape estimation," in *2013 IEEE Power Energy Society General Meeting*, pp. 1–6, 2013.

[46] W. Hu, T. Lin, Y. Gao, F. Zhang, J. Li, J. Li, Y. Huang, and X. Xu, "Disturbance source location of forced power oscillation in regional power grid," in *2011 IEEE Power Engineering and Automation Conference*, vol. 2, pp. 363–366, 2011.

[47] Y. Yu, Y. Min, L. Chen, and P. Ju, "The disturbance source identification of forced power oscillation caused by continuous cyclical load," in *2011 4th International Conference on Electric Utility Deregulation and Restructuring and Power Technologies (DRPT)*, pp. 308–313, 2011.

[48] Y. Li, C. Shen, and F. Liu, "A methodology for power system oscillation analysis based on energy structure," *Dianli Xitong Zidonghua/Automation of Electric Power Systems*, vol. 37, pp. 49–56, 07 2013.

[49] L. Chen, Y. Min, and W. Hu, "Low frequency oscillation analysis and oscillation source location based on oscillation energy. part one: Mathematical foundation and energy flow computation," *Dianli Xitong Zidonghua/Automation of Electric Power Systems*, vol. 36, pp. 22–27+86, 02 2012.

[50] L. Chen, Y. Min, and W. Hu, "An energy-based method for location of power system oscillation source," *IEEE Transactions on Power Systems*, vol. 28, no. 2, pp. 828–836, 2013.

[51] J. W. Pierre, D. Trudnowski, M. Donnelly, N. Zhou, F. K. Tuffner, and L. Dosiek, "Overview of system identification for power systems from measured responses1," *IFAC Proceedings Volumes*, vol. 45, no. 16, pp. 989–1000, 2012. 16th IFAC Symposium on System Identification.

[52] P. Kundur, N. J. Balu, and M. G. Lauby, *Power system stability and control*, vol. 7. McGraw-hill New York, 1994.

[53] R. W. Longman and J.-N. Juang, "Recursive form of the eigensystem realization algorithm for system identification," *Journal of Guidance, Control, and Dynamics*, vol. 12, no. 5, pp. 647–652, 1989.

[54] S. J. Hossain and S. Kamalasadan, "Online measurement based power system reduced order model generation and validation," in *2019 North American Power Symposium (NAPS)*, pp. 1–6, IEEE, 2019.

[55] K. D. Cock, G. MercÃšre, and B. D. Moor, "Recursive subspace identification for in-flight modal analysis of airplanes."

[56] P. Kundur, *Power System Stability And Control*. EPRI power system engineering series, McGraw-Hill, 1994.

[57] M. A. Pai and P. W. Sauer, "Stability analysis of power systems by lyapunov's direct method," *IEEE Control Systems Magazine*, vol. 9, 1989.

[58] A. Fouad and V. Vittal, *Power System Transient Stability Analysis Using the Transient Energy Function Method*. Pearson Education, 1991.

[59] R. Yousefian, A. Sahami, and S. Kamalasadan, "Hybrid energy function based real-time optimal wide-area transient stability controller for power system stability," in *2015 IEEE Industry Applications Society Annual Meeting*, pp. 1–8, Oct 2015.

[60] R. Yousefian, A. Sahami, and S.Kamalasadan, "Hybrid transient energy function-based real-time optimal wide-area damping controller," *IEEE Transactions on Industry Applications*, pp. 1506–1516, 2017.

[61] M. Tajdinian, A. R. Seifi, and M. Allahbakhshi, "Transient stability of power grids comprising wind turbines: New formulation, implementation, and application in real-time assessment," *IEEE Systems Journal*, pp. 1–12, 2018.

[62] T. L. Vu and K. Turitsyn, "Lyapunov functions family approach to transient stability assessment," *IEEE Transactions on Power Systems*, vol. 31, pp. 1269–1277, March 2016.

[63] N. G. Bretas and L. F. C. Alberto, "Energy function for power systems with transmission losses: extension of the invariance principle," in *PowerCon 2000. 2000 International Conference on Power System Technology. Proceedings (Cat. No.00EX409)*, vol. 1, pp. 145–150 vol.1, 2000.

[64] A. M. Eskicioglu and O. Sevaioglu, "Feasibility of lyapunov functions for power system transient stability analysis by the controlling uep method," *IEE Proceedings C - Generation, Transmission and Distribution*, vol. 139, pp. 152–156, March 1992.

[65] A. Ishigame and T. Taniguchi, "Transient stability analysis for power system using lyapunov function with load characteristics," in *2003 IEEE Power Engineering Society General Meeting (IEEE Cat. No.03CH37491)*, vol. 2, pp. 736–740 Vol. 2, July 2003.

[66] M. F. Bedrinana, V. L. Paucar, and C. A. Castro, "Transient stability using energy function method in power systems close to voltage collapse," in *2007 Large Engineering Systems Conference on Power Engineering*, pp. 226–228, Oct 2007.

[67] T. F. Orchi, T. K. Roy, M. A. Mahmud, and A. M. T. Oo, "Feedback linearizing model predictive excitation controller design for multimachine power systems," *IEEE Access*, vol. 6, pp. 2310–2319, 2018.

[68] A. Sahami and S. Kamalasadan, "Potential energy prediction based control for transient stability enhancement," in *2019 IEEE Industry Applications Society Annual Meeting*, pp. 1–8, 2019.

[69] S. J. Hossain and S. Kamalasadan, "Online measurement based power system reduced order model generation and validation," in *2019 North American Power Symposium (NAPS)*, pp. 1–6, 2019.

[70] P. Aylett, "The energy-integral criterion of transient stability limits of power systems," *Proceedings of the IEE - Part C: Monographs*, vol. 105, pp. 527–536(9), September 1958.

[71] A. Sahami and S. Kamalasadan, "Prediction and enhancement of power system transient stability using taylor series," in *2018 North American Power Symposium (NAPS)*, pp. 1–6, 2018.

[72] A. K. Singh, B. C. Pal, *et al.*, "Report on the 68-bus, 16-machine, 5-area system," *IEEE PES Task Force on Benchmark Systems for Stability Controls. Ver*, vol. 3, 2013.

[73] A. Vahidnia, G. Ledwich, E. Palmer, and A. Ghosh, "Wide-area control through aggregation of power systems," *IET Generation, Transmission Distribution*, vol. 9, no. 12, pp. 1292–1300, 2015.

[74] A. Vahidnia, G. Ledwich, and E. W. Palmer, "Transient stability improvement through wide-area controlled svcs," *IEEE Transactions on Power Systems*, vol. 31, no. 4, pp. 3082–3089, 2016.

[75] P. Pourbeik, P. S. Kundur, and C. W. Taylor, "The anatomy of a power grid blackout - root causes and dynamics of recent major blackouts," *IEEE Power and Energy Magazine*, vol. 4, pp. 22–29, Sept 2006.

[76] "Identification of electromechanical modes in power systems," May 2018.

[77] N. Zhou, D. J. Trudnowski, J. W. Pierre, and W. A. Mittelstadt, "Electromechanical mode online estimation using regularized robust rls methods," *IEEE Transactions on Power Systems*, vol. 23, pp. 1670–1680, Nov 2008.

[78] S. A. N. Sarmadi and V. Venkatasubramanian, "Electromechanical mode estimation using recursive adaptive stochastic subspace identification," *IEEE Transactions on Power Systems*, vol. 29, pp. 349–358, Jan 2014.

[79] T. Jiang, H. Yuan, H. Jia, N. Zhou, and F. Li, "Stochastic subspace identification-based approach for tracking inter-area oscillatory modes in bulk power system utilising synchrophasor measurements," *IET Generation, Transmission Distribution*, vol. 9, no. 15, pp. 2409–2418, 2015.

[80] M. Ghorbaniparvar, "Survey on forced oscillations in power system," *Journal of Modern Power Systems and Clean Energy*, vol. 5, pp. 671–682, Sep 2017.

[81] S. A. N. Sarmadi and V. Venkatasubramanian, "Inter-area resonance in power systems from forced oscillations," *IEEE Transactions on Power Systems*, vol. 31, pp. 378–386, Jan 2016.

[82] R. Bhattarai, S. J. Hossain, J. Qi, J. Wang, and S. Kamalasadan, "Sustained system oscillation by malicious cyber attacks on distributed energy resources," in *2018 IEEE Power Energy Society General Meeting (PESGM)*, pp. 1–5, Aug 2018.

[83] A. Thakallapelli, S. J. Hossain, and S. Kamalasadan, "Coherency and online signal selection based wide area control of wind integrated power grid," *IEEE Transactions on Industry Applications*, vol. 54, pp. 3712–3722, July 2018.

[84] B. Peeters and G. D. Roeck, "Stochastic system identification for operational modal analysis : A review," 2001.

[85] J. Follum, J. W. Pierre, and R. Martin, "Simultaneous estimation of electromechanical modes and forced oscillations," *IEEE Transactions on Power Systems*, vol. 32, pp. 3958–3967, Sept 2017.

[86] V. S. PeriÄ and L. Vanfretti, "Power-system ambient-mode estimation considering spectral load properties," *IEEE Transactions on Power Systems*, vol. 29, pp. 1133–1143, May 2014.

[87] S. Maslennikov, B. Wang, Q. Zhang, a. Ma, a. Luo, a. Sun, and E. Litvinov, "A test cases library for methods locating the sources of sustained oscillations," in *2016 IEEE Power and Energy Society General Meeting (PESGM)*, pp. 1–5, July 2016.

[88] J. W. Pierre, D. Trudnowski, M. Donnelly, N. Zhou, F. K. Tuffner, and L. Dosiek, "Overview of system identification for power systems from measured responses1," *IFAC Proceedings Volumes*, vol. 45, no. 16, pp. 989 – 1000, 2012.

[89] D. A. Gray, M. J. Gibbard, and D. J. Vowles, "Characterisation of ambient noise in electricity power grids," in *Proceedings of the Eighth International Symposium on Signal Processing and Its Applications, 2005.*, vol. 2, pp. 835–838, Aug 2005.

[90] W. Li, M. Wang, and J. H. Chow, "Real-time event identification through low-dimensional subspace characterization of high-dimensional synchrophasor data," *IEEE Transactions on Power Systems*, vol. 33, pp. 4937–4947, Sep. 2018.

[91] R. Bhattarai, S. J. Hossain, J. Qi, J. Wang, and S. Kamalasadan, "Sustained system oscillation by malicious cyber attacks on distributed energy resources," in *2018 IEEE Power Energy Society General Meeting (PESGM)*, pp. 1–5, Aug 2018.

[92] R. W. Wies, J. W. Pierre, and D. J. Trudnowski, "Use of arma block processing for estimating stationary low-frequency electromechanical modes of power systems," *IEEE Transactions on Power Systems*, vol. 18, no. 1, pp. 167–173, 2003.

[93] L. Dosiek and J. W. Pierre, "Estimating electromechanical modes and mode shapes using the multichannel armax model," *IEEE transactions on power systems*, vol. 28, no. 2, pp. 1950–1959, 2013.

[94] W. Yao, L. Jiang, J. Wen, Q. Wu, and S. Cheng, "Wide-area damping controller for power system interarea oscillations: A networked predictive control approach," *IEEE Transactions on Control Systems Technology*, vol. 23, no. 1, pp. 27–36, 2014.

[95] S. Moghadasi and S. Kamalasadan, "Voltage security cost assessment of integrated ac-dc systems using semidefinite programming," in *2016 IEEE Power & Energy Society Innovative Smart Grid Technologies Conference (ISGT)*, pp. 1–5, IEEE, 2016.

[96] A. Sahami, R. Yousefian, and S. Kamalasadan, "An approach based on potential energy balance for transient stability improvement in modern power grid," in *2018 IEEE Power and Energy Conference at Illinois (PECI)*, pp. 1–7, IEEE, 2018.

[97] M. Ahmed and S. Kamalasadan, "An approach for local net-load ramp rate control using integrated energy storage based on least square error minimization technique," in *2018 IEEE Power and Energy Conference at Illinois (PECI)*, pp. 1–6, IEEE, 2018.

[98] F. Al Hasnain, A. Sahami, and S. Kamalasadan, "An online wide-area direct coordinated control architecture for power grid transient stability enhancement based on subspace identification," *IEEE Transactions on Industry Applications*, vol. 57, no. 3, pp. 2896–2907, 2021.

[99] N. Zhou, Z. Huang, L. Dosiek, D. Trudnowski, and J. W. Pierre, "Electromechanical mode shape estimation based on transfer function identification using pmu measurements," in *2009 IEEE Power & Energy Society General Meeting*, pp. 1–7, IEEE, 2009.

[100] H. Liu, L. Zhu, Z. Pan, F. Bai, Y. Liu, Y. Liu, M. Patel, E. Farantatos, and N. Bhatt, "Armax-based transfer function model identification using wide-area measurement for adaptive and coordinated damping control," *IEEE Transactions on Smart Grid*, vol. 8, no. 3, pp. 1105–1115, 2015.

[101] Y.-H. Moon, B.-H. Cho, Y.-H. Lee, and H.-S. Hong, "Energy conservation law and its application for the direct energy method of power system stability," in *IEEE Power Engineering Society. 1999 Winter Meeting (Cat. No.99CH36233)*, vol. 1, pp. 695–700 vol.1, 1999.

[102] J. E. Price and J. Goodin, "Reduced network modeling of wecc as a market design prototype," in *2011 IEEE Power and Energy Society General Meeting*, pp. 1–6, 2011.

[103] D. B. Rathnayake, M. Akrami, C. Phurailatpam, S. P. Me, S. Hadavi, G. Jayasinghe, S. Zabihi, and B. Bahrani, "Grid forming inverter modeling, control, and applications," *IEEE Access*, vol. 9, pp. 114781–114807, 2021.

[104] M. Farrokhabadi, S. Konig, C. A. Canizares, K. Bhattacharya, and T. Leibfried, "Battery energy storage system models for microgrid stability analysis and dynamic simulation," *IEEE Transactions on Power Systems*, vol. 33, no. 2, pp. 2301–2312, 2018.

[105] K. Divya and J. Østergaard, "Battery energy storage technology for power systemsâan overview," *Electric power systems research*, vol. 79, no. 4, pp. 511–520, 2009.

[106] F. Al Hasnain, S. Kamalasadan, and M. Smith, "Electro-mechanical mode identification of a bess integrated grid system through subspace identification method," in *2022 IEEE Global Conference on Computing, Power and Communication Technologies (GlobConPT)*, pp. 1–6, 2022.

[107] L. Mariam, M. Basu, and M. F. Conlon, "A review of existing microgrid architectures," *Journal of engineering*, vol. 2013, 2013.

[108] L. Mariam, M. Basu, and M. F. Conlon, "Microgrid: Architecture, policy and future trends," *Renewable and Sustainable Energy Reviews*, vol. 64, pp. 477–489, 2016.

[109] X. Fu, J. Sun, M. Huang, Z. Tian, H. Yan, H. H.-C. Iu, P. Hu, and X. Zha, "Large-signal stability of grid-forming and grid-following controls in voltage source converter: A comparative study," *IEEE Transactions on Power Electronics*, vol. 36, no. 7, pp. 7832–7840, 2021.

[110] O. Ogundairo, S. Kamalasadan, A. R. Nair, and M. Smith, "Oscillation damping of integrated transmission and distribution power grid with renewables based on novel measurement-based optimal controller," *IEEE Transactions on Industry Applications*, vol. 58, no. 3, pp. 4181–4191, 2022.

[111] P. Nema, R. Nema, and S. Rangnekar, "A current and future state of art development of hybrid energy system using wind and pv-solar: A review," *Renewable and Sustainable Energy Reviews*, vol. 13, no. 8, pp. 2096–2103, 2009.

[112] S. Sinha and S. Chandel, "Review of recent trends in optimization techniques for solar photovoltaic–wind based hybrid energy systems," *Renewable and Sustainable Energy Reviews*, vol. 50, pp. 755–769, 2015.

[113] R. Luna-Rubio, M. Trejo-Perea, D. Vargas-Vázquez, and G. Ríos-Moreno, "Optimal sizing of renewable hybrids energy systems: A review of methodologies," *Solar energy*, vol. 86, no. 4, pp. 1077–1088, 2012.

[114] S. Upadhyay and M. Sharma, "A review on configurations, control and sizing methodologies of hybrid energy systems," *Renewable and Sustainable Energy Reviews*, vol. 38, pp. 47–63, 2014.

[115] P. Prakash and D. K. Khatod, "Optimal sizing and siting techniques for distributed generation in distribution systems: A review," *Renewable and sustainable energy reviews*, vol. 57, pp. 111–130, 2016.

[116] Y. Yang, S. Bremner, C. Menictas, and M. Kay, "Battery energy storage system size determination in renewable energy systems: A review," *Renewable and Sustainable Energy Reviews*, vol. 91, pp. 109–125, 2018.

[117] N.-K. C. Nair and N. Garimella, "Battery energy storage systems: Assessment for small-scale renewable energy integration," *Energy and Buildings*, vol. 42, no. 11, pp. 2124–2130, 2010.

[118] A. Poullikkas, "A comparative overview of large-scale battery systems for electricity storage," *Renewable and Sustainable energy reviews*, vol. 27, pp. 778–788, 2013.

[119] J. Cho, S. Jeong, and Y. Kim, "Commercial and research battery technologies for electrical energy storage applications," *Progress in Energy and Combustion Science*, vol. 48, pp. 84–101, 2015.

[120] X. Luo, J. Wang, M. Dooner, and J. Clarke, "Overview of current development in electrical energy storage technologies and the application potential in power system operation," *Applied energy*, vol. 137, pp. 511–536, 2015.

[121] T. Bowen, I. Chernyakhovskiy, and P. L. Denholm, "Grid-scale battery storage: frequently asked questions," tech. rep., National Renewable Energy Lab.(NREL), Golden, CO (United States), 2019.

[122] F. Al Hasnain, S. J. Hossain, and S. Kamalasadan, "Investigation and design of a measurement based electro-mechanical oscillation mode identification and detection in power grid," in *2021 IEEE Power & Energy Society General Meeting (PESGM)*, pp. 1–5, IEEE, 2021.

[123] F. Al Hasnain, A. Sahami, and S. Kamalasadan, "An online wide-area direct coordinated control architecture for power grid transient stability enhancement based on subspace identification," *IEEE Transactions on Industry Applications*, vol. 57, no. 3, pp. 2896–2907, 2021.

[124] F. Al Hasnain, S. J. Hossain, and S. Kamalasadan, "A novel hybrid deterministic-stochastic recursive subspace identification for electromechanical mode estimation, classification, and control," *IEEE Transactions on Industry Applications*, vol. 57, no. 5, pp. 5476–5487, 2021.

APPENDIX A: Identifying States

A.1 Generator Equations

With generator amortisseurs included. The assumption is that the model includes one d-axis amortisseur and two q-axis amortisseurs.

Rotor Circuit equations:

$$\dot{\psi_{fd}} = \frac{\omega_o R_{fd}}{L_{adu}} E_{fd} - \omega_o R_{fd} i_{fd} \tag{A.1}$$

$$\dot{\psi_{1d}} = -\omega_o R_{1d} i_{1d} \tag{A.2}$$

$$\dot{\psi_{1q}} = -\omega_o R_{1q} i_{1q} \tag{A.3}$$

$$\dot{\psi_{2q}} = -\omega_o R_{2q} i_{2q} \tag{A.4}$$

The rotor currents are given by:

$$i_{fd} = \frac{1}{L_{fd}} (\psi_{fd} - \psi_{ad}) \tag{A.5}$$

$$i_{1d} = \frac{1}{L_{1d}} (\psi_{1d} - \psi_{ad}) \tag{A.6}$$

$$i_{1q} = \frac{1}{L_{1q}} (\psi_{1q} - \psi_{aq}) \tag{A.7}$$

$$i_{2q} = \frac{1}{L_{2q}}(\psi_{2q} - \psi_{aq}) \tag{A.8}$$

The d-axis and q-axis mutual flux linkages are given by:

$$\begin{aligned}\psi_{ad} &= -L_{ads}i_d + L_{ads}i_{fd} + L_{ads}i_{1d} \\ &= L''_{ads}\left(-i_d + \frac{\psi_{fd}}{L_{fd}} + \frac{\psi_{1d}}{L_{1d}}\right)\end{aligned} \tag{A.9}$$

$$\psi_{aq} = L''_{aqs}\left(-i_q + \frac{\psi_{1q}}{L_{1q}} + \frac{\psi_{2q}}{L_{2q}}\right) \tag{A.10}$$

Where,

$$L''_{ads} = \frac{1}{\frac{1}{L_{ads}} + \frac{1}{L_{fd}} + \frac{1}{L_{1d}}} \tag{A.11}$$

$$L''_{aqs} = \frac{1}{\frac{1}{L_{aqs}} + \frac{1}{L_{1q}} + \frac{1}{L_{2q}}} \tag{A.12}$$

The expressions for i_d and i_q become,

$$i_q = \frac{X_{Tq}E_{qN} - R_T E_{dN}}{D} \tag{A.13}$$

$$i_d = \frac{R_T E_{qN} + X_{Td}E_{dN}}{D} \tag{A.14}$$

Where,

$$
\begin{aligned}
E_{dN} &= E''_d + E_B sin\delta \\
E_{qN} &= E''_q + E_B cos\delta \\
E''_d &= \bar{\omega} L''_{ads} \left(\frac{\psi_{1q}}{L_{1q}} + \frac{\psi_{2q}}{L_{2q}} \right) \\
E''_q &= \bar{\omega} L''_{ads} \left(\frac{\psi_{fd}}{L_{fd}} + \frac{\psi_{1d}}{L_{1d}} \right) \\
X_{Td} &= X_E + \bar{\omega}(L''_{ads} + L_l) \\
&= X_E + X''_{ds} \\
X_{Tq} &= X_E + \bar{\omega}(L''_{aqs} + L_l) \\
&= X_E + X''_{qs} \\
R_T &= R_a + R_E \\
D &= R_T^2 + X_{Td} X_{Tq}
\end{aligned} \tag{A.15}
$$

Expressing equations (24) to (26) in terms of perturbed values, we get,

$$
\begin{aligned}
\Delta i_d &= m_1 \Delta d + m_2 \Delta \psi_{fd} + m_3 \Delta \psi_{1d} + m_4 \Delta \psi_{1q} + m_5 \Delta \psi_{2q} \\
\Delta i_q &= n_1 \Delta d + n_2 \Delta \psi_{fd} + n_3 \Delta \psi_{1d} + n_4 \Delta \psi_{1q} + n_5 \Delta \psi_{2q}
\end{aligned} \tag{A.16}
$$

Where,

$$
\begin{aligned}
m_1 &= \frac{E_B}{D}(X_{Tq} sin\delta_o - R_T cos\delta_o) \\
m_2 &= \frac{X_{Tq}}{D}\frac{L''_{ads}}{L_{fd}} \\
m_3 &= \frac{X_{Tq}}{D}\frac{L''_{ads}}{L_{1d}} \\
m_4 &= -\frac{R_T}{D}\frac{L''_{aqs}}{L_{1q}} \\
m_5 &= -\frac{R_T}{D}\frac{L''_{aqs}}{L_{2q}} \\
n_1 &= \frac{E_B}{D}(R_T sin\delta_o - X_{Td} cos\delta_o) \\
n_2 &= \frac{R_T}{D}\frac{L''_{ads}}{L_{fd}} \\
n_3 &= \frac{R_T}{D}\frac{L''_{ads}}{L_{1d}} \\
n_4 &= \frac{X_{Td}}{D}\frac{L''_{aqs}}{L_{1q}} \\
n_5 &= \frac{X_{Td}}{D}\frac{L''_{aqs}}{L_{2q}}
\end{aligned} \tag{A.17}
$$

The expressions for $\Delta\psi_{ad}$ and $\Delta\psi_{aq}$ are given by,

$$
\begin{aligned}
\Delta\psi_{ad} &= (-m_1 L''_{ads})\Delta\delta + L''_{ads}\left(\frac{1}{L_{fd}} - m_2\right)\Delta\psi_{fd} \\
&+L''_{ads}\left(\frac{1}{L_{1d}} - m_3\right)\Delta\psi_{1d} + (-m_4 L''_{ads})\Delta\psi_{1q} + (-m_5 L''_{ads})\Delta\psi_{2q}
\end{aligned} \tag{A.18}
$$

$$
\begin{aligned}
\Delta\psi_{aq} &= (-n_1 L''_{aqs})\Delta\delta + (-n_2 L''_{aqs})\Delta\psi_{fd} + (-n_3 L''_{aqs})\Delta\psi_{1d} \\
&+L''_{aqs}\left(\frac{1}{L_{1q}} - n_4\right)\Delta\psi_{1q} + L''_{aqs}\left(\frac{1}{L_{2q}} - n_5\right)\Delta\psi_{2q}
\end{aligned} \tag{A.19}
$$

The expression for ΔT_e is given by,

$$\Delta T_e = \psi_{adO}\Delta i_q + i_{qO}\Delta\psi_{ad} - \psi_{aqO}\Delta i_d + i_{dO}\Delta\psi_{aq}$$
$$= K_1\Delta\delta + K_2\Delta\psi_{fd} + K_{21}\Delta\psi_{1d} + K_{22}\Delta\psi_{1q} + K_{23}\Delta\psi_{2q} \quad \text{(A.20)}$$

Where,

$$K_1 = n_1(\psi_{adO} + L''_{aqs}i_{dO}) - m_1(\psi_{aqO} + L''_{ads}i_{qO})$$
$$K_2 = n_2(\psi_{adO} + L''_{aqs}i_{dO}) - m_2(\psi_{aqO} + L''_{ads}i_{qO}) + \frac{L''_{ads}}{L_{fd}}i_{qO}$$
$$K_3 = n_3(\psi_{adO} + L''_{aqs}i_{dO}) - m_3(\psi_{aqO} + L''_{ads}i_{qO}) + \frac{L''_{ads}}{L_{1d}}i_{qO}$$
$$K_4 = n_4(\psi_{adO} + L''_{aqs}i_{dO}) - m_4(\psi_{aqO} + L''_{ads}i_{qO}) + \frac{L''_{aqs}}{L_{1q}}i_{dO}$$
$$K_5 = n_5(\psi_{adO} + L''_{aqs}i_{dO}) - m_5(\psi_{aqO} + L''_{ads}i_{qO}) + \frac{L''_{aqs}}{L_{2q}}i_{dO} \quad \text{(A.21)}$$

Now,

$$\Delta\dot{\omega}_r = \frac{1}{2H}\left[\Delta T_m - \Delta T_e - K_D\Delta\omega_r\right]$$
$$= \frac{1}{2H}\left[\Delta T_m - K_1\Delta\delta - K_2\Delta\psi_{fd} - K_{21}\Delta\psi_{1d}\right.$$
$$\left. -K_{22}\Delta\psi_{1q} - K_{23}\Delta\psi_{2q} - K_D\Delta\omega_r\right] \quad \textit{sub}$$
$$= a_{11}\Delta\omega_r + a_{12}\Delta\delta + a_{13}\Delta\psi_{fd} + a_{14}\Delta\psi_{1d}$$
$$+a_{15}\Delta\psi_{1q} + a_{16}\Delta\psi_{2q} + b_{11}\Delta T_m \quad \text{(A.22)}$$

Where,

$$
\begin{aligned}
a_{11} &= -\frac{K_D}{2H} \\
a_{12} &= -\frac{K_1}{2H} \\
a_{13} &= -\frac{K_2}{2H} \\
a_{14} &= -\frac{K_{21}}{2H} \\
a_{15} &= -\frac{K_{22}}{2H} \\
a_{16} &= -\frac{K_{23}}{2H} \\
b_{11} &= -\frac{1}{2H}
\end{aligned} \tag{A.23}
$$

And,

$$
\dot{\Delta\delta} = a_{21}\Delta\omega_r \tag{A.24}
$$

Where,

$$
a_{21} = \omega_0 = 2\pi f_0 \tag{A.25}
$$

Now,

$$
\begin{aligned}
\Delta\dot{\psi}_{fd} = a_{31}\Delta\omega_r + a_{32}\Delta\delta + a_{33}\Delta\psi_{fd} + a_{34}\Delta\psi_{1d} \\
+a_{35}\Delta\psi_{1q} + a_{36}\Delta\psi_{2q} + b_{32}\Delta e_{fd}
\end{aligned} \tag{A.26}
$$

Where,

$$
\begin{aligned}
a_{31} &= 0 \\
a_{32} &= -\frac{\omega_0 R_{fd}}{L_{fd}} m_1 L''_{ads} \\
a_{33} &= -\frac{\omega_0 R_{fd}}{L_{fd}} \left(1 - \frac{L''_{ads}}{L_{fd}} + m_2 L''_{ads}\right) \\
a_{34} &= -\frac{\omega_0 R_{fd}}{L_{fd}} \left(m_3 L''_{ads} - \frac{L''_{ads}}{L_{fd}}\right) \\
a_{35} &= -\frac{\omega_0 R_{fd}}{L_{fd}} m_4 L''_{ads} \\
a_{36} &= -\frac{\omega_0 R_{fd}}{L_{fd}} m_5 L''_{ads} \\
b_{32} &= \frac{\omega_0 R_{fd}}{L_{adu}}
\end{aligned}
\tag{A.27}
$$

Similarly,

$$
\begin{aligned}
\Delta\dot{\psi}_{1d} &= -\omega_0 R_{1d} \Delta i_{1d} \\
&= a_{41}\Delta\omega_r + a_{42}\Delta\delta + a_{43}\Delta\psi_{fd} + a_{44}\Delta\psi_{1d} \\
&\quad + a_{45}\Delta\psi_{1q} + a_{46}\Delta\psi_{2q}
\end{aligned}
\tag{A.28}
$$

Where,

$$
\begin{aligned}
a_{41} &= 0 \\
a_{42} &= -\frac{\omega_0 R_{1d}}{L_{1d}} m_1 L''_{ads} \\
a_{43} &= -\frac{\omega_0 R_{1d}}{L_{1d}} \left(m_2 L''_{ads} - \frac{L''_{ads}}{L_{fd}} \right) \\
a_{44} &= -\frac{\omega_0 R_{1d}}{L_{1d}} \left(1 - \frac{L''_{ads}}{L_{fd}} + m_3 L''_{ads} \right) \\
a_{45} &= -\frac{\omega_0 R_{1d}}{L_{1d}} m_4 L''_{ads} \\
a_{46} &= -\frac{\omega_0 R_{1d}}{L_{1d}} m_5 L''_{ads}
\end{aligned} \tag{A.29}
$$

For q-axis,

$$
\begin{aligned}
\Delta\dot{\psi}_{1q} &= -\omega_0 R_{1q} \Delta i_{1q} \\
&= a_{51}\Delta\omega_r + a_{52}\Delta\delta + a_{53}\Delta\psi_{fd} + a_{54}\Delta\psi_{1d} \\
&\quad + a_{55}\Delta\psi_{1q} + a_{56}\Delta\psi_{2q}
\end{aligned} \tag{A.30}
$$

Where,

$$
\begin{aligned}
a_{51} &= 0 \\
a_{52} &= -\frac{\omega_0 R_{1q}}{L_{1q}} n_1 L''_{aqs} \\
a_{53} &= -\frac{\omega_0 R_{1q}}{L_{1q}} n_2 L''_{aqs} \\
a_{54} &= -\frac{\omega_0 R_{1q}}{L_{1q}} n_3 L''_{aqs} \\
a_{55} &= -\frac{\omega_0 R_{1q}}{L_{1q}} \left(1 - \frac{L''_{aqs}}{L_{1q}} + n_4 L''_{aqs}\right) \\
a_{56} &= -\frac{\omega_0 R_{1q}}{L_{1q}} \left(n_5 L''_{aqs} - \frac{L''_{aqs}}{L_{2q}}\right)
\end{aligned} \tag{A.31}
$$

And,

$$
\begin{aligned}
\Delta\dot{\psi}_{2q} &= -\omega_0 R_{2q} \Delta i_{2q} \\
&= a_{61}\Delta\omega_r + a_{62}\Delta\delta + a_{63}\Delta\psi_{fd} + a_{64}\Delta\psi_{1d} \\
&\quad + a_{65}\Delta\psi_{1q} + a_{66}\Delta\psi_{2q}
\end{aligned} \tag{A.32}
$$

Where,

$$
\begin{aligned}
a_{61} &= 0 \\
a_{62} &= -\frac{\omega_0 R_{2q}}{L_{2q}} n_1 L''_{aqs} \\
a_{63} &= -\frac{\omega_0 R_{2q}}{L_{2q}} n_2 L''_{aqs} \\
a_{64} &= -\frac{\omega_0 R_{2q}}{L_{2q}} n_3 L''_{aqs} \\
a_{65} &= -\frac{\omega_0 R_{2q}}{L_{2q}} \left(n_4 L''_{aqs} - \frac{L''_{aqs}}{L_{1q}} \right) \\
a_{66} &= -\frac{\omega_0 R_{2q}}{L_{2q}} \left(1 - \frac{L''_{aqs}}{L_{2q}} + n_5 L''_{aqs} \right)) \qquad \text{(A.33)}
\end{aligned}
$$

The complete state equation is given by,

$$
\begin{vmatrix} \Delta\dot{\omega}_r \\ \Delta\dot{\delta} \\ \Delta\dot{\psi}_{fd} \\ \Delta\dot{\psi}_{1d} \\ \Delta\dot{\psi}_{1q} \\ \Delta\dot{\psi}_{2q} \end{vmatrix} = \begin{vmatrix} a_{11} & a_{12} & a_{13} & a_{14} & a_{15} & a_{16} \\ a_{21} & 0 & 0 & 0 & 0 & 0 \\ 0 & a_{32} & a_{33} & a_{34} & a_{35} & a_{36} \\ 0 & a_{42} & a_{43} & a_{44} & a_{45} & a_{46} \\ 0 & a_{52} & a_{53} & a_{54} & a_{55} & a_{56} \\ 0 & a_{62} & a_{63} & a_{64} & a_{65} & a_{66} \end{vmatrix} \begin{vmatrix} \Delta\omega_r \\ \Delta\delta \\ \Delta\psi_{fd} \\ \Delta\psi_{1d} \\ \Delta\psi_{1q} \\ \Delta\psi_{2q} \end{vmatrix} + \begin{vmatrix} b_{11} & 0 \\ 0 & 0 \\ 0 & b_{32} \\ 0 & 0 \\ 0 & 0 \\ 0 & 0 \end{vmatrix} \begin{vmatrix} \Delta T_m \\ \Delta E_{fd} \end{vmatrix} \qquad \text{(A.34)}
$$

A.2 Generator Equation Part II

All the generators of the power system are represented using the sub-transient models with four equivalent rotor coils. The mechanical torques to the generators are considered as constant inputs.

$$\frac{d\delta_i}{dt} = \omega_B(\omega_i - \omega_s) = \omega_B S_{mi} \tag{A.35}$$

$$2H_i \frac{dS_{mi}}{dt} = (T_{mi} - T_{ei}) - D_i S_{mi} \tag{A.36}$$

Where,

$$\begin{aligned} T_{ei} = E'_{di} I_{di} \frac{(X''_{qi} - X_{lsi})}{(X'_{qi} - X_{lsi})} + E'_{qi} I_{qi} \frac{(X''_{di} - X_{lsi})}{(X'_{di} - X_{lsi})} - I_{di} I_{qi} \\ (X''_{di} - X''_{qi}) + \psi_{1di} I_{qi} \frac{(X'_{di} - X''_{di})}{(X'_{di} - X_{lsi})} - \psi_{2qi} I_{di} \frac{(X'_{qi} - X''_{qi})}{(X'_{qi} - X_{lsi})} \end{aligned} \tag{A.37}$$

and,

$$\begin{aligned} I_{qi} + jI_{di} = \frac{1}{R_{ai} + jX''_{di}} \Bigg(E'_{qi} \frac{(X''_{di} - X_{lsi})}{(X'_{di} - X_{lsi})} \\ + \psi_{1di} \frac{(X'_{di} - X''_{di})}{(X'_{di} - X_{lsi})} - V_{qi} + j \Bigg[E'_{di} \frac{(X''_{qi} - X_{lsi})}{(X'_{qi} - X_{lsi})} \\ + \psi_{2qi} \frac{(X'_{qi} - X''_{qi})}{(X'_{qi} - X_{lsi})} - V_{di} + E'_{dci} \Bigg] \Bigg) \end{aligned} \tag{A.38}$$

and,

$$T_{ci} \frac{dE'_{dci}}{dt} = I_{qi}(X''_{di} - X''_{qi}) - E'_{dci} \tag{A.39}$$

The other differential equations are:

$$T'_{q0i}\frac{dE'_{di}}{dt} = -E'_{di} + (X_{qi} - X'_{qi})\Bigg(- I_{qi} + \frac{(X'_{qi} - X''_{qi})}{(X'_{qi} - X_{lsi})^2} \Big[(X'_{qi} - X_{lsi})I_{qi} - E'_{di} - \psi_{2qi}\Big] \Bigg) \tag{A.40}$$

$$T'_{d0i}\frac{dE'_{qi}}{dt} = E_{fdi} - E'_{qi} + (X_{di} - X'_{di})\Bigg(I_{di} + \frac{(X'_{di} - X''_{di})}{(X'_{di} - X_{lsi})^2} \Big[\psi_{1di} - (X'_{di} - X_{lsi})I_{di} - E'_{qi}\Big] \Bigg) \tag{A.41}$$

$$T''_{d0i}\frac{d\psi_{1di}}{dt} = E'_{qi} + (X'_{di} - X_{lsi})I_{di} - \psi_{1di} \tag{A.42}$$

$$T''_{q0i}\frac{d\psi_{2qi}}{dt} = -E'_{di} + (X'_{qi} - X_{lsi})I_{qi} - \psi_{2qi} \tag{A.43}$$

Here,

The subscript i in the above equations refers to the i^{th} generator

δ is the rotor angle in radians

ω_B is the rotor baase angular speed in radians per second

ω is rotor angular velocity

ω_s is the synchronous angular velocity

S_m is the slip

H is the inertia constant in seconds

T_m is the mechanical torque

T_e is the electrical torque

D is the machine rotor damping

E'_d is the transient emf due to flux linkage in q-axis damper coil

E'_q is the transient emf due to field flux linkages

ψ_{1d} and ψ_{2q} are the sub-transient emfs due to d-axis and q-axis damper coils

E_{fd} is the field excitation voltage

E'_{dc} is the transient emf across the dummy rotor coil

I_d and I_q are the d-axis and q-axis components of the stator current respectively

V_d and V_q are the d-axis and q-axis components of the stator terminal voltage respectively

X_d, X'_d and X''_d are synchronous, transient and sub-transient reactances along the d-axis respectively

Similarly, X_q, X'_q and X''_q are synchronous, transient and sub-transient reactances along the q-axis respectively

R_a is the armature resistance

X_{ls} is the armature leakage reactance

T'_{d0} and T''_{d0} are d-axis open circuit transient and sub-transient time constants in seconds

Similarly, T'_{q0} and T''_{q0} are q-axis open circuit transient and sub-transient time constants in seconds

Finally, T_c is time constant for dummy rotor coil

A.3 Excitation Systems (AVR)

Two types of automatic voltage regulators (AVR) are used for excitation of the generators. They are IEEE standard DC exciter (DC4B) and the second type is the standard static exciter (ST1A). The differential equations for IEEE-DC4B excitation system are following:

$$T_{fd}\frac{dE_{fd}}{dt} = V_a - (K_e E_{fd} + E_{fd} A_{ex} e^{B_{ex} E_{fd}}) \tag{A.44}$$

Where, $E_{fdmin} \leq V_a \leq E_{fdmax}$

$$T_r \frac{dV_r}{dt} = V_t - V_r \tag{A.45}$$

$$T_f \frac{dV_f}{dt} = E_{fd} - V_f \tag{A.46}$$

$$T_a \frac{dV_a}{dt} = K_a V_{PID} - V_a \tag{A.47}$$

Where, $E_{fdmin}/K_a \leq V_{PID} \leq E_{fdmax}/K_a$

$$V_{PID} = \left(V_{ref} - V_r - \frac{K_f}{T_f}[E_{fd} - V_f]\right) \left[K_p + \frac{K_i}{s} + \frac{sK_d}{sT_d + 1}\right] \tag{A.48}$$

The following equations are for IEEE-ST1A excitation system:

$$E_{fd} = K_A(V_{ref} - V_r) \tag{A.49}$$

where, Where, $E_{fdmin} \leq E_{fd} \leq E_{fdmax}$

and,

$$T_r \frac{dV_r}{dt} = V_t - V_r \tag{A.50}$$

Here,

E_{fd} is the field excitation voltage

K_e is the exciter gain, K_f is the stabilizer gain and K_a is the dc regulator gain

T_{fd} is the exciter time constant, T_r is the input filter time constant, T_f is the stabilizer time constant and T_a is the regulator time constant

V_a is the regulator emf, V_r is the input filter emf and V_f is the stabilizer emf

A_{ex} and B_{ex} are the saturation constants

K_p, K_i, $K - d$ and $T - d$ are the PID-controller parameters

V_{ref} is the reference voltage and V_{PID} is the PID controller voltage

K_A is the static regulator gain

The states for the generators with IEEE-DC4B excitation systems are:

$$x = \begin{vmatrix} S_m \\ \delta \\ E'_d \\ E'_q \\ \psi_{1d} \\ \psi_{2q} \\ E_{fd} \\ V_r \\ V_f \\ V_a \\ V_{kd} \\ V_{ki} \end{vmatrix} \tag{A.51}$$

The states for the generators with IEEE-ST1A excitation systems are:

$$x = \begin{vmatrix} S_m \\ \delta \\ E'_d \\ E'_q \\ \psi_{1d} \\ \psi_{2q} \\ E_{fd} \\ V_r \end{vmatrix} \tag{A.52}$$

Input matrix u is:

$$u = \left| T_m \right| \tag{A.53}$$

Output matrix is:

$$y = \left| S_m \right| \tag{A.54}$$

A.4 Mapping states between two methods

Dynamic data and parameters are collected for different parts of the power system for model based methods. By performing power flow algorithm, initial states can be obtained. Then by solving linearized algebraic differential equation, a small signal stability analysis is performed and the system matrix can be achieved. Then by applying SVD, a reduced order model can be found. This system matrix is stored as the states are known for this matrix. Through measurement based method a reduced order matrix of similar order can be calculated. Then a transformation matrix method can be used to transform measurement based state space matrix to match with the model based method and the states of the measurement based method identification can be mapped. Fig. A.1 shows the overall method and also Section 5.3.3 of this work explains the transformation procedure.

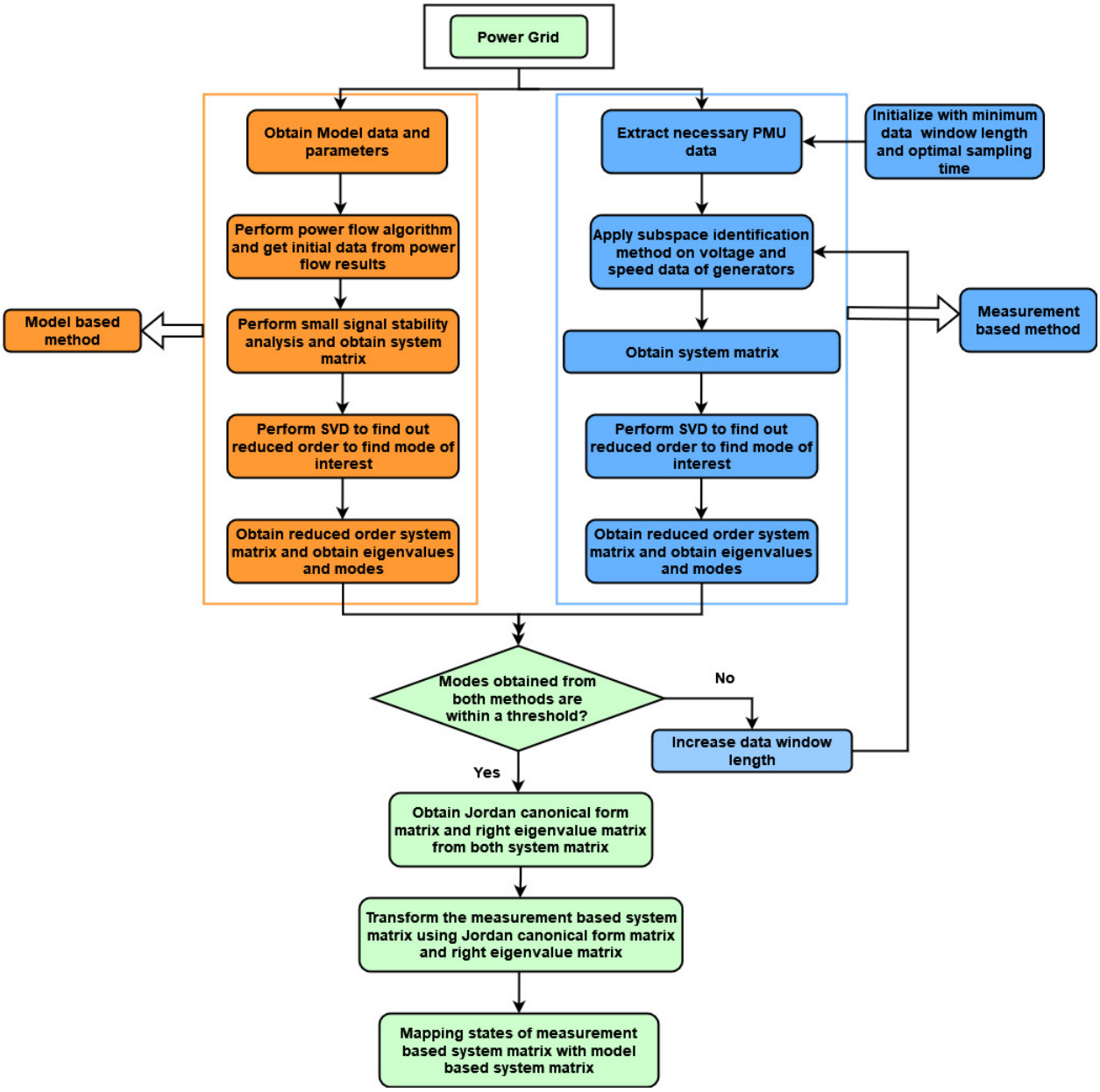

Fig. A.1: Mapping states from model based method and measurement based methods